Multiferroic oxide nanostructures : multi-resistance states

Anton Khanas

Sorbonne Université

Ecole doctorale 397 Physique et Chimie des Matériaux

Institut des NanoSciences de Paris
Couches Nanométriques: Formation, Interfaces, Défauts

Multiferroic Oxide Nanostructures: Multi-resistance States

Par Anton Khanas

Thèse de doctorat de Physique et Chimie des Matériaux

Dirigée par Prof. Dr. Nathalie Jedrecy

Présentée et soutenue publiquement le 30.01.2023

Devant un jury composé de:

Manuel Bibes	Directeur de Recherche, CNRS/Thales	Président du Jury
Nick Barrett	Directeur de Recherche, CEA-Saclay	Rapporteur
Maximilien Cazayous	Professeur des Universités, Université Paris Cité	Rapporteur
Brahim Dkhil	Professeur, CentraleSupelec	Examinateur
Nathalie Jedrecy	Professeur des Universités, Sorbonne Université	Directrice de Thèse

Résumé étendu

La multitude de matériaux disponibles dans l'univers et le large spectre de propriétés physico-chimiques afférentes a conduit à la conception de dispositifs de plus en plus élaborés, dans des secteurs aussi divers que l'aéronautique, le génie civil, l'énergie, la microélectronique, le biomédical, pour n'en citer que quelques-uns. Un des défis auxquels se sont attelés les scientifiques a été de multiplier les fonctionnalités au sein d'un même dispositif électronique, de plus en plus réduit en taille (sub-micrométrique notamment). Néanmoins, certaines propriétés physiques sont parfois antagonistes, c'est le cas du ferromagnétisme versus la ferroélectricité. De très rares matériaux, dits multiferroïques, possèdent ces deux propriétés, mais l'une au détriment de l'autre. Pour pallier à des performances généralement très réduites à température ambiante, un contournement possible est d'utiliser une combinaison de deux matériaux différents, possédant chacun la propriété désirée, utilisable sur une large gamme de températures.

Le fonctionnement actuel de notre société induit le développement exponentiel d'appareils d'informatique, de détection, d'actionnement, de connexion / communication. La plupart de ces appareils s'appuient sur une électronique miniaturisée, mais leur utilisation incessante et mondiale commence à générer un coût énergétique - et en ressources premières - non négligeable. Bien que l'énergie consommée par opération logique dans un transistor (technologie CMOS) ne soit que de l'ordre de 100 pJ, si la demande et la consommation de composants électroniques continuait à augmenter, la consommation totale d'énergie primaire via la microélectronique pourrait atteindre 20% d'ici à 2030, alors qu'elle n'est encore aujourd'hui que de 5%. Dans le même temps, un nouveau paradigme a vu le jour : la conception d'architectures de traitement/stockage des données sans explicite programmation des tâches («machine-learning» et intelligence artificielle). Des réseaux de connexion plus «intelligents» ou des composants électroniques radicalement nouveaux par rapport à la technologie CMOS actuelle pourraient permettre une réduction de la consommation énergétique. C'est le défi qui s'impose en partie aux scientifiques, notamment via la conception de composants qui combineraient en un seul dispositif logique et mémoire.

Les dispositifs multiferroïques, combinant ferromagnétisme et ferroélectricité, sont à la croisée de différentes recherches/avancées. D'une part, un contrôle électrique direct ou indirect du magnétisme entrainerait une réduction de l'énergie consommée par les mémoires magnétiques (c'est la voie du couplage magnéto-électrique) ; d'autre part, une manipulation continue à l'aide de faibles tensions de la résistance des mémoires résistives permettrait des avancées majeures pour le traitement optimisé des données et le développement de l'intelligence artificielle (c'est la voie des «memristors»). L'idée sous-jacente est de se rapprocher du système neuronal biologique idéal où l'information reçue est non seulement traitée, mémorisée, mais aussi génératrice

de nouveaux apprentissages (apprentissage non-supervisé).

Cette thèse, effectuée à l'INSP, se situe en amont des développements sur les dispositifs-mémoires commercialisables. Elle concerne l'élaboration et l'étude de jonctions multiferroïques à base de couches atomiques d'un oxyde ferroélectrique $BaTiO_3$ (*a priori* isolant) et d'un oxyde ferromagnétique (La,Sr)MnO_3 (*a priori* métallique), sous la forme finale de l'empilement (La,Sr)MnO_3 / $BaTiO_3$ / (La,Sr)MnO_3. Nous nous efforçons de décrire les mécanismes sous-jacents au comportement de ces jonctions soumises à excitation électrique ou magnétique.

Après lithographie des jonctions sous forme de «μ-devices», de multiples états de résistance électrique peuvent être obtenus en fonction du stimulus appliqué (tension électrique ou champ magnétique). La réponse en tension dépend des épaisseurs de jonction considérées et de la concentration de défauts inhérents à la croissance des couches oxydes : réponse stochastique ou quasi-analogue, basée respectivement sur une conduction sous forme de nano-filaments ou sur un transport en partie tunnel à travers la barrière oxyde.

En particulier, nous avons conçu des «memristors» aux multiples états de résistance (quasi-continus) et dont la réponse dynamique aux impulsions de tension est du second ordre. La dynamique mise en évidence présente de fortes analogies avec celle des synapses neuronales. Un processus d'oxydo-réduction des ions Mn aux interfaces induirait le changement quasi-continu et stabilisé des états de résistance sur le long terme, tandis que la polarisation électrique de $BaTiO_3$ et la diffusion des lacunes d'oxygène interviendraient dans les processus à court terme. La résistance de la jonction s'apparente au poids synaptique entre neurones biologiques, avec potentialisation ou déplétion à court ou à long terme, selon la stimulation.

Le memristor de second-ordre mis en évidence au cours de cette thèse pourrait constituer la brique d'un système informatique «matériel» neuro-morphique, capable de résoudre dans le futur des tâches perceptives ou comportementales complexes avec des besoins en énergie particulièrement faibles.

Le manuscrit est organisé suivant 7 chapitres principaux.

Le chapitre 1 présente les défis à relever dans le domaine des processeurs et mémoires électroniques, dont le fameux memristor («memory» + «resistor»), ainsi que l'état de l'art dans la conception de jonctions donnant lieu à une commutation résistive, basées sur différents matériaux. En particulier, la distinction est faite entre les jonctions où le transport électrique est réalisé via des filaments (après étape de pré-formation), les jonctions où les changements de résistance sont liés à un changement de phase du matériau, et enfin les jonctions où le transport s'effectue par effet tunnel, c'est-à-dire les jonctions magnétiques tunnel (MTJs) et les jonctions ferroélectriques tunnel (FTJs). Dans ces deux derniers cas, les changements de résistance liés respectivement à l'orientation des aimantations des électrodes ferromagnétiques impliquées ou à l'orientation de la polarisation du ferroélectrique en couche barrière sont expliqués. Le cas particulier des jonctions multiferroiques qui peuvent combiner les deux effets de magnétorésistance tunnel (TMR) et d'électrorésistance tunnel (TER) conclue le chapitre.

Le chapitre 2 décrit la structure et les propriétés particulières (état de l'art) des deux matériaux utilisés dans cette thèse, en particulier dans le contexte des couches

minces ou très minces. La ferroélectricité de $BaTiO_3$ ainsi que son caractère isolant peuvent notamment être altérés ou masqués par la présence de lacunes d'oxygène, qui peuvent aisément migrer en présence d'un champ électrique. Le ferromagnétisme de (La,Sr)MnO_3, associé à sa demi-métallicité et au caractère fortement corrélé des électrons impliqués dans le transport (mécanisme de double-échange via les ions oxygène), est lui fortement dépendant du rapport existant entre cations Mn^{4+} et Mn^{3+}. Ce rapport est *a priori* déterminé par le taux d'insertion d'ions Sr^{2+} dans la structure, mais aussi dépendant de la stoechiométrie du film formé (i.e. du taux de lacunes d'oxygène). Enfin, une présentation des résultats antérieurs à la thèse - dont ceux obtenus par l'équipe - avec le système $BaTiO_3$ / (La,Sr)MnO_3 est faite : polarisation native de $BaTiO_3$ orientée vers la couche (La,Sr)MnO_3, présence d'une couche interfaciale mixte ($\sim$2$-$3 nm) avec substitution des ions Ba par (La,Sr) et substitution des ions Ti par Mn, réduction de la valence des ions Mn dans la couche interfaciale. La commutation résistive du système Au / $BaTiO_3$ / (La,Sr)MnO_3 est expliquée par un processus redox (réduction/oxydation) sous champ à l'interface, avec une migration probable des lacunes d'oxygène.

Le chapitre 3 est dévolu à la présentation des différentes techniques expérimentales utilisées. Tout d'abord, les conditions de croissance des couches oxydes sous forme de jonctions par la méthode de déposition laser pulsée (PLD) sont présentées. Puis, le processus de lithographie des jonctions pour obtenir les µ-dispositifs finaux utilisés lors des mesures électriques est détaillé. Ensuite, les techniques de caractérisation structurale/chimique sont présentées : diffraction de rayons X (XRD) et réflectivité X puis spectroscopie de rétrodiffusion d'ions (RBS). Enfin, les appareils utilisés pour les mesures de transport électrique avec ou sans champ magnétique et jusqu'aux températures cryogéniques sont brièvement décrits.

Le chapitre 4 est consacré à la présentation des caractéristiques physiques des jonctions élaborées par PLD sur différents substrats $SrTiO_3$ et MgO, avec différentes épaisseurs de barrière $BaTiO_3$ et/ou des conditions de croissance légèrement variées. En préambule, une étude comparative par microscopie à force atomique (AFM) des surfaces des films obtenus sur des substrats $SrTiO_3$ préparés chimiquement ou pas est présentée, qui conclut à la non-pertinence de cette préparation préalable des substrats dans le cadre des jonctions finales étudiées. Ensuite, les résultats de la caractérisation par diffraction de rayons X des jonctions est donnée : détermination des paramètres de maille de la barrière $BaTiO_3$ et des électrodes supérieure et inférieure de (La,Sr)MnO_3. La réflectivité X est par ailleurs utilisée pour déterminer les épaisseurs des couches mais aussi extraire la rugosité moyenne aux deux interfaces supérieure et inférieure. La technique RBS permet de vérifier les épaisseurs des couches et leur composition. Quelques images/analyses chimiques de microscopie électronique en transmission sont données à titre de confirmation des conclusions tirées des analyses précédentes. Enfin, une présentation détaillée des propriétés magnétiques à différentes températures des jonctions élaborées suit, mettant en exergue le comportement différencié de l'aimantation due à chacune des couches de (La,Sr)MnO_3, dans les deux cas d'une barrière $BaTiO_3$ épaisse et fine. En particulier, la présence de couches interfaciales, avec une réponse au champ magnétique différenciée, est mise en évidence dans le cas des jonctions fines.

Le chapitre 5 est centré sur les résultats de commutation résistive (électro- et

magnéto-résistance) obtenus dans le cas des jonctions épaisses. Les principes de la mesure du courant I et de la résistance R de la jonction obtenus à la suite d'une tension appliquée V sont rappelés. Généralement, les courbes $I(V)$ et $R(V)$ prennent la forme d'un cycle hystérèse entre deux états de haute (HRS) et faible (LRS) résistance, la jonction se trouvant avant excitation électrique dans un état HRS. Selon le dispositif testé, la commutation sur 3 ordres de grandeur de résistance entre les deux états HRS et LRS est plus ou moins reproductible et stabilisée dans le temps. Une observation récurrente pour tous les dispositifs testés est le caractère abrupte de la commutation HRS $\rightarrow$ LRS sous l'effet de pulses de tension positive (excédant une valeur seuil), tandis que la commutation LRS $\rightarrow$ HRS s'établit sous la forme d'une succession aléatoire de sauts. Par ailleurs la conduction est de type tunnel direct pour l'état HRS - avec une épaisseur de barrière très significativement inférieure à l'épaisseur effective de $BaTiO_3$ - et ohmique pour l'état LRS. L'ensemble des observations permet de conclure sur la formation de nano-filaments conducteurs dans l'état LRS tandis que leur rupture conduit à l'état HRS, généré par la présence permanente d'une couche intermixée isolante (3 nm) à l'interface inférieure. Enfin, nous mettons en évidence sur la base de mesures de magnétorésistance à différentes températures et pour différentes orientations du champ magnétique la présence de deux couches interfaciales, vraisemblablement aux deux interfaces, à l'origine d'une magnétorésistance intrinsèque de faible intensité.

Le chapitre 6 est consacré aux résultats de commutation résistive (électrorésistance) obtenus dans le cas des jonctions fines. A contrario des jonctions épaisses, l'hystérèse de commutation s'opère toujours dans le sens LRS $\rightarrow$ HRS, l'état LRS étant l'état initial stable du système. Selon le dispositif testé sur l'échantillon, l'ordre de grandeur du rapport de résistance HRS/LRS peut varier de plus de 10^3 à 1.4 (aux basses températures), et la jonction présenter corollairement un caractère semi-conducteur (SC) ou métallique. Un modèle phénoménologique universel du transport électrique au travers des jonctions est proposé, basé sur une conduction en parallèle impliquant une partie diélectrique pure (à l'origine de la forte électro-résistance) et une partie de fuite (à l'origine des performances possiblement dégradées de la jonction vis-à-vis de la valeur d'électro-résistance finale).

Quel que soit le caractère de la jonction (SC ou métallique), la reproductibilité et stabilité des hystérèses LRS $\rightarrow$ HRS $\rightarrow$ LRS est remarquable. Le chapitre 6 (sections 6.3 et 6.4) décrit en détails la réponse «memristive» d'un archétype de jonction SC, faisant varier le nombre d'impulsions de tensions, la valeur maximale testée de celles-ci, la durée des impulsions. La reproductibilité et stabilité des multiples états de résistance possibles, ainsi que l'endurance du dispositif, sont également testés. L'appendice A de la thèse fournit les détails de la réponse « memristive » d'un archétype de jonction métallique, et dont le comportement reste similaire à celui des jonctions SC.

Le caractère novateur de notre étude par rapport à la littérature abondante au sujet des «memristors» réside dans l'analyse (section 6.5) que nous menons de l'évolution de la résistance en fonction du temps suite à une impulsion isolée de tension et à l'interprétation qui s'ensuit de cette évolution – au niveau du matériau.

Tout d'abord, nous analysons les courbes $I(V)$ conformes dans les deux états HRS et LRS à une conduction de type tunnel à travers la barrière, qui dans ce cas précis des jonctions fines excède légèrement l'épaisseur effective de $BaTiO_3$ déposé

(4.3 nm au lieu de 2.4 nm), en conformité avec la présence d'une couche inter-mixée à l'interface avec l'électrode inférieure (cf. chap. 4−5). La réponse en fonction du temps de la résistance du dispositif soumis à une brève impulsion de tension ($V > 0$ ou $V < 0$ pendant 1 ms) est ensuite analysée ; selon la polarité, la valeur de la résistance croît ou décroît abruptement puis décroît ou croît sur la base de deux ou une fonction exponentielle(s), deux constantes de temps de relaxation de 1 et 27 s étant clairement impliquées dans le cas de la polarité positive (contre 7 s pour la polarité négative). Les valeurs finales de résistance sont majorées ($V > 0$) ou diminuées ($V < 0$) par rapport à la valeur initiale. La répétition séquentielle des pulses isolés de tension suivis de la relaxation permettent une évolution quasi-continue de la valeur de la résistance. Ces mesures démontrent, outre le changement memristif sur le long terme, l'existence d'états transitoires lorsque le dispositif a été soumis à un champ électrique. Nous interprétons ces résultats par le modèle qui suit. Sous l'effet d'un pulse de tension positive, la polarisation (initialement vers le bas) commute vers le haut, induisant la hausse abrupte de la résistance. La polarisation vers le haut est cependant un état instable du système, ce qui est corroboré par les mesures de microscopie à force piezoélectrique (PFM) qui révèlent clairement l'existence d'un champ permanent. S'ensuit un retournement naturel de la polarisation vers le bas (lorsque le champ n'est plus appliqué) avec une constante de temps de l'ordre d'1 seconde. Tenant compte du fait que la stabilisation momentanée de la polarisation vers le haut induit un écrantage des charges liées positives à l'interface supérieure et donc une oxydation partielle des ions Mn^{3+} en Mn^{4+}, l'élévation de la résistance à cette interface explique la hausse globale de résistance observée. L'effet inverse qui doit s'opérer à l'interface inférieure est vraisemblablement atténué par le fait que cette interface inférieure est déjà fortement inter-mixée et de caractère isolant. La seconde relaxation de l'état de résistance observée pour $V > 0$ serait due à une diffusion des lacunes d'oxygène accumulées à l'interface supérieure sous l'effet du champ appliqué. Dans le cas d'un pulse appliqué de tension négative, seule la diffusion des lacunes d'oxygène est impliquée dans le processus de relaxation de la résistance.

Le chapitre 7 est dévolu à la description des effets de second-ordre du dispositif «memristor» détaillé dans le chapitre 6. En effet, la dynamique particulière de notre dispositif (induite par l'instabilité de l'orientation vers le haut de la polarisation dans la couche $BaTiO_3$) permet différentes manipulations de l'état de résistance, en étroite connexion avec celles qui s'opèrent naturellement dans les synapses biologiques, et qui constituent l'interconnexion entre neurones individuels.

En effet, le memristor est un dispositif électronique à deux bornes, dont la résistance peut être réglée de manière continue au moyen d'une tension externe, tout en étant stockée de manière non volatile. Ces deux caractéristiques figurent la plasticité synaptique, c'est-à-dire la modulation de l'intensité du signal («spike») transmis depuis un pré-neurone vers le post-neurone, et la conservation dans le temps de l'état de la synapse. L'apprentissage humain consiste en la variation du poids (i.e. le renforcement ou l'inhibition) des différents contacts synaptiques. Pour simuler le degré de transmission des synapses biologiques, la variable de premier ordre dans le cas d'un memristor est sa conductance/résistance. Utilisant des pulses de tension ou des profils temporels de tension adéquats, un certain nombre de fonctions synaptiques, telles la potentiation/dépression à long terme (LTP/LTD) ou la plasticité dépendante d'intervalles entre «spikes» (STDP), peuvent être réalisées. Nous avons

montré les effets LTP/LTD au chapitre 6.

Dans les systèmes biologiques réels, la transmission d'un signal électrique (le potentiel d'action) s'opère par la libération par un pre-neurone de neurotransmetteurs dans la fente synaptique et la re-capture de ces derniers par le post-neurone, via une séquence complexe d'évènements : ouverture de canaux perméables aux ions au niveau des membranes cellulaires, fusion de vésicules,... En particulier, la sensibilité du poids synaptique aux stimuli dépend de la concentration d'ions Ca^{2+}, qui monte sous l'effet du stimuli puis décroît de manière exponentielle dans une plage de 10^{-3} à 100 s. Cet effet fournit les conditions transitoires pour un réglage de la transmission sur une courte échelle de temps, avec - ou pas - des effets à long terme. Des réponses aux stimuli similaires à celles des synapses peuvent être réalisées avec des memristors dits de second ordre, pour lesquels l'application de tension agit directement sur une variable de second ordre qui, à son tour, va influencer la variable de premier ordre. Dans le cas de notre memristor, la résistance s'apparente au poids synaptique. Le facteur qui détermine la résistance à long terme est le degré de réduction/oxydation des deux couches d'interface à l'équilibre, en raison (i) de la migration des lacunes d'oxygène et du changement de polarisation induit par la tension, puis (ii) de la diffusion des lacunes et de la dépolarisation. Le piégeage/dépiégeage des charges au niveau des couches LSMO accompagne ces processus de (i) stimulation et de (ii) relaxation. La réponse temporelle de notre memristor pendant et après la stimulation est déterminée par des effets de second et de premier ordre, comme dans les systèmes biologiques.

Différentes réponses synaptiques spécifiques du second ordre ont été émulées avec notre memristor. La première est celle de facilitation par paire d'impulsions (PPF). Lorsqu'une paire d'impulsions ($V > 0$) est envoyée, la résistance du dispositif va croître mais plus ou moins fortement suivant l'intervalle de temps entre les deux impulsions. Dit autrement, l'effet de deux pulses n'est pas simplement cumulatif mais exacerbé lorsque les intervalles de temps sont suffisamment courts. Nous mettons en évidence cette facilitation PPF non seulement sur des échelles de temps courtes mais aussi longues. La seconde réponse décrite est celle de la plasticité dépendante de la fréquence des impulsions (SRDP). Pour un train d'impulsions donné, selon que la fréquence utilisée soit courte (1 Hz par exemple) ou longue (150 Hz par ex.), le poids synaptique croîtra ou décroîtra. Ici, une particularité importante de l'évolution du poids synaptique sous l'effet d'un train d'impulsions est sa dépendance au train d'impulsions qui le précède, i.e. à «l'histoire» de la synapse. Si la fréquence du train précédent est plus élevée, alors le poids décroît tandis qu'il croît si la fréquence du train précédent est plus faible. En fonction de l'état du memristor (excitation préalable par un train d'impulsion à la fréquence f), il est nécessaire d'utiliser un train de fréquence plus élevé ($> f$) pour augmenter sa résistance. Ce phénomène peut être relié à l'apprentissage dans les synapses réelles, la force des connexions neuronales évoluant plus ou moins avec la répétitivité des stimulations. Ces mesures de plasticité dépendantes de l'expérience ont été inspirées par la théorie Bienenstock-Cooper-Munro (BCM) de la plasticité corticale. Dans le cadre BCM, la plasticité est contrôlée uniquement par l'activité postsynaptique déterminée par les impulsions présynaptiques.

L'émulation SRDP nécessite un memristor de second ordre. D'une manière différente, les effets des activités pré- et post-synaptiques sur une synapse, en fonction de leur «timing», peuvent être émulés par des expériences de plasticité dépendante

de celui-ci (STDP), que le memristor soit du premier ou du second ordre.

Conclusion :

Par la voie logicielle, certaines fonctionnalités du cerveau humain peuvent être émulées *via* des réseaux de neurones «artificiels». Des formes d'apprentissage encore plus sophistiquées peuvent de nos jours être envisagées avec la mise en œuvre «matérielle» de réseaux de composants électroniques, reproduisant le comportement des neurones et synapses biologiques. Les memristors de second-ordre, révélés au cours de ce travail de thèse, basés sur un empilement (jonction) de trois couches d'oxydes d'épaisseur nanométrique, peuvent être considérés comme de bons candidats pour émuler les synapses. Leur résistance peut être modulée à la hausse ou à la baisse en changeant uniquement la fréquence du train d'impulsions excitatrices, et pour une amplitude d'impulsions fixe. Cette plasticité est également dépendante de l'«histoire» du memristor, à savoir ses précédentes potentialisation / dépression. Ce comportement est expliqué par le mécanisme suivant : la valeur de la résistance générée par les impulsions de tension est conditionnée par le degré d'oxydo-réduction aux deux interfaces de la couche barrière ferroélectrique avec les électrodes ferromagnétiques, des mécanismes transitoires de second-ordre étant à l'œuvre, notamment le retournement de la polarisation électrique et la diffusion de lacunes d'oxygène.

Nota Bene : Une partie des résultats de cette thèse ont été publiés (en accès libre) dans une revue internationale avec comité de lecture :

https://onlinelibrary.wiley.com/doi/full/10.1002/aelm.202200421

Acknowledgments

First of all, I would like to thank Christophe Testelin and Massimiliano Marangolo, successive directors of the Institute of Nanosciences of Paris (INSP), for welcoming me into the laboratory. I also thank members of the Doctoral School 397 of Sorbonne Université and its director Nadine Witkowski for providing me with the doctoral contract.

I am extremely grateful to my thesis supervisor, Nathalie Jedrecy. These three years have been a time of reevaluating many things I thought I was sure of, sometimes of intellectual struggle, but ultimately of learning and improving. I thank you for countless hours of discussions about science, work and life, and for freedom and support in work given to me. I will certainly remember your eternal commitment to the pedagogical approach of the country of Descartes.

I would like to thank the members of the thesis jury: Nick Barrett, Maximilien Cazayous, Brahim Dkhil and Manuel Bibes, who kindly agreed to report or examine the manuscript, and participate in the oral defense.

I deeply appreciate the help of Christian Hebert, who introduced me to the major part of equipment and everyday life at INSP and assisted in solving any issue I was facing. I thank you for the moments of reason and composure when some things seemed preposterous and overwhelming to me.

I am thankful to Loïc Becerra and Erwan Dandeu for their invaluable help and contribution in the cleanroom, and to David Hrabovsky for support and guidance with magnetic and low temperature measurements and, especially, programming of the source-measure units. Without you this work would not have been possible.

My gratitude also goes to SAFIR team at INSP for conducting RBS measurements and to Xavier Portier for his work with TEM and EELS.

I would like to acknowledge the help of Omar Ibder and Zechao Li from CentraleSupélec and Roman Khakimov from Moscow Institute of Physics and Technology who provided us with reference ferroelectric samples and greatly assisted in our understanding of ferroelectric measurements.

I thank the members of the thesis monitoring committee, Fabio Pietrucci, Laura Thevenard and Pierre-Eymeric Janolin. Although our meetings were happening only once a year, they have been of great value as a practice of public reports of the results and an outside view that allowed to improve my work.

I also thank all the colleagues at INSP who were kind to assist me with everyday operation.

I would also like to thank people that helped shape my way to the doctorate: my teachers, Mykola Babenko and Tariel Sanikidze, who showed me the beauty of physics and math; teachers, fellow students and colleagues at my *alma mater*, Moscow Institute of Physics and Technology, for incredible atmosphere of knowledge and opportunities; my first supervisor, Andrei Zenkevich, who guided me to the

world of modern science; and my best friend of over 10 years, Denys Miakota, with whom we started this journey together and who I wish best of luck in his future endeavors.

Finally, words cannot express my deepest gratitude to my family: my parents, my brother and my wife, Lena. Your love and support, the feeling that we are together despite the distance and difficulties, are the main reasons that kept me standing through these years.

Contents

Introduction **1**

1 State of the art **3**
1.1 Challenges in computing and memory . . . 3
1.2 Memristor: source of potential breakthrough . . . 6
1.3 Materials and emerging concepts in memory and neuromorphic devices 8
1.3.1 *Chemical switching: anion- and cation-based* . . . 8
1.3.2 *Phase-change memory* . . . 10
1.3.3 *Magnetoresistive devices* . . . 11
1.3.4 *Ferroelectric memory and neuromorphic devices* . . . 13
1.3.5 *Multiferroic materials and device concepts* . . . 16
1.4 Conclusion and project motivation . . . 18

2 Materials for thin films **19**
2.1 $BaTiO_3$: relevant features . . . 19
2.2 $La_{1-x}Sr_xMnO_3$: relevant features . . . 23
2.3 Properties of $BaTiO_3/La_{1-x}Sr_xMnO_3$ interface . . . 25
2.4 Conclusion . . . 29

3 Methods **31**
3.1 Growth and fabrication . . . 31
3.1.1 *Pulsed laser deposition* . . . 31
3.1.2 *Device fabrication* . . . 33
3.2 Material characterization methods . . . 34
3.2.1 *X-ray diffraction and reflectometry* . . . 34
3.2.2 *Atomic force microscopy* . . . 37
3.2.3 *Transmission electron microscopy* . . . 38
3.2.4 *Rutherford backscattering spectrometry* . . . 38
3.3 Electrical measurements . . . 40
3.4 Magnetic and low temperature measurements . . . 40

4 Preliminary characterization of experimental samples **43**
4.1 Growth of the films . . . 43
4.2 Structure, composition and morphology . . . 44
4.2.1 *Surface morphology* . . . 44
4.2.2 *Structural analysis* . . . 45
4.2.3 *X-ray reflectometry* . . . 52
4.2.4 *Rutherford backscattering spectrometry* . . . 53
4.2.5 *Cross-sectional microscopy* . . . 55

4.3 Magnetic properties . . . 57
4.3.1 *Thick barrier samples* . . . 57
4.3.2 *Thin barrier samples* . . . 62

5 Electro- and magnetoresistance in thick barrier junctions 65
5.1 Write-read experiments . . . 65
5.2 Conduction mechanism consideration . . . 68
5.3 Magnetoresistance experiments . . . 70

6 Analog resistive switching in thin barrier junctions 75
6.1 Write-read experiments . . . 75
6.2 Phenomenological model of conduction circuit . . . 78
6.3 Multilevel resistance . . . 81
6.4 Additional switching features . . . 84
6.5 Conduction and switching mechanism considerations . . . 86

7 Second order memristor for biorealistic emulation of synapses 93
7.1 Justification and prerequisites . . . 93
7.2 Paired-pulse facilitation . . . 95
7.3 Spike rate-dependent plasticity . . . 98
7.4 Spike timing-dependent plasticity . . . 104

8 Conclusions and perspectives 109
8.1 Short summary of the main results . . . 109
8.2 Some perspectives for future work . . . 110

A Appendix: Resistive switching and memristive data from additional devices 113
A.1 Additional semiconducting-like device . . . 113
A.2 Additional metal-like device . . . 117

Bibliography 123

Abbreviations 141

Symbols 143

List of Figures 145

List of Tables 149

Introduction

Microelectronic industry has provided an incredible breakthrough in the development of civilization over the past half century. However, the new challenges in this field, such as the processing and storage of large amounts of data, reducing device power consumption, or development of software and hardware for artificial intelligence, require an ever-increasing intensity of research in material science and electronic engineering.

Ferroic perovskite oxide materials are able to provide the necessary functionalities for the development of novel microelectronic device concepts, conducting proof-of-concept experiments and production of operating device prototypes. In this work, we concentrate on the study of $La_{1-x}Sr_xMnO_3$ / $BaTiO_3$ / $La_{1-x}Sr_xMnO_3$ multiferroic heterostructures. We investigate their resistive switching properties from various perspectives and propose the new concept in the framework of second order memristive systems, which may be of use in development of future hardware artificial neural networks.

Chapter 1 presents a review of the main problems of modern microelectronics, among which the emphasis is put on prospective non-volatile memory and memristors - devices, closely related to the former, but aimed at hardware implementation of artificial neural networks. The main concepts for realization of these devices are considered. In chapter 2 we briefly describe functional materials used in this work: from fundamentals to potential applications in the fields of non-volatile memory and memristors. Next, description of methods used to fabricate $La_{0.7}Sr_{0.3}MnO_3$ / $BaTiO_3$ / $La_{0.7}Sr_{0.3}MnO_3$ experimental samples, carry out the preliminary characterization of those, and obtain the key results of this work is given in chapter 3. Chapter 4 presents the results of preliminary characterization of the morphological, structural, composition and magnetic properties of the samples. In chapter 5 the results of electro- and magnetoresistance measurements of patterned multiferroic $La_{0.7}Sr_{0.3}MnO_3$ / BTO_3 / $La_{0.7}Sr_{0.3}MnO_3$ devices with a thick barrier are demonstrated. Chapter 6 presents in detail the properties of analog resistive switching in thin barrier devices, and the proposed switching mechanism. In chapter 7 we demonstrate the possibility of using thin barrier analog resistive switching device as a second-order memristor - an emerging concept of the neuromorphic devices with intrinsic temporal dynamics. Next, we summarize this work and outline possible routes for future research in the field. In appendix A we provide the resistive switching and memristive measurement data from additional experimental devices, in order to demonstrate reproducibility of the results and validity of the generalized model of the device operation.

Chapter 1

State of the art

1.1 Challenges in computing and memory

The golden age of microelectronics gave us many technological advances and shaped the modern world as we see it today. This period of intense progress was going on under the sign of Moore's law - the famous empirical pattern, noticed by one of the founders of Intel, Gordon Moore, according to which the number of transistors on a chip doubles every 2 years [1]. While the pure form of the trend - the transistor count - still applies, improvement of other important device parameters has significantly slowed down (**figure 1.1**) [2, 3]. The fundamental limitations of silicon technology began to appear at the 90 nm technology node, which made industry leaders turn to development of new electronic materials and led to creation of high-k/metal gate technology in CMOS production [4]. This marked the transition to an era of much more intense search for new materials and device concepts in order to keep the industry growing. Since then, as the microelectronic device feature size has been reducing further, the number of emerging physical and engineering problems has grown (including, but not limited to: transition from FinFET to gate-

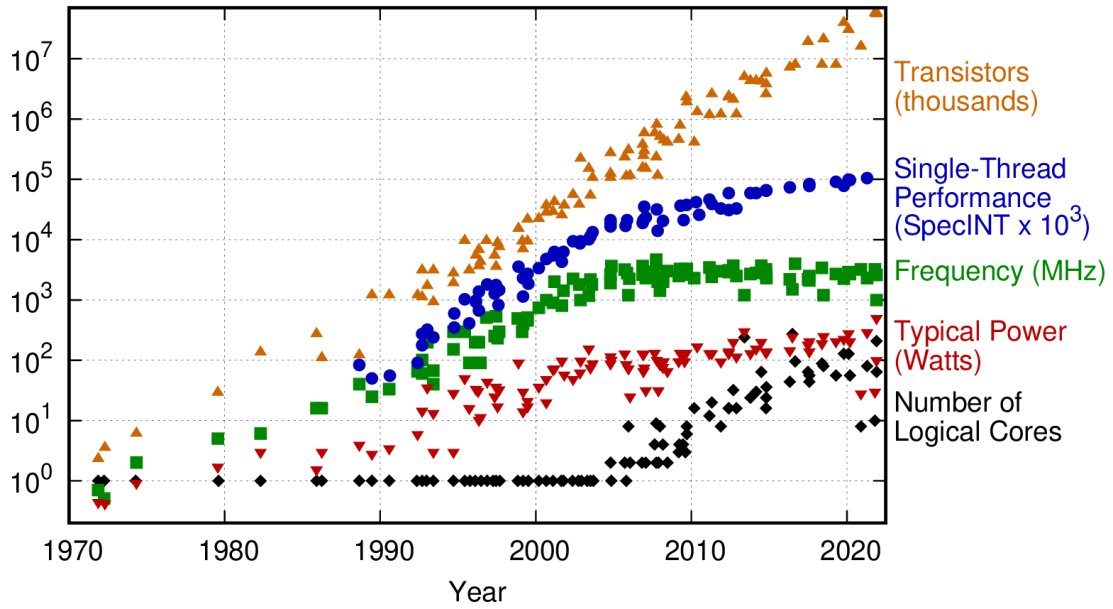

Figure 1.1: 50 years of microprocessor trend data, taken from ref.2 (updated in 2022 [3]).

all-around and nanowire transistors; integration of new high-k and ultra-high-k gate dielectrics; integration of low-k interlevel dielectrics for the metallization step to reduce the parasitic capacitance and latency; reduction of metal interconnect resistivity at nano-dimensions; achieving higher carrier mobility in semiconductors; full-fledged 3D integration [5]). These required more and more new developments at all levels: from fundamental materials science to industrial research and development.

However, the hardware issues, although primary, are not the only source of difficulties in information and communication technologies (ICT). The rate of information accumulation in the world nowadays is unprecedented. This requires production of growing amounts of consumer devices, data centers for data storage and processing, development of communication networks. The main problem here is energy consumption. It has been estimated that, with current rate of technological progress, 21% of the world's electric power generation will be occupied by ICT infrastructure by 2030 [6] (**figure 1.2**). This challenge requires to concentrate particular efforts on the development of energy efficient electronic devices and information processing paradigms.

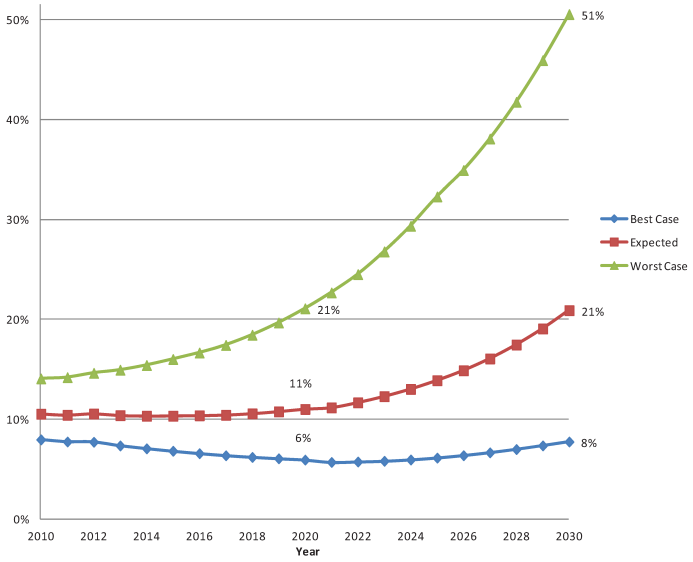

Figure 1.2: Share of communication technology of global electricity usage 2010–2030, taken from ref.6.

Another set of issues emerged at the intersection of hardware and computing architectures. It has been noticed [7, 8], that processors surpass dynamic random access memory (DRAM) in the operation speed growth rate, and the discrepancy is growing year by year (**figure 1.3**). This means that intense data transferring to and from the memory puts significant limitations on the overall computing device performance, despite the major progress in processor development. The effect is referred to as the *memory wall* or the *von Neumann bottleneck*, since it is one of the fundamental properties of the classical von Neumann computing paradigm that logic and memory units are separated and all the operations are performed sequentially [9]. Many efforts have been made to get around it, for example, multi-core processor organization, that allowed to perform the computations in parallel threads, or introduction of additional cache levels, that reduced the memory latency to some extent. However, eventually this fundamental limit is still going to affect the device performance, triggering the search for not only alternative architectures

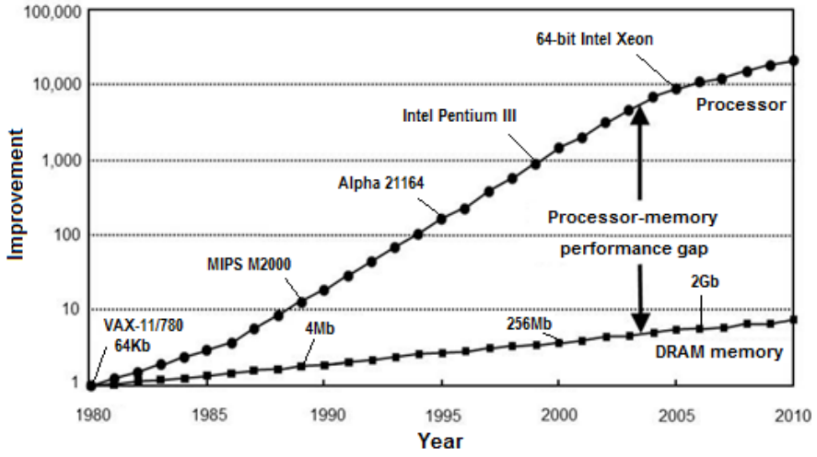

Figure 1.3: Yearly improvement of processor and DRAM memory speeds, for a time period of three decades, taken from ref.8.

of the processing units, but also for novel memory device concepts that would solve the issue by design. The so called *in-memory computation* devices are one of such solutions [10, 11]. In this concept, the logic and memory are combined in a single elementary device, what completely eliminates the problem of data transfer between isolated processing and memory units.

A problem, closely related to von Neumann bottleneck, arose with widespread implementation of artificial neural network (ANN) algorithms. ANNs were inspired by biological brains operation, mechanisms of which started to be unveiled in the middle of the 20th century [13,14]. Brain-like algorithms have provided a huge boost in efficiency of conventionally complex tasks, such as pattern recognition, optimization, natural language processing and many more, so nowadays they are an integral part of the technologies that are used in our everyday life [15]. However, purely software ANNs, while already showing significant efficiency, are still very limited in number of neurons and synapses, in comparison to human brain (**figure 1.4**).

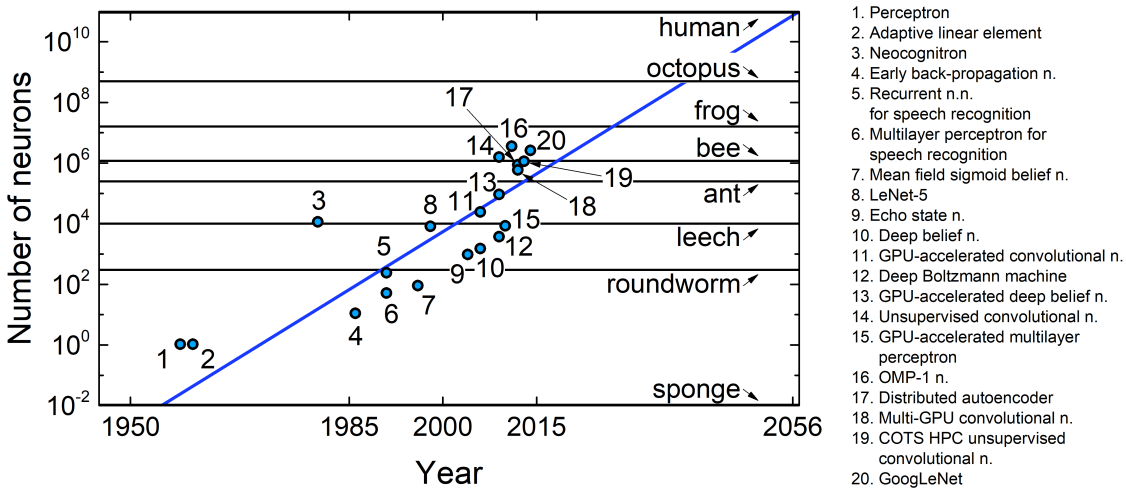

Figure 1.4: Artificial neural network size increase over time (circles). Correspondence of labels to computer model names is given in the legend ("(n.)n." is short for "(neural) network"), blue line shows the exponential trend. Black lines indicate the neural network size of different species. Adapted from ref.12.

Number of synaptic connections per neuron has already increased close to human brain level, however effective number of neurons is projected to reach the latter with current progress rate only by 2056 [12] - which could be postponed even more due to the mentioned Moore's law slowdown. Together with von Neumann bottleneck, which also has an effect here due to necessity in an intense data transfer for model weights updates, this became a drive for development of various hardware implementations of ANNs. Historically, the first idea here was to emulate neuronal behavior with a set of conventional CMOS transistors, which led to the most elaborate solutions to date [16, 17]. However, these realizations are usually very large scale and store parameters of the trained model in a conventional way. This is the reason why particular interest of researchers and engineers is drawn to the concept of *memristor* - device, resistance of which may be modulated by amount and history of electric charge flow through it.

1.2 Memristor: source of potential breakthrough

The concept of memristor was first proposed by Leon Chua in 1971 [18]. It emerged as a result of an observation, that if four fundamental circuit parameters - i (current), v (voltage), q (charge) and ϕ (flux) - are considered, six simple pairwise relation combination for those are mathematically possible. Two of those are the definitions: of current $\dot{q} = i$ and of the flux $\dot{\phi} = v$, where the relation is made through time derivation. Three more simple relations define the fundamental passive two-terminal circuit elements, namely, resistor, capacitor and inductor:

$$v = Ri, q = Cv, \phi = Li,$$

respectively, where R is resistance of the resistor, C is capacitance of the capacitor and L is inductance of the inductor. Thus, one of the possible relations remains unused, for which the *memristance* M is defined as:

$$\phi = Mq,$$

that is said to characterize an initially missing fundamental two-terminal circuit element - memristor. It is interesting to note, that differentiating the last equation over time, with the use of other relations, we obtain:

$$v = M(q)i,$$

which is a kind of Ohm's law for memristor, but here the memristance M acts as resistance, which value at any moment in time t may be dependent on the history of the charge, that was flowing through the memristor up to the moment t. This observation marked the birth of the memristor as the resistor, resistance of which may be tuned and memorized, hence the name *memristor* = *memory* + *resistor*.

However, later it was shown, that the simple relation between ϕ and q is not in a full agreement with the initial memristor definition, so it was revised [19]. In the updated understanding, the concepts of conventional resistors, capacitors and inductor are expanded to take into account possible dependence on the operation history of resistance, capacitance and inductance, respectively. Thus, the concepts of memristor, memcapacitor and meminductor were settled as the generalization of three fundamental two-terminal circuit elements with memory.

◆ An experimental realization of the memristor was first demonstrated by Hewlett-Packard Labs in 2008 [22] on the basis of the emerging resistive random access memory (ReRAM), in which the resistance states of the memory cell are switched with voltage. It was quickly realized that ReRAM devices are fully analogous to memristors [23], and that memristors may be used as a compact hardware implementation of both synapses [20, 24] (**figure 1.5**) and neurons [25, 26]. Since it is possible in principle to integrate memristors in the up-to-date fabrication nodes, this discovery opened the route to compact hardware ANNs and marked the beginning of the search for the most efficient and technologically viable realization of memristors.

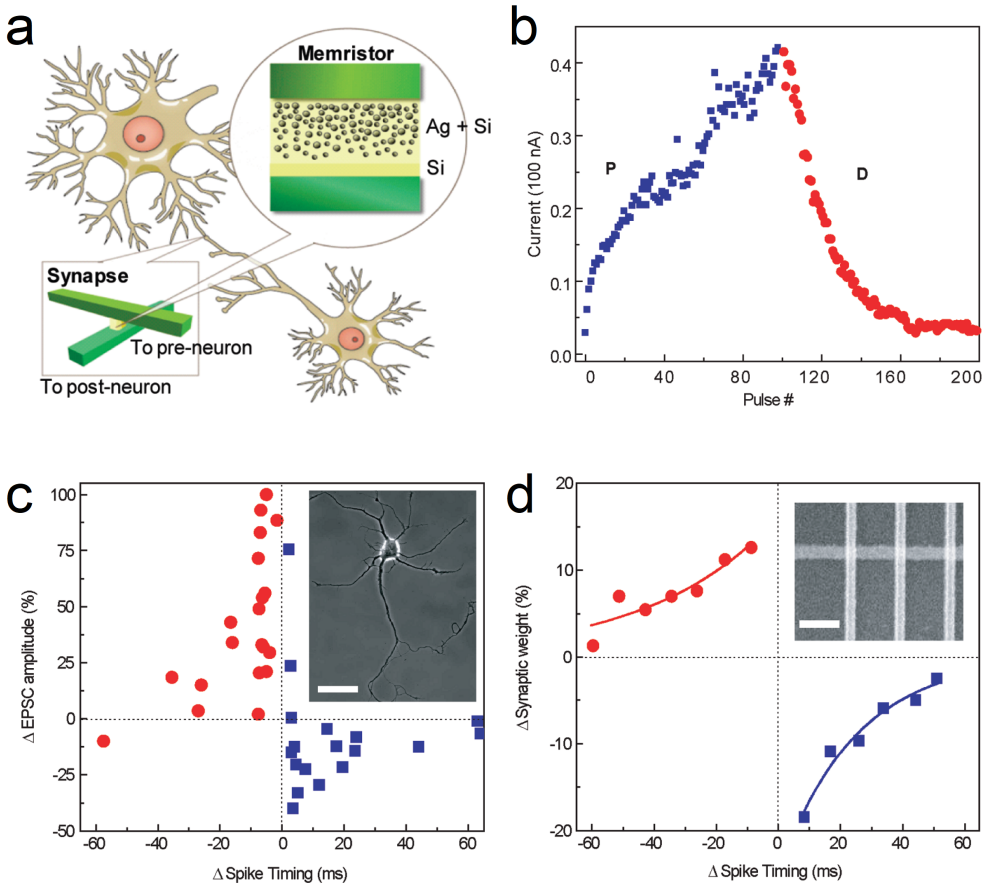

Figure 1.5: Memristor-synapse analogy, adapted from ref.20. a) Sketch of the memristor as an artificial synapse. b) Incremental change of the memristor conductance by consecutive potentiating (P) or depressing (D) pulses. c) Individual neural pulses - or spikes - fired by the pre-synaptic neuron, after passing through the considered synapse, induce an excitatory post-synaptic current (EPSC) in the post-synaptic neuron. If the integrated input of the post-synaptic neuron exceeds the threshold, a new spike is fired along its axon, and an echo pulse propagates in the opposite direction, arriving, among others, at the original synapse. The spike timing-dependent plasticity (STDP) rule states that the synaptic weight change occurs in a narrow time interval between the onset of EPSC and the post-synaptic spike peak (here $\Delta t = t_{EPSC} - t_{post}$). Moreover, the condition of causality is observed: potentiation occurs if the pre-spike arrives before the post-spike ($\Delta t < 0$), and depression - in the opposite case ($\Delta t > 0$). Reconstructed from ref. [21]. d) STDP realized in the Si-Ag cross-bar memristor though the modulation of its conductance - one of the main features to prove the ability of a memristor for synapse emulation.

1.3 Materials and emerging concepts in memory and neuromorphic devices

The most important aspect of the memristor design is the choice of the functional material, that would allow to realize both key memristor properties: memory and electric control. Multi-level memory cells are a closely related concept, since the quasi-continuous conductance tuning over discrete set of states may be relevant for neuromorphic applications as well, while ensuring potentially more reliable state storage than memristors. Therefore, here we give a brief overview of some of the main physical concepts, on which the memristor and novel memory type research is concentrated [27–30].

1.3.1 *Chemical switching: anion- and cation-based*

Chemical switching devices are based on the naturally or artificially organized deficiency of some kind of ions in the thin film, that allows to control the device resistance with the application of the electric field [27].

For example, in metal oxide films a slight deficiency of oxygen may result in the formation of oxygen vacancies, which possess an effective positive electric charge and are able to migrate through the device under electric field application. This redistribution of the oxygen anions in the device leads to reconfiguration of the chemical bonds, i.e. the reduction-oxidation (redox) reactions occurs, that modifies the valence of metal cations - which is why this type of devices is sometimes called "valence change memory". The new chemical configuration can be stable for substantial amount of time.

Alternatively, metal cations can act as mobile particles, able to migrate under the electric field application. This may be organized, for example, through co-deposition of metal particles into a chemically stable matrix or electrolyte, or by tearing out the metal ions from the chemically active electrode (such as Cu or Ag) in the beginning of the operation. The latter devices are also referred to as "electrochemical metallization memory".

◆ Among the anion- and cation-based chemical devices together, there is also a division into filamentary and non-filamentary types.

Conducting filament (CF) is an ionic structure that connects the top and bottom electrodes of the device and possesses the lower resistance than the regions outside it [29]. It is formed in the pristine devices, that are in the high resistance state (HRS), via the ordering of mobile ions after the application of the first voltage pulse, which is usually higher in value than the operating voltage (**figure 1.6**). The process of initial CF creation is called "(electro)forming" or "soft breakdown", and in case of cationic devices the CF is sometimes called "conducting bridge" (hence the name CBRAM). Following the CF formation, the device operates in the low resistance state (LRS), but the application of the voltage of opposite polarity may lead to the filament rupture. Conventionally, the electric field simply drags the ions away (bipolar switching), but in some cases the CF can be broken by voltage of the same polarity (unipolar switching), if in the LRS the current reaches a certain threshold value and CF is subjected to a substantial amount of Joule heat (thermochemical mechanism). After that the device may be cycled between the LRS and the new HRS. Usually, the set switching (HRS to LRS) is abrupt and reset (LRS to HRS)

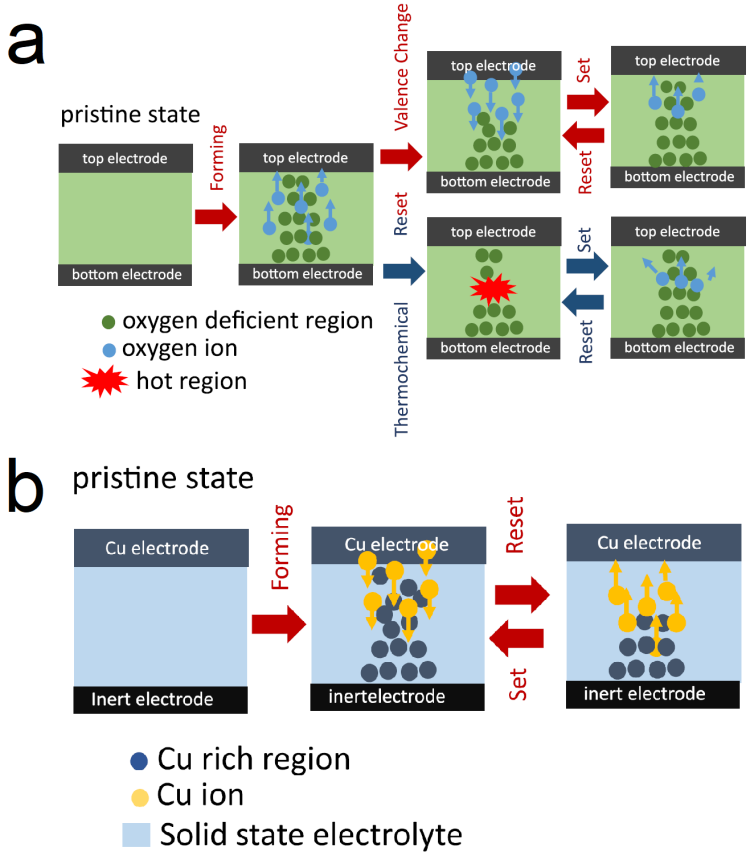

Figure 1.6: Sketches of the filamentary switching mechanisms, taken from ref.29. a) Anion-based (oxygen vacancy) switching. Rupture of the filament occurs due to vacancy migration (valence change) or thermal destruction with Joule heat (thermochemical), while the filament formation mechanism is the same. b) Cation-based switching. Metal cations form the conducting bridge in the solid-state electrolyte. Application of the voltage of opposite polarity leads to cation migration and filament rupture.

is more gradual, presenting an opportunity to organize a multi-level memory cell or an analog memristor.

The forming process in the filamentary resistive switching (RS) devices is considered to be a disadvantage: it requires additional preparation procedures before the cell becomes fully functional and introduces uncertainty into device parameters, since the resulting LRS, location and forming voltage of the CF are hard to control. Non-filamentary RS devices are devoid of this drawback. Here, the oxygen vacancies are mobile as well, however they do not form the CF under voltage application. Instead, the vacancies are accumulated at the interface with the corresponding electrode (**figure 1.7a**). There they may either be held purely by electric field, so after it is removed, the oxygen vacancies diffuse back (thus only the volatile memory cell is realized); or get pinned at the interface via some physical or chemical mechanism, so the final configuration is retained even after the electric field removal (realizing the non-volatile memory cell). Effect of the accumulated vacancy layer on the device resistance has to be considered individually for each case: it could be similar to the filamentary device case, thus leading to the resistance decrease [31]; alternatively, the vacancies may react with the electrode materials, which can lead both to resistance decrease (when the oxidized layer of the metal, formed by proximity to an

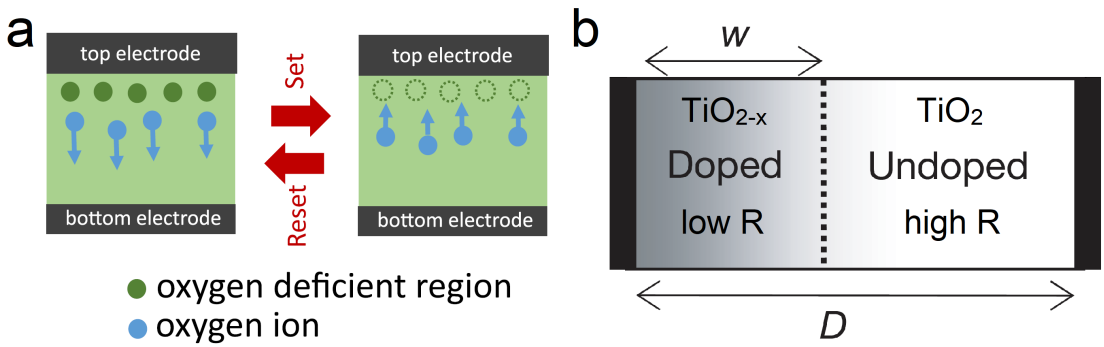

Figure 1.7: Sketches of the non-filamentary switching mechanisms. a) Homogeneous oxygen ion movement resistive switching. Note, that no forming is necessary. Taken from ref.29. b) Switching based on the movement of the bondary between the undoped TiO_2 and doped TiO_{2-x} regions. Adapted from ref.22.

oxide, is reduced) and increase (when the electrode material conductivity involves oxygen in some way, so introduction of the vacancies breaks the transport mechanism) [32]. In case the oxygen deficiency is substantial, accumulation of the oxygen vacancies at the interfaces leads to formation of the "doped" (of lower resistivity) layer of the dielectric, the thickness of which may be comparable to the "undoped" (of the higher resistivity) part, such as in the first experimentally demonstrated memristor [22], based on the movement of the imaginary boundary between TiO_2 and TiO_{2-x} layers (**figure 1.7b**).

1.3.2 *Phase-change memory*

Phase-change memory (PCM) is based on the specific type of materials, that can be rapidly and reversibly transformed between the low resistivity crystalline and high resistivity amorphous phases (**figure 1.8**). The materials used are usually chalcogenide alloys, such as $Ge_2Sb_2Te_5$ (GST). The application of long low current pulses keeps the film around its crystallization temperature, which makes it uniformly crys-

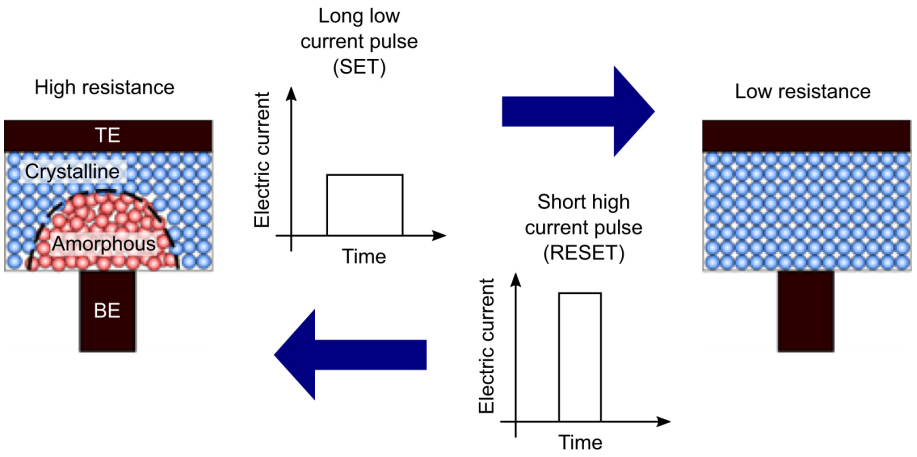

Figure 1.8: Phase-change memory device principle. A long low current pulse (set) is applied to fully crystallize the film and induce LRS. A short high current pulse (reset) is applied to induce the partially amorphous HRS. Taken from ref.33.

talline and sets LRS. On the other hand, short high current pulses rapidly bring the material above the melting point and after quick cooling (quenching) result in the partially disordered amorphous state and sets HRS [33]. Varying the parameters of the current pulses, a continuous range of resistances may be accessed, making PCM devices eligible for multi-bit and memristive operation.

1.3.3 *Magnetoresistive devices*

Ferromagnetic materials have been used for information storage since the dawn of computers: from magnetic tapes to hard disks [34]. The turning point in the field was the discovery of giant magnetoresistance (GMR) effect independently by groups of A. Fert [35] and P. Grünberg [36], awarded for this with the Nobel Prize in Physics in 2007. GMR allowed to improve the accuracy of the hard disk drive (HDD) reading heads and significantly reduce the size of the magnetic bit on the disk, i.e., to increase the storage density. Technological success of GMR effect inspired the revisiting of the long-discovered tunneling magnetoresistance (TMR) effect [37] and improving the HDD capabilities even further [38, 39]. Active search for material combinations for GMR- and TMR-based devices marked the birth of new branch of solid-state physics - *spintronics*, i.e. electronics that exploits the spins of electrons as the physical basis of the device operation. Nowadays, spintronic memory and memristors are among the leading concepts for the next generation microelectronic devices.

◆ Prior to describing the operation of spintronic memory and memristors, let us address the physics behind GMR and TMR effects [40].

In ferromagnetic metals (FM), density of electronic states at the Fermi level significantly differs for the electron spin* projections parallel (majority) and antiparallel (minority) to the magnetization direction. Thus, when the electric current flows in the FM, it is so called "spin-polarized", i.e. spins of the moving electrons on average are aligned with the magnetization. As a consequence, partial resistivity of the spin-majority electron channel is lower than of the spin-minority one, since the spin scattering is introduced as an additional scattering contribution. When the spin-polarized current flows from a FM into a non-magnetic metal (NM), electrons start to scatter without the spin-dependent contributions, therefore the spin-polarization starts to decay in the NM up to the characteristic spin diffusion length (SDL) from the interface, where it reaches 0. Now, if the structure is comprised of two FM layers and a NM spacer with the thickness smaller than SDL, the behavior of electrons, spin-polarization of which is largely retained, starts to depend on the magnetization direction of the second FM layer with respect to the first one. Thus, if the magnetization directions are parallel (P), the spin-scattering conditions in the second FM layer (called "spin-analyzer") are the same as in the first FM layer ("spin-polarizer"), and resistivity of the whole structure is almost the same as of a single FM layer. However, if the magnetization directions are antiparallel (AP), the spin-majority and spin-minority electrons of the polarizer switch the roles after entering the analyzer layer. Spin scattering intensifies, what results in the increased resistivity of the

*Hereinafter, for the sake of brevity, "spin" refers to the magnetic moment of the electron. However, in fig.1.9 arrows near electrons and density of states indicate the electron spin in direct meaning, so the electron magnetic moment is antiparallel to it, due to g-factor being equal to -2.

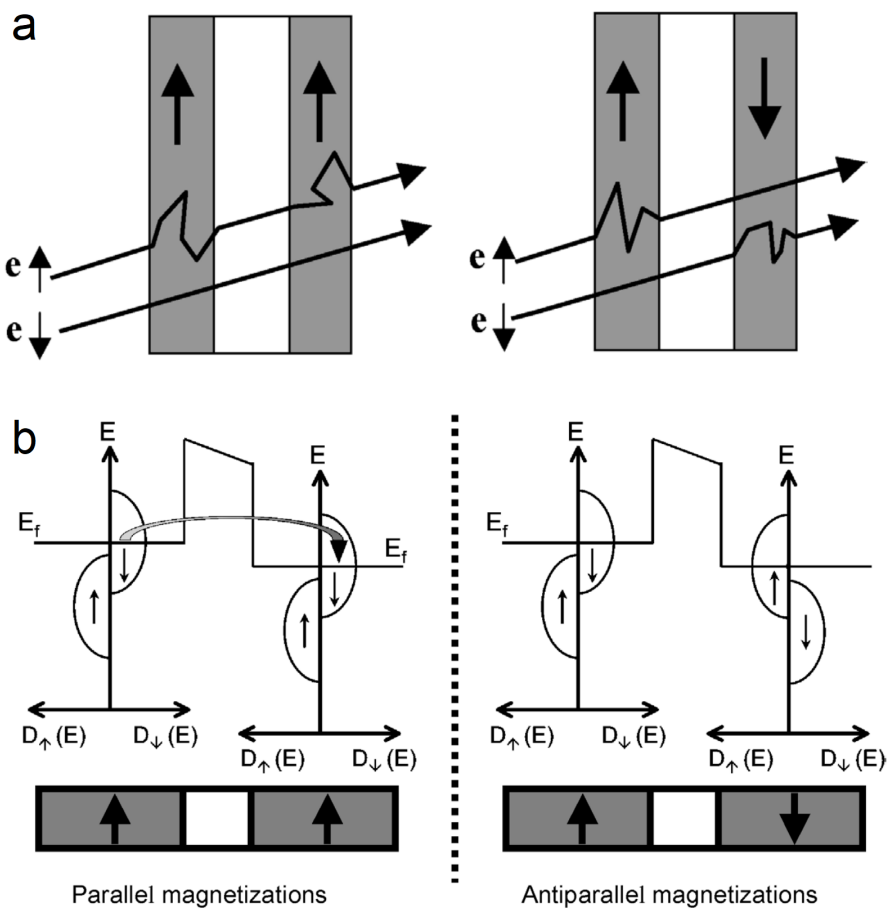

Figure 1.9: Schematic pictures of giant (a) and tunneling (b) magnetoresistance effects, adapted from ref.40.

structure. This is the short description of the GMR effect principle (**figure 1.9a**). Such a tri-layer structure is called "spin valve", and FM layers - "spin filters".

TMR effect is roughly similar to GMR, but instead of the non-magnetic metal the spacer between two FM layers is a dielectric (**figure 1.9b**). In the same way, parallel orientation of the spin filters' magnetization vectors leads to LRS, and antiparallel - to HRS[†] (**figure 1.10**). This tri-layer FM/dielectric/FM structure is referred to as a "magnetic tunnel junction" (MTJ). Here the dielectric thickness has to be low enough to ensure the high tunneling transparency. Moreover, it is important to eliminate other conductance contributions, such as defects in the barrier, and keep the spin-polarization at the FM/barrier interfaces as high as possible, otherwise the TMR ratio $(R_{AP} - R_P)/R_P$ will significantly decrease. Therefore, extremely high quality of the barrier itself and its interfaces with the FM electrodes is required in the fabrication of MTJs. In practice, one of the FM layers is made thick and with a fixed magnetization direction ("fixed" layer) with the help of additional magnetic layers, while the second one is thin and able to rotate its magnetization vector ("free" layer), depending on the external magnetic field. Thus, the free layer magnetization direction with respect to the fixed layer can be used for magnetic field sensing.

[†]In the case of two FM layers, magnetized uniformly. When magnetic structure of the junction is more complex, e.g., involving multiple magnetic sublattices, the correspondence of junction resistance value to the relative magnetization orientation may be more complicated.

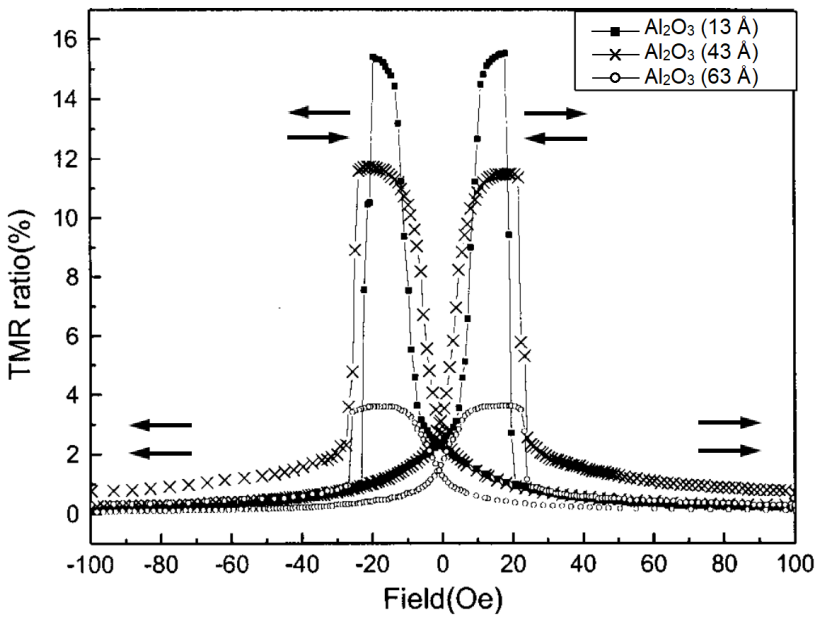

Figure 1.10: Tunneling magnetoresistance ratio vs applied magnetic field for SiO_2 / NiFe / Co / Al_2O_3 (13, 43 and 63 Å) / Co structure. Adapted from ref.41.

◆ Concepts of GMR and TMR proved to be efficient in the operation of HDD reading heads, however the requirement of magnetic field generation (which is highly energy consuming) to change the magnetization state did not allow MTJs to be a viable option for storage or memory cells, although the principle of magnetic state storage is widely implemented. The breakthrough occurred with the discovery of the "spin-transfer torque" effect, predicted by J. Slonczewski [42]. In this concept, firstly, the flow of spin-polarized electrons is generated from the fixed layer into the free layer. Since the spin-polarized current carries the net magnetic moment, i.e. net angular moment as well, it can generate a substantial torque that can affect the free layer magnetization and, eventually, align it in parallel to the fixed layer magnetization, so the LRS is set. When current direction reversed, the electron flow is polarized by the free layer. The spin-majority electrons tunnel into the fixed layer, while the spin-minority ones are reflected back. With the accumulation of the spin-minority electrons in the free layer, its magnetization gets flipped in the antiparallel direction with respect to the fixed layer, so the HRS is induced (reset). Thus, the resistance state of the so called spin-transfer torque magnetic RAM (STT-MRAM) cell can be controlled purely by electric current, with no need to generate magnetic fields, so the amount of energy required to write the bit state is significantly reduced.

Both magnetic field and electric current control allow the gradual device resistance tuning via fine evolution of the magnetic domain structure, so MTJ is a viable concept for multi-state memory and memristor implementation.

1.3.4 *Ferroelectric memory and neuromorphic devices*

Ferroelectric (FE) materials have always been among the leading concepts in non-volatile memory - e.g., the first demonstrated prototype of the non-volatile memory device was based on the FE $BaTiO_3$ [43], and by 2019 Fujitsu has shipped more than 4 billion pieces of PZT-based memory [44]. The abilities of FEs to retain

the spontaneous polarization and switch it with the application of electric fields, as well as the possibility to sustain the conducting channel in field-effect transistors with the gate FE when voltage is not applied to the gate electrode, are particularly attractive for low-power high-speed memory cells. However, full integration of FE memory in the microelectronic production remained problematic for years due to poor compatibility of conventional perovskite FE materials, like $BaTiO_3$ or PZT, with Si technology [45]. In 2011 FE properties were discovered in polycrystalline thin films of doped HfO_2, a high-k dielectric material that was already fully integrated in the modern CMOS production. This presented the opportunity to develop the latest technological node commercial electronic devices, based on ferroelectricity, such as FE memory (FeRAM), field-effect transistors (FeFET) and tunnel junctions (FTJ).

FeRAM device is a simple capacitor with a FE sandwiched between two metal electrodes. In practice, it is usually integrated with a transistor as a selector, so in this case the memory cell is referred to as 1T1C (1 transistor, 1 capacitor) FeRAM (**figure 1.11a**). Memory state here is retained with the spontaneous polarization direction along the line from one electrode to another. Writing is performed with application of the appropriate polarity voltage pulse, value of which is chosen so the induced electric field exceeds the coercive field E_c. Readout is performed with writing to the fixed state and tracking the concomitant current - if it is high, then the polarization reversal has occurred and the cell should be set to the initial state with another writing pulse; otherwise, the polarization state was not modified and can be left as is. As seen from the description, the destructive readout of FeRAM is not advantageous in terms of energy efficiency, however other features, such as reliability and ease of manufacturing and compatibility with back end of line (BEOL) of CMOS production, make it an attractive solution in some applications.

FeFET is a field-effect transistor, in which the gate dielectric is replaced or combined with a FE (**figure 1.11b**). Due to ability of FEs to retain the spontaneous polarization after external electric field removal, FeFET can be left open in a non-

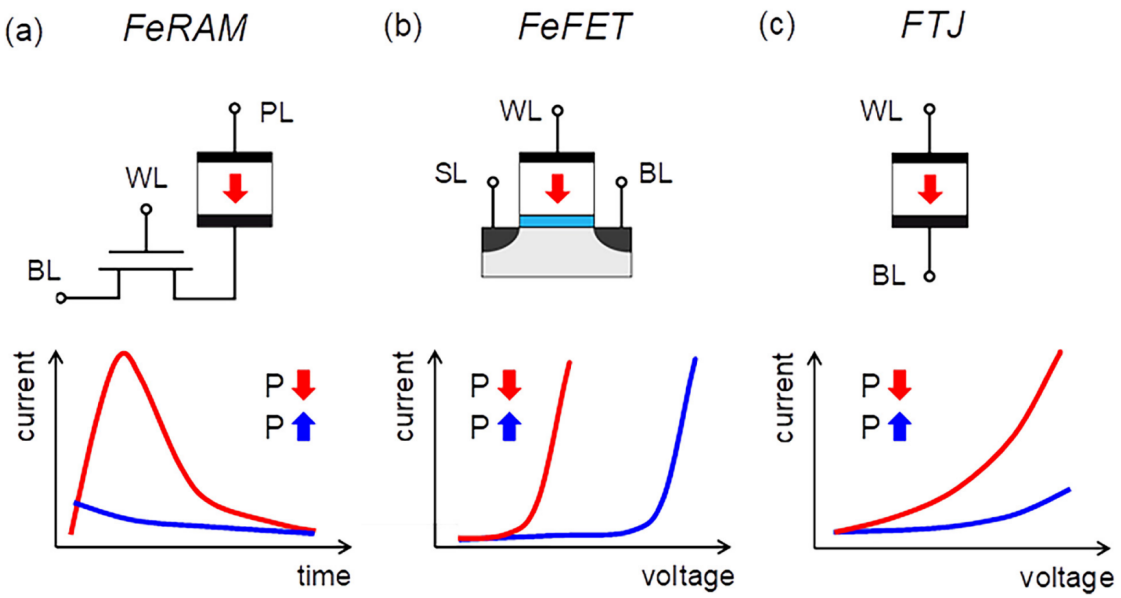

Figure 1.11: Three types of ferroelectric devices together with the corresponding current response curves for opposite polarization directions. Taken from ref.45.

volatile way. While writing is performed by applying voltage to the gate, readout is done simply with tracking the source-drain current, i.e. not involving the FE layer directly. The non-destructive readout, non-volatile state storage and direct integration in the CMOS are the main advantages of FeFET.

Concept of FTJ is a hybrid between FeRAM and ReRAM. Similarly to FeRAM, it is a capacitor with a FE sandwiched between two electrodes, and writing of the state if performed in the same way. But similarly to ReRAM, readout is non-destructive and is performed via application of small (below E_c) voltage pulse and measuring the current, and, consequently, the device resistance, which depends on the polarization direction (**figure 1.11c**). This effect is called "tunneling electroresistance" (TER) and is caused by the reconstruction of the band structure of the device when the spontaneous polarization is reversed [46]. If the metal electrodes of the FTJ possess different screening lengths, the polarization reversal results in different effective tunneling barrier heights, which allows to distinguish LRS and HRS (**figure 1.12**). Besides demonstrating the operation advantages, such as energy efficient writing and readout, the main disadvantage of FTJ is the requirement of ultrathin FE barrier layer, what is quite difficult to ensure, similarly to MTJs. To avoid this, sometimes an additional insulating interlayer is introduced to the FTJ stack between the FE and one of the electrodes. In this way, with the polarization direction away from the insulator, the barrier is very high and thick, resulting in HRS. The band structure may be organized in such a way that in the case of opposite polarization direction, the barrier effectively is reduced to the insulating interlayer, so after tunneling through it electrons get directly to the FE conduction band, which results in drastically lower resistance value in the LRS. In this scheme, ultralow thickness of the FE is not required, while the HRS/LRS ratio is even higher than in conventional FTJs.

◆ Existence of the FE domain structure leads to switching of only some fraction of the domains at a given applied voltage, what makes it possible to organize the gradual switching, similarly to MTJ. This is exploited in various concepts of FE memristive devices, such as memristors based on FTJ [47–49], or memtransistors [50].

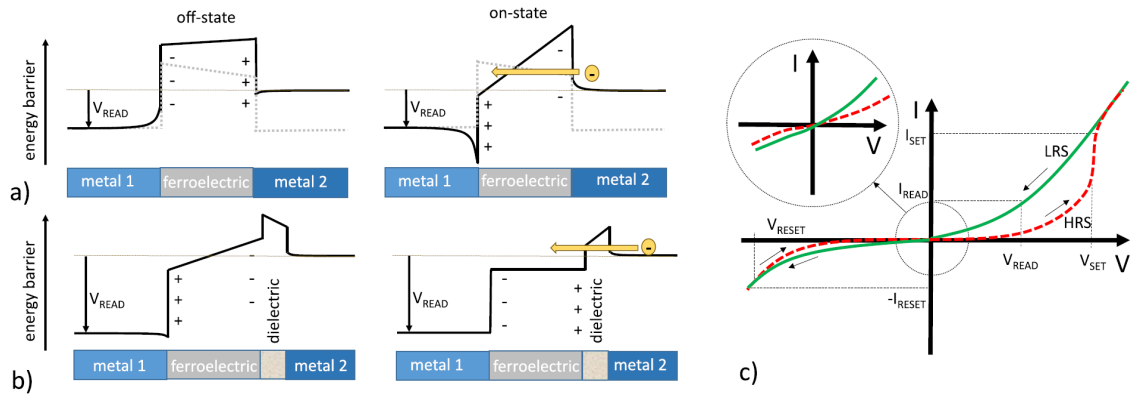

Figure 1.12: Ferroelectric tunnel junction operation principle. a) Band structure of a metal-FE-metal (MFM) FTJ, in which the FE is sandwiched between two metal electrodes with different screening length. The dotted lines show the profile without polarization. b) Conduction band structure of a metal-FE-insulator-metal (MFIM) stack. c) Typical $I(V)$ characteristic of a MFIM FTJ. Taken from ref.29.

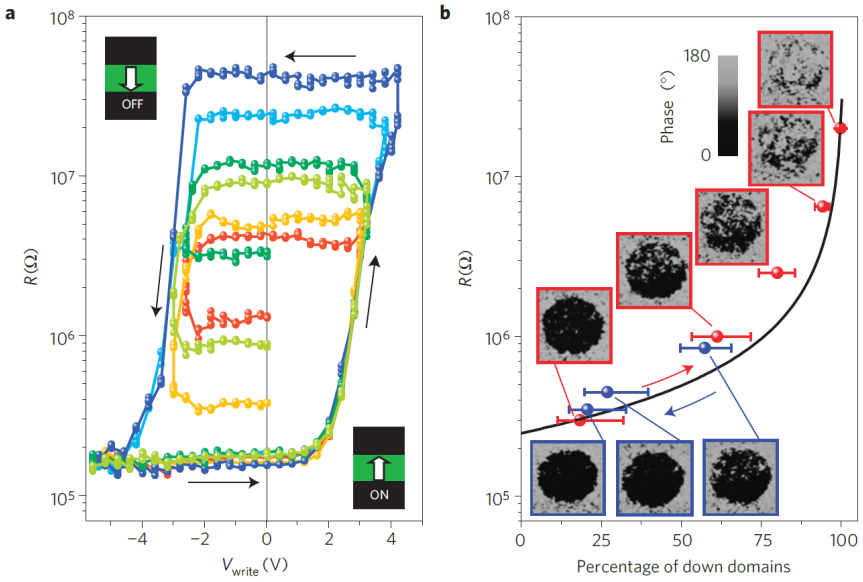

Figure 1.13: Ferroelectric memristor operation. a) Resistance tuning with voltage pulses. The different curves correspond to different consecutive measurements, with varying maximum (positive or negative) V_{write} b) Ferroelectric capacitor resistance tuning with the relative fraction of reversed domains extracted from the piezoresponse force microscopy images. Taken from ref.47.

1.3.5 *Multiferroic materials and device concepts*

In attempts to combine the advantages of FM (stability of the state) and FE (electric field control) orderings, the concept of *multiferroic* materials was developed. A material is called multiferroic, if it possesses two or more types of *ferroic* ordering, i.e. (anti)ferroelectric, ferromagnetic (antiferromagnetic, ferrimagnetic) or ferroelastic [51, 52]. The closest attention of researchers and engineers is drawn to magnetoelectric multiferroics, which are ordered ferroelectrically and magnetically. Such materials in a single phase and operating in reasonable conditions (temperature, first of all) are quite rare [53]. By far, the most popular single-phase multiferroic material is $BiFeO_3$, which is a ferroelectric and an antiferromagnet or weak (canted) ferromagnet [54]. However, it's magnetization is still insufficient to exploit it for magnetic storage by itself, therefore it is used in combination with a conventional FM as an interfacial multiferroic. It was successfully demonstrated that switching of the $BiFeO_3$ polarization leads to reversal of its magnetic sublattices (i.e., rotation of the Néel vector or of the canted magnetic moment), which, in turn, results in the detectable changes of the magnetization of the adjacent FM [55, 56] (**figure 1.14**). This effect is used in the emerging concept of the magnetoelectric spin-orbit (MESO) logic-in-memory device [57, 58].

However, the use of single-phase multiferroic materials is not necessary for interface multiferroics - a FE/FM bilayer would suffice as well. This significantly widens the selection of suitable materials. There are multiple reports on the ferroelectric control of magnetism in such systems through various magnetoelectric coupling mechanisms [59–61].

Moreover, ferroic orders in non-single-phase multiferroics may be independent, i.e., establishment of magnetoelectric coupling is not required. Additional function-

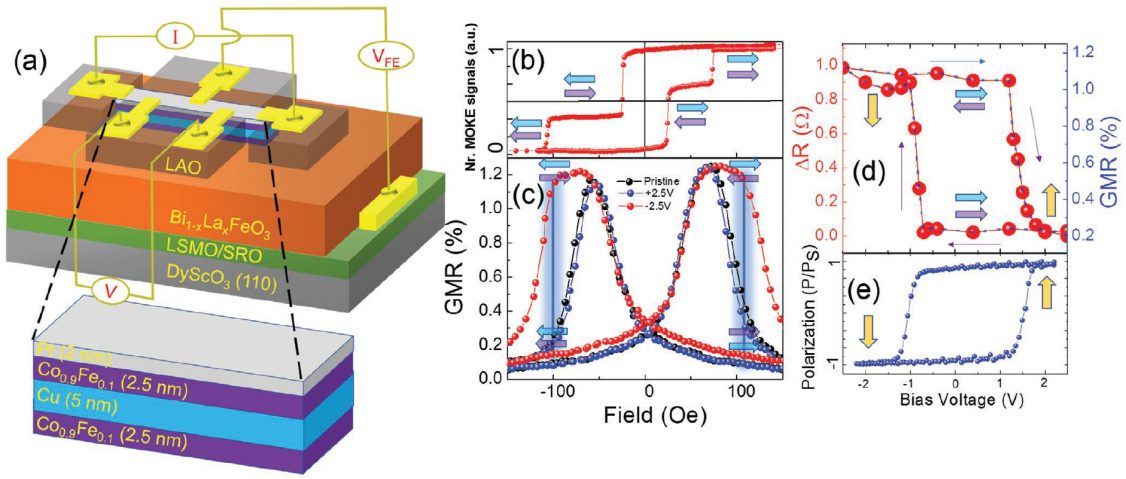

Figure 1.14: Magnetoelectric La:$BiFeO_3$-based device. a) Experiment scheme for testing the magnetoelectric coupling: $Co_{0.9}Fe_{0.1}$ (2.5 nm)/Cu (5 nm)/$Co_{0.9}Fe_{0.1}$ (2.5 nm) spin valve is integrated on multiferroic $Bi_{0.85}La_{0.15}FeO_3$ (BLFO) with $La_{0.7}Sr_{0.3}MnO_3/SrRuO_3$ as the bottom electrode on $DyScO_3$ (110) substrate. b) Magnetization hysteresis loop of a spin valve. c) Modulation of the GMR response of a spin valve upon the application of ±2.5 V across the BLFO film along with the GMR response for pristine case. d) Modulation of resistance state (parallel/antiparallel) of the spin valve structure with applied voltage across BLFO and e) corresponding ferroelectric $P(V)$ loop. Taken from ref.56.

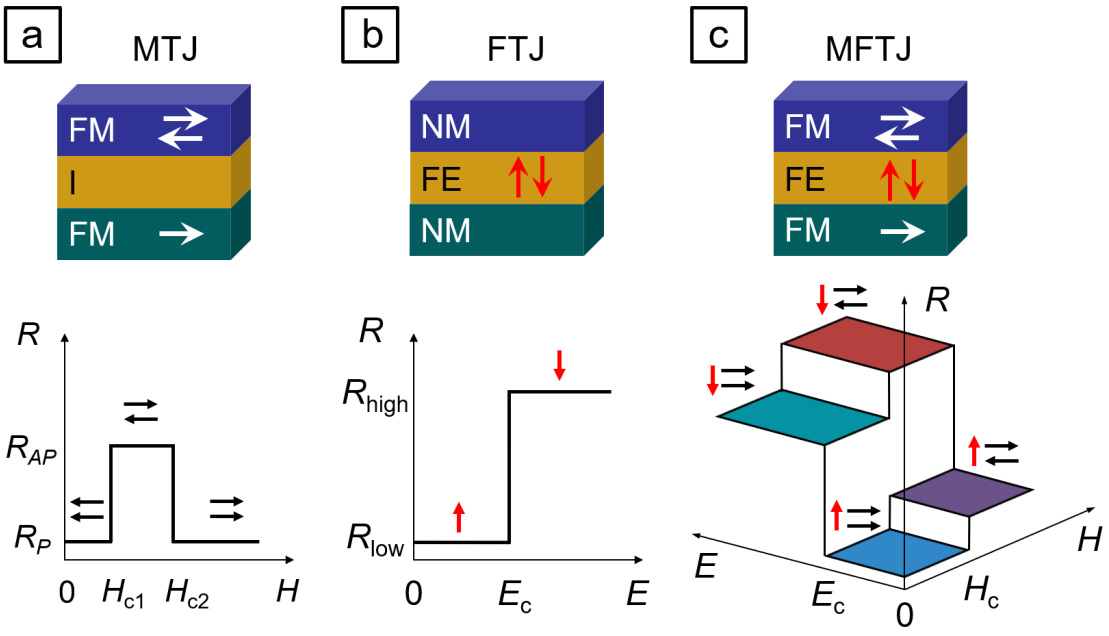

Figure 1.15: A magnetic tunnel junction (a) and a ferroelectric tunnel junction (b) are combined into a multiferroic tunnel junction (c). Bottom panels show the resistance response of these junctions to magnetic (H) and electric (E) fields. Horizontal and vertical arrows indicate orientations of magnetization and electric polarization, respectively. Reconstructed from ref.62.

ality of combined ferroelectricity and ferromagnetism is manifested in the form of multiple memory levels. This can be achieved with a multiferroic tunnel junction (MFTJ), a combination of MTJ and FTJ - a FE barrier between two FM electrodes (**figure 1.15**). In this way, two ferroelectric resistance states, independent of two magnetic resistance states, result in four multiferroic resistance states [62–64]. Even more resistance levels are possible with the use of additional effects: careful exploitation of magnetocrystalline anisotropy allows to obtain octonary resistance states [65], and gradual ferroelectric switching results in at least ten stable and distinguishable levels [66]. The latter case can be also classified as a continuously tuned multiferroic memristor.

1.4 Conclusion and project motivation

After the overview of popular concepts for novel multi-level memory cells and memristors, it is clear that devices based on ferroic materials (FM, FE, multiferroic) are of particular interest in the field thanks to the combination of reliable magnetic storage and potentially very low voltage switching with FEs. If magnetoelectric interaction between two ferroic orders is established in some way, the advantages are used to the fullest extent. However, even in case of independent ferroic subsystems some useful features can be exploited, such as existence of at least four stable levels of resistance and the possibility to gradually tune it. These considerations motivated the choice of MFTJ as the concept of interest for this thesis.

Chapter 2

Materials for thin films

The multiferroic tunnel junction was chosen as the object of study for this dissertation. For realization of this concept, it is necessary to choose ferroelectric and ferromagnetic materials suitable for integration in the form of thin films. Classical perovskite materials $BaTiO_3$ and $La_{1-x}Sr_xMnO_3$ are perfect for these purposes as model systems for proof-of-concept experiments. The efficiency of their use in the field of artificial multiferroics and tunnel junctions has been successfully demonstrated over the years, while many scientific questions in this area still remain open. Thus, this chapter provides an overview of the key properties of $BaTiO_3$ and $La_{1-x}Sr_xMnO_3$, relevant for their application as components of a multiferroic tunnel junction.

2.1 $BaTiO_3$: relevant features

Barium titanate ($BaTiO_3$, BTO) belongs to the family of perovskite oxide crystals ABO_3: A^{n+} is a cation in the vertices of the unit cell, B^{m+} $(n + m = 6)$ is a cation in the center of the unit cell and O^{2-} anions are located in the centers of the unit cell faces (**figure 2.1**). Ideal cubic perovskite structure is immanent to BTO only above 120 °C (**figure 2.2**) - here the unit cell is centrosymmetric and

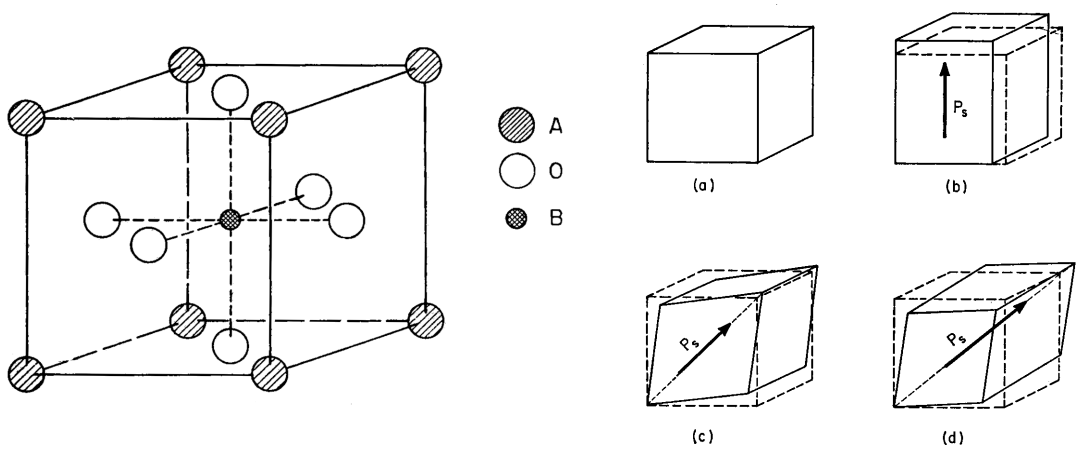

Figure 2.1: Unit cell of BTO. (Left) Cubic perovskite structure of ABO_3 compounds. (Right) Unit cells of four stable BTO phases: cubic (a), tetragonal (b), orthorhombic (c) and rhombohedral (d). Adapted from ref.67.

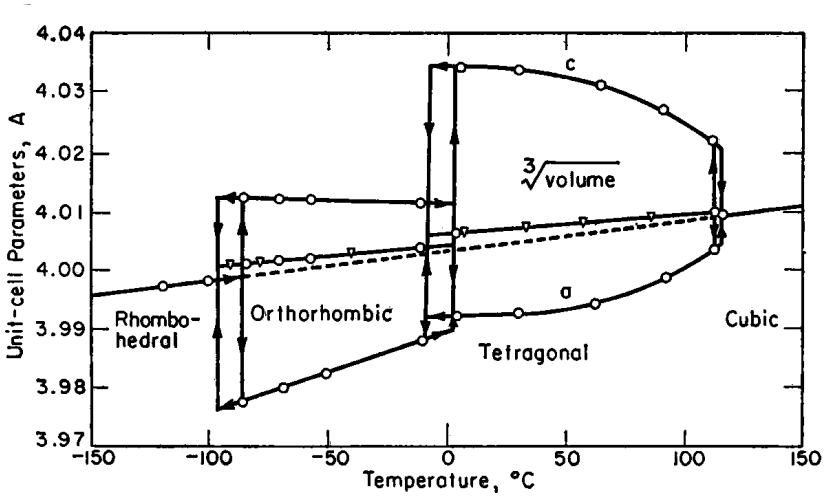

Figure 2.2: Temperature dependence of BTO unit cell parameters. Adapted from ref.67, 68.

material is paraelectric (i.e., regular dielectric, spontaneous polarization equals 0). At 120 °C transition to tetragonal phase occurs: the unit cells elongates along one of the sides of the cube. This phase, stable down to 5 °C, is ferroelectric (FE), with spontaneous polarization pointing in the direction of tetragonal distortion - conventionally, a vertical direction 001 is chosen for clarity, so the unit cell is characterized by two parameters: in-plane (a) and out-of-plane (c). Between -90 °C and 5 °C the orthorhombic phase is stabilized, formed through the additional distortion along one of the in-plain sides. In this phase, which is also FE, spontaneous polarization is stabilized in 101 direction. Finally, below -90 °C BTO exists in the rhombohedral phase, transition to which occurs through distortion along the other in-plane side, so spontaneous polarization points along 111 crystallographic direction.

BTO is a classical FE material (**figure 2.3**), that has been widely studied on the matter of various applications for more than half a century [70, 71]. In particular,

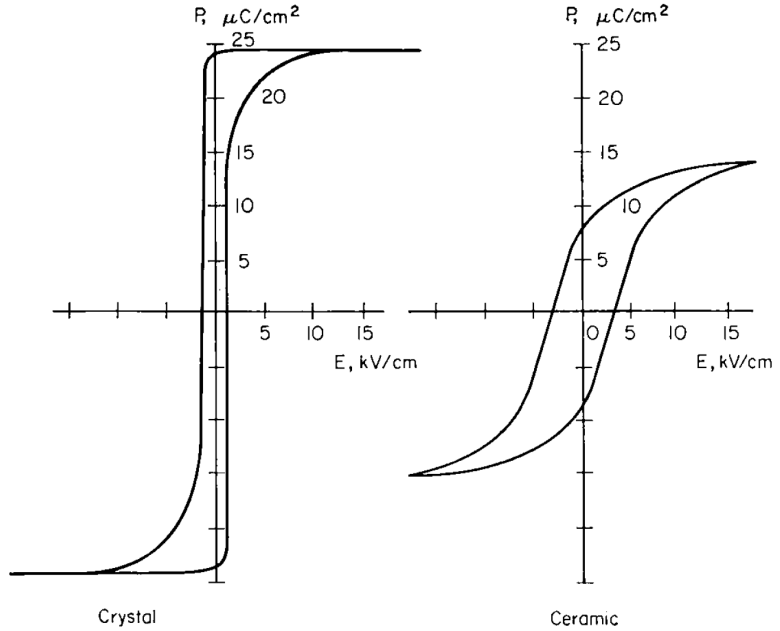

Figure 2.3: BTO hysteresis loops: (100) crystal (a) and high-quality ceramic (b). Taken from ref.69.

FE memory is among the attractive implementations: the first non-volatile memory device prototype was based on BTO [43]. However, integration of BTO, as well as other perovskite oxide FEs, into microelectronic production has been problematic ever since [45]. Despite this, researchers continue to design viable BTO-based devices on Si [72, 73].

◆ Excluding technological issues, BTO remains a widely used material for FE-related proof-of-concept experiments and theoretical calculations and modeling. This is due to a rather simple crystal structure (that allows to relatively easily perform *ab initio* calculations) and availability of many other perovskite oxide materials for various experimental device configuration, as well as due to a mature growth technology, which allows to create ultra-high quality epitaxial thin-film layers and interfaces between them [74]. One of the phenomena that was discovered mainly thanks to these features of BTO is tunneling electroresistance (TER, described in section 1.3.4) in ferroelectric tunnel junctions (FTJ) [75, 76] (**figure 2.4**).

Use of appropriate perovskite substrates, such as $NdGaO_3$ [75] or $SrTiO_3$ (STO) [76], with the growth of bottom electrode (BE) layer also of the perovskite family -

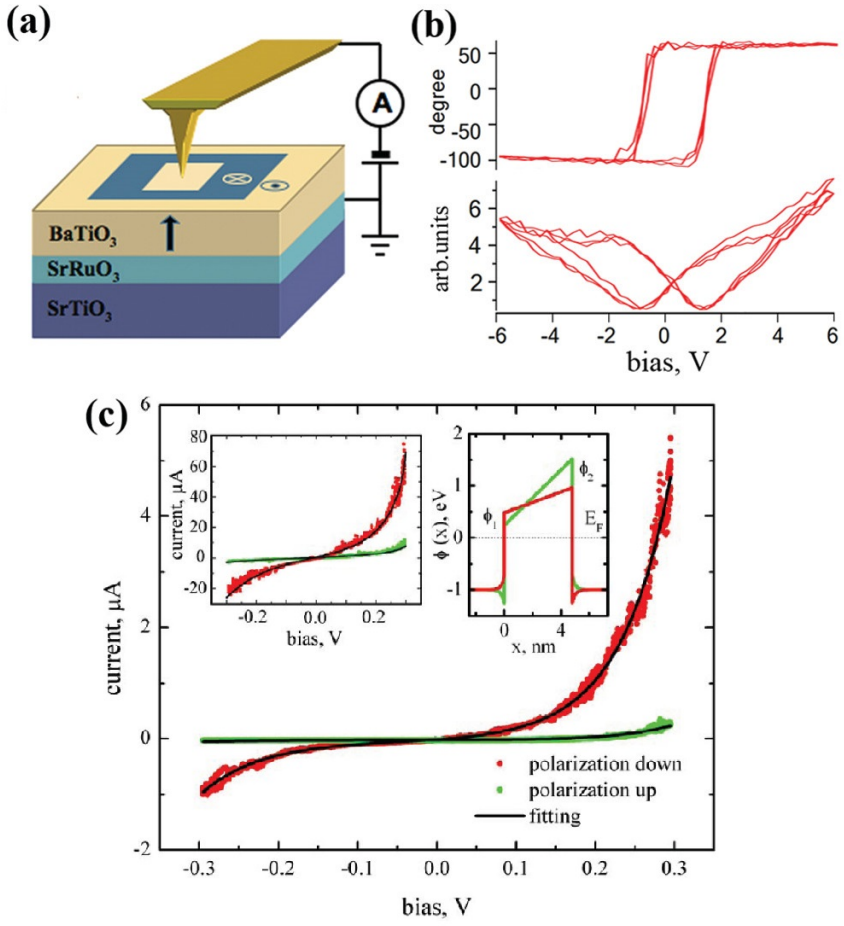

Figure 2.4: Tunneling electroresistance effect in a ferroelectric tunnel junction at the nanoscale. a) Sketch of the experiment geometry, using piezoresponse and conducting atomic force microscopy (PFM/C-AFM). b) Local PFM hysteresis loops measured in the 4.8 nm thick BTO film (top, phase signal; bottom, amplitude signal). c) $I(V)$ curves for two opposite polarization directions in the 4.8 nm thick BTO film measured by C-AFM. $I(V)$ curves in the inset were measured for two opposite polarizations in the 2.4 nm thick BTO film. Adapted from ref.76.

$La_{0.67}Sr_{0.33}MnO_3$ (LSMO) or $SrRuO_3$, respectively - allowed to obtain high quality experimental samples and observe the effect that was predicted earlier theoretically [46]. Later other materials for epitaxial BE in BTO-based FTJs were explored, such as Pt [77] and $LaNiO_3$ [78].

As an alternative, Nb:$SrTiO_3$ (NSTO) semiconducting substrates are used as a BE for BTO-based FTJs [79–82] (**figure 2.5**). This allows to grow the epitaxial BTO layer of even higher quality, since it is deposited directly on the substrate, and to enhance the TER value, defined as (HRS−LRS)/LRS. Increase in TER occurs due to the modulation of the Schottky barrier: higher screening length in the semiconductor, in comparison to metals, leads to the formation of the region of the space charge, sign of which is defined by the FE polarization orientation. This, in turn, causes the band bending in the vicinity of the FE/semiconductor interface, as a result, the polarization controlled modulation of the total potential barrier transparency is high (HRS/LRS $\gtrsim 10^4$ and up to 10^7 [83]).

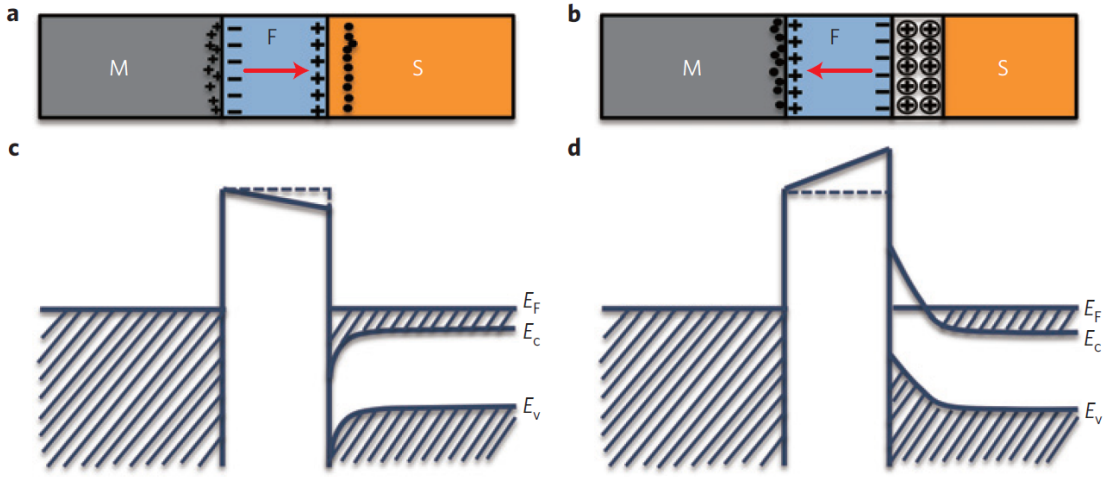

Figure 2.5: Resistive switching mechanism of the metal/FE/semiconductor (MFS) tunnel junctions. Schematic drawings of the device structures (a, b) and corresponding potential energy profiles (c, d) for the low (a, c) and the high (b, d) resistance states. Taken from ref.79.

◆ However, purely FE nature of resistive switching (RS) in BTO is not always the case. In practice, in thin BTO films it is very hard to eliminate parasitic conductance contributions, such as leakage through film imperfections, defects, grain boundaries and, most notably, oxygen vacancy migration. The latter should be considered with particular attention, since behavior of the oxygen vacancies is dynamic and electric field-dependent (due to their positive charge), in contrast to other static phenomena.

It was demonstrated that the oxygen deficiency significantly affects the ferroelectric and dielectric properties ($P(E)$ loop asymmetry, reduced dielectric constant and increased dielectric loss) even of thick (450 nm) BTO films [84], when the effect of oxygen vacancy drift is eliminated.

In case of films of moderate and low thickness, contribution of oxygen vacancy dynamics to device performance becomes significant. Effectively, oxygen deficiency manifests as doping, so BTO starts to behave electrically similar to semiconductors. It was shown that in this approach, space charge regions at the FE interfaces cannot be neglected, so a conventional metal-FE-metal (MFM) structure effectively can be treated as two back-to-back Schottky diodes [85]. This leads to the competition of

the FE and oxygen vacancy dynamics, resulting in electroresistance (ER) effects of opposite signs (i.e., when, for example, LRS-to-HRS switching occurs after application of the voltage pulses of opposite polarities), depending on oxygen vacancy concentration in the film [86], which can be tuned during operation [87,88], or on film thickness, voltage pulse duration and temperature [89] (**figure 2.6**). Also, it was reported that this competition may be manifested in the significant TER variation for different top electrode materials, both in MFM [90] and MFS [91] configurations. The general issue of oxygen vacancy dynamics analysis is the principal impossibility to distinguish it from the FE switching with conventional electrical means [92], what requires the use of complementary techniques, such as contact Kelvin probe force microscopy [93].

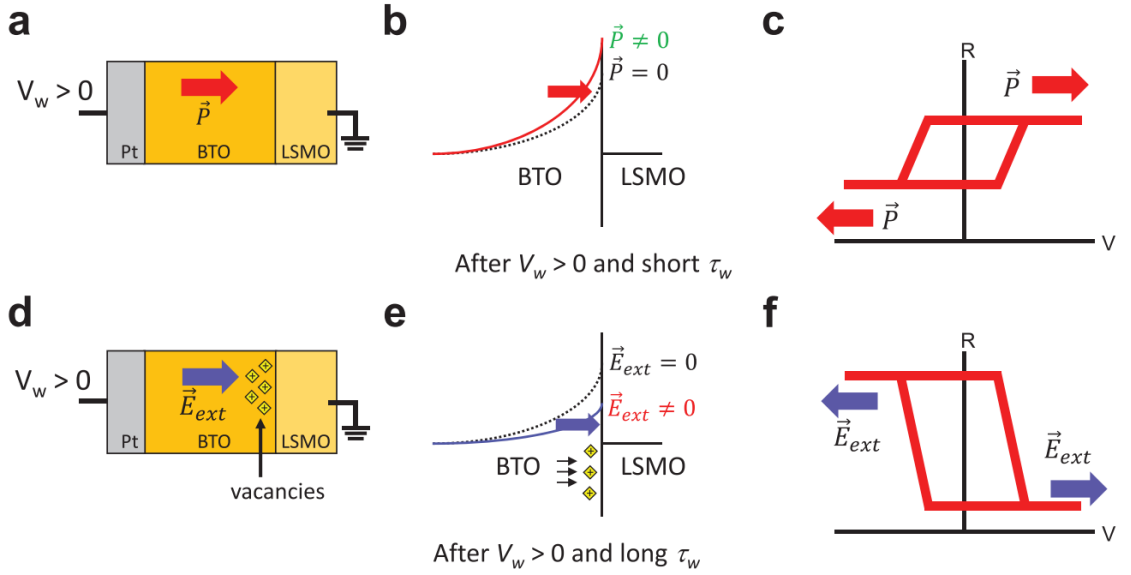

Figure 2.6: Competition between ferroelectric switching and oxygen vacancy migration in Pt/BTO (73 nm)/LSMO device. a) Sketch of the device and polarization for $V_w > 0$ (writing pulse voltage). b) Sketch of the energy band diagram near the BTO/LSMO interface. If polarization is not taken into account, the band diagram is as indicated by the dashed line. If polarization is taken into account, for $V_w > 0$, it points to LSMO, the band diagram is as indicated by the solid line. c) Sketch of amplitude and sign of ER loop for short writing times when ferroelectric polarization and residual depoling field are relevant; ER is small and positive d) Sketch of the device and the electric field produced for $V_w > 0$. Accumulation of oxygen vacancies (yellow rhombi) at the BTO/LSMO interface for $V_w > 0$ is also depicted. e) Sketch of the energy band diagram near the BTO/LSMO interface for no applied voltage (dashed line) and for $V_w > 0$ (solid line). f) Sketch of amplitude and sign of ER loop for long writing times when oxygen vacancies are relevant; ER is large and negative. Adapted from ref.89.

2.2 $La_{1-x}Sr_xMnO_3$: relevant features

$La_{1-x}Sr_xMnO_3$ (LSMO) is a mixed manganite that, as well as BTO, belongs to the perovskite family, however, the peculiarities of it's electronic structure cause it to demonstrate drastically different physical behavior. In a $LaMnO_3$ compound, both cations are trivalent, La^{3+} and Mn^{3+}, and this configuration is shown to result

in the electronic behavior close to crossover between localized and itinerant [94]. Substitution of x part of La^{3+} ions by Sr^{2+} leads to the transformation of the same amount of Mn^{3+} ions to Mn^{4+} oxidation state to comply with electroneutrality. This pushes the electronic configuration to the itinerant behavior by activating the possibility of electron hopping between Mn^{3+} and Mn^{4+} ions along the $Mn^{3+}-O^{2-}-Mn^{4+}$ chains. Moreover, the probability of electron hopping is largest when the magnetic moments of Mn^{3+} and Mn^{4+} ions are aligned [94, 95] (**figure 2.7a,b**). This characteristic phenomenon is referred to as "double exchange" interaction, and in LSMO it leads to the variety of phases, distinguished by conducting and magnetic behavior [96] (**figure 2.7c**). The ferromagnetic metallic phase is stabilized at 300 K for Sr content x between 0.2 and 0.5, with the optimum at ∼0.33.

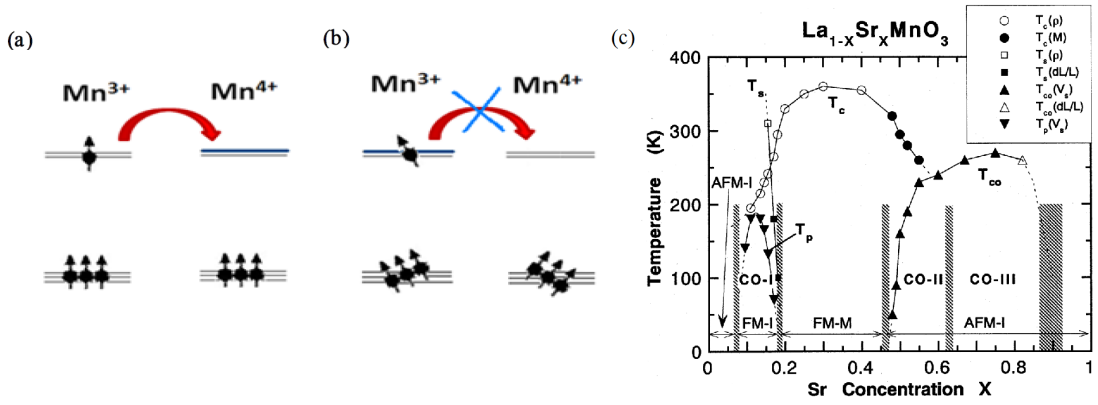

Figure 2.7: (a, b) Schematic image of double exchange interaction in LSMO. Electron hopping probability is higher for aligned Mn^{3+} and Mn^{4+} spins (a), than for misaligned (b). Adapted from ref.95. c) LSMO phase diagram with respect to Sr content x. Adapted from ref.96.

Thus, in the appropriate mixing proportion, LSMO demonstrates the high conductivity and ferromagnetism, which are strongly correlated due to double exchange mechanism. This is manifested in nearly 100% spin-polarization in LSMO [97] (**figure 2.8a**), which is why it is considered to be a half-metal - a material in which a spin-split density of states at the Fermi level is fully dominated by the band for one of the spin directions. As one of the notable consequences: thermal fluctuations lead to the spin disordering to some extent, maximized in the vicinity of ferromagnetic transition temperature T_C, which results in the increased resistivity and allows to obtain substantial resistivity reduction with the application of the magnetic field. In the optimized conditions, the resistivity change may reach several orders of magnitude (**figure 2.8b**), which is why the effect was considered to be a type of metal-insulator transition (MIT) [98] and dubbed "colossal magnetoresistance" (CMR) [99].

However, the most widespread application of LSMO is as a BE material for various perovskite oxide heterostructures, since it is conducting enough for the role of electrode in, for example, FTJ and MTJ (for the latter, the above room temperature ferromagnetic transition point is also important), and with the appropriate selection of a substrate (in terms of cell parameter) it assists in mediating the desired lattice strain into a functional layer. Also, it is important for an electrode material to ensure that it does not introduce the unnecessary physical and chemical activity to

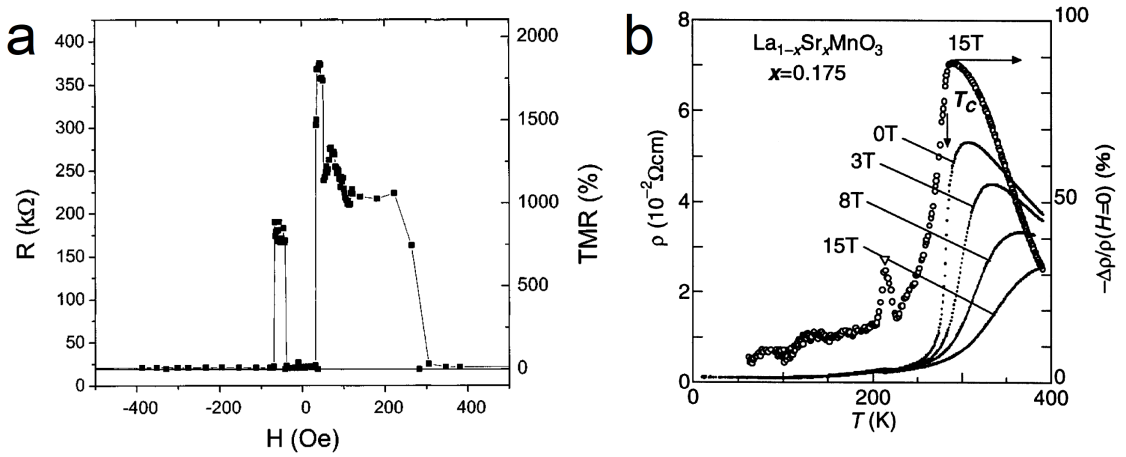

Figure 2.8: a) $R(H)$ loop for a 5.6×5.6 μm^2 LSMO 350 Å/ STO 28 Å/ LSMO 100 Å junction measured at 4.2 K. From TMR value of 1850%, an average spin polarization of at least 95% was deduced. Adapted from ref.97. b) Resistivity temperature dependence curves for LSMO ($x = 0.175$) crystal at various magnetic fields. Adapted from ref.99.

the device, and in case of LSMO this is possible to achieve in principle [100]. However, in the majority of cases, some inherent LSMO issues do have an effect on the device performance, which might be detrimental, but in some cases is intentionally exploited. The main phenomenon here is the formation of so called "dead layers".

"Dead layer" in LSMO is a region close to the surface or interface, in which the magnetic and, consequently, conducting properties are significantly weakened [101–103]. The same effect is observed with the decrease of LSMO film thickness [104]. Various explanation of the dead layer formation have been proposed, such as orbital reconstruction at the interfaces and surfaces [103, 105, 106], oxygen octahedral rotations [107, 108], charge redistribution [109], interfacial epitaxial strains [110–114], as well as oxygen vacancy formation [115–117]. In the majority of cases, the common underlying cause is the rupture of double exchange chains, what promotes local antiferromagnetic ordering and increased resistivity, however some recent experiments demonstrated that a similar effect may be due to the structural phase transition from perovskite to brownmillerite phase [118, 119]. Such negative consequences of the dead layer formation, as the locally reduced LSMO film magnetization and interface conductivity, substantially hinder the operation of LSMO spin filters in the MTJs. However, in some cases the dead layers can be controlled by electric field [120, 121], what may be exploited as an alternative route to resistive switching devices (**figure 2.9**).

2.3 Properties of $BaTiO_3/La_{1-x}Sr_xMnO_3$ interface

It is worth giving a brief review of BTO/LSMO heterostructures in particular, since it is one of the most widely addressed systems for ferroelectric and multiferroic tunnel junctions, search for magnetoelectric coupling and memristors.

Within the concept of artificial multiferroics, composed of a FE/FM bilayers, BTO/LSMO is a classical system, in which magnetoelectric coupling was demonstrated via multiple approaches. Specifically, it was suggested that remnant polar-

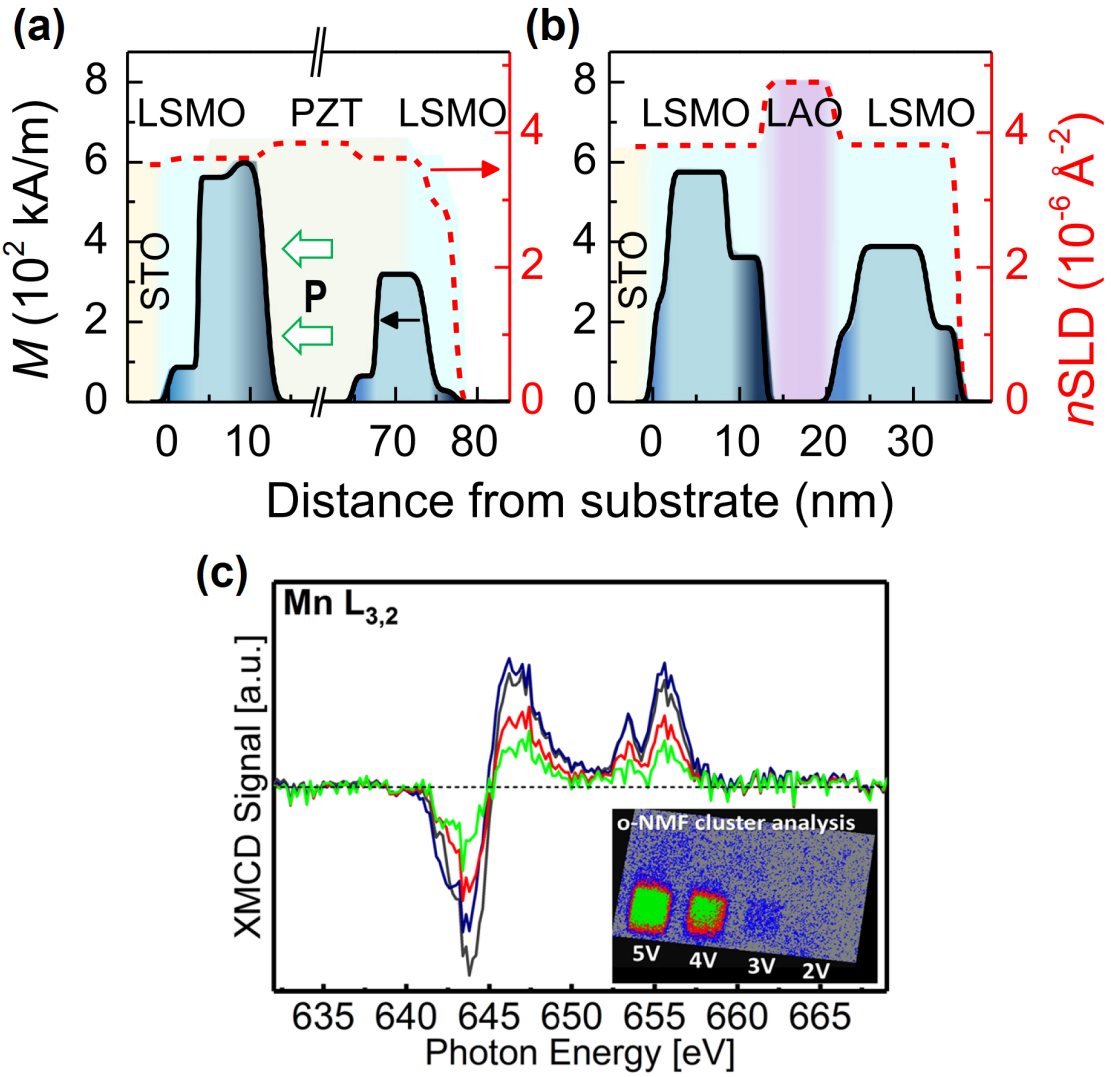

Figure 2.9: Electric field modification of dead layers in LSMO. (a, b) Magnetization profiles of LSMO/PZT/LSMO//STO and LSMO/$LaAlO_3$/LSMO//STO heterostructures, extracted from polarized neutron reflectometry data fitting. Magnetically dead layers are seen at each LSMO interface, except for an enhanced magnetization region at one of the PZT/LSMO interfaces, towards which the polarization of PZT is pointing. Adapted from ref.120. b) X-ray magnetic circular dichroism (XMCD) map recorded over LSMO surface, where rectangular regions were poled with the local conductivity AFM tip (inset), and the XMCD spectra of the Mn $L_{3,2}$-edge extracted and averaged over the colorcoded cluster regions. The XMCD signal decreases with increasing positive voltage and reveals a significant ferromagnetic contrast between 3 V and 4 V (LRS-to-HRS switching). Adapted from ref.121.

ization of BTO can perform electrostatic doping in the LSMO ($x = 0.33$) layer close to the interface (∼3 nm thick) [122]. This induces the MIT and results in about 27% magnetization change in the 25 nm thick LSMO film, what was shown with the results of SQUID magnetometry and magneto-optical Kerr effect measurements. In an alternative approach, magnetoelectric coupling was organized through the reconstruction of orbital hybridization between Ti and Mn ions at the interface [123]. In one of the BTO polarization states the shuttle movement of Ti ions affected the Mn

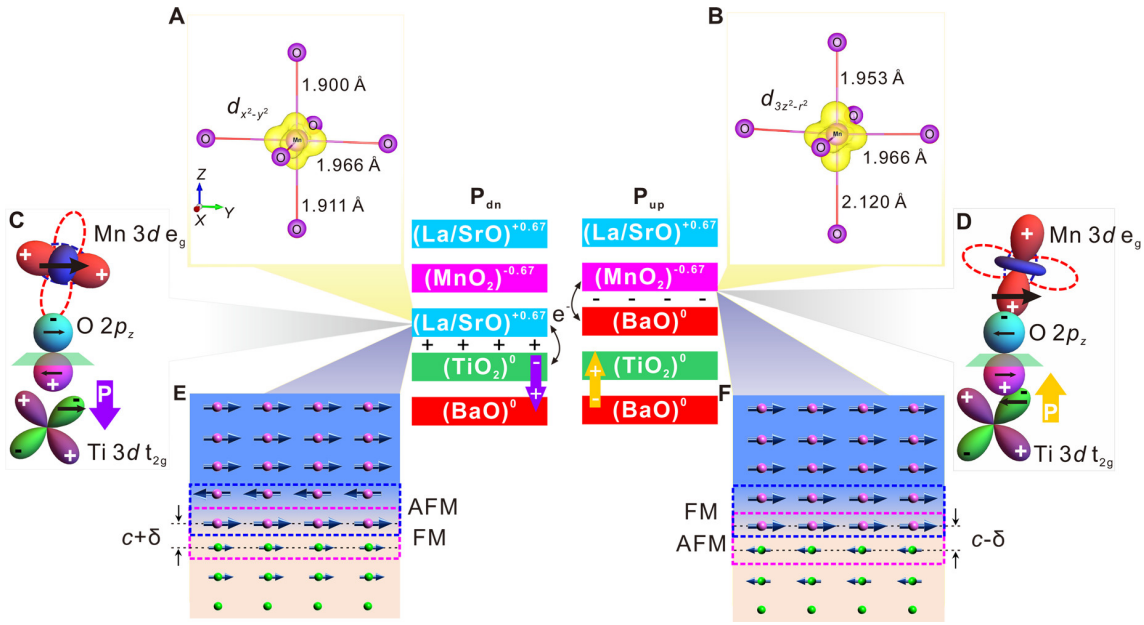

Figure 2.10: Interfacial magnetic couplings across the BTO/LSMO interfaces via Mn orbital occupation. (a, b) Calculated real-space charge density at the LaO/TiO interface (a) and the BaO/MnO interface (b). (c, d) The sketches of the orbital hybridization between Mn and Ti via O. (e, f) Proposed interfacial spin configuration and magnetic coupling mechanism at the LSMO/BTO heterointerfaces. The center shows the charge redistribution at the interfaces. Taken from ref.124.

double exchange bonds in the interfacial layers of LSMO, leading to local magnetic state alteration from ferromagnetic to antiferromagnetic, seen in magnetoresistance and X-ray linear dichroism (XLD) measurements of the samples with various LSMO thickness. Also, Ti ions at the BTO/LSMO interface were shown to be magnetized, what induced Ti-Mn exchange interaction that could be tuned with field effect of the ferroelectric polarization, thus combining the orbital and charge redistribution effects [124] (**figure 2.10**). Even more complex behavior was recently demonstrated in BTO/LSMO ($x = 0.5$) system, where the interplay of spin, orbital and lattice degrees of freedom led to the large value of TMR (remarkably, induced in a system with a single FM layer), that in addition to that was ferroelectrically modulated, thus producing the combined tunneling electro-magnetoresistance (TEMR) effect of ∼2000% [125].

Another interesting effect is built on the sensitivity of TER mechanism to termination of the layers [126]. Evidently, in BTO/LSMO//STO heterostructures, the initially SrO-terminated substrate after the growth leads to the sharp $TiO_2/La_{0.7}Sr_{0.3}O$ interface, while TiO_2-terminated one - to BaO/MnO_2. Despite the identical ferroelectric behavior, the TER effect for two types of interfaces is of opposite polarity. This is explained by the opposite signs of polar BTO/LSMO interface ionic charges, that are not completely screened by LSMO. As a result, the Fermi level can be shifted closer to conduction band minimum (CBM) or valence band maximum (VBM), what makes, respectively, electron or hole tunneling dominate.

The experiments with LSMO/BTO interfaces may be expanded, if LSMO / BTO / LSMO junctions are considered. For instance, ferroelectrically induced MIT was explored further via insertion of 1−5 unit cell thick $La_{0.5}Ca_{0.5}MnO_3$ (LCMO) layers

at one of the BTO/LSMO interfaces [127]. This allowed to switch between ferromagnetic metallic and antiferromagnetic insulating phase of LCMO and enhance TER at 5 K by almost 2 orders of magnitude, compared to the junction without the interlayer. The ferroelectric control of Ti-Mn orbital reconstruction also allowed to modulate TMR between 10% and 1000% with polarization switching [128].

◆ The above mentioned effects were observed in the samples with atomically sharp interfaces. Additional effects emerge when intermixing occurs between BTO and LSMO. Thus, it was shown that Mn-Ti mixing enhances the ferroelectric control of MIT in LSMO, and results in room temperature TER equal to 10^4 for LSMO/BTO/NSTO MFS junctions, compared to 10^2 for Pt/BTO/NSTO [130]. In another example (**figure 2.11**) it was demonstrated how in the structurally sharp BTO/LSMO interface the intermixing occurred over 1−3 unit cells, while the remaining 20 nm thick BTO layer was quite highly conducting due to activity of oxygen vacancies [129]. The intermixed layer together with the mediation of oxygen vacancies was shown to be susceptible to the reversible redox reaction. This resulted in the formation of ∼2.6 nm thick effective barrier layer, which turned out to demonstrate robust resistive switching, likely independently of ferroelectric switching. The similar effect was observed in LSMO / barrier / LSMO heterostructures with BTO,

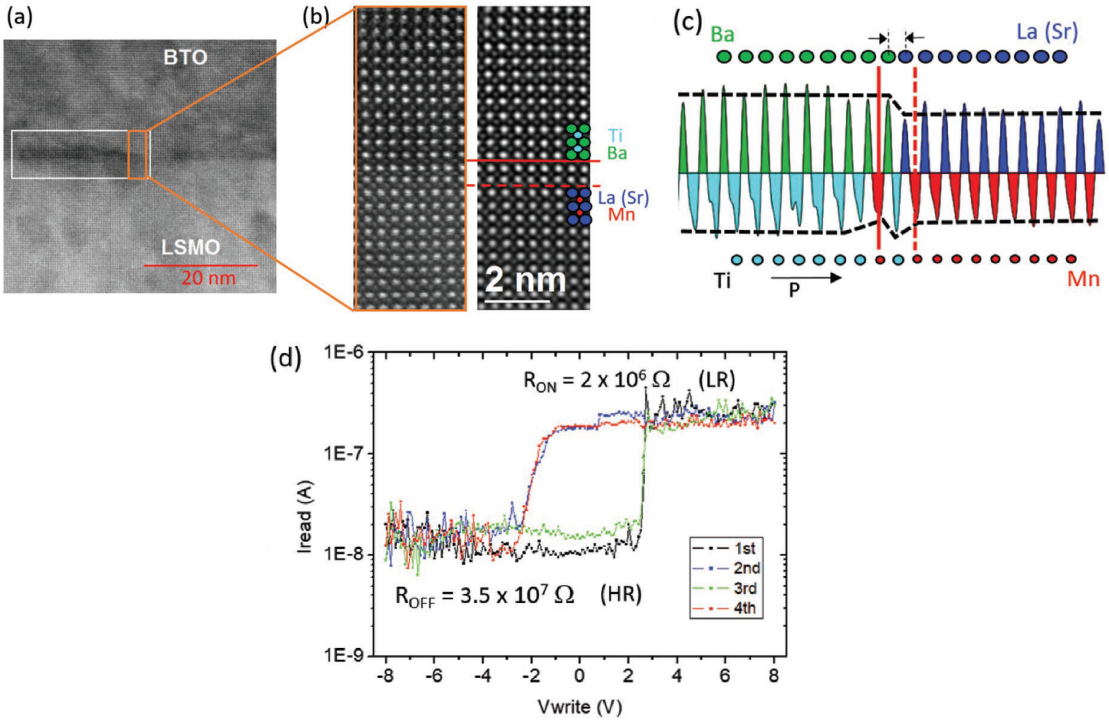

Figure 2.11: Properties of the intermixed BTO/LSMO interface. a) Transmission electron micrograph of the BTO/LSMO structure showing contrast inhomogeneities (pockets) along the interface. b) The high resolution raw (left) and filtered (right) image taken at the level of the pocket seen in image (a). c) Intensity profile extracted from filtered image (b), each peak being the integration of a line of 8−9 atoms along the interface. d) The I_{read} current at V_{read} as a function of V_{write} for two complete hysteresis cycles. The two high (OFF) and low (ON) resistance values are indicated. Taken from ref.129.

PZT and STO as barrier layers [131]. By reproducing the resistive switching with paraelectric STO identically to the cases of PZT and BTO, and supported by modeling of the asymmetric $I(V)$ curves, it was demonstrated that reversible oxygen vacancy migration could be, in fact, the primary resistive switching factor. Finally, the asymmetric cation intermixing at two LSMO/BTO interfaces in LSMO / BTO / LSMO heterostructure was suggested to determine the locally preferred spontaneous polarization direction, which can influence the resistive switching performance of the multiferroic tunnel junction [132].

2.4 Conclusion

To summarize, BTO and LSMO are suitable materials for use in the MFTJ architecture for proof-of-concept experiments. Under certain conditions, multilevel storage, voltage control of magnetic order, or memristive properties are possible in a system consisting of these materials. It is worth noting that, in addition to such advantages as the availability of methods for growth of high-quality samples and the relative convenience of *ab initio* modeling, when working with these materials, it is necessary to pay attention to the complex magnetoresistance behavior of LSMO, the oxygen content in the layers (and, as a consequence, the participation of oxygen vacancies in resistive switching processes), as well as the presence of dead layers near the LSMO surface/interfaces and their effect on the device operation.

Chapter 3

Methods

In this chapter we describe the experimental methods, used to fabricate the samples, such as pulsed laser deposition, high temperature annealing in oxygen atmosphere and cleanroom processes, and to perform the preliminary characterization and main experiments, such as X-ray diffraction and reflectometry, Rutherford backscattering spectrometry, atomic force and transmission electron microscopies, magnetic field and low temperature measurements and electrical experiments. All the experiments and analyzes presented in this thesis manuscript were carried out at the Institut des NanoSciences de Paris (INSP), except for the analysis by transmission electron microscopy, which was carried out at CIMAP in Caen by Xavier Portier, and the low temperature experiments, which were carried out using the PPMS apparatus at Mesures Physiques à basses Températures (MPBT) platform of Sorbonne Université under the supervision of David Hrabovsky.

Concerning the experiments carried out at platforms directly managed by the INSP laboratory:

- the X-ray measurements on the Rigaku diffractometer were carried out with the help of Nicolas Casaretto;

- Rutherford backscattering spectrometry (RBS) measurements were carried out on the SAFIR experimental platform, which couples a Van de Graaff accelerator to various analysis chambers. Spectra acquisition was carried out with the help of Ian Vickridge (SAFIR manager), Emrick Briand, Jean-Jacques Ganem, Jacques Perriere;

- the lithography of the samples was carried out in the INSP cleanroom under the supervision of Loïc Becerra and with the help of Erwan Dandeu.

All the other experiments were carried out at the INSP independently, on equipment specific to the team (including growth via pulsed laser deposition), under the supervision of Nathalie Jedrecy and with the help of Christian Hebert.

3.1 Growth and fabrication

3.1.1 *Pulsed laser deposition*

Functional oxide thin films were grown via pulsed laser deposition (PLD). The method is based on the effect of rapid evaporation (ablation) of the solid material from the target by focused laser radiation of high power density, and the subsequent condensation of the generated solid, liquid and plasma particles on the substrate

[133]. A simplified sketch of the PLD set-up is demonstrated in the **figure 3.1**.

A solid-state Nd:YAG laser (λ = 1064 nm, with the option of 2^{nd}, 3^{rd} and 4^{th} harmonic generation) is used in the Q-switch mode to generate short ($\sim 10^{-8}$ s) pulses of high power density ($\sim 10^{8}$–10^{9} W cm^{-2}). Laser radiation is then focused onto a deposition material target. The target absorbs the radiation (via various mechanisms, depending on the target material), leading to evaporation of the target matter. Interaction of the ejected material flow with the laser radiation brings the matter into plasma state - the phenomenon is called "plasma plume". The material then is being condensed onto the substrate, which is usually heated for the growth mode adjustment. The ablation process creates craters on the target surface, which may complicate the subsequent operation. To avoid this, the laser beam should cover the target area uniformly by either a scanning motor-operated mirror system, or target rotation with external motor - as in our case. Internal chamber environment is also an important degree of freedom during PLD. The total gas pressure strongly affects the growth rate, and the partial pressures (and ionization states) of various gases (Ar, O_2, N_2, H_2S, etc.) allow to tune film composition and other physical and chemical properties.

PLD proved to be especially effective in the epitaxial growth of complex oxide films, with cuprate superconductors [133] and perovskite-like oxides of various functionalities [134] as primary examples. The rapid ablation process levels out the variations of the melting and evaporation points of the components of the target material and allows to preserve the stoichiometry, at least for the cations. The oxygen content loss is dynamically compensated by adjustment of partial O_2 pressure and substrate temperature.

In our case, deposition of BTO and LSMO was performed from commercial ceramic targets using 4^{th} harmonic of Nd:YAG laser (λ = 266 nm) with 10 Hz pulse repetition rate. During the growth, substrate temperature was kept at 600 °C, oxygen pressure at 10^{-2} mbar, laser pulse fluence at 100 mJ cm^{-2}. Each growth was followed by an *ex situ* annealing in the dedicated high temperature oven at 800 °C in 100 mbar of oxygen pressure for 30 min to replenish the oxygen content in the films, which is especially important for the LSMO magnetic ordering.

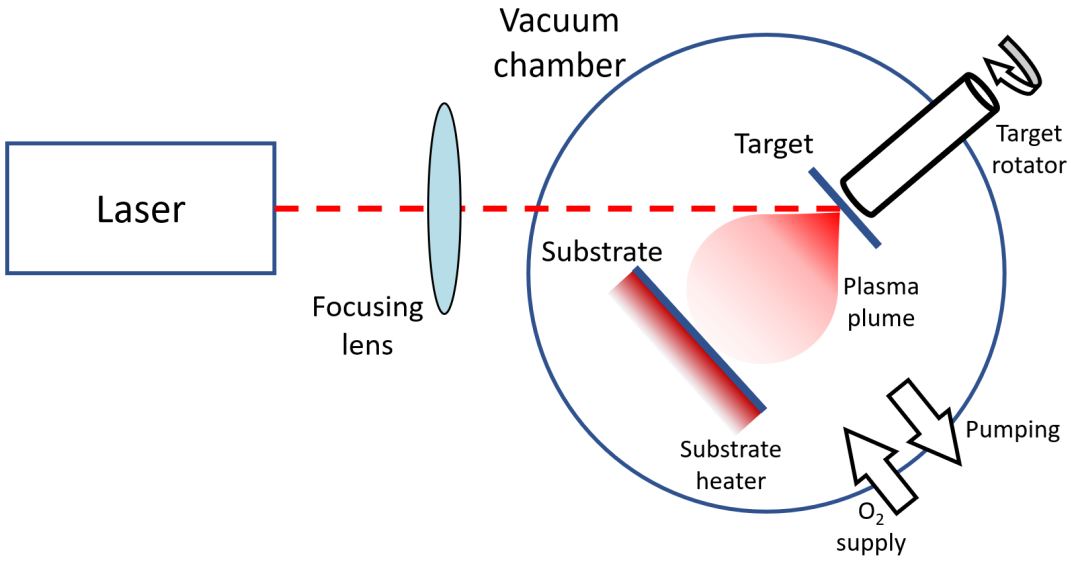

Figure 3.1: Simplified sketch of the pulsed laser deposition method

3.1.2 *Device fabrication*

Further manipulations with the experimental samples were performed in the cleanroom facility of INSP. All the lithography steps (**figure 3.2**) were made with conventional photolithography technique, using maskless direct UV laser writing DWL 66FS Heidelberg apparatus for first test samples of the designed patterns and photomask preparation, and mask aligner SUSS MicroTec MJB4 with the photomasks of the settled pattern for faster operation.

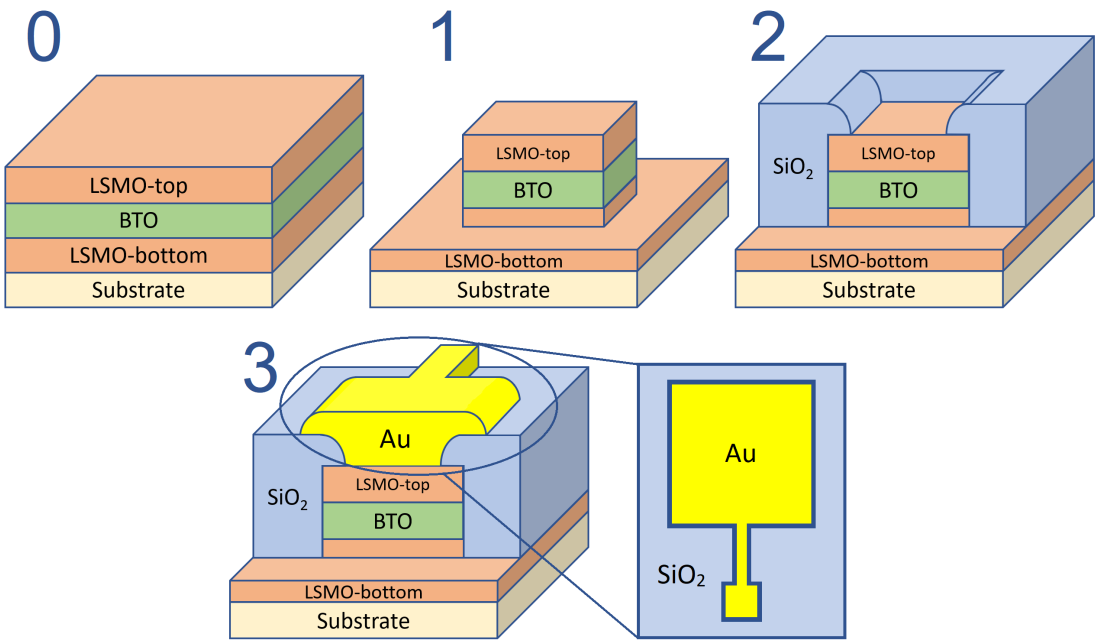

Figure 3.2: Sketch of the lithography steps. Step numeration corresponds to the text. Zoom in the step 3 shows the top view of the Au pad on SiO_2.

Prior to patterning steps, the samples should be subjected to the cleaning procedure, which is repeated when necessary further. The samples are put in acetone in the ultrasonic bath for 5−10 minutes, followed by flushing in isopropyl alcohol (IPA), then in deionized (DI) water, and purging in N_2 flow. To remove the organic residues, the final cleaning step in oxygen plasma is performed using Harrick Plasma PDC-002 machine at maximum power for 5 min.

The first patterning step is defining the micro-pillars. The samples are covered with the bilayer positive photoresist film (AZ-1512 with TI Prime adhesion promoter underlayer), using the spin coater. After exposition in one of the UV lithography systems, the photoresist is developed in 1:4 water solution of AZ-351b developer. After development, the oxygen plasma (30 s at minimum power) is used again to remove the residues of the resist on the sample area that should be uncovered. Then the etching in 10% solution of HCl is performed to define the pillars by etching off the material in the areas, uncovered with photoresist, down to the level of bottom LSMO electrode (30−60 nm). To finely control the etching depth, etching is done in 0.5−5 min rounds, measuring the height difference between the resist surface and the etched level surface (i.e., resist thickness + etching depth) after each round with the stylus profilometer Dektak 150 Veeco*. Upon reaching the desired etching

*It was verified that the chosen combination of photoresist layers and HCl concentration does not lead to the resist degradation, therefore allowing the described fine etching control.

depth, the samples are cleaned from photoresist following the previously described acetone-IPA-DI water procedure.

At the second step, the inter-pillar dielectric isolation is formed. The samples are covered with the bilayer negative photoresist (AZ-nLof-2035 with Prime underlayer). After the exposition, the samples have to be additionally baked on the hot plate at 110 °C for 1 min to convert the pattern (specific operation for negative resists). Only then the development can be performed in AZ-726 developer, followed by the mild O_2 plasma cleaning (30 s at min power). After this, the deposition of 200 nm of SiO_2 is done using Alcatel magnetron sputtering machine. To remove the resist together with SiO_2 in unnecessary areas, the lift-off is performed in acetone for 15-60 min under minimum agitation in the ultrasonic bath, followed by the cleaning procedure. Thus, the area outside the pillars is covered with SiO_2, slightly overlapping the pillars, so the pads for contacting top LSMO electrode could be deposited with no risk of electric short circuit between top and bottom electrodes.

Finally, the metallization for safe device contacting is done last. The photoresist related procedures are repeated as in the first step (etching). After the resist pattern is defined, the deposition of 200 nm Au layer (with 20 nm Cr or Ti underlayer for better adhesion) is performed with Vinci PVD-4E thermal evaporation system. Next, the lift-off procedure is done in the same way as in the step two (SiO_2 isolation). In the end, the 400×400 μm^2 Au pads with 40 μm wide leads to the top electrode square caps of various lateral sizes (25, 50 and 100 μm) are formed. This allows to safely use ultrasonic wire bonding or Ag paste for connection of the wires for electrical measurements: large pad size facilitates the access, whatever bonding method is used, and $200+20$ nm pad thickness together with 200 nm SiO_2 thickness secure from potential shortcut.

It should be noted that some of the pillars after etching were not subjected to isolation and metallization steps in order to avoid abrupt topography changes and secure the probe tip for atomic force microscopy.

3.2 Material characterization methods

3.2.1 *X-ray diffraction and reflectometry*

Structural properties of the thin-film layers were characterized with X-ray diffraction (XRD) and reflectometry (XRR).

A symmetric $\theta/2\theta$ experiment is organized in the conventional scheme (**figure 3.3a**). X-ray beam of the wavelength λ is incident on the sample surface with glancing angle ω. The condition to observe a diffracted beam intensity maximum is equality of total optical path difference (OPD) Δ to integer number of wavelengths, what from the geometric consideration is expressed via Bragg's law [135]:

$$\Delta = 2d \sin\theta = m\lambda,$$

where m is the diffraction order (in XRD $m = 1$), θ is the glancing angle of the diffracted beam (equal to ω by construction in symmetric geometry). Thus, varying θ, the diffraction pattern $I(\theta)$ - dependency of the diffracted beam intensity on the diffraction angle - is obtained, allowing to determine the characteristic interplanar spacing values of the sample. Normals to these planes are aligned in direction of the X-ray scattering vector $\Delta\vec{k} = \vec{k}_{diffracted} - \vec{k}_{incident}$, or, since the scattering is

elastic, along the bisector of the angle between the incident and diffracted beams. In the symmetric $\theta/2\theta$ geometry this direction coincides with the perpendicular to the sample surface.

◆ In order to address the periodic structures along other crystallographic directions, an asymmetric geometry has to be implemented. When the sample is monocrystalline or epitaxial, it is possible to orient it (with appropriate diffractometer) in the way that $\Delta\vec{k}$ is aligned with any chosen crystallographic direction (**figure 3.3b**) among those that are instrumentally accessible. Thus, combination of the symmetric and asymmetric measurements allows to assess all the unit cell parameters.

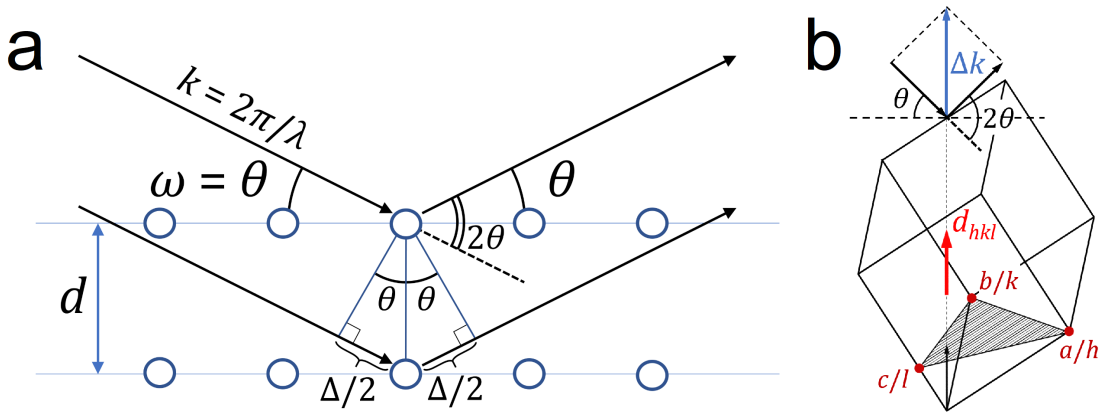

Figure 3.3: Sketch of the XRD measurements. a) Symmetric $\theta/2\theta$ measurement. b) Asymmetric measurement with tilted sample.

◆ Reciprocal space mapping (RSM) allows to directly visualize the diffraction patterns in the cross-sections of reciprocal space [136]. Firstly, position of the peak of interest is determined based on the information obtained with $\theta/2\theta$ scans, and the diffractometer angles are aligned accordingly, in particular, in ω and 2θ. These values act as scan offsets: ω_{offset} and $2\theta_{offset}$. Then ω is slightly varied by $\Delta\omega$, and for each fixed $\Delta\omega$ value $\Delta 2\theta$ is scanned around $2\theta_{offset}$. This is so called $2\theta/\omega$ scan. A series of one-dimensional $2\theta/\omega$ scans is combined to obtain a two-dimensional intensity map with ω and 2θ as axes. Angle maps are further transformed into wavevector RSM with the following formulae:

$$Q_x = \frac{2}{\lambda}\sin\left(\Delta\theta + \theta_{offset}\right)\sin\left(\Delta\omega + \omega_{offset} - \theta_{offset}\right),$$
$$Q_z = \frac{2}{\lambda}\sin\left(\Delta\theta + \theta_{offset}\right)\cos\left(\Delta\omega + \omega_{offset} - \theta_{offset}\right),$$

where Q_x (Q_z) is a reciprocal space coordinate, corresponding to in-plane x (out-of-plane z) crystallographic axis.

◆ X-ray reflectometry (XRR) [137] is a complementary analysis method that can be implemented with the use of X-ray diffractometer. In this technique, an X-ray beam is incident on a sample surface at a small angle (typically, with θ in $0{-}5°$ range), with source and detector angles being varied synchronously, similar to symmetric $\theta - 2\theta$ XRD scan (**figure 3.4a**). Up to a certain angle value θ_c, called critical angle, total external reflection of the beam occurs (since the refraction index for X-ray radiation is negative), after which the intensity of the reflected beam rapidly decreases with θ increase. Analysis of θ_c and intensity decay character allows to determine the sample

material electron density and surface roughness, respectively. When the sample is a multilayer thin film, reflections of the X-rays occur at each interface between the layers, leading to interference of the beams, reflected at different interfaces. OPD of the X-rays, that pass a certain layer, depends on the value of θ and is proportional to the layer thickness. The condition to observe the interference maxima is equality of OPD to integer number of wavelengths. This, in the measured reflectivity curve $I(\theta)$, interference manifests in emergence of the oscillation pattern, referred to as Kiessig oscillations or fringes [138, 139]. Distance in θ between the fringes is roughly proportional to the thickness of the corresponding thin layer.

In case of a multilayer film, a more accurate analysis is required, based on the numerical simulation of the reflectivity curve with subsequent fitting to the experimental data. This allows to extract the layer thicknesses, interface roughness values, electron density values, estimate the material composition for alloyed films. As an example of that, an XRR experimental curve, measured on the $BaTiO_3$/MgO sample, is demonstrated in **figure 3.4b** together with the corresponding simulated curve. In order to reach the best fit, three layers of BTO had to be taken into account: the main part of the film close to substrate, the thin layer on top of that with lower density, and the thinnest layer on the surface with lower density and higher roughness on top (simulation parameters are presented in the inset table of fig.3.4b). Excellent fitting accuracy allowed to determine that total BTO layer thickness equals 786 Å, and to unveil the presence of a 41 Å thick surface layer that possesses lower density and higher roughness, than the main part if the film. The necessity of three BTO layers effectively indicates the presence of the density gradient at the films' surface, which could be accounted to even higher degree of precision with the use of appropriate software. In our case, the version of Bede REFS software, that was used for XRR simulation, allows to introduce only the fixed number of layers with uniform parameters, leading to a rather crude approximation of the film properties gradient, which is, however, enough for the accurate analysis of the available experimental data, as seen from the figure.

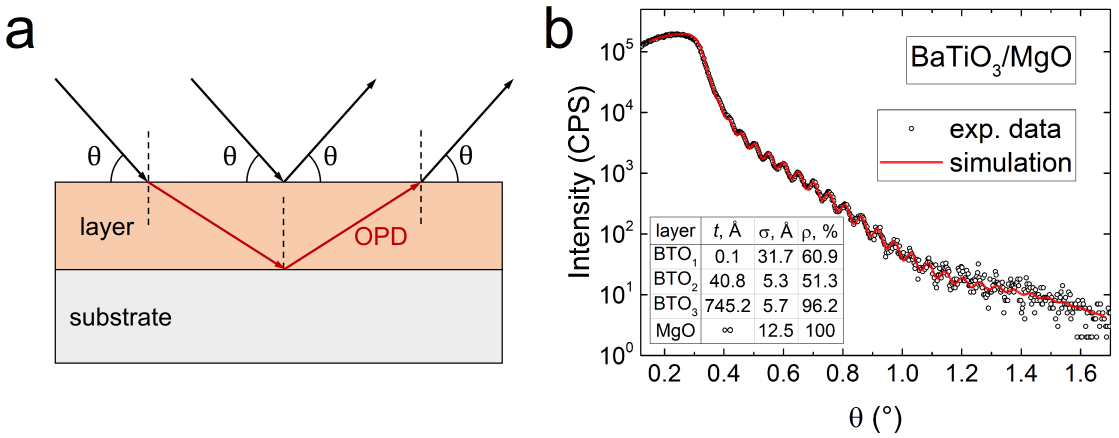

Figure 3.4: a) Sketch of the XRR measurement. b) XRR experimental curve of $BaTiO_3$/MgO sample with its simulation, inset table shows the simulation parameters: t - thickness, σ - roughness of the top surface of the layer, ρ - electron density in percents of the table value for the material of the layer.

3.2.2 *Atomic force microscopy*

Atomic force microscopy (AFM) is a powerful scanning probe tool used for imaging of the sample surface topography and mapping other physical properties with the use appropriate extensions, such as conductive, magnetic, piezoresponse or Kelvin probe force microscopies and many more.

Surface scanning is performed with a sharp tip, attached to a cantilever. The tip interacts with the surface in multiple ways, what results in cantilever bending. This is detected via the deflection of the laser beam from the bent cantilever surface. The processing of the detected signal allows to form the feedback action, depending on the measurement mode, e.g., to adjust the probe height in order to keep the tip-to-surface distance or interaction force constant (**figure 3.5a**).

For characterization of ferroelectric surfaces, the method of piezoresponse force microscopy (PFM) was developed. Here the inverse piezoelectric effect is exploited in the following way (**figure 3.5b-e**). A tip with conducting coating is brought into contact with the surface of a ferroelectric and an AC voltage signal is applied to it. The voltage amplitude is adjusted to be smaller than the ferroelectric coercive field, so the polarization does not get reversed. The phase of mechanical domain deformation depends on the local polarization direction $\vec{P}$ with respect to external electric field $\vec{E}$: if $\vec{P}$ and $\vec{E}$ are parallel, the piezoresponse is in phase (0°) with the excitation; if $\vec{P}$ and $\vec{E}$ are anti-parallel, the piezoresponse is out of phase (180°). Application of DC voltage bias allows to access any polarization state over the ferroelectric hysteresis loop, and scanning the ferroelectric surface with a 0 V bias allows to obtain the out-of-plane polarization direction maps. Usually, in the beginning a "writing" scan is performed with a non-zero bias to induce a fixed polarization state over some area, which is followed by a "reading scan" over a larger area, what allows to test the polarization stability and provide an argument for the ferroelectric nature of the studied material.

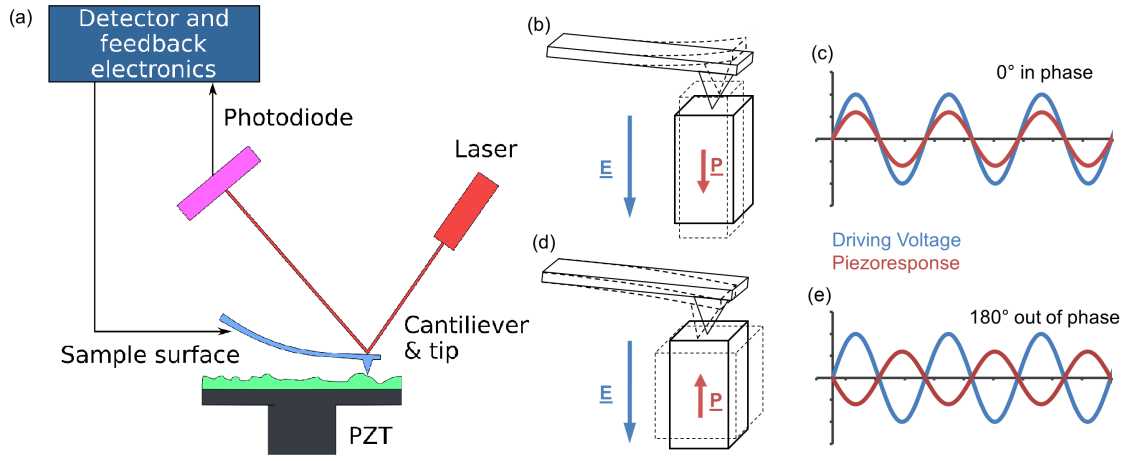

Figure 3.5: Atomic and piezoresponse force microscopy description. a) Schematic image of atomic force microscopy set-up. Taken from ref.140. b-e) Piezoresponse force microscopy principle (taken from ref.141.): AC electric field excitation of the domain with parallel polarization direction with respect to external field (b) yields an in-phase piezoresponse (c), while excitation of the anti-parallel direction domain (d) yields an out-of-phase piezoresponse (e).

AFM Park XE7 was used for surface topography mapping and PFM mapping and spectroscopy. Topography was mapped in the tapping mode with ∼20 nm tip height set point and ∼45 nm amplitude. PFM measurements were performed in contact mode with the use of a built-in voltage generator for DC biasing and Stanford Research SR830 DSP lock-in amplifier at ∼8 kHz frequency for AC voltage generation and detection. In both modes the Park Multi75E-G cantilevers with conductive tip coating were used (resonance frequency = 75 ± 15 kHz in the fully lifted state). We should note that PFM measurements were done over the LSMO top electrode surface, since conductivity of LSMO in our case is not high enough to completely screen the electric field from the probe tip and lose the locality of field application, necessary for mapping.

3.2.3 *Transmission electron microscopy*

For structural analysis of the sample cross-section by scanning transmission electron microscopy (STEM) a double aberration-corrected cold FEG ARM200F JEOL microscope, equipped with a high-angle annular dark field (HAADF) detector was used. The microscope was operating at 200 kV; an electron energy loss spectrometer (EELS) QUANTUM ER from GATAN was used for valence state analysis. The TEM lamella was prepared by a focused ion beam (FIB) system FEI HELIOS Nanolab 660.

3.2.4 *Rutherford backscattering spectrometry*

Rutherford backscattering spectrometry (RBS) is an ion beam analysis technique that allows to assess the composition of the samples with depth resolution. It is a development [142] of the classical Geiger-Marsden gold foil experiment [143], explained theoretically by Rutherford [144], what lead to the discovery of atomic nuclei and formulation of planetary atomic model.

The experiment principle is as follows (**figure 3.6**). The sample under investigation serves as a target for alpha particles ($^4_2He^{2+}$ nuclei). The alpha particles

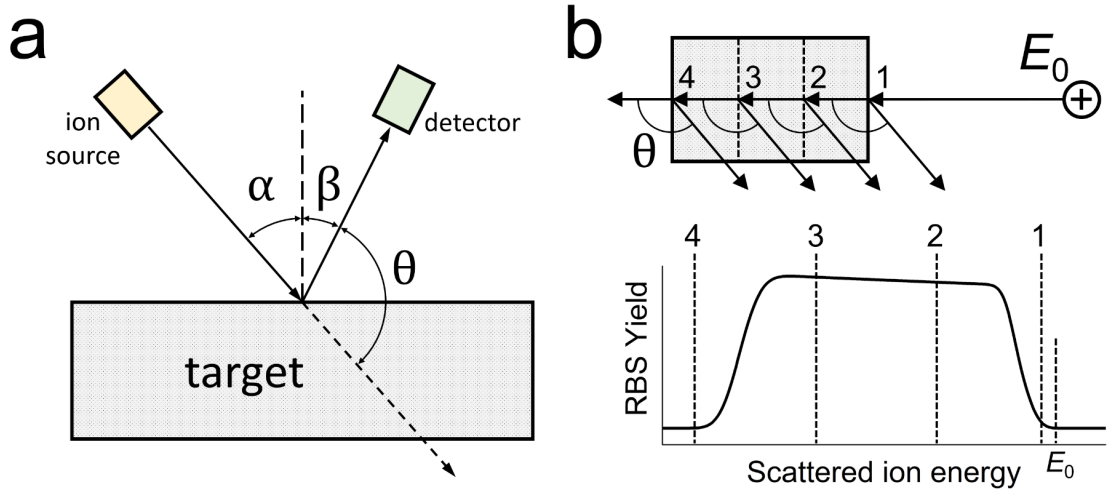

Figure 3.6: RBS measurement description. a) Simplified scheme of the experiment. b) Formation of the spectrum.

enter the target at an incident angle α (usually equals 0°, i.e., normal incidence) with the typical energy in the range of MeV. Inside the target, the particles scatter from the target material nuclei - they change the direction and lose the kinetic energy, as a function of the nuclei charge, target thickness and density, initial alpha particle energy. Moreover, the deeper the particles go inside the target, the higher the scattering probability (for the same type of nuclei) and the higher the energy loss. Then the scattered particles are gathered by the detector, located at the exit angle β with respect to the sample surface normal. The detector angle is chosen so that the particle scattering angle θ is close to 180°[†]. The detector sorts the collected particles by kinetic energy and counts them in different channels. Thus, the value of so called RBS yield is obtained - number of the particles counted in a channel per unit time. With some a priori knowledge of the target composition, detector channels can be accurately calibrated into particle energy with no need to use the standard samples, since the alpha particle scattering cross-sections for all the nuclei of the periodic table are well known.

In the end, the obtained experimental backscattering spectrum can be simulated with dedicated software. For example, as presented in **figure 3.7**. In this case, the sample is a Ta_2O_5 thin film on Si. The simulation fitting procedure verifies the nominal film composition with the accuracy better than 0.5% and gives the film thickness equal to 186 nm.

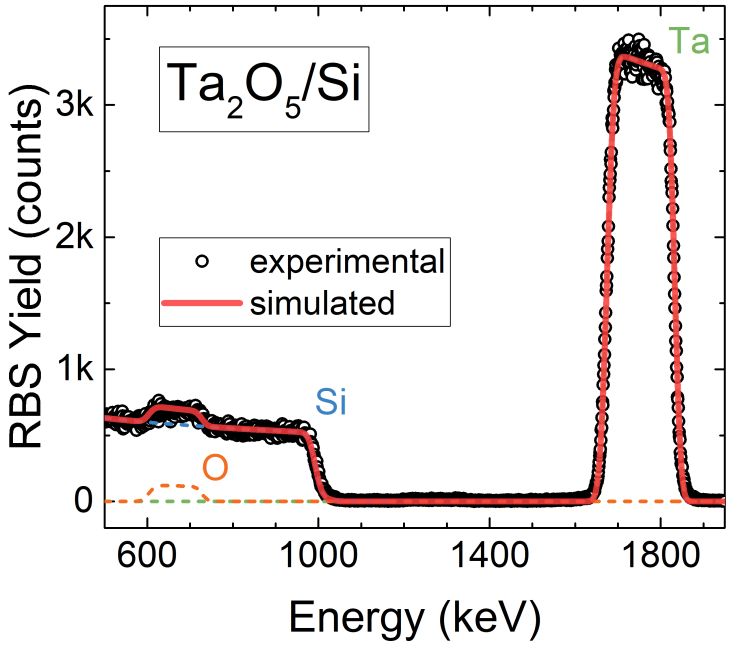

Figure 3.7: RBS spectrum of Ta_2O_5/Si sample with its simulation (total and by element).

[†]Note that $\alpha+\beta+\theta$ does not have to equal 180°, as shown in the fig.3.6a. Practically, detector is sometimes located at the same side with respect to the normal to ion beam incidence point, as the ion source. In this case, $\alpha-\beta+\theta=180°$. However, if the angles are defined strictly according to fig.3.6a up to the sign of the angle value, β in the second case would be negative, so the entity $\alpha+\beta+\theta=180°$ holds.

3.3 Electrical measurements

In all electrical measurements the source-measure units (SMU), manufactured by Keithley, were used: model 2400 for magnetoresistance measurements (chapter 5), and model 2635B for all other experiments. These SMUs combine the DC voltage generator and simultaneous voltmeter + ammeter functionalities, which allows to acquire $I(V)$ curves and measure resistance of a device-under-test while varying external physical parameters. 2635B device is distinguished by the possibility to implement voltage or current pulse generation. Minimal digital resolution of the SMU is 50 μs, what is limited by the capabilites of analog-to-digital and digital-to-analog converters. This makes for the minimal accessible pulse duration of 70 μs (to adjust for the voltage/current ramps). Minimal idle time duration between the pulses equals approximately 1.7 ms, which in the case of pulse trains limits their frequency to ∼580 Hz.

Experimental sample connection was kept the same for all the electrical measurements (**figure 3.8**). The common bottom electrode (BE) is connected to the positive terminal of the SMU ("HI"), while the top electrode (TE) of the individual device is connected to the SMU ground terminal ("LO").

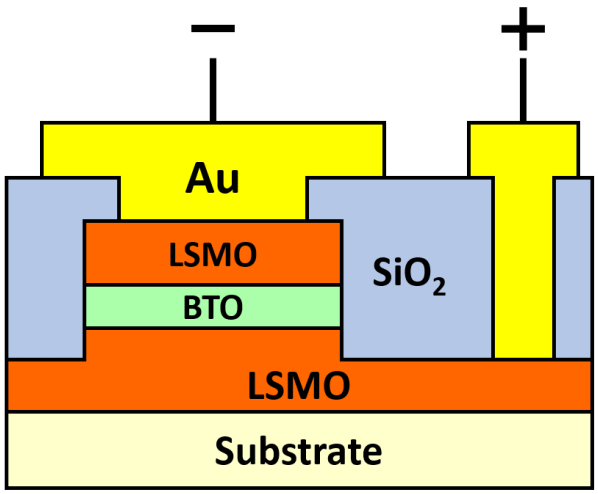

Figure 3.8: Sketch of the device connection for electrical measurements.

Programming of the low-level commands for SMU (up to pulse trains and routine $I(V)$ sequences) was performed in the Keithley Test Script Builder environment using Lua programming language with proprietary libraries. High-level programming for measurements and data collection was performed in the Quantum Design PPMS MultiVu environment using WinWrap Basic for COM (WWB-COM) version of the Visual Basic programming language.

3.4 Magnetic and low temperature measurements

Magnetic field- and temperature-dependent measurements were performed with Quantum Design Physical Property Measurement System (PPMS), equipped with a superconducting coil magnet capable of generating magnetic fields up to 9 T. Accessible temperature range is 1.8−400 K.

$M(H)$ curves were measured with the conventional [145] vibrating sample magnetometer (VSM) option (0.5% accuracy of magnetic moment measurement, sensitivity better than 10^{-6} emu, noise level less than $6 \cdot 10^{-7}$ emu at 300 K).

Electrical measurements with optional dependence on magnetic field and temperature were performed with the use of the Quantum Design Multi-Function Probe, that allows to connect up to 8 wires to the experimental sample (1 to BE + 7 to TE of various devices), and to rotate the sample with respect to magnetic field from the in-plane (IP) to the out-of-plane (OP) orientation. To perform the electrical measurements the SMU, described above, is connected externally. The wires are connected to the experimental sample on the holder using ultra-sound wire bonder or manually with 50 μm Au wire and low temperature compatible Ag paste.

Chapter 4

Preliminary characterization of experimental samples

4.1 Growth of the films

Four growth sessions of LSMO/BTO/LSMO trilayers were performed (**table 4.1**). Approximate deposition rates were obtained through preliminary calibration growths and are equal to ∼2.2 nm/min for LSMO and ∼4 nm/min for BTO, which allowed to set the deposition time in order to achieve the desired nominal film thicknesses. Corrected thickness values were determined via cross-sectional transmission electron microscopy (TEM), XRR and RBS analyses and are discussed in this chapter below. To track the differences in tunneling and resistive switching behavior, BTO barrier thickness was varied: nominally 8, 4 and 6 nm films will be hereinafter referred to as "thick", "thin" and "middle", respectively. Another degree of freedom, that was varied, is the short annealing in the PLD chamber after the growth of each layer. It was considered that this short annealing may have an effect on the quality of the LSMO/BTO interfaces, and, as a consequence, on the device perfor-

Table 4.1: Summary table of all grown samples.

Growth date	Substrate	Deposition time (Nominal thickness)			After layer anneal	Sample nickname
		LSMO bottom	BTO	LSMO top		
31/07/2019	$SrTiO_3$	20 min (45 nm)	2 min (8 nm)	7 min (15 nm)	15 min	Jul STO
	Nb:$SrTiO_3$					Jul NSTO
	MgO					Jul MgO
01/02/2021	$SrTiO_3$		1 min (4 nm)		15 min	Feb STO
	Nb:$SrTiO_3$					Feb NSTO
	MgO					Feb MgO
15/03/2021	$SrTiO_3$		1 min (4 nm)		no	Mar STO
	Nb:$SrTiO_3$					Mar NSTO
	MgO					Mar MgO
31/05/2021	$SrTiO_3$		1.5 min (6 nm)		no	May STO
	Nb:$SrTiO_3$					May NSTO
	MgO					May MgO

mance. Thus, in the first two growths it was performed for 15 min after the growth of each layer, and was not performed in the last two growths. Three monocrystalline substrates at a time were used in each growth: $SrTiO_3$ (STO), Nb doped $SrTiO_3$ (NSTO) and MgO, all oriented in $\langle 001 \rangle$ direction. After the growth all the samples were annealed in O_2 atmosphere (800 °C, 100 mbar, 30 min) to eliminate as much as possible the oxygen vacancies in the films and improve magnetic properties of LSMO, as discussed in section 3.1.1.

4.2 Structure, composition and morphology

4.2.1 *Surface morphology*

Preparation of the substrate is an important step in the process of high quality epitaxial films growth. While MgO substrates are rarely used for the growth of perovskite oxide films due to quite large lattice mismatch and different crystal structure, many various procedures have been developed that allow to prepare an ultra-high quality surface of the $SrTiO_3$ substrates with atomically flat terraces and various terminations [146–149]. We performed a testing growth and compared the resulting quality of the surface of films grown on as supplied and prepared STO substrates.

The as supplied STO substrate was cleaned in acetone, isopropyl alcohol (IPA) and deionized (DI) water to remove possible dust particles or organic residues. Special preparation of the other STO substrate was performed in three steps, following the combined approach of refs. [149, 150]. Firstly, the substrate was put in DI water for 10 min to hydroxylate the SrO-terminated layers, after which it was dipped for 30 s in commercial buffered HF (BHF) solution (NH_4F:HF = 87.5:12.5) to etch the hydroxylated SrO, which is known to be more soluble in acids than chemically stable TiO_2-terminated layers. After that, in order to recrystallize the surface, the substrate was annealed in air at 950 °C for 1 h. Lastly, the substrate was put in DI water for 30 s to remove possible SrO aggregations, formed during annealing.

BTO/LSMO bilayer was grown on the substrates in a single process, following the procedure of Feb STO growth (table 4.1), but without the top LSMO layer. After the growth, the samples were annealed in O_2, as described above.

Surface topography of the samples was studied with atomic force microscopy (AFM) in tapping mode (**figure 4.1**). Microscopy was performed three times: before the growth, right after the growth (as grown) and after the oxygen annealing. BHF treatment of STO substrate indeed results in the terrace formation with low root-mean-square roughness of 0.2 nm (fig.4.1d). However, the as supplied substrate also is sufficiently smooth (0.3 nm roughness), nevertheless the termination is random and the terraces are hardly seen (fig.4.1a). After the BTO/LSMO growth the picture is changed drastically: visually, the difference between the as supplied (fig.4.1b) and prepared (fig.4.1e) substrates is not seen, and the roughness of the latter is now larger, 0.9 nm vs 0.7 nm for as supplied. High temperature annealing in the oxygen atmosphere does not result in qualitative changes, but the roughness is further increased up to 1.8 nm for the as supplied STO substrate (fig.4.1c) and up to 1.9 nm for the BHF-treated one (fig.4.1f).

Thus, we conclude that the specific STO substrate preparation is unnecessary for our PLD growth conditions, and the post-growth annealing in oxygen exacerbates

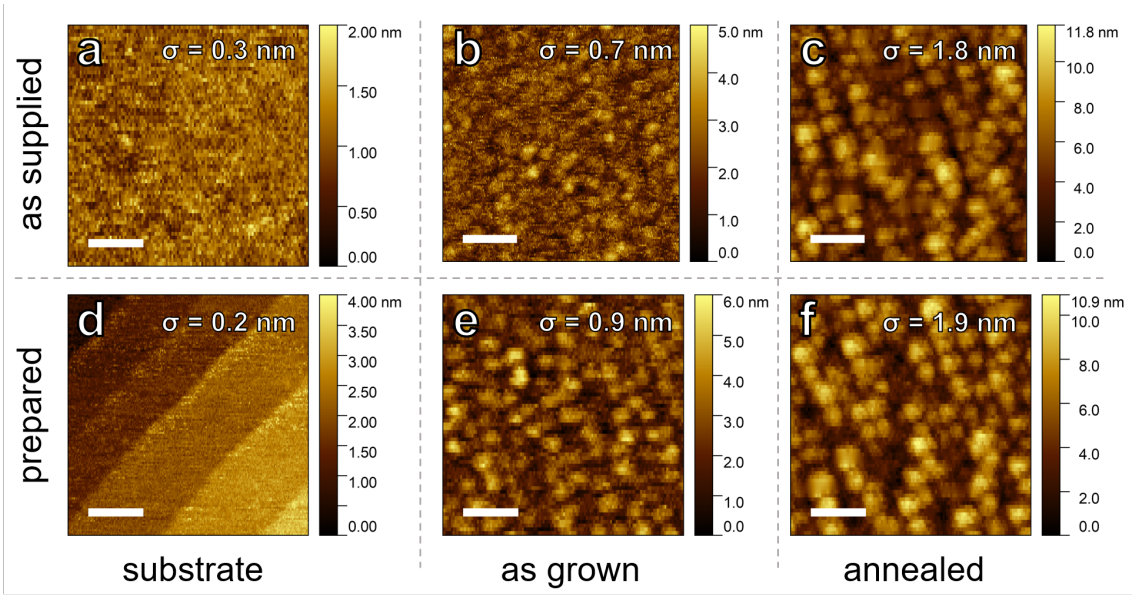

Figure 4.1: Surface topography of the samples: as supplied (a) and BHF-treated (d) STO substrates before the growth; as grown BTO/LSMO bilayer surface on as supplied (b) and BHF-treated (e) substrates; annealed BTO/LSMO bilayer surface on as supplied (c) and BHF-treated (f) substrates. Scale bar in all figures: 100 nm.

the situation even further. All the growths, described in table 4.1, were performed on the as supplied substrates, cleaned lightly in acetone, IPA and DI water. Moreover, we have found that the surface roughness after the growth of BTO and O_2 annealing is equal to almost 2 nm. For the samples with the second LSMO layer grown on top of BTO, roughness of the top LSMO/BTO interface can be expected to be close to this value.

4.2.2 *Structural analysis*

Structural quality of the films was characterized with X-ray diffraction analysis (XRD). Symmetric θ-2θ diffraction patterns of the thick-barrier samples (July 2019 growth) were firstly obtained with Rigaku Smartlab apparatus, for high acquisition rate and automatic filter implementation to secure the detector at high intensity substrate peaks (**figure 4.2**).

All the diffraction peaks are grouped close to the high intensity substrate peaks. The substrates are all of cubic symmetry with $\langle 001 \rangle$ normal orientation, which allows to unambiguously index the substrate peaks as $00l$. For STO and NSTO l is equal to 1, 2, 3, while for MgO only even l values are allowed among the $00l$ peaks by symmetry considerations, which results in presence of only 002 peak in the diffraction pattern of the MgO substrate sample, so 001 and 003 families in the latter case originate only from the films. Thus, the peaks of BTO and LSMO have to be of $h00/0k0$ or $00l$ indices, if we leave the possibility for tetragonality in the layers and conventionally assign the tetragonal axis to the l index or c lattice parameter. A detailed indexing may be performed with some additional lattice parameter considerations. BTO at room temperature possesses the tetragonal lattice,

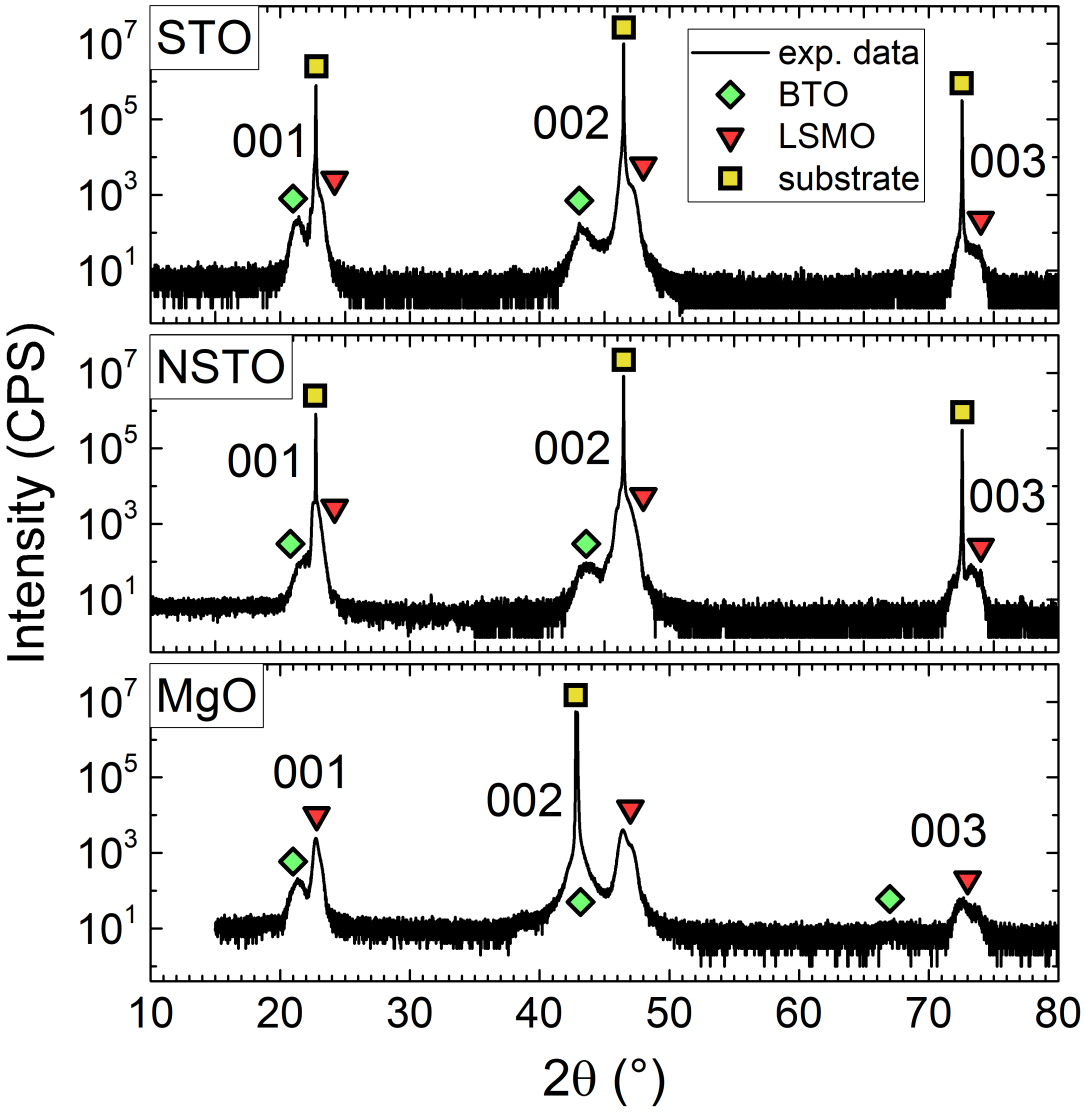

Figure 4.2: Symmetric θ-2θ diffraction patterns of the LSMO/BTO (thick)/LSMO heterostructures grown on $SrTiO_3$, Nb:$SrTiO_3$ and MgO substrates

with the out-of-plane lattice parameter c in case of thin films significantly increased to $4.1 - 4.2$ Å from the bulk value of 4.036 Å [68]. Together with the fact that BTO is the thinnest layer in the stack - thus, should have the lowest intensity - it may be confidently deduced, that the small peaks with the lowest diffraction angle value (i.e. the highest corresponding interplanar spacing) in the peak groups near $00l$ substrate peaks, are unambiguously assigned to the BTO $00l$ peaks. Bulk pseudo-cubic lattice parameter of LSMO is equal to 3.87 Å and in the heterostructures it usually stays in the range of $3.84 - 3.90$ Å [151]. Thus, the remaining peak of relatively low intensity, and with slightly higher 2θ value than of the substrate peaks, can be associated with LSMO $00l$ reflections.

◆ For higher resolution, in particular in the 003 region, the MgO substrate sample was additionally measured with Panalytical X'Pert apparatus (**figure 4.3**). Here it

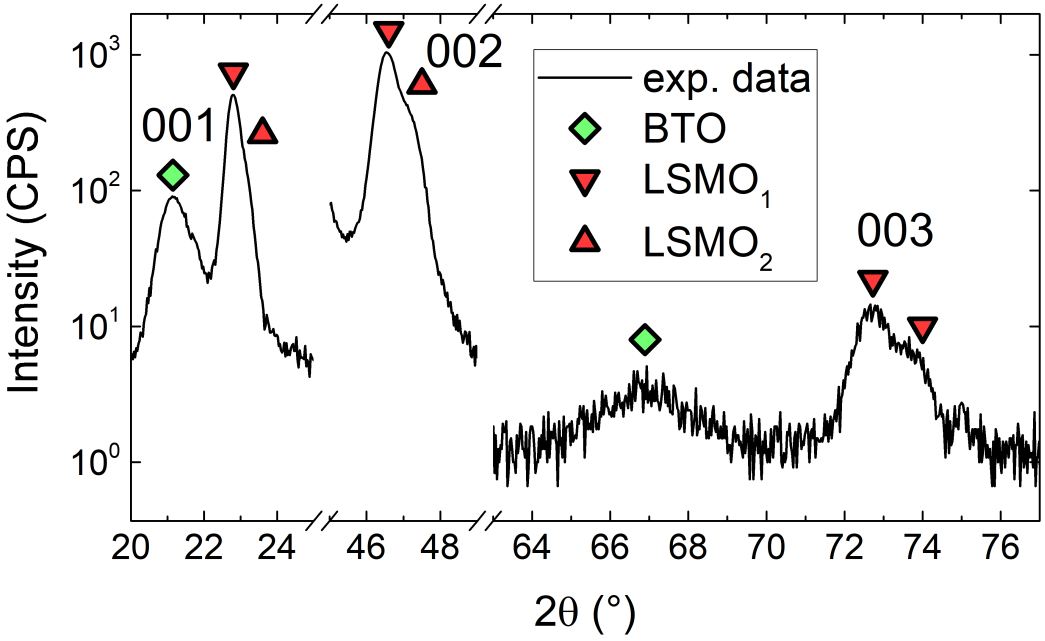

Figure 4.3: Symmetric θ-2θ diffraction pattern of the LSMO/BTO (thick)/LSMO//MgO heterostructure, measured with higher resolution.

is clearly seen that the LSMO peaks are asymmetric, with a bump on the right side, which is a sign of presence of at least two peaks. For a detailed analysis each $00l$ peak group was fitted with the sum of pseudo-Voigt curves: three peaks ($1 \times$ BTO and $2 \times$ LSMO) for 001 and 003 reflexes, and just two LSMO peaks for 002 (since out-of-plane BTO peak is very close to the MgO peak), for which case the slope of the MgO 002 peak was subtracted as baseline (**figure 4.4**). With the obtained 2θ values for each $00l$ reflection, the out-of-plane lattice parameters c were calculated using Bragg's law:

$$\frac{2\sin\theta}{\lambda} = \frac{l}{c},$$

where $\lambda = 1.54059$ Å - Cu K_α wavelength.

To evaluate the in-plane lattice parameters a of the films, an asymmetric geometry scan ($\varphi = 0°$, $\psi = 45°$) was performed around 101 reflection (fig.4.4). The fitting was made with two curves as well ($1 \times$BTO and $1 \times$LSMO), because here the second LSMO peak was indistinguishable. The reason for this may be that in this specific direction the interplanar spacing is the same for the two LSMO parts, which still results in different a parameters. In-plane parameter was calculated using the average c value, obtained earlier:

$$\frac{2\sin\theta}{\lambda} = \sqrt{\frac{1}{a^2} + \frac{1}{c^2}}.$$

Results of peak fitting are summarized in **table 4.2**. Uncertainty of c values arises from the fitting procedure and therefore is purely statistical, no other sources of error were considered. Uncertainty of a values includes both c uncertainty and 101 fitting uncertainty. Although, it should be significantly higher due to unaccounted

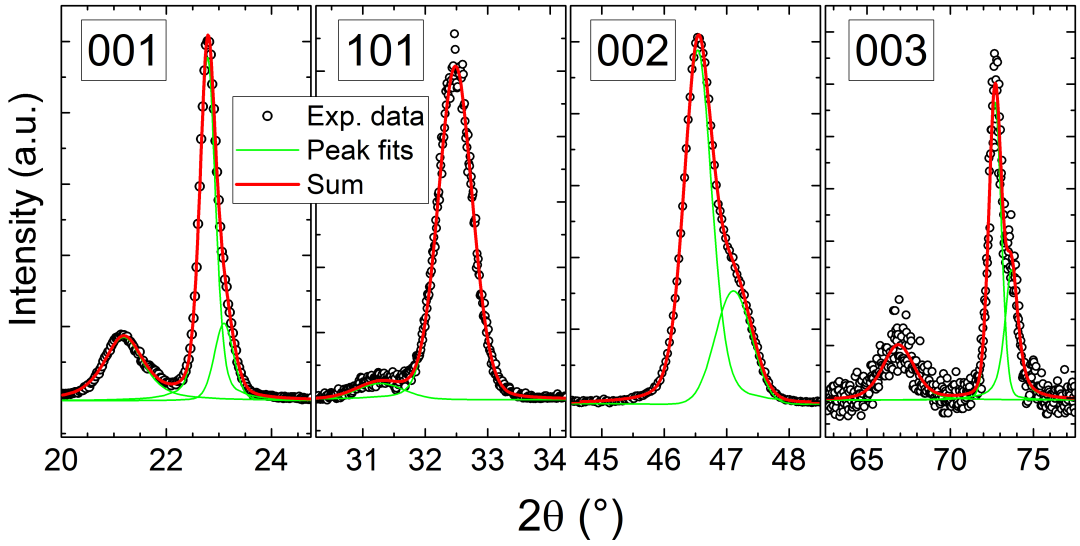

Figure 4.4: Fits of the 001, 002, 003 peaks, taken from fig.4.3) with baseline subtraction, and a 101 peak, measured in asymmetric geometry, from the MgO substrate sample with thick BTO barrier.

instrumental error: diffractometer was set to asymmetric geometry only once, based on the assumption of pseudo-cubic films' structure, while for more accurate measurement the 2θ, φ, ψ angles should have been adjusted iteratively. Thus, with this measurement we are not guaranteed to obtain the reciprocal space cut that contains the global maximum points of either of the peaks, and the uncertainty here is rather complicated to account.

◆ The performed analysis reveals that two distinct regions of LSMO are present in the heretostructure - bulk-like pseudo-cubic $LSMO_1$ and tetragonally distorted $LSMO_2$. The $LSMO_1$ share in all LSMO in the junction, calculated from integral peak intensity ratios, is equal to $72 \pm 6\%$. On the basis of the available data, two hypotheses about the nature of the observed LSMO phases separation can be made. Firstly, we may attribute this distinction to large lattice mismatch of LSMO with MgO (-8.1% for bulk values), that induces in-plane tensile strain (and out-of-plane compression) in the region of LSMO that is adjacent to MgO. According to this suggestion, upon the growth, the LSMO lattice should get slowly relaxed, leading to cubic-dominated region starting at some point of the bottom LSMO layer. As the

Table 4.2: Lattice parameters of the films grown on MgO substrate (thick BTO), calculated from the XRD fits of fig.4.4 (all values in Å).

Lattice parameter	BTO	$LSMO_1$	$LSMO_2$
c out-of-plane	4.19 ± 0.18	3.89 ± 0.06	3.85 ± 0.16
a in-plane	3.90 ± 0.19	3.89 ± 0.06	3.94 ± 0.17

second version, it can be assumed that the well separated diffraction peaks should be produced by spatially well separated layers (on the contrary to the continuous broadening, which generally should be the most probable result in case of the gradual strain relaxation along the film thickness), and thus correspond to individual top and bottom LSMO layers. This hypothesis is supported by the ratio of the peak intensities ($72 \pm 6\%$) that is close to the ratio of the nominal film thicknesses (75%), thus naturally associating the strained contribution with the top LSMO layer (which is the thinner one). We also should note here that for the case of thick BTO in the junctions grown on MgO the BTO tetragonality ratio c/a is equal to 1.074, what is traditionally associated with strong ferroelectric properties [152], but also could be caused by high concentration of oxygen vacancies [84, 153], which, however, was shown to not compromise entirely the ferroelectricity of BTO [154, 155].

◆ Locations of the film peaks in cases of STO and NSTO substrates are roughly the same as for MgO, with signs of the same asymmetric features of LSMO peaks. However, a similar detailed analysis is significantly hindered - fits get dominated by the high intensity substrate peak in all the $00l$ families. On the other hand, it was observed that 001 family in case of STO substrate demonstrates clear Laue oscillations (**figure 4.5**). A simple simulation was performed to compare with the experimental data and extract some structural parameters. Laue function was implemeted in the following form [156]:

$$I(Q) \propto \frac{\sin^2\left(\frac{N}{2}Qc\right)}{\sin^2\left(\frac{1}{2}Qc\right)},$$
$$Q = \frac{4\pi}{\lambda}\sin\theta,$$

where Q is the X-ray scattering vector, $\lambda = 1.5406$ Å is the Cu K_α radiation wavelength, N is the number of coherently diffracting unit cells. Damping of the X-rays at rough interfaces was accounted with a Debye-Waller-like factor $\exp\left(-(\Delta Q)^2\sigma^2\right)$ [137], where σ is the roughness and $\Delta Q = Q - 2\pi/c$. It turns out that a sum of three Laue function curves (associated with one BTO film and two LSMO contributions of some kind) and one pseudo-Voigt curve (associated with STO substrate) captures well all the features of the diffraction pattern, except the high order oscillations, which experimentally are below the noise level. Parameters derived from the fit are (**table 4.3**): $c_{\mathrm{BTO}} = 4.16$ Å, which is slightly smaller than in the MgO case, but still counts for a highly strained BTO film; $N_{\mathrm{BTO}} = 19$, what gives 7.9 nm of the coherently diffracting BTO layer and is very close to the nominal thickness; $c_{\mathrm{LSMO\ 1}} = 3.92$ Å, which is slightly larger than for the bulk; $N_{\mathrm{LSMO\ 1}} = 116$, what gives 45.7 nm of coherently diffracting LSMO in a large c part; $c_{\mathrm{LSMO\ 2}} = 3.85$ Å, which is slightly smaller than for the bulk (therefore, is a sign of the presence of the tensile strain of the film) and agrees with the previous reports [151], as well as the 3.89 Å c value of $LSMO_1$ layer in the case of MgO substrate; $N_{\mathrm{LSMO\ 2}} = 38$, giving 14.6 nm. The roughness of the layers is: $\sigma_{\mathrm{BTO}} = 1.5$ nm, $\sigma_{\mathrm{LSMO\ 1}} = 0.5$ nm, $\sigma_{\mathrm{LSMO\ 2}} = 3$ nm. Since the interference here is a result of X-rays reflecting from each lattice plane, the physical meaning of the roughness here is an average on all contributing atomic layers - in contrast to XRR, for example, where it is a statistical characteristic of the film's surface/interface deviations from the perfect plane [137]. Its use is absolutely necessary to eliminate the higher interference orders of the BTO and $LSMO_2$ peaks, which otherwise would be quite wide, due to high widths of the

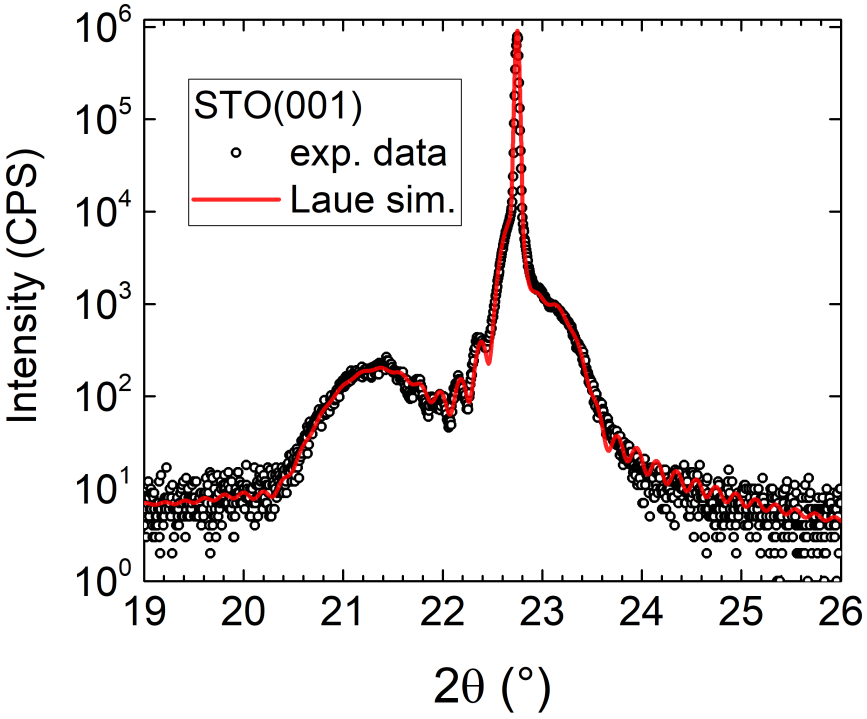

Figure 4.5: Diffraction pattern of the thick barrier junction on STO substrate in 001 region (black line, taken from 4.2) and simulation with three Laue function curves and one pseudo-Voigt (red line shows the sum).

Table 4.3: Parameters of the Laue oscillations simulation for thick barrier STO substrate sample: t - thickness, c - out-of-plane lattice parameter, σ - roughness.

Layer	t (nm)	c (Å)	σ (nm)
BTO	7.9	4.16	1.5
$LSMO_1$	45.7	3.92	0.5
$LSMO_2$	14.6	3.85	3.0

main orders (which are determined unambiguously), and, therefore, clearly visible in the diffractograms. Instead, experimentally they are not seen on the shoulders of these peaks on the left (19°-20°) and on the right (24°-26°), respectively. Thus, the distinct oscillations from 21.5° to 23.2° may only be formed by a $LSMO_1$ contribution. It must also be noted that the coherent interference thicknesses of the BTO and two LSMO contributions are remarkably close to the nominal layer thicknesses, so it is a strong evidence that allows to associate presented here $LSMO_1$ and $LSMO_2$ parts with the bottom and top LSMO layers. Therefore, the difference in the roughness values may indicate that the bottom layer is of higher crystalline quality than the top one (possibly due to proximity to the substrate, or higher thickness), i.e. shows minor deviations of lattice parameter throughout the planes and/or fewer structural defects. In case of NSTO substrate, some signs of the Laue oscillations around 001 peak family are seen too, with very similar picture, but of lower quality, which does not allow for an accurate reproduction of the observed features.

◆ XRD was performed on the junctions with the thin BTO barrier as well (**figure 4.6**). The peak positions are almost the same as for the thick barrier samples*. The asymmetry of LSMO peaks is however less pronounced (while the second contribution in the form of a bump on the right side is present, but its intensity is much lower).

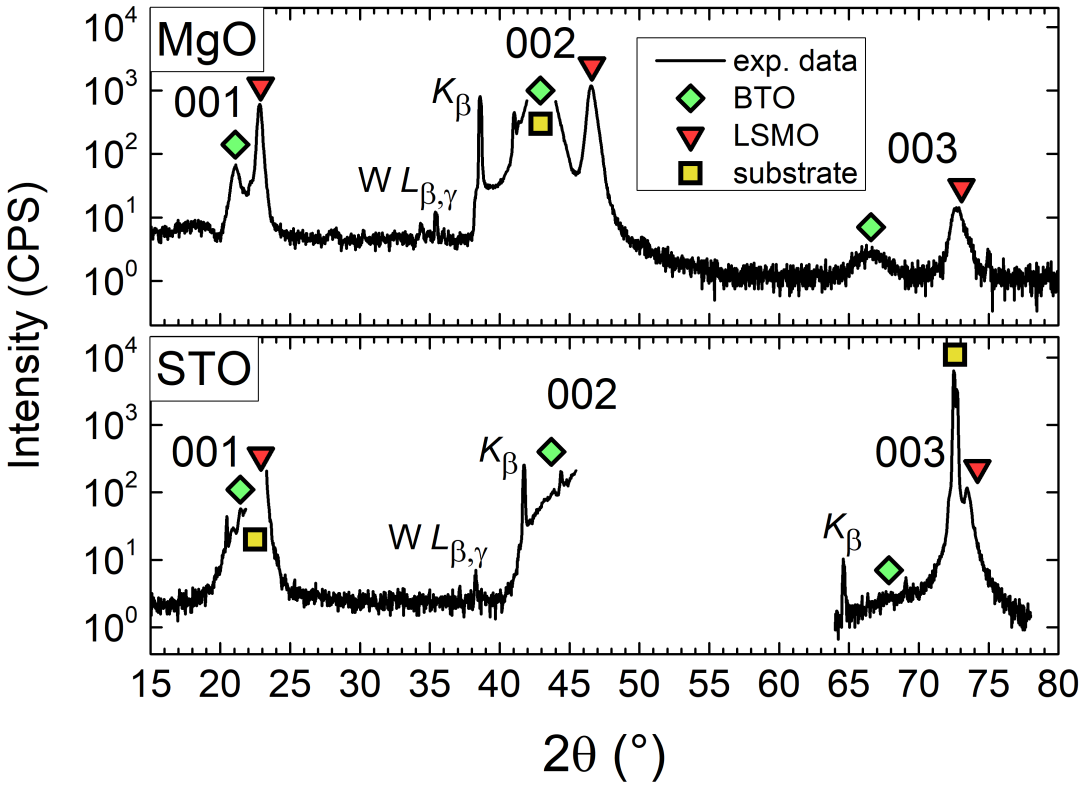

Figure 4.6: Symmetric θ-2θ diffraction patterns of the LSMO/BTO (thin)/LSMO heterostructures grown on $SrTiO_3$ and MgO substrates (Feb STO and Feb MgO samples).

◆ Another important result was obtained by reciprocal space mapping (RSM). RSM around 103 reflections for MgO substrate sample allows to visualize the distribution of lattice spacing for LSMO in the out-of-plane (Q_z) and in-plane (Q_x) directions (**figure 4.7**). It is observed that the spread of the in-plane parameter of the main LSMO peak (centered at $c = 3.91$ Å and $a = 3.85$ Å) is more than twice higher than of the out-of-plane one. A distinct small second peak is observed at a slightly shifted position - centered at $c = 3.87$ Å and $a = 3.84$ Å, originating from $LSMO_2$ top layer part. A small symmetric BTO 103 peak is also seen.

◆ Overall, it may be concluded that the films of the LSMO/BTO/LSMO junctions, grown on all three substrate types, are of high structural quality. In cases of STO and NSTO a high quality epitaxy is confirmed by the observation of Laue oscillations, while on the MgO substrate the films are likely epitaxial as well (or, at the very

*Additional peaks arise from parasitic X-ray radiation lines: Cu K_β was not cut out with the slits to increase the intensity, and various W L lines indicate degradation of the X-ray tube.

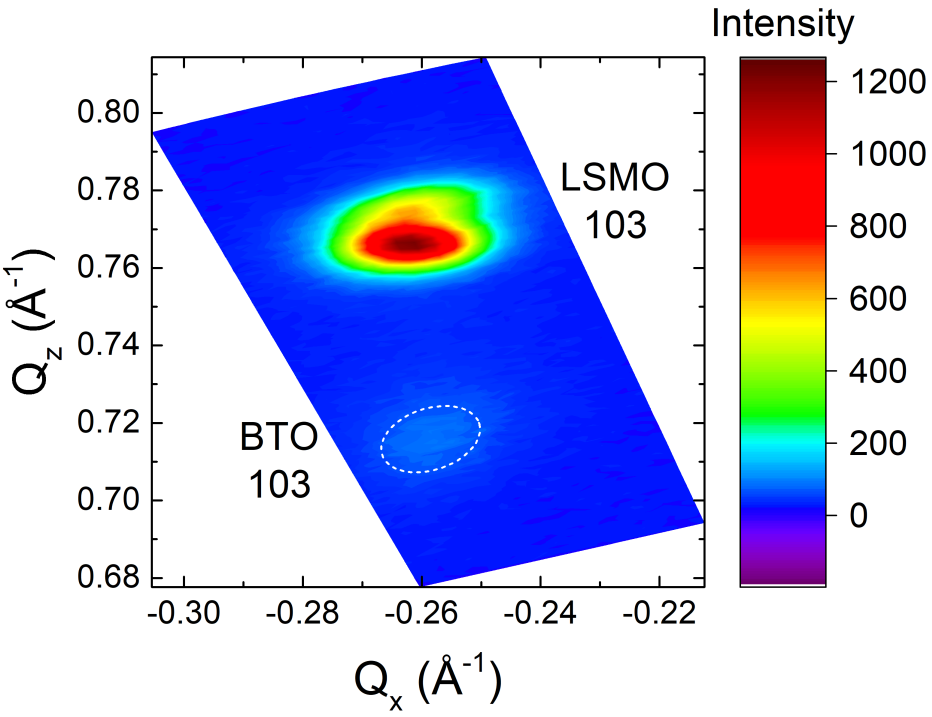

Figure 4.7: RSM in the region of 103 reflections from thick barrier sample grown on MgO.

least, highly textured in ⟨001⟩ direction, with no peaks of other directions observed either out-of-plane, or in-plane) with two separate LSMO contributions, one of which is highly strained (in-plane tension). Also, the BTO film is highly strained in the tetragonal direction.

4.2.3 *X-ray reflectometry*

XRR allowed to estimate the thicknesses of each layer and to acquire some information on the quality of the interfaces, since it is the multiple reflections at the film interfaces that generate the interference pattern in this method. The experiments were performed on the samples with thick barrier (**figure 4.8**).

As the first observation, it is seen that the visibility of the interference pattern is rather low, which is likely caused by the rough interfaces. Simulation of the experimental curves with three layers did not yield a satisfactory convergence, both with and without roughness. Therefore, based on the earlier research that suggests the high likelihood of LSMO/BTO intermixed layer formation in the similar systems, simulation was made with additional interlayers of LSMO/BTO, BTO/LSMO and LSMO/STO (simulation converged at zero thickness of LSMO/MgO mixed layer). With this adjustment the simulations successfully reproduced experimental data, the parameters are presented in the **table 4.4**.

The intermixed LSMO/BTO layers are in average about 2 nm thick, with roughness of comparable value. The total thicknesses of the layers are quite close to nominal values and XRD analysis based on Laue oscillation, except for MgO substrate sample, where all three thicknesses are slightly smaller, which could be due to positioning of the substrate aside from the maximum of the matter flow during growth.

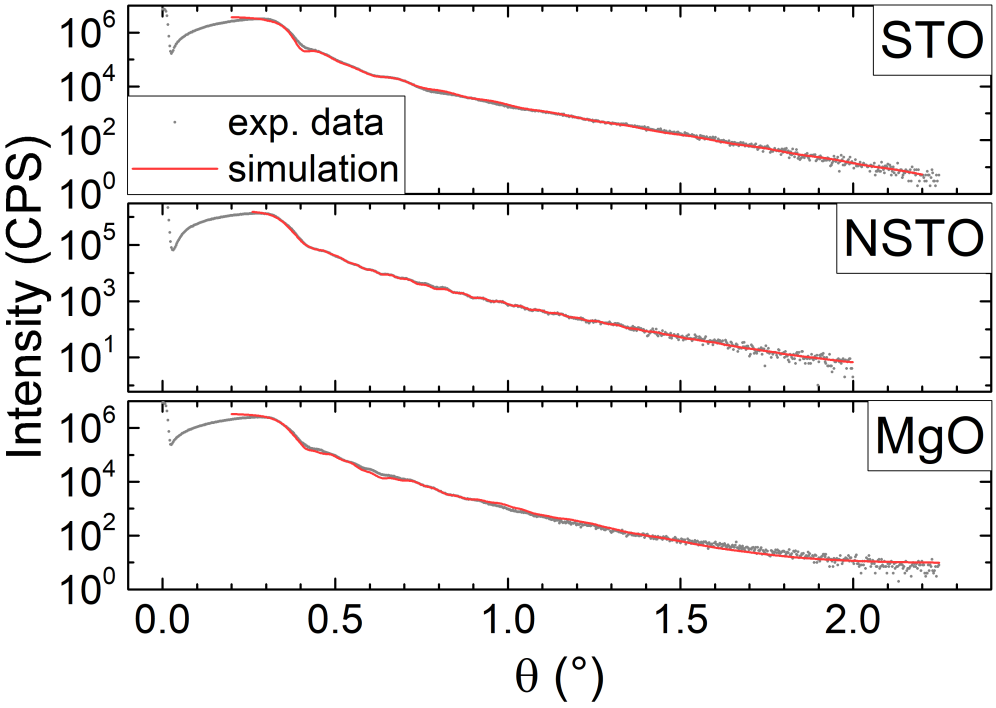

Figure 4.8: XRR curves of the thick barrier samples (grey circles) together with the simulations (red lines).

Table 4.4: Summary table of the film thicknesses, obtained by XRR simulation (thick BTO samples). All values in nm, t - thickness, σ - roughness.

Layer \ Substrate	STO		NSTO		MgO	
	t	σ	t	σ	t	σ
LSMO top	18.7	2.3	16.9	3.0	16.8	1.2
LSMO/BTO	3.2	0.7	1.7	2.3	2.2	2.4
BTO	7.0	1.7	9.4	0.8	6.2	2.5
BTO/LSMO	1.7	1.9	1.9	2.6	1.5	2.0
LSMO bottom	41.1	2.6	45.9	1.2	37.8	1.4
LSMO/substrate	1.6	2.9	0.8	1.8	-	-

4.2.4 *Rutherford backscattering spectrometry*

RBS allowed to estimate the thicknesses of the layers independently. Experimental spectra, obtained for thick barrier samples, are presented in **figure 4.9**. Thin barrier spectra are qualitatively similar. Due to many overlaps of the elemental lines of the materials in our samples, small variations of composition and (to a lesser extent) thickness often insignificantly affect the final simulation curve, which increases the uncertainty of both quantities. Within the reasonable error estimation range, simulated compositions of the layers were found to correspond to the nominal target compositions. The thickness values for thick barrier junctions roughly correlate with XRR data (interfacial mixed layers are not included into the simulation due to low sensitivity of RBS to the interface imperfections). On the other hand, the thickness values of all the layers of the thin barrier samples are more significantly dispersed,

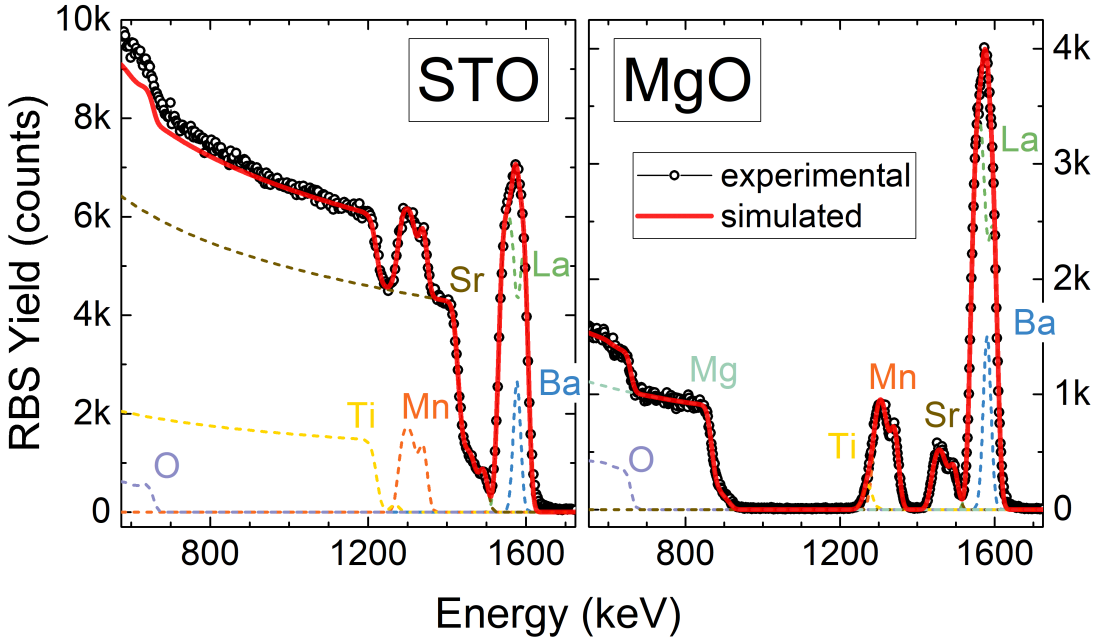

Figure 4.9: RBS spectra of thick barrier junctions grown on STO and MgO (NSTO spectrum is similar to STO). Colored dashed lines show elemental spectra.

than in the thick barrier cases (**table 4.5**). This may be caused by variations in the substrate positioning with respect to the PLD plume during the growth, as suggested for XRR above, and by the non-uniformity of the layer thicknesses over the sample area, since RBS probes smaller sample region than XRR.

The case of Feb STO sample should be highlighted particularly. The aforementioned consideration on the substrate positioning during growth are valid, if the thickness deviations from sample to sample are proportional for each layer. As an alternative hypothesis, the changes in deposition rate during the growth could affect the thickness as well. However, since the sample location on the holder is fixed, the result of such changes would be seen in each sample, proportionally to the total film thickness. Instead, for the Feb STO sample, while the BTO and bottom LSMO thicknesses are approximately twice smaller than nominally, the top LSMO thickness is almost as thick as nominally - and for Feb MgO sample this anomally applies only for the BTO layer. This observation sets the limit of accuracy for RBS method. While it does not allow to neglect this measurement completely, complementary measurements, which, for example, preserve the 1:2-1:3 thickness ratio for top LSMO:bottom LSMO layers of the Feb STO sample, should be prioritized.

Table 4.5: Summary table of the film thicknesses, obtained by RBS simulation (thick and thin BTO samples). All values in nm.

Layer \ Sample	July STO	July NSTO	July MgO	Feb STO	Feb MgO	Mar STO	Mar MgO
LSMO top	21.7	22.0	20.4	18.8	22.0	23.2	19.3
BTO	8.1	8.6	8.0	1.9	2.0	5.8	3.2
LSMO bottom	45.0	47.8	41.3	22.0	40.1	49.2	43.8

4.2.5 *Cross-sectional microscopy*

TEM images allowed to visualize the junction structure and verify some data and hypotheses, mentioned above.

Measurements on the thin barrier sample show that the junctions, grown on STO, indeed are epitaxial throughout the whole film thickness (**figure 4.10**). In the bright field image (fig. 4.10a,b) distinction between BTO and LSMO may be made mainly through presence of the interfaces. Intensity profile (fig. 4.10c), integrated from the region, indicated in (fig. 4.10a), makes the BTO layer distinguishable and shows that the top LSMO/BTO interface is abrupt, while the bottom one is gradual on the side of LSMO. The latter is a sign of LSMO/BTO intermixing or oxygen vacancy accumulation. HAADF imaging may provide the intensity contrast and allows to visually distinguish the layers (fig. 4.10d). Intensity profile (fig. 4.10e) provides additional information. Resulting thicknesses of top LSMO/BTO/bottom LSMO are equal to 10.3 nm/2.5 nm (averaged)/25.8 nm, respectively. Region of the bottom LSMO with the gradual transition from the interface is 1.6 nm thick. TEM images give thickness values closer to the expected ratio between top and bottom LSMO films, than RBS for the same sample, and thus has to be considered more reliable and prioritized over RBS, as suggested in the corresponding section. While on the other hand, the region of the sample, overviewed by TEM, is less than 100 nm in lateral size and thus only shows a very local picture, in contrast to RBS (μm-mm scale of the ion beam spot) and, especially, XRR (the whole sample, mm-cm scale), accuracy of the TEM method in the local scale is significantly higher, since

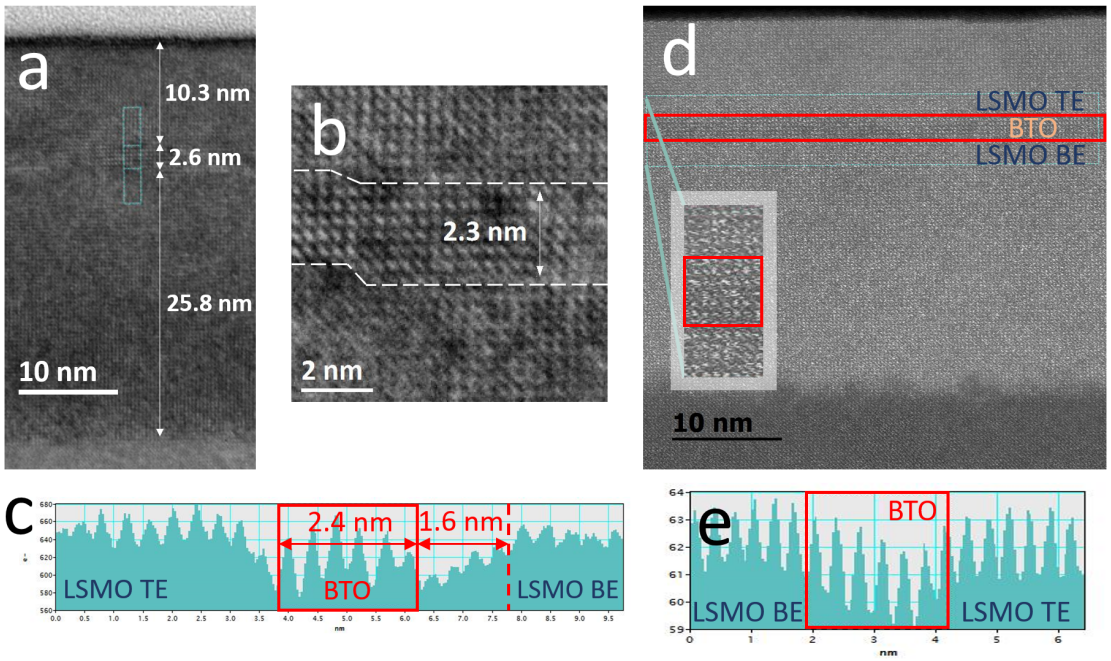

Figure 4.10: TEM of Feb STO sample cross-section. a) Bright field image of the cross-section. b) High resolution bright field image of the cross-section. c) Depth dependence of atomic intensity, integrated horizontally in region, highlighted in (a). d) HAADF image of the cross-section. e) Depth dependence of atomic intensity, integrated horizontally in region, highlighted in (d).

it involves only direct measurements, instead of complicated multi-parameter curve fitting. The measured thickness values at a particular point of the sample confirms the hypothesis of the non-uniform film thickness at least over the Feb STO sample, since the Feb MgO sample, grown in the same process in parallel, shows higher layer thicknesses, closer to the nominal. Thus, while accurate average layer thickness determination has not been completed with this method, a good estimation has been obtained, and objectively high uncertainty of the value has to be taken into account in the further analysis.

In more detail the intermixed layers are assessed through the analysis of Mn ions chemical state via electron energy loss spectroscopy (EELS). Spectra were recorded at different heights across the junction with a thick BTO barrier to illustrate the interfaces (**figure 4.11a**). Extracted spectra close to Mn $L_{2,3}$ edge in LSMO at various distances from both interfaces with BTO are shown in **figure 4.11b**. Black vertical lines in the figure indicate positions of Mn lines in the bulk-like state of LSMO, while red lines indicate positions of the shifted lines. It is seen that far from both interfaces Mn $L_{2,3}$ lines are in the bulk-like state, and the closer to the interfaces, the more lines in both top and bottom LSMO shift to the lower energies. This chemical shift is associated with reduction of Mn ions in LSMO close to

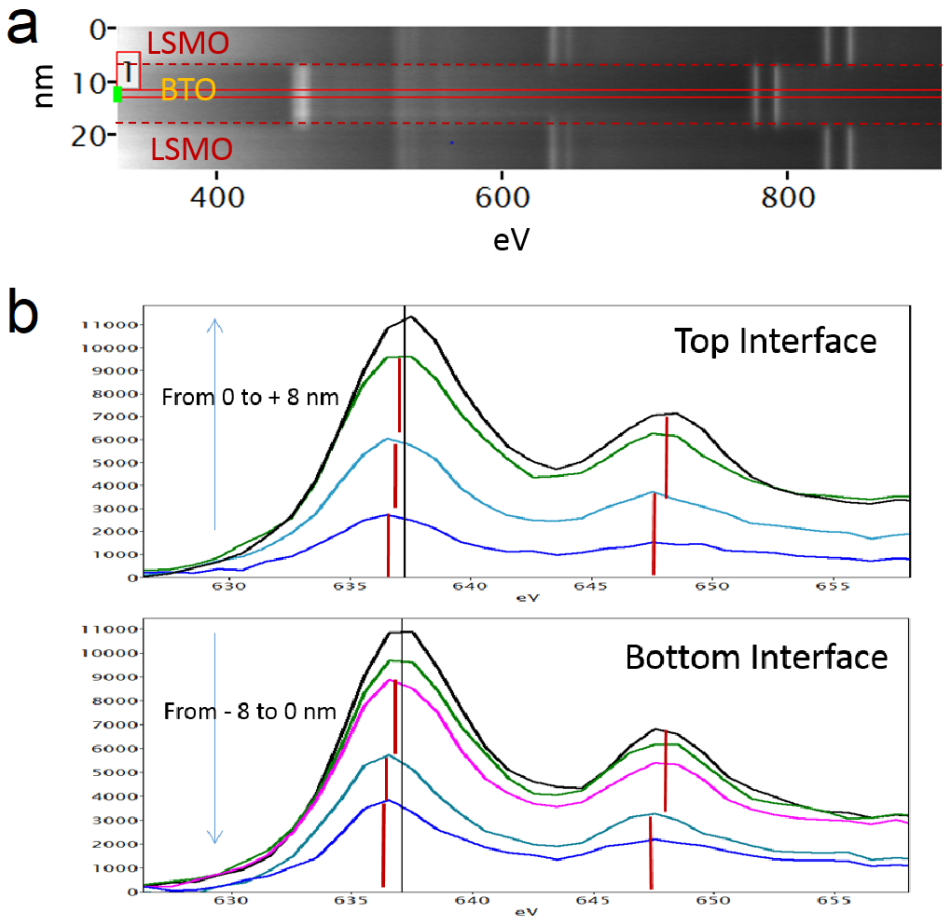

Figure 4.11: EELS spectra from a thick barrier sample, recorded at different heights. a) The image corresponds to 90 spectra from 350 to 900 eV, acquired at different heights across the junction. b) Results of integration of series of 5 spectra, measured close to Mn $L_{2,3}$ edge.

the surface/interface [64, 132], which may happen due to interface mixing with the adjacent material or accumulation of oxygen vacancies. Thus, we see the regions of reduced Mn ions in both LSMO layers close to the interfaces with BTO, with the bottom one more pronounced than the top, confirming high intermixing of the bottom interface.

4.3 Magnetic properties

4.3.1 *Thick barrier samples*

Magnetic properties of both STO and MgO substrate samples with thick BTO barrier were assessed with vibrating sample magnetometry. First measurements were made at an in-plane orientation of magnetic field to the sample surface, aligned additionally along the side of the substrate, i.e. ⟨100⟩ or ⟨010⟩ crystallographic axes. Magnetization loops for 50 K and 300 K may be seen in the **figure 4.12**.

We may clearly observe in case of MgO substrate that the magnetization loop has two distinct contributions with different coercive fields. Hereinafter we will refer to the larger coercivity component as "hard", and to smaller one - as "soft". In case of STO some weak hints of the same effect are also observed, but significantly less pronounced (bumps close to saturation at ±150 Oe, in the I and III quadrants of the graph). Taking this observation into account, the saturation magnetization M_s (**figure 4.13**), coercive field H_c values and relative contribution magnitudes (**figure 4.14**) were extracted for all the loops, measured in a wide range of temperatures.

$M_s(T)$ extracted data was fitted for both MgO and STO substrate samples with

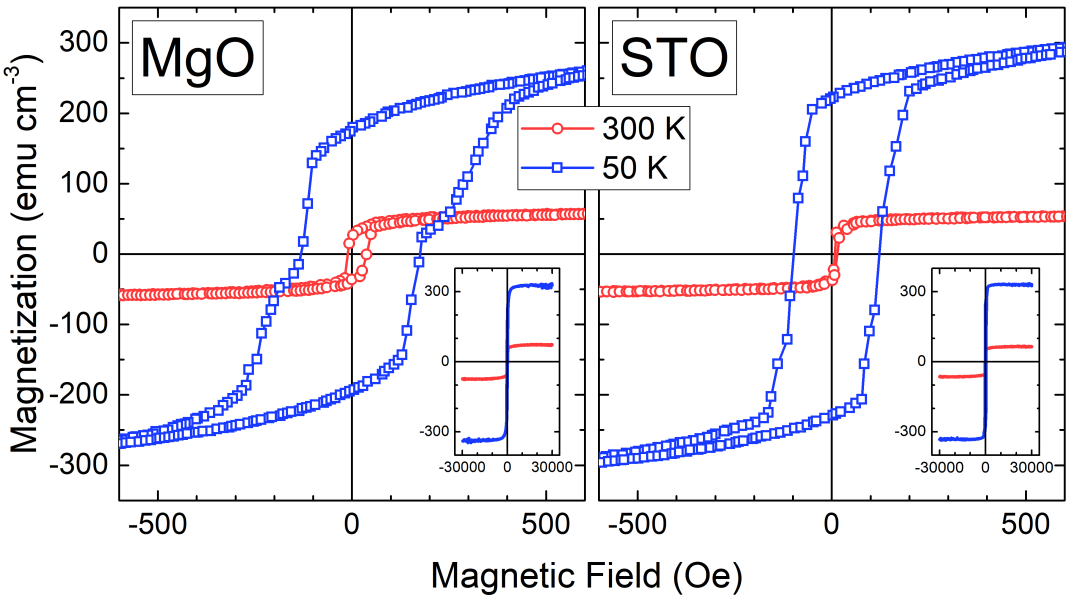

Figure 4.12: $M(H)$ loops of thick barrier junctions grown on MgO and STO, measured at 50 K (blue squares) and 300 K (red circles). Insets show the saturation region.

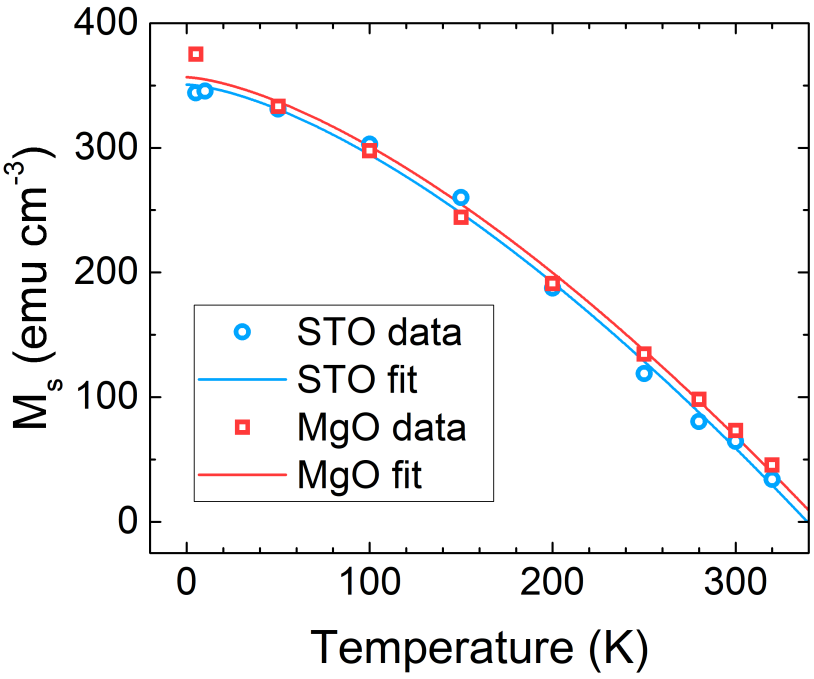

Figure 4.13: Temperature dependency of M_s, extracted from magnetization loops of MgO and STO substrate samples with thick BTO. Fits were performed with Bloch 3/2 law.

the Bloch 3/2 law:

$$M_s(T) = M_s(0)\left(1 - \left(\frac{T}{T_C}\right)^{3/2}\right),$$

where T_C is a Curie temperature. For MgO T_C was found to be equal to 346 K, $M_s(0) = 357$ emu cm^{-3}, for STO $T_C = 339$ K, $M_s = 351$ emu cm^{-3}.

It should be noted here that saturation magnetization in these two cases is significantly lower than expected for a perfectly ferromagnetic LSMO thin film. We can make a simple estimation of M_s as follows. Ferromagnetism in LSMO is achieved through double exchange chains Mn^{3+}–O^{2-}–Mn^{4+}, as was discussed earlier. Mn^{3+} and Mn^{4+} ions have only d-electrons on the outer shell [157], which leads to electronic configurations [Ar]$3d^4$ and [Ar]$3d^3$, respectively. Magnetic moments of corresponding ions are produced purely by spin angular momenta, since the orbital angular momenta contributions are suppressed for the transition metals' ions [158], and are equal to $4\mu_B$ and $3\mu_B$, respectively. With 0.67 La content in LSMO, average magnetic moment of Mn ions of $3.67\mu_B$ allows to obtain the value of 577.7 emu cm^{-3} for LSMO saturation magnetization, if for unit cell volume calculation we consider the pseudo-cubic lattice parameter value of 3.89 Å, as discussed in the XRD section. In the best cases, magnetization of thin-film LSMO is equal to theoretically estimated value [129, 159], although values, similar to our current thick BTO barrier samples, were reported earlier as well [160, 161]. Our M_s values were calculated by dividing the measured total magnetic moment of the sample (with the substrate contribution subtracted) by the total thickness of LSMO layers (verified via RBS, XRR and TEM earlier). The discrepancy from the ideal value suggests that in our case not the whole film is ordered ferromagnetically or with the uniform magnetization. The

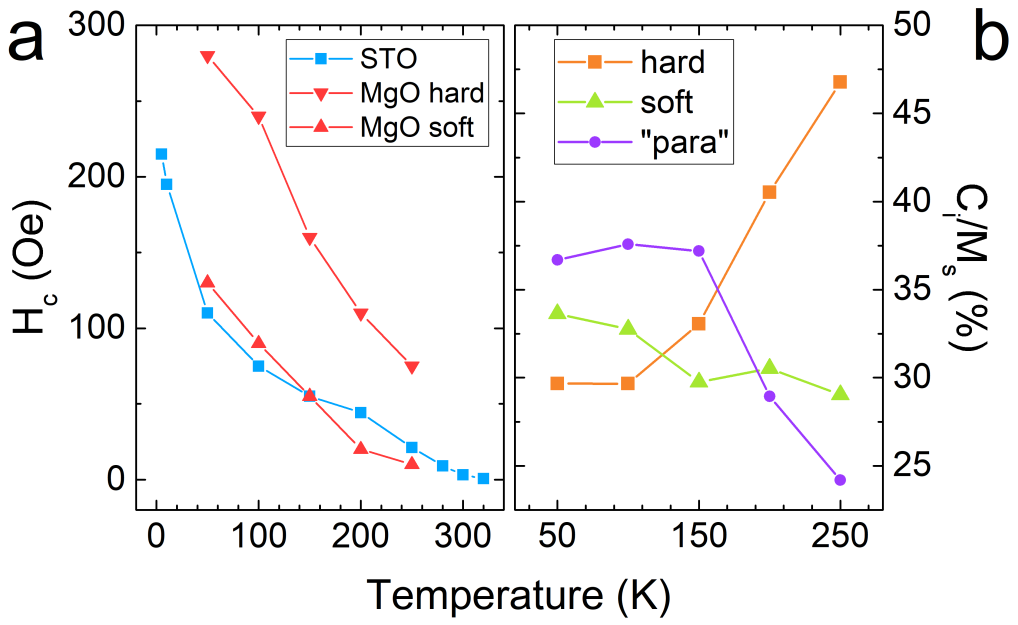

Figure 4.14: Temperature dependencies of H_c (a) for both MgO and STO samples and relative magnetic moment of the magnetization components (b) of MgO sample. Data for MgO was extracted from the magnetization loop fits with Langevin curves.

problem of partial magnetization loss in LSMO is widely studied and is conventionally connected to the existence of magnetically "dead" layers [101, 103, 104, 162]. Layers with reduced or completely zero magnetization tend to form at the LSMO film surface or interfaces (both with the layers below or above it) due to structural imperfections or oxygen deficit.

◆ To extract the coercive field values and component magnitudes with some level of accuracy in cases, when in MgO substrate sample data two clear contributions are seen, fitting of the loops was performed with the sum of Langevin function curves:

$$M(H) = \sum_i C_i L\left(\frac{H \mp H_{ci} - H_{bi}}{s_i}\right),$$

$$L(x) = \coth(x) - \frac{1}{x},$$

where i is the component index, C - magnetic moment of the i^{th} component of the total $M(H)$, divided by the total LSMO volume (thus sum of C_i gives the saturation magnetization of the whole heterostructure), H_c is the coercive field (signs differ for the branches of the loop), H_b is the bias field (seen as the shift of the loop along the H axis) and s is the scale parameter[†]. Presence of H_b may be explained by the residual currents in the superconducting magnet coil of the PPMS (of the order of ∼10 Oe).

Extracted values of H_c follow a qualitatively similar law, decreasing non-linearly with the T increase. In case of MgO substrate, hard and soft contributions are clearly distinct, with soft part demonstrating behavior very close to STO substrate sample.

[†] $s = kT/\mu$, where μ is the magnetic moment of the gas particle in Langevin paramagnetic gas model. The model likely does not apply in our case, here it is used only for curve parameter extraction.

We must specify that this method is valid in our case only for extraction of the very limited amount of information from the $M(H)$ curves with better accuracy than manually, and is not an attempt of hysteresis simulation, like Stoner-Wohlfarth model or other more elaborate ones. Thus, it is rather complicated to consider the gradual saturation from ∼100 Oe up to ∼10000 Oe. Within this simple approach, in order to fit the whole $M(H)$ curve accurately, the third Langevin curve has to be added to the first two. Although, assigning this third contribution to one of the LSMO layers - or two, in some proportion - is not obvious without some additional considerations. For example, in case of MgO substrate sample with thick BTO barrier, the necessary third contribution has to be paramagnetic ($H_c = 0$). In the fig.4.14b we may see the temperature dependence of the components' magnetic moments in relative units. Behavior of the contributions is significantly different: soft part is decreasing slightly with T increase, while hard part grows substantially. Interestingly, paramagnetic contribution behaves closely to the soft one. This implies that soft and "para" components are magnetically coupled with each other stronger than with the hard one individually. Moreover, at 50 K, where magnetization is close to the maximum possible M_s(0 K), soft and "para" contributions combined make up for ∼70% of the total magnetic moment, which is quite close to the relative weight of the bottom LSMO layer. Since the inverse proportionality of coercivity to thickness is well known for LSMO thin films [163], we may infer that the "para" and soft contributions in this case should correspond to the bottom LSMO, and the hard contribution - to the top one. The necessity of two Langevin curves for description of bottom LSMO layer behavior likely indicates the complexity of magnetic anisotropy in it due to structural imperfections that may occur at the LSMO/MgO interface.

◆ An additional series of measurements was performed on MgO substrate sample to better resolve the region near coercive fields (**figure 4.15**). Sample was manually rotated in-plane in order to maximize the distinction between hard and soft contributions. The resulting rotation angle turned out to be equal to 34° from one of the sample sides (which does not necessary align with ⟨100⟩ or ⟨010⟩ directions, since the sample was additionally cut after growth, which could induce some miscut angle). Here two contributions are clearly distinguished (fig. 4.15a).

A similar procedure, involving Langevin function fitting, was performed to extract the temperature dependencies of M_s (fig. 4.15b), H_c and C_i (**figure 4.16**). It may be seen that coercive field behavior is qualitatively the same, while its values are slightly higher than in the case of alignment to the sample sides. This indicates the presence of easy axes along ⟨100⟩ and ⟨010⟩ directions, and hard axes along ⟨110⟩ and $\langle 1\bar{1}0\rangle$, which is a typical situation in strained or oxygen deficient LSMO films [164]. Temperature behavior of C_i well reproduces the case of sample side alignment, but with paramagnetic part being slightly smaller. This supports the assumption that soft and para contributions combined correspond to the bottom LSMO layer, while the hard contribution to the top LSMO. Such features in the temperature behavior of the partial magnetic moments of the contributions may be explained as follows. It is known that Curie temperature and magnetization of LSMO films thinner than 30 u.c. (12 nm) strongly depend on the thickness [111, 165]. This means that the complex magnetic structure of one of the layers may result in a T_C that would differ from the other layer - thus, synchronous temperature behavior of the contribution's magnetic moments C_i may be a sign that the contributions actually correspond to different regions of the same LSMO layer.

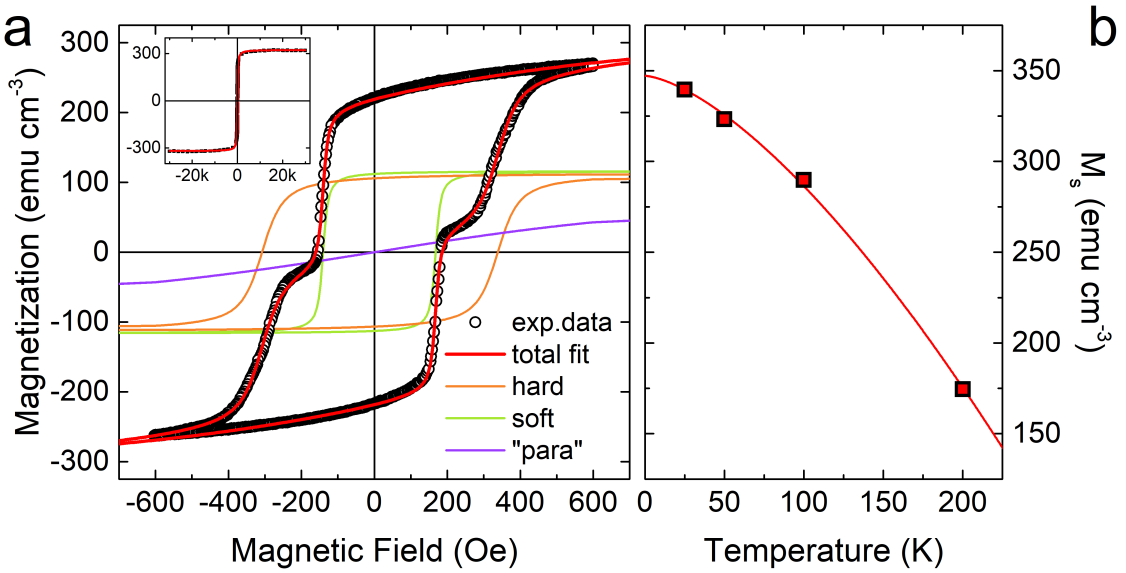

Figure 4.15: a) Magnetization loop of the LSMO/BTO/LSMO//MgO heterostructure at 50 K, measured at the optimized orientation. Inset shows the saturation region. Colored lines show the components of the Langevin function fit and their sum. b) Temperature dependence of total saturation magnetization with a Bloch 3/2 law fit.

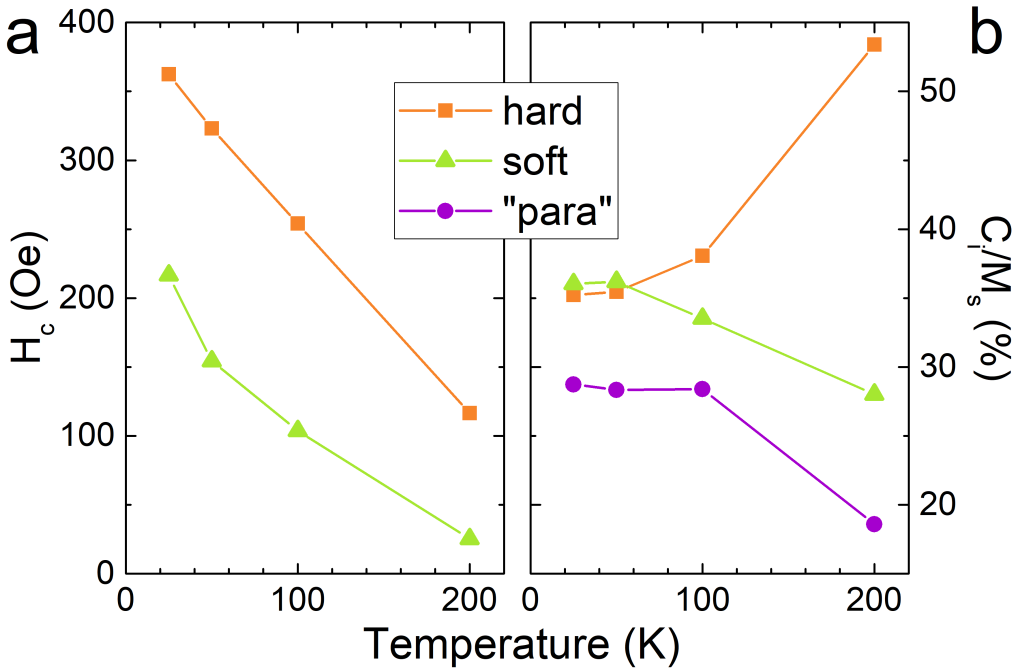

Figure 4.16: Temperature dependencies of H_c (a) and relative magnetic moment of the magnetization components (b) of thick barrier MgO substrate sample, measured at the optimized orientation and extracted from the magnetization loop fits with Langevin curves.

4.3.2 *Thin barrier samples*

The thin BTO samples (of the February 2021 growth) were magnetically characterized only in standard geometry - in-plane magnetic field application, aligned along the sample edge.

The MgO substrate sample with thin BTO barrier demonstrates characteristics, very similar to the corresponding thick barrier sample (**figure 4.17**). Coercive field temperature behavior is qualitatively the same, although the absolute values at low T are slightly lower. The $M(T)$ fit yields higher values of both $M_s(0)$ and T_C - 405 vs 357 emu cm^{-3}, and 386 vs 346 K, respectively. However, the $M_s(0)$ value is still significantly lower than theoretically estimated, thus the same argument about reduced volume of fully magnetized films remains valid.

Here the third (also paramagnetic) contribution cannot be unambiguously assigned to any of the LSMO layers, since both $C_i(T)$ behavior and H_c are not similar to just one of the main contributions (**figure 4.18**). C_i ratio is not changing at all in the major part of the T range. Ratio of soft to hard contributions at low T is 45% : 25%, which is very close to the thickness ratio of bottom to top LSMO for this sample, measured with RBS. Therefore, it is natural to assign the third contribution to both the soft and the hard ones, and potentially to the dead layers at the LSMO/BTO interfaces as well.

◆ The case of STO substrate with thin BTO is drastically different from the thick BTO (**figure 4.19**). Coercive fields in this sample are especially low (**figure 4.20a**), comparable to residual field of the superconducting coil. Starting from 90 K and above, coercive field of the soft part is effectively negative, and from 200 K - of the hard part as well. This effect occurs due to coercivity becoming even smaller than the residual fields, what shifts the whole branches of the $M(T)$ loop in direction of the recent large magnetic field, and makes them switch the side, on which it crosses

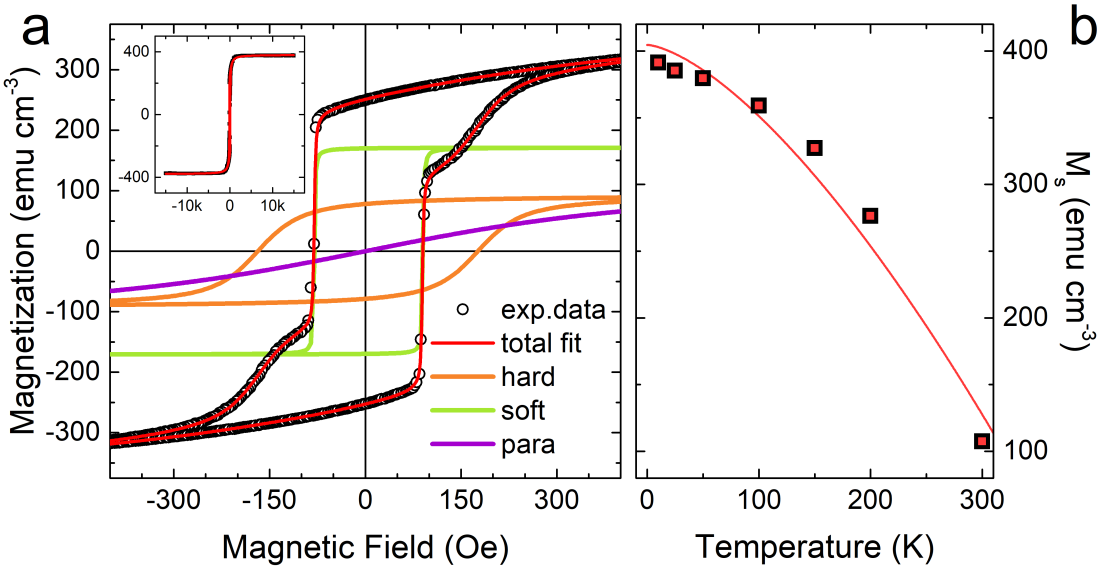

Figure 4.17: a) Magnetization loop of the LSMO/BTO (thin)/LSMO//MgO heterostructure at 50 K. Inset shows the saturation region. Colored lines show the components of the Langevin function fit and their sum. b) Temperature dependence of total saturation magnetization with a Bloch 3/2 law fit.

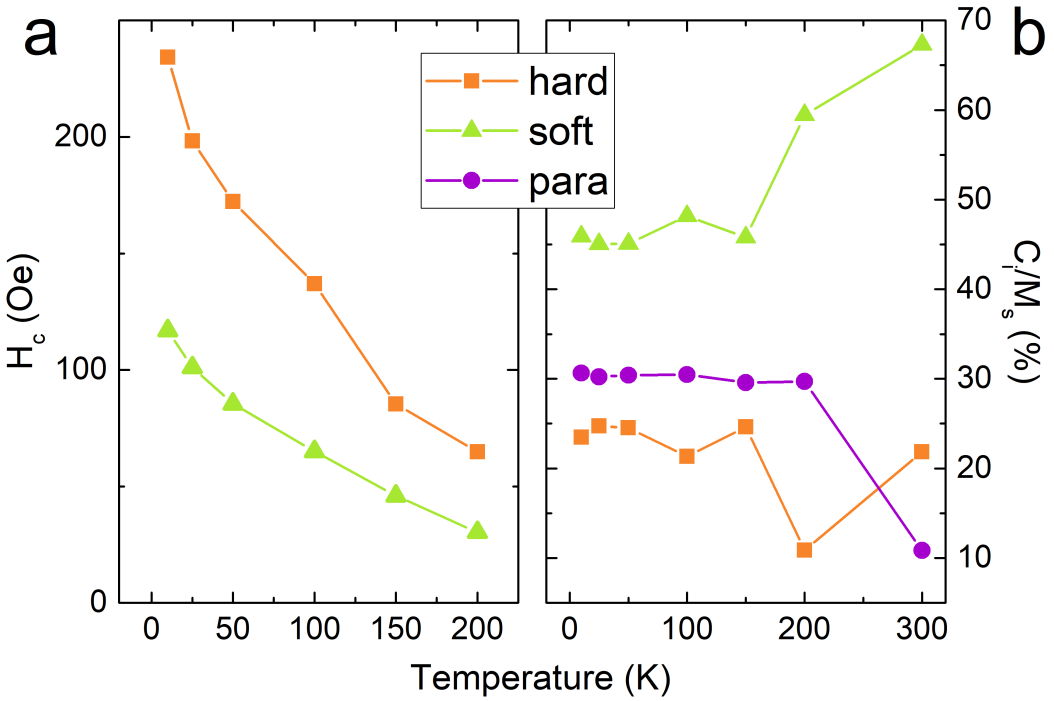

Figure 4.18: Temperature dependencies of H_c (a) and relative magnetic moment of the magnetization components (b) of thin barrier MgO substrate sample, extracted from the magnetization loop fits with Langevin curves.

the magnetic field axis. However, the Langevin curve fitting still may be performed, and the values of H_c and C_i may be extracted. We should keep in mind that in this case all the H_c values are shifted down by the coil residual field (of the order of 10 Oe), and only the analysis of relative changes with T makes sense.

The third contribution in this case has the same coercive field as the hard contribution. Necessity of the second hard component is governed by the different scale parameter values s_i, which explicitly depends only on T and the value of elementary magnetic moment of the subsystem - thus, it may indicate that, for example, there could be two regions of significantly different mean domain size in the hard region. Analyzing the dependence of partial magnetic moments of the components (**figure 4.20b**), we observe that the two hard contributions indeed evolve with temperature synchronously. Combining hard_1 and hard_2 parts together at T below 50 K, where all the contributions are far from corresponding partial T_C, we obtain the ratio of magnetic moments of the soft and hard contributions of 55% : 45%. This is close to the thickness ratio of bottom to top LSMO, measured with RBS on this sample - although, not as close to the TEM value, which was considered more accurate previously.

Another difference for this sample is the value of $M_s(0)$, which equals 554 emu cm^{-3}, if calculated using the film thicknesses, measured by TEM. This is significantly higher and closer to theoretical estimation than the other samples. Also, T_C is slightly higher than in case of thick BTO barrier sample and STO substrate - 361 vs 339 K earlier.

◆ Overall conclusion of the magnetic characterization is as follows: the contributions of the top and bottom LSMO layers to the total magnetization are well distinguishable in the majority of samples and roughly correspond to the thickness

ratio value; total magnetization of the sample varies from sample to sample, but generally does not reach the theoretically expected value, which could be a sign of structural or chemical imperfections of LSMO layers, presence of dead layers at the interfaces. Magnetization value is still relatively high, compared to various literature reports. Curie temperature of the samples is consistently higher than RT.

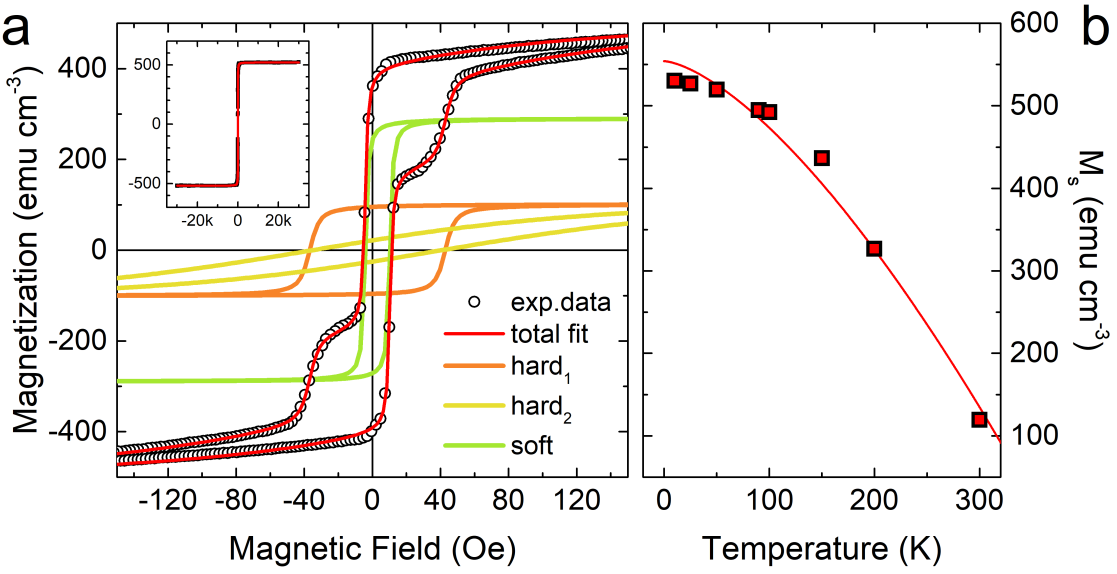

Figure 4.19: a) Magnetization loop of the LSMO/BTO (thin)/LSMO//STO heterostructure at 50 K. Inset shows the saturation region. Colored lines show the components of the Langevin function fit and their sum. b) Temperature dependence of total saturation magnetization with a Bloch 3/2 law fit.

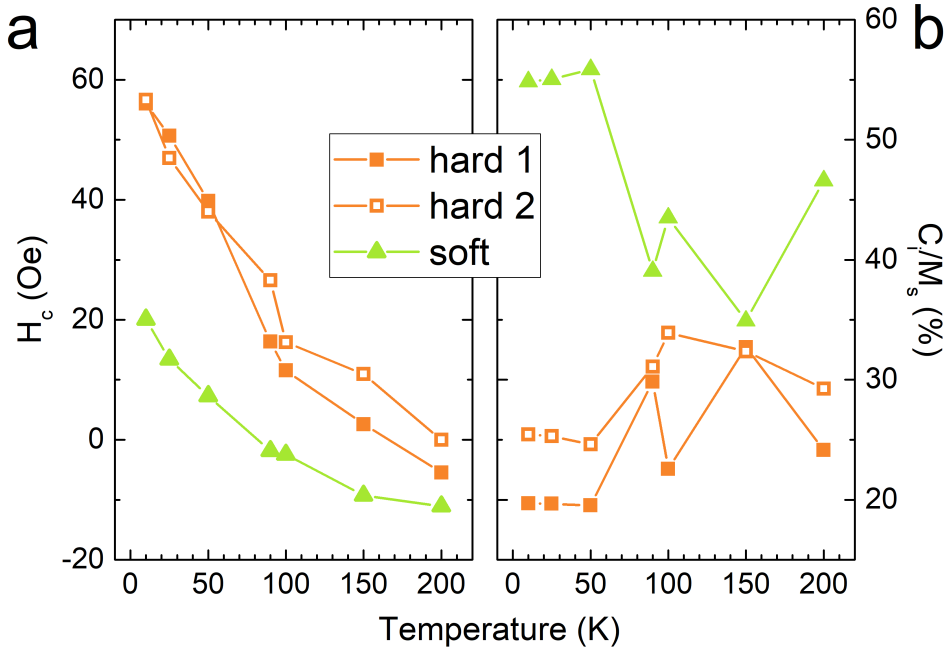

Figure 4.20: Temperature dependencies of H_c (a) and relative magnetic moment of the magnetization components (b) of thin barrier STO substrate sample, extracted from the magnetization loop fits with Langevin curves.

Chapter 5

Electro- and magnetoresistance in thick barrier junctions

After the thick barrier samples (July 2019 growth, see table 4.1) were patterned into the shape of micro-pillar devices (see sections 3.1.2 and 3.3), various electronic transport experiments in the current-perpendicular-to-plane configuration were performed in order to test possible resistive switching (RS) and tunnel junction operation

5.1 Write-read experiments

Write-read measurement is the first type of transport experiments, used extensively throughout the whole study. The principle is as follows (**figure 5.1**): a sequence of voltage pulses (duration of the pulses and time distances in between them can be varied) is applied to the device under test, with the values following a triangular profile - these are so called "writing" pulses, which are used to set the device in a particular state. The electric current value is averaged during the pulse application and is plotted against the corresponding voltage value, thus, the $I_{write}(V_{write})$ curve is obtained. Each writing pulse is followed by a so called

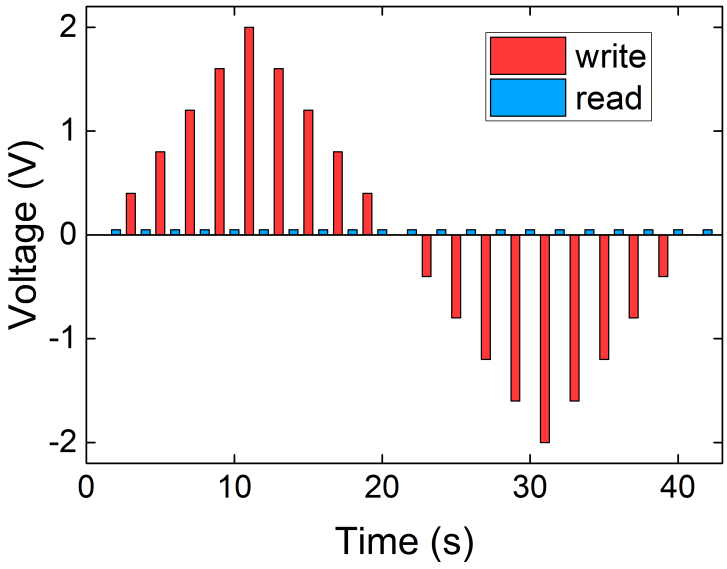

Figure 5.1: Sketch of the voltage profile for write-read measurements.

"reading" pulse, which has a fixed voltage value that is sufficiently small to ensure little disturbance to the device state during the measurement. Here current is also averaged during the pulse, but then it is used to calculate the instantaneous value of device resistance according to Ohm's law (which is valid, since the low reading voltage value is in the linear limit of the $I(V)$ curve):

$$R = \frac{V_{read}}{I_{read}}.$$

R is plotted against voltage value of the preceding writing pulse. Thus, the $R(V_{write})$ characteristic is obtained.

◆ It was found that several devices of the July 2019 growth samples demonstrate RS. Device-to-device variability of the switching behavior is very high, however, some common features can be distinguished. We will illustrate this with the example of a 50 μm device from STO substrate sample, characterized at room temperature (**figure 5.2**).

In the beginning of device electrical cycling, using moderate V_{write} values between −4 V and +3 V, resistance is quite stable and no RS is observed (fig.5.2, "pristine"). Then at a random moment, for a voltage value around +2 V, an abrupt resistance drop occurs. By increasing V_{write} up to +4 V, resistance may be reduced further. In the voltage range between +4 V and -2 V, the low resistance value is stabilized. Then, an abrupt resistance jump occurs around −3 V, resulting in retrieval

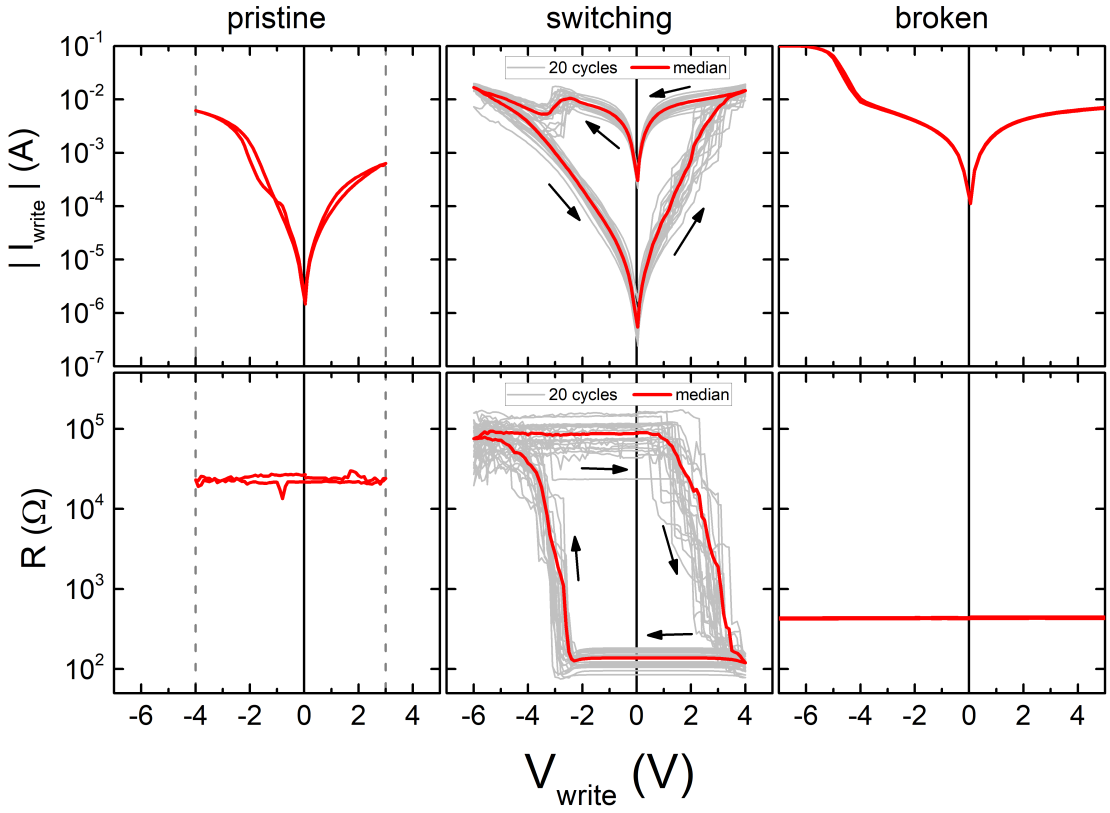

Figure 5.2: $I_{write}(V_{write})$ and $R(V_{write})$ curves of a 50 μm device on Jul STO sample. In the "switching" state raw data from 20 consecutive cycles are shown in grey, the median cycle is shown in red. Switching direction is indicated with the arrows. V_{read} equals 50 mV, pulse duration equals 1 ms, pulse interval equals 10 ms.

of the high resistance value (fig.5.2, "switching"). Switching in both directions is essentially stochastic and step-like (with two and more steps necessary for complete switching). This stable (20 consecutive cycles shown) RS regime may be sustained for various periods of time, depending on the device. In the illustrated case, after ∼100 cycles, performed in a number of sessions during one month, the switching gradually degraded to the stable low resistance state (LRS), with no possibility of switching to high resistance state (HRS) even at very large negative voltages (fig.5.2, "broken").

An inherent feature of RS behavior is the hysteresis of $I(V)$ and $R(V)$ curves, which is seen very clearly in the fig.5.2("switching"). Its quantitative measure is so called *electroresistance* (ER):

$$\mathrm{ER} = \frac{\mathrm{HRS} - \mathrm{LRS}}{\mathrm{LRS}} \cdot 100\%.$$

In the considered example, averaged values of LRS and HRS are equal to 138 Ω and 87 kΩ, respectively, which yields ER ≈ 63 000 %, or HRS/LRS ≈ 630, another important metric. The other devices showed HRS/LRS ∼ 10^2, sometimes only at low T.

◆ The important aspects of RS that should be addressed are the kinetics of switching from HRS to LRS and back and the stability of the HRS and LRS levels themselves (and of any number of intermediate levels, if such levels exist). For this, the resistance was measured as a function of the number of applied pulses (**figure 5.3**). Each point on the graph was acquired as a write-read pair. Here an initial HRS (LRS) was set with 100 pulses of -6 V (+4 V), what should be certainly enough based on the $R(V)$ loops. Then the switching was performed with pulses of various V_{write} values. In the case of HRS-to-LRS switching (fig.5.3a), conventionally referred to as "set", two resistance levels are defined with the threshold voltage at

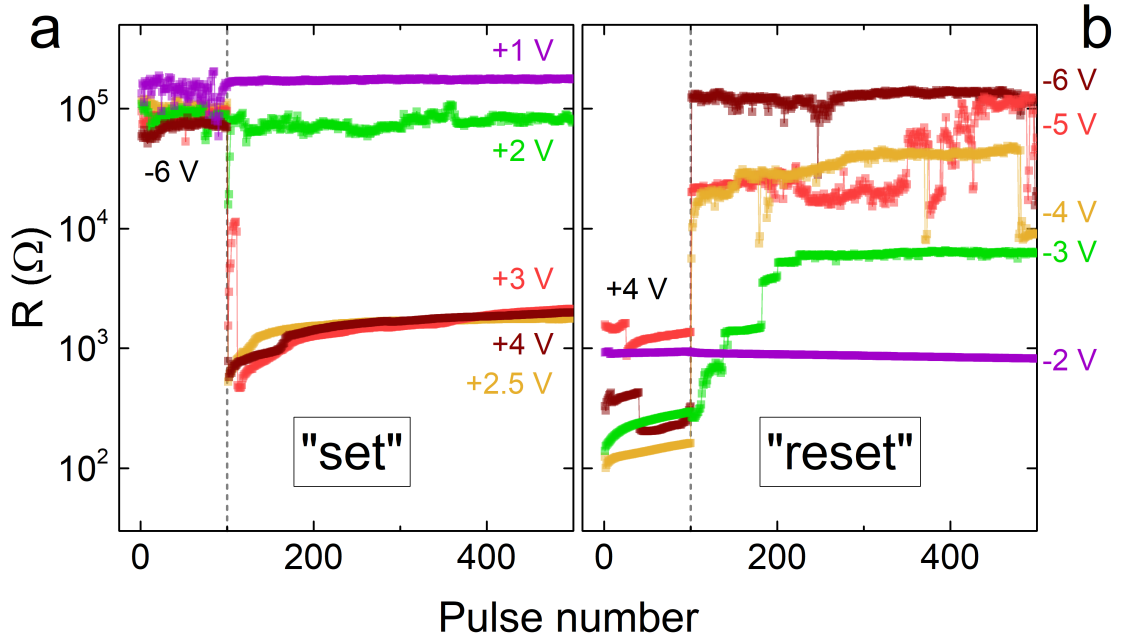

Figure 5.3: Switching curves from HRS to LRS (a) and from LRS to HRS (b) with pulses of various V_{write}. V_{read} equals 50 mV, pulse duration equals 1 ms and pulse interval equals 10 ms.

about +2.5 V. Above the threshold voltage, the switching curves almost coincide. Below the threshold (+1 V and +2 V), the curves differ a little in the resistance value and stability (+2 V pulses induce stronger disturbance of the system), but behavior is the same, no stable changes are induced with these voltage values. The case of LRS-to-HRS switching (fig.5.3b), or "reset", is slightly different from set. Here threshold also exists, above -2 V, and starting from -4 V, an abrupt change of resistance is observed. When -3 V pulses are used, resistance value does not change abruptly in one jump, as for -4 V, but in a series of small abrupt steps. In the end, the -3 V resistance state seems to be stabilized in the middle between HRS and LRS values, that were well defined in the set case. One may note that the curves for -4 V and lower are not stable and tend to randomly drop almost to the final step of -3 V. Therefore, the uncertainty and instability of HRS during reset do not allow to distinguish a stable intermediate level between LRS and HRS. We should note that the $R(V_{write})$ loop shows several steps in set as well, however the voltage window of this effect is narrower than in reset case, which is why it was not captured with the large steps in voltage values of switching curves.

◆ The intermediate conclusion here is that in the considered device case we observe RS between two well defined resistance states, which is driven through a set of small abrupt jumps in a rather stochastic manner. Importantly, by increasing the number of cycles, the device may lose its RS properties. Several devices with thick BTO battier were tested, which demonstrated RS with initially set LRS or HRS (or no RS at all), with ER values being of different orders of magnitude.

5.2 Conduction mechanism consideration

Prior to proposing any RS mechanism, $I(V)$ characteristics in a low V range should be analyzed to investigate the device response to small field perturbations. The curves, corresponding to HRS and LRS, were measured as conventional $I(V)$ characteristics (i.e., without reading pulses, only triangular voltage profile for writing pulses) between -0.5 V and +0.5 V, preliminary setting the device state with −6 V and +4 V, respectively (**figure 5.4**).

The experimental current density was considered as $j_{exp} = I/A$, where A is the device area (50×50 μm^2). The simulated current density was derived from the direct tunneling (DT) model with a trapezoidal barrier in Wentzel–Kramers–Brillouin approximation, according to:

$$j_{DT} = C \cdot \frac{\exp\left\{\alpha\left[\left(\Phi_2 - \frac{eV}{2}\right)^{3/2} - \left(\Phi_1 + \frac{eV}{2}\right)^{3/2}\right]\right\}}{\alpha^2\left[\sqrt{\Phi_2 - \frac{eV}{2}} - \sqrt{\Phi_1 + \frac{eV}{2}}\right]^2} \times$$
$$\times \sinh\left\{\frac{3eV}{4}\alpha\left[\sqrt{\Phi_2 - \frac{eV}{2}} - \sqrt{\Phi_1 + \frac{eV}{2}}\right]\right\},$$

where $C = -4em_{eff}/9\pi^2\hbar^3$, $\alpha = 4d\sqrt{2m_{eff}}/3\hbar(\Phi_1 + eV - \Phi_2)$, m_{eff} is the effective mass of tunneling electrons, Φ_1 and Φ_2 - barrier heights in top and bottom LSMO, respectively [166]. As a result of the fit, potential barrier heights at the interfaces give reasonable estimation with respect to expected work function for LSMO. The

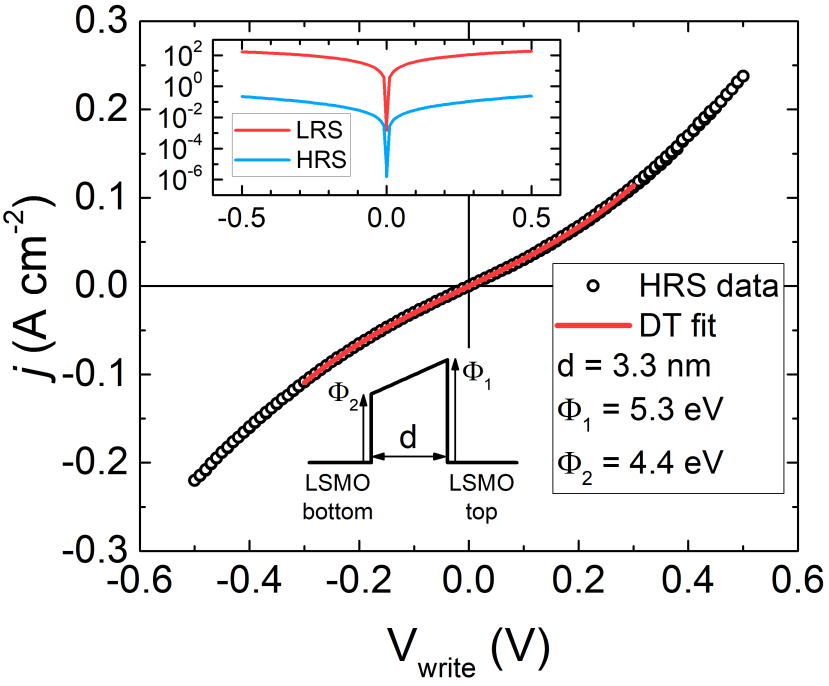

Figure 5.4: $j(V_{write})$ curves of a 50 µm device on Jul STO sample in low V range. Fit of HRS data was performed with direct tunneling model. Inset shows the low V curves at LRS and HRS in log scale for comparison.

extracted barrier thickness value is equal to 3.3 nm, significantly smaller than the expected value of ∼8 nm (see tab.4.4 and tab.4.5). This is probably due to leakage currents through BTO barrier, with 3.3 nm thickness value being an evaluation of the average thickness of the insulating part. All values of j in the LRS case are around 3 orders of magnitude higher than for HRS. Conductance here is very high for an 8 nm thick dielectric, which is why the curve could not be fitted with simple tunneling models. $j(V)$ in LRS is rather close to linear dependence, i.e. Ohmic conduction.

◆ On the basis of the aforementioned observations, it can be assumed that the considered device is switching in accordance to filamentary valence change mechanism [29]. Indeed, two defined resistance states and step-like stochastic switching are the signs of conducting filament formation and rupture; Ohmic conductance in LRS also is in agreement with this assumption. On the other hand, the HRS behavior is not as trivial in this context. It was shown in the previous study of our group that the BTO/LSMO system may possess a sufficiently high conductance with the insulating barrier forming only at the interface with intermixing [129]. In this case the thickness of the barrier is close to the value extracted from DT fitting of HRS $I(V)$ curve. Moreover, the DT fitting converged using the nominal device area of 50×50 µm^2, while the typical filament cross-section area is several orders of magnitude smaller. This suggests that in the HRS the filament disappears completely, instead of remaining in the partially formed state, while for switching to LRS it is forming again "freshly", possibly even at the different spot. Absence of the distinguished high voltage electroforming to launch the RS process supports the assumption additionally - in the pristine state, the device is ready for the switching, provided that sufficient voltage is applied, and the switching voltage is not changing

later in the operation. However, this assumption is largely speculative without additional investigation, which could be, e.g., conductive AFM mapping on the bare BTO surface of the BTO/LSMO junctions with similar BTO layer thickness.

5.3 Magnetoresistance experiments

Magnetic field dependence of resistance (magnetoresistance, MR) is an important aspect of tunnel junction device performance when ferromagnetic electrodes are used. It was measured simply with single pulses of various voltages and calculated into resistance with Ohm's law, while magnetic field was being varied in parallel.

Device on STO substrate sample considered earlier did not demonstrate either sufficiently stable resistance levels, or MR in any experiments, and neither did any other device from this sample. On the other hand, devices from MgO substrate sample showed some interesting examples of hysteretic MR, while RS behavior was observed here significantly weaker and rarer, than in STO case. Device-to-device variability is very high for this sample as well, therefore only the most prominent MR case will be presented below.

A 100 μm thick barrier device on the MgO substrate sample demonstrated the $I_{write}(V_{write})$ characteristic at 150 K (**figure 5.5a**) similar to a single branch of the $I_{write}(V_{write})$ curve of the previously described STO substrate sample. Very mild RS was observed for this device (**figure 5.5b**). Temperature dependence of device resistance was measured with 0.5 V pulses in 150–300 K range (**figure 5.5c**). In the major part of the T range resistance increases with the T increase, reaching the maximum value at 265 K. This kind of behavior is consistent with reports for LSMO films grown on MgO, the resistance maximum point is usually associated with the metal-insulator transition. [167–169].

MR was measured at various temperatures (10–250 K) and magnetic field orientations with respect to sample surface: angle between magnetic field and normal to

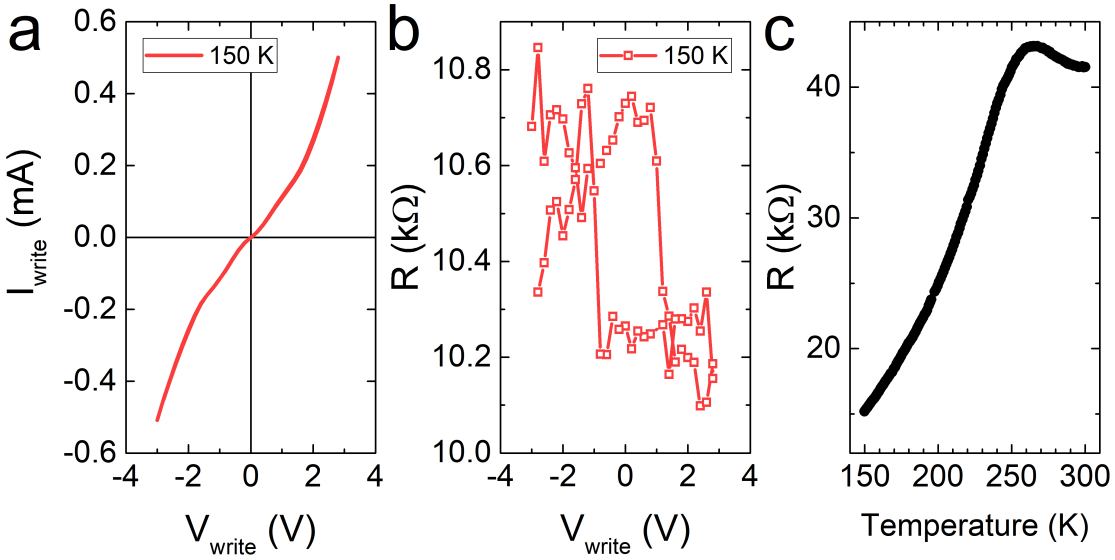

Figure 5.5: a,b) $I_{write}(V_{write})$ (a) and $R(V_{write})$ (b) curves at 150 K. c) Temperature dependence of resistance of a 100 μm square device on LSMO/BTO/LSMO//MgO sample.

sample surface was varied from 90°, which corresponds to in-plane (IP) orientation, to 0°, out-of-plane (OP). Consolidated measurement results are shown in **figure 5.6**.

In all the MR measurements 1 V pulses were used. MR value was calculated as follows:

$$MR = \frac{R(H) - R(0)}{R(0)} \cdot 100\%.$$

Hysteretic MR is observed at 150 K (weak hints) and below, reaching the maximum value of ∼1% at 10 K (fig.5.6b). In all cases four distinct regions of elevated resistance are observed. In addition to that, all the curves show resistance decay with magnetic field. Magnitude of this linear decay is largest at 250 K, close to $R(T)$ peak, and smallest at 150 K, increasing slightly with T decrease. Measurements at different angles of magnetic field to normal of the sample surface (fig.5.6a) reveal the strong angle dependence of the switching fields. The elevated resistance regions get gradually wider in magnetic field, when its orientation is changed from IP to OP, while the MR values vary insignificantly. Also it should be noted that the elevated resistance regions have sharp peak shape at H orientation close to IP, what is different from usually broad or rectangle-like in cases of TMR on similar structure samples [66].

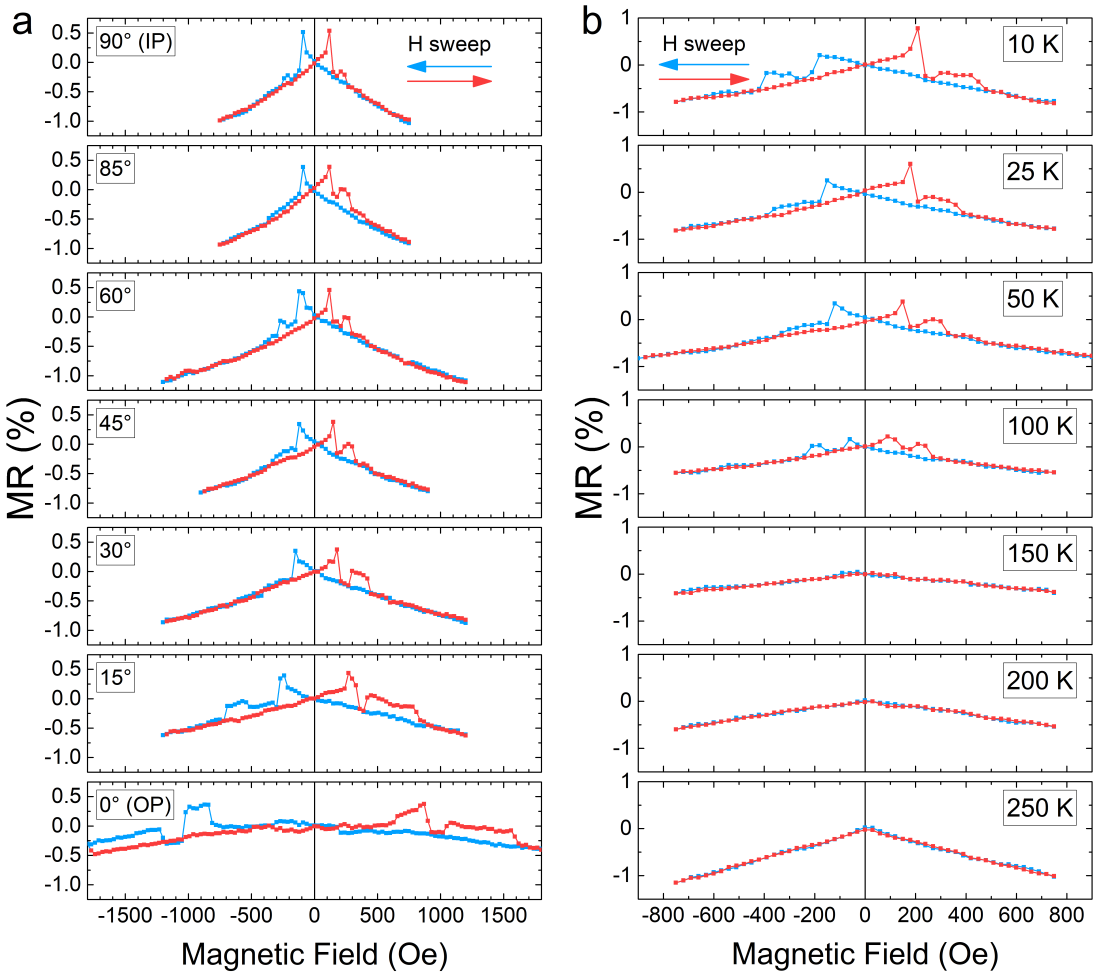

Figure 5.6: MR measurements a) at 50 K and various angles of magnetic field to sample surface, and b) at various T and 45° field angle.

Key curve parameters were extracted from MR data at different temperature (**figure 5.7**). Magnetic fields, at which MR reaches local peaks with respect to the other branch, were averaged to adjust for horizontal curve shift due to residual fields of the superconducting coil of PPMS. ΔMR was calculated as the maximum difference of MR, taken at one field value for two branches of the curve (magnetic field sweeps up and down).

As seen from the extracted temperature dependence, two groups of MR peak fields are quite close to the coercive fields of the same sample, measured with VSM (see fig.4.14 and fig.4.16), with the same behavior with T. Temperature dependence of ΔMR for hard and soft parts also correlates with the corresponding behavior of hard and soft layer magnetic moments: soft part significantly decreases with T, while decrease of the hard part is quite slow in comparison.

◆ On the base of the described observations, we may conclude that MR nature in our sample is different from conventional TMR, where the regions of increased or decreased resistance are caused by anti-parallel orientation of the magnetizations of top and bottom electrodes, and therefore these regions are enclosed between the values of coercive fields of the electrodes. This mechanism provides two regions of magnetoresistance. Instead, we observe four regions of magnetoresistance, peaks of which are at the coercive field values of corresponding hard and soft layers. This implies that the magnetoresistance behavior of the top and bottom LSMO layers is decoupled, and thus, in principle, could occur even in single layers. And indeed, there is an effect in LSMO films that may explain this behavior, the so called low-field magnetoresistance (LFMR).

LFMR is a well-known effect in polycrystalline, textured or artificially disordered LSMO films [170–174]. It consists in a significant resistance decrease with the applied magnetic fields that are of much smaller value than necessary for colos-

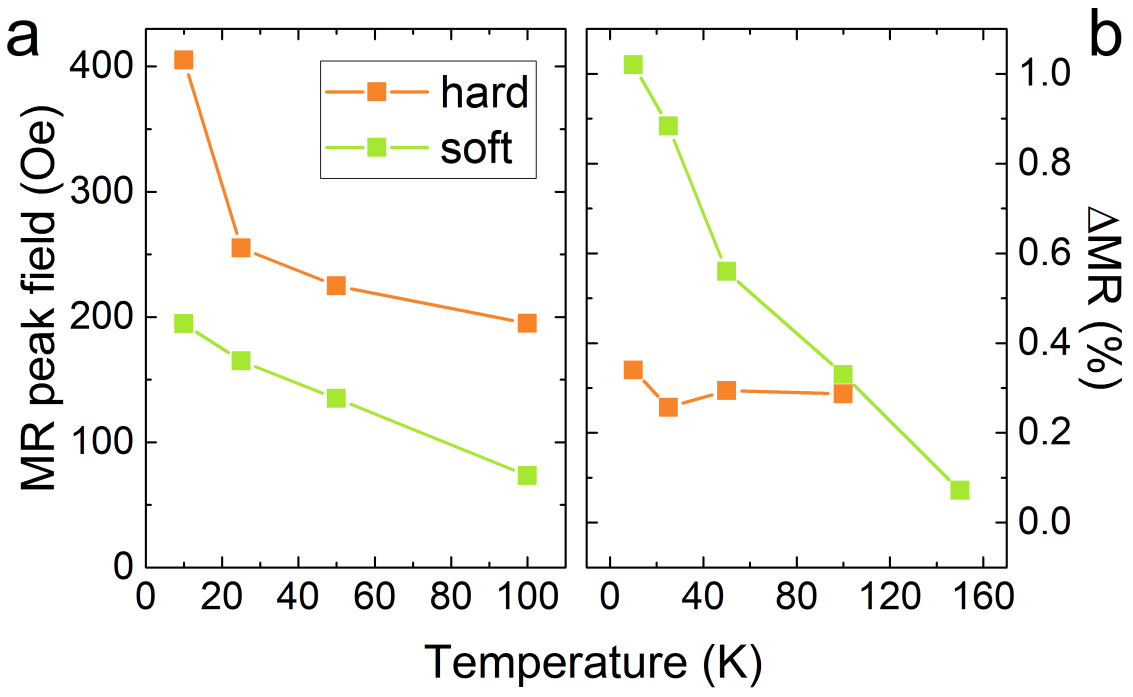

Figure 5.7: Extracts from fig.5.6b data of temperature dependencies of MR peak field (a) and maximum MR change from branch to branch (b).

sal magnetoresitance effect (CMR), traditional in manganites [175]. The nature of the phenomenon lies in the spin-polarized electron tunneling between the grains, which is highly sensitive to the field induced domain rotations at the grain boundaries [170]. Another manifestation of LFMR may be in the presence of hysteresis in MR(H) data with sharp resistance maxima at the coercive field [171–174] in a single LSMO layer. This extension of the effect is directly connected to the magnetization hysteresis of the film: at the coercive field net sample magnetization is zero, which is achieved by the maximal grain magnetization disorder - which, in turn, enhances spin scattering at grain boundaries.

Thus, we believe that on the basis of LFMR effect, MR(H) behavior of our sample may be explained to some extent. It should be noted that LFMR is observed mainly in polycrystalline films, while in our case both LSMO films are epitaxial. In our STO substrate samples the similar effect was not observed, however there is a case when for LSMO/STO epitaxial heterostructures LFMR of 0.2% was reported [173]. Likely, this effect was not observed in our experiments due to the presence of BTO barrier, which significantly increases the electron spin scattering and may lead to damping of the whole effect. On the other hand, MgO substrate lattice is largely mismatched with LSMO, what can be a source of structural defect formation in both top and bottom LSMO layers. These defects are eligible for the role of grain boundaries that enhance spin scattering and induce LFMR of moderate magnitude. Together with the presence of the BTO barrier, it explains the discrepancy of the largest value of MR, measured in our experiments (1%), with the report for LSMO grown on mica (16%) [173]. Lastly, the mentioned magnetic field dependence of the MR(H) curve baseline is in agreement with CMR effect, that intensifies in the vicinity of metal-insulator transition, i.e. peak of $R(T)$ dependence (265 K in our case).

Possible alternative explanations of the MR effect in our heterostructures involve the separation of each LSMO layer to two regions, parallel to the film surface. One of the parts is close to the interface with BTO, where some magnetic order reconstruction may occur, for instance, due to peculiar interplay of spin, orbital and lattice degrees of freedom [125]. In order to verify the MR mechanism, additional complex investigation is required, using, e.g., X-ray magnetic circular dichroism spectroscopy (XMCD), magnetic circular dichroism in the angular distribution of photoelectrons (MCDAD) or polarized neutron reflectometry (PNR) with *in operando* magnetoresistance measurement.

◆ In conclusion, it was found that some devices on both STO and MgO substrate samples with thick BTO barrier demonstrate RS with very high device-to-device variability. RS was illustrated on an example of a device from STO substrate sample. The switching is between two well defined, but not highly stable resistance states. After ∼100 cycles the device degrades to non-switching LRS. STO substrate sample devices do not demonstrate any magnetic field-dependent behavior. On the contrary, the junctions grown on MgO substrate show hysteretic magnetoresistance at 150 K and lower. It may originate from LFMR effect in LSMO, and likely is not related to TMR. Presence of LFMR in this case may be explained by the formation of structural defects in both top and bottom LSMO layers due to large lattice mismatch with MgO substrate. However, further investigation is necessary to verify the MR mechanism.

Chapter 6

Analog resistive switching in thin barrier junctions

Necessity of thin-barrier LSMO/BTO/LSMO junctions growth was governed mainly by the poor controllability of RS in thick-barrier samples. The thin barrier indeed manifested in a different type of RS behavior with high reproducibility. The sample, thoroughly characterized in this chapter, is of February 2021 growth on NSTO substrate.

6.1 Write-read experiments

Write-read measurements were performed on a number of devices in temperature range from 50 K to 300 K, following the same procedure as described in section 5.1. Typical $I_{write}(V_{write})$ curves of a 100×100 μm^2 device are shown in **figure 6.1a,b** for 50 K and 300 K. The corresponding $R(V_{write})$ loops, where reading was performed with 50 mV pulses, are shown in figure **6.1c,d**. Data at 50 K are shown for 10 consecutive cycles, together with the median curves, where each point is obtained by arithmetic averaging of the I_{write} and R values, corresponding to the same V_{write}. Both $I_{write}(V_{write})$ and $R(V_{write})$ curves show strong, stable hysteretic behavior, and a bipolar resistive switching between LRS and HRS. The $I_{write}(V_{write})$ curves are highly asymmetric, similar to a diode characteristic. Note, that hysteresis of both $I(V)$ and $R(V)$ curves gets significantly more pronounced at low T. The ratio of HRS to LRS (taken at $V_{write} = 0$ V) is largest at 50 K, reaching at least 10^3, and gradually decreases to a value of 4 at 300 K. ER magnitude, calculated as ER $= 100 \times (\text{HRS} - \text{LRS})/\text{LRS}$, is equal to 10^5 % and 300 %, respectively. Saturation of the resistance state is observed only for LRS close to -2 V, while up to the maximum tested positive voltage of $+4.5$ V, resistance is increasing monotonously with no signs of HRS saturation.

Device-to-device variability is quite high for this sample. Mainly, it concerns the quantitative parameters of the $I_{write}(V_{write})$ and $R(V_{write})$ characteristics, while qualitatively the RS behavior is similar. As an example of such variations, the $I_{write}(V_{write})$ and $R(V_{write})$ curves at 300 K and 50 K of another 100×100 μm^2 device are shown in **figure 6.2**.

Resistance range of the second device is significantly lower (100–1000 Ω) in the whole temperature range in comparison to the first one. The ER magnitude here is below 100%. The diode-like character is completely suppressed; at 300 K the

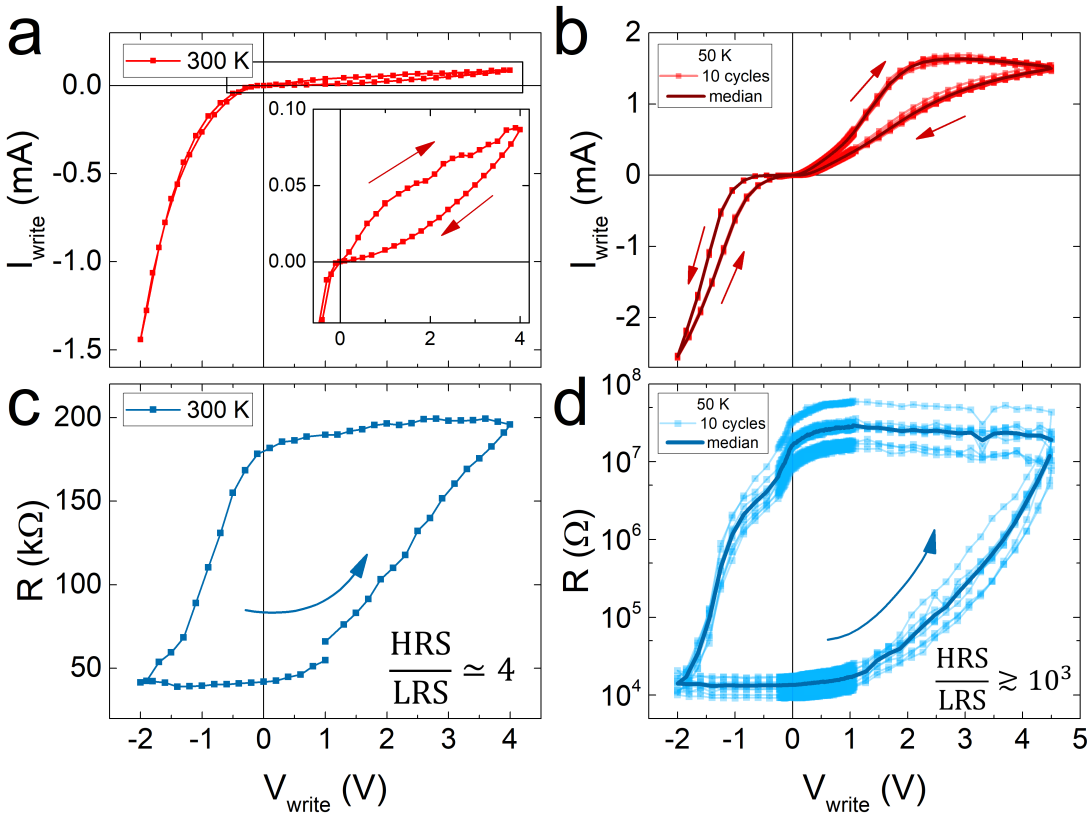

Figure 6.1: $I_{write}(V_{write})$ (a, b) and $R(V_{write})$ (c, d) curves of a 100 μm SC-like device from Feb NSTO sample, measured at 300 K (a, c) and 50 K (b, d). Arrows indicate direction of switching. Inset in (a) shows enlarged view of the hysteresis region. In (c) and (d) 10 consecutive cycles are shown (in light red and light blue, respectively) with their median (dark red and dark blue, respectively).

$I_{write}(V_{write})$ curve is closer to the straight line, or Ohmic behavior. However, the same $I_{write}(V_{write})$ peculiarities are seen: branches of the curve intersect after continuous modification, with significantly stronger hysteresis at low T.

The key parameters of the $R(V_{write})$ curves, obtained at various temperatures, namely, LRS, HRS and ER, have been extracted from the data and are shown in **figure 6.3**. As seen on the graph, for the first device LRS has almost no dependence on T, while HRS demonstrates a steady decrease from ∼10 MΩ at 50 K down to 200 kΩ at 300 K. ER behaves similarly to HRS. The temperature behavior of LRS, HRS and ER for the second device is markedly different. Notably, both resistance state values are increasing with the temperature growth. ER, although non-monotonous with respect to T, which here could be due to uncertainty of ER values, does not change significantly.

◆ Aggregating the described resistive switching properties of different devices, we will refer to the first one as "semiconducting-like" (SC-like) and to the second one as "metal-like". Indeed, for the SC-like device we observe the relatively high resistance range, diode-like $I(V)$ characteristic and strong resistance increase with cooling, similarly to the behavior of semiconductors, while in the case of metal-like device the resistance range is orders of magnitude smaller, the $I(V)$ curve is closer to linear

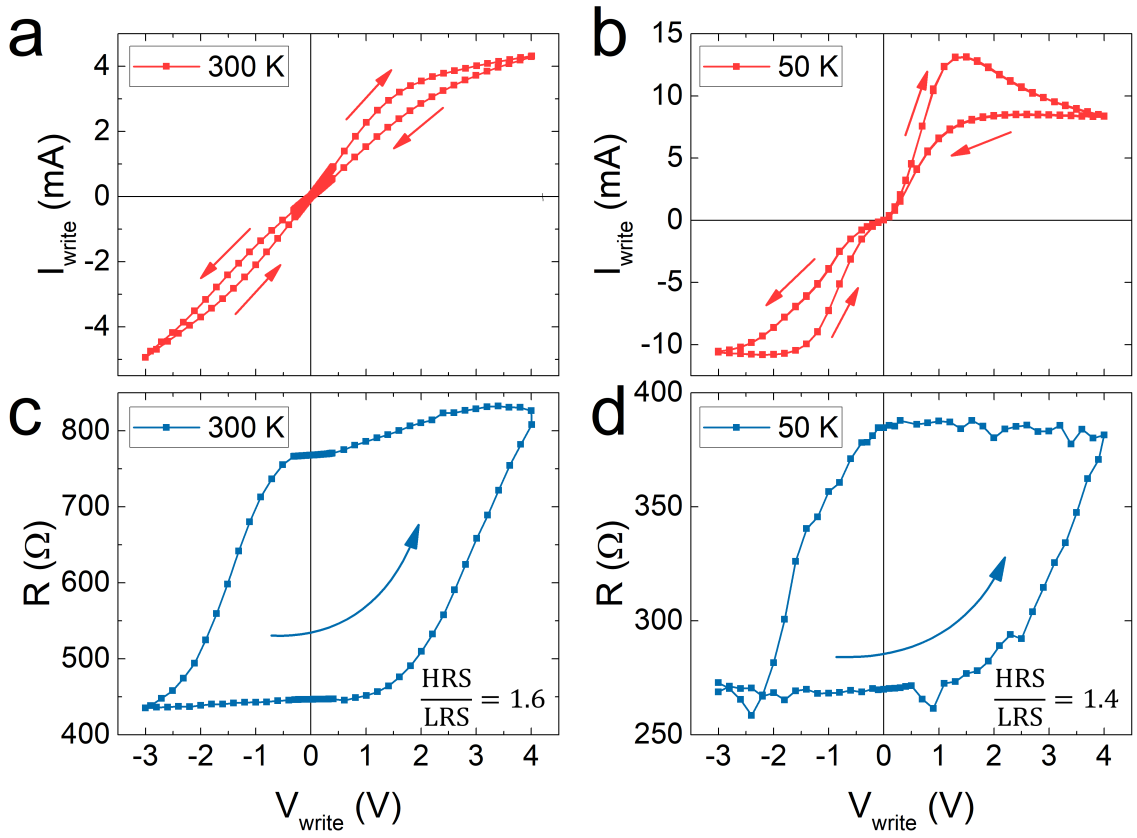

Figure 6.2: $I_{write}(V_{write})$ (a, b) and $R(V_{write})$ (c, d) curves of a 100 µm metal-like device from Feb NSTO sample, measured at 300 K (a, c) and 50 K (b, d). Arrows indicate direction of switching.

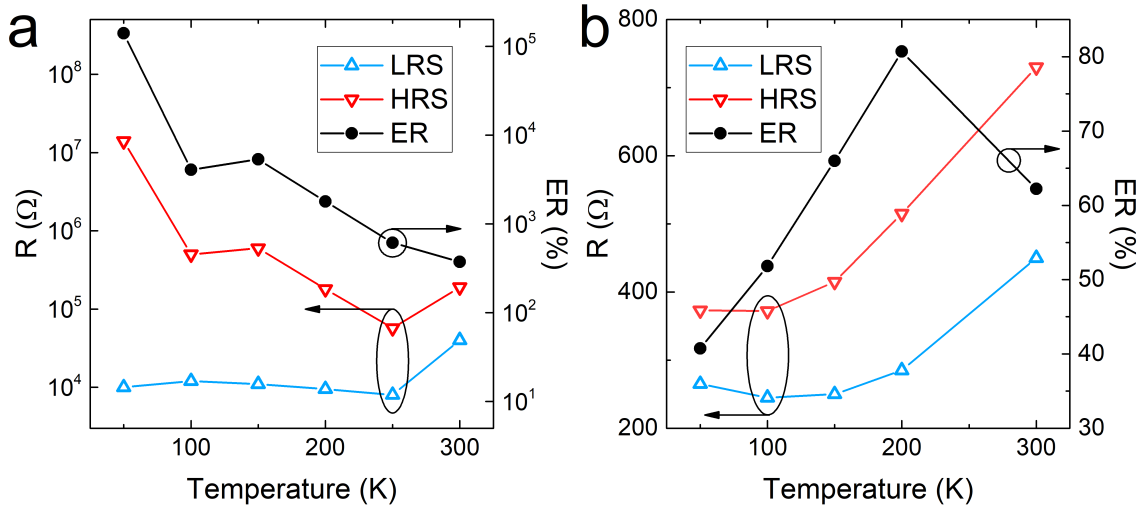

Figure 6.3: Extracted temperature dependencies of LRS, HRS and ER of the SC-like (a) and metal-like (b) devices.

and with T increase resistance grows as well, similar to metals. Moreover, all the devices from the Feb NSTO sample are somewhere in the spectrum between SC-like and metal-like behavior. Resistance range and ER value are systematically correlated with the intensity of SC-like behavior. Remarkably, qualitative RS features nevertheless are the same: shape of the $I(V)$ and $R(V)$ curves (gradual transition between $I(V)$ curve branches in the form of a bump), saturation of LRS at the negative voltages with no signs of HRS saturation.

Together, the observations imply that RS mechanism in two different device types - SC-like and metal like - is the same, but the device resistance range and the temperature behavior differ, which might arise from the variation of some additional device properties over the sample area.

6.2 Phenomenological model of conduction circuit

The described similarity in resistive switching behavior, with the variations that manifest in existence of the SC-like and metal-like devices, may be explained on the basis of simple phenomenological circuit model (**figure 6.4**).

Let us assume that a variable resistor R_{switch} emulates the observed analog resistive switching effect, in series with it a diode is connected to reproduce the diode-like $I(V)$ characteristic. Then another resistor $R_{leakage}$ is connected in parallel to the diode and the first resistor. This second resister represents the leakage paths that differ from device to device and affect drastically the overall performance. Therefore, the first variable resistor is treated as dielectric contribution, inherent to the barrier.

We assume that the initial value of R_{switch} corresponds to LRS. A "true" HRS/LRS value for R_{switch} is denoted as γ.

The diode is modeled with the Shockley equation [176]:

$$I_d = -I_0 \cdot \left(\exp\left(-\frac{V_d}{nV_T} \right) - 1 \right), \tag{6.1}$$

where I_0 is the saturation current of the diode, $V_T = k_B T/q_e$ is the temperature potential (equal to 26 mV at 300 K), n is the ideality factor, V_d is the voltage drop

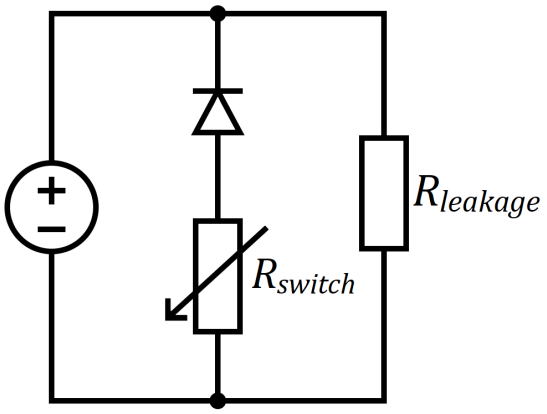

Figure 6.4: Circuit diagram of the simplified device model.

across the diode. Minus signs are adjusted to obtain inverted $I(V)$ curves that match the polarity of our set-up.

To calculate the current through the diode with respect to the source voltage V we follow the procedure proposed by Banwell and Jayakumar [177], which involves the implementation of the Lambert W-function, an inverse function to $f = xe^x$, i.e. it is defined as $W(xe^x) = x$.

At first, let us consider the left closed circuit, that contains the source, diode and R_{switch}. We denote:

$$x = -\frac{I_0 R_{switch}}{nV_T}\left(\frac{I_d}{I_0} - 1\right). \tag{6.2}$$

Then, substituting from (6.1):

$$xe^x = \frac{I_0 R_{switch}}{nV_T}\exp\left(-\frac{V_d}{nV_T}\right)\exp\left[-\frac{I_0 R_{switch}}{nV_T}\left(\frac{I_d}{I_0} - 1\right)\right].$$

By Kirchhoff's second law for the closed circuit:

$$V_d = V - I_d R_{switch} \Rightarrow$$
$$\Rightarrow xe^x = \frac{I_0 R_{switch}}{nV_T}\exp\left(-\frac{V}{nV_T}\right)\exp\left(\frac{I_d R_{switch}}{nV_T}\right)\exp\left(-\frac{I_d R_{switch}}{nV_T}\right)\exp\left(\frac{I_0 R_{switch}}{nV_T}\right).$$

Finally:

$$xe^x = \frac{I_0 R_{switch}}{nV_T}\exp\left(-\frac{V - I_0 R_{switch}}{nV_T}\right).$$

Now, using the Lambert function:

$$x(V) = W\left[\frac{I_0 R_{switch}}{nV_T}\exp\left(-\frac{V - I_0 R_{switch}}{nV_T}\right)\right].$$

Hence, we derive I_d from (6.2):

$$I_d(V) = I_0 - \frac{x(V)\cdot nV_T}{I_0 R_{switch}}.$$

Then, since $R_{leakage}$ is connected in parallel to the source:

$$I_{leakage} = V/R_{leakage}.$$

Therefore, total current intensity, measured from the device:

$$I(V) = I_d(V) + I_{leakage}.$$

Taking R_{switch} as the LRS value we obtain the whole $I(V)$ curve for LRS, and the same for HRS, but we take γR_{switch} as the HRS value.

However, this form does not account for the gradual switching process. We emulate it with the Boltzmann sigmoidal function:

$$\sigma(x) = A_2 + \frac{A_1 - A_2}{1 + \exp\left(\frac{x - x_0}{dx}\right)},$$

where A_1 is the initial level, A_2 is the final level, x_0 is the zero shift of the curve, dx is the step slope. x_0 corresponds to the switching voltage, depending on the voltage sweep direction up or down, dx is set manually to match the experimental curves.

We consider the initial state as LRS, when the voltage sweep begins from $-|V_{neg}|$, which fixes the value of A_1 to equal 0. On the sweep up voltage is increased up to $|V_{pos}|$, passing the switching voltage V_{up}, where the junction is half way switched, i.e. sigmoid is at 0.5 level. $A_2 = 1$, but this state is never reached in practice, since in this case the resistance loop would saturate, what was shown to not be the case in any of our measurements. Therefore we should manually adjust the $\sigma_{upmax} < 1$ to match the experiment. Then on the sweep down the voltage change direction is reversed, with the beginning at HRS, reached at the sweep up, i.e. $A_{2down} = \sigma_{upmax}(V_{max})$, and passing the V_{down} switching voltage.

Thus, the final $I(V)$ curves are obtained via mixing $I_{LRS}(V)$ and $I_{HRS}(V)$ with the weights, calculated with sigmoidal function:

$$I_{up(down)}(V) = I_{LRS}(V) \cdot \big(1 - \sigma_{up(down)}(V)\big) + I_{HRS}(V) \cdot \sigma_{up(down)}(V).$$

$R(V)$ curves are calculated through read process emulation. At each V the weight value $\sigma(V)$ is changed, therefore, "instant" $I(V)$ curve is different for each point. "Reading" is made by dividing V_{read} by the current value of the instant curve at V_{read} point:

$$R(V) = \frac{V_{read}}{I_{LRS}(V_{read}) \cdot \big(1 - \sigma_{up(down)}(V)\big) + I_{HRS}(V_{read}) \cdot \sigma_{up(down)}(V)}.$$

Results of the modeling are shown in **figure 6.5**. Parameters of the model:

$$I_0 = 0.25 \text{ mA}, n = 1.8, R_{switch} = 1 \text{ k}\Omega, \gamma = 100.$$

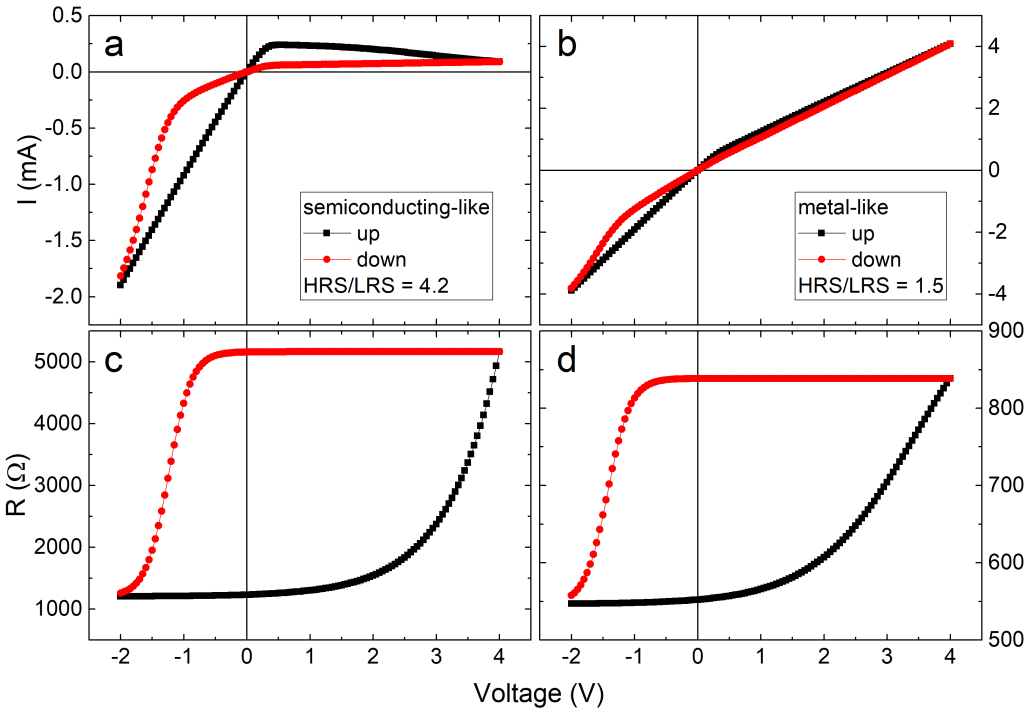

Figure 6.5: Modelled $I(V)$ (a,b) and $R(V)$ (c,d) curves of SC-like (a,c) and metal-like (b,d) devices.

$R_{leakage}$ equals 1 kΩ for metal-like and 1 MΩ for semiconducting-like device. Here we can clearly see how varying only the leakage resistance qualitatively changes the $I(V)$ characteristics, what correlates with the effective HRS/LRS ratio: 4.2 in the SC-like case and 1.5 in the metal-like.

◆ Thus, we can see that the observed variety of devices in our samples by resistance range may indeed arise from the common RS mechanism and variable leakage conditions. This variation may be related to some non-uniformity of the thin-film layer properties over the sample area. The source of this could be in the growth parameter deviations that may have occurred for the samples located far from the maximum intensity of the plasma plume, which was discussed in detail in section 4.2.4. Hereinafter we consider that the RS features are universal for all devices on the regarded sample, according to the performed phenomenological modelling.

6.3 Multilevel resistance

Previously in the chapter we demonstrated the nonvolatility of the resistance states, namely, two of them (HRS and LRS) obtained by applying extremum voltages of +4 V and −2 V in the case of a SC-like device. Here we focus on a similar SC-like device ($100 \times 100 \mu m^2$ in lateral size), where the investigated V_{write} range is wider: from −3.5 V to +7 V. We explore the multilevel resistance states, that can be set and stabilized in between of LRS and HRS, their switching dynamics and retention. We recall here that SC-like and metal-like devices demonstrate similar RS behavior, and illustrate that with the data from additional devices, presented in Appendix A. All the measurements in this section were performed at room temperature.

In $I_{write}(V_{write})$ and $R(V_{write})$ measurements (**figure 6.6**), the maximum negative voltage, that induces the LRS, was kept at −3.5 V, while the maximum positive voltage was changed progressively from +4 V to +7 V. In all the cases switching

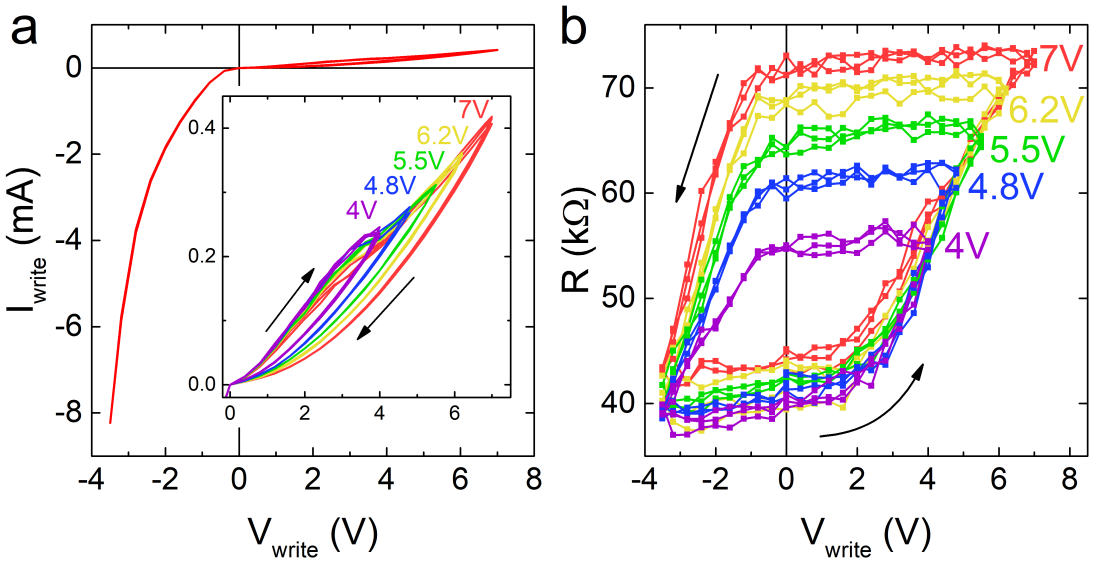

Figure 6.6: Multilevel $I_{write}(V_{write})$ (a) and $R(V_{write})$ (b) curves, cycling between −3.5 V and various V_{max} values. Inset in (a) displays the zoomed-in hysteretic region of the $I(V)$ curve. Arrows indicate the voltage sweeping order

from LRS to HRS (reset) begins around 1.5-2 V and the $R(V_{write})$ curve follows the same switching path whatever the value of the maximum positive voltage. Notably, switching from HRS to LRS (set) starts at around -0.8 V in all the cases as well and leads to the common LRS at -3.5 V, with different slopes necessary to reach it, depending on the initial resistance level. The situation is similar in the $I_{write}(V_{write})$ curves as well: the curves follow the same path on the voltage sweep up, superimposed with the $+7$ V curve, independent of the stopping voltage value.

◆ Dynamics of resistance state switching were assessed in detail (**figure 6.7**). To set the resistance multilevels, series of 250 pulses of -3.5 V ($+7$ V) were applied to preliminary switch the device into LRS (HRS), followed by 1000 voltage pulses of various positive (negative) magnitudes (all 1 ms long). Each writing pulse was followed with a 50 mV reading pulse of the same duration. Pulse application period equaled $\sim$250 ms, which made the period of write pulse application equal $\sim$0.5 s.

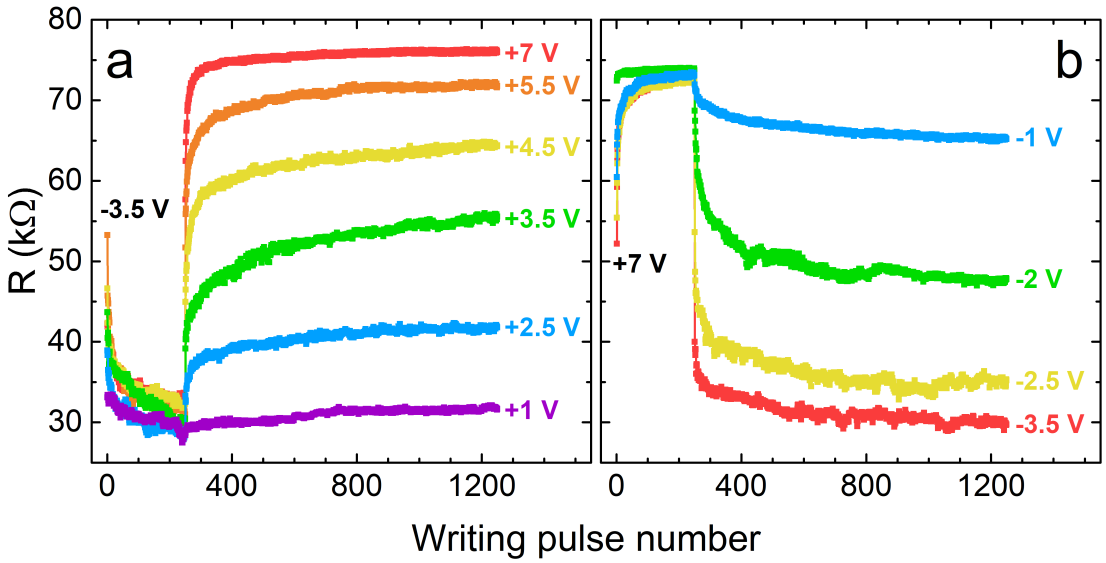

Figure 6.7: Multilevel resistance states set with positive (a) or negative (b) writing pulses, after 250 prepulses of -3.5 V (a) or $+7$ V (b). Reading was made with 50 mV and duration of 1 ms, period of write pulse application equal to 0.5 s.

It is clearly seen that writing pulses of different magnitudes switch the device into different resistance levels, which reach gradual saturation with the series of pulses. Note that these different resistance levels are not intermixed for cases of different V_{write}, if the same amount of pulses was applied.

◆ Next, the series of -3.5 V pulses followed by the series of $+5$ V pulses (**figure 6.8a**) were applied, using different sequences where the number of $+5$ V pulses doubles each turn. Similar measurements were done with $+7$ V pulses followed by -2 V pulses (**figure 6.8b**). The couples of voltage values were selected to prepare the same reference state, as quickly as possible, with the series that have a fixed number of pulses (-3.5 V and $+7$ V, respectively, corresponding to the steepest switching curves of fig.6.7), as well as to demonstrate the gradual switching with the series where the number of pulses is doubled at each sequence ($+5$ V and -2 V, respectively, corresponding to the curves of intermediate steepness in fig.6.7). The switching paths during any series with doubled number of pulses are well reproduced, while switching in -3.5 V is occasionally more random (see similar devices with

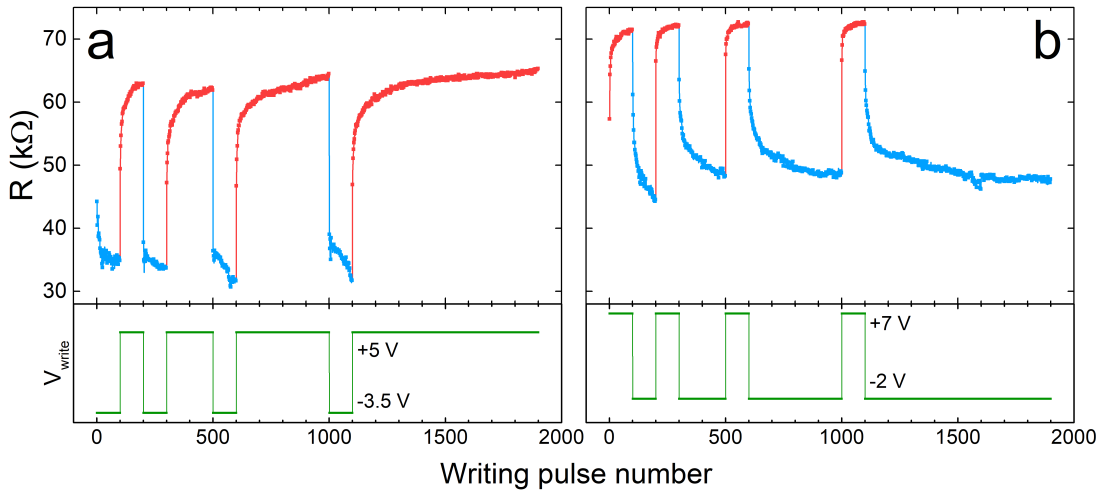

Figure 6.8: a) Pulse series of −3.5 V writing, followed by +5 V writing, repeated in sequences, in which the number of pulses in the even groups doubles. Reading was made with 50 mV and duration of 1 ms, period of write pulse application equal to 0.5 s. Red and blue colors are used for differentiating potentiation from depression. b) The same with +7 V pulse series, followed by −2 V pulse series.

better reproducibility in Appendix A).

These measurements are a manifestation of long-term potentiation and depression (LTP/LTD), a basic feature of synaptic plasticity. By selecting an appropriate voltage and number of the writing pulses, it is possible to cover a wide range of resistance states, i.e., potentiate or depress the synaptic weight of the artificial synapse, or memristor.

◆ To test the state retention, resistance was set with several voltage values and measured every 10 s during 10 min period, with 50 mV and 1 ms reading pulses (**figure 6.9**). Preliminary, we applied one pre-set pulse of high negative or positive

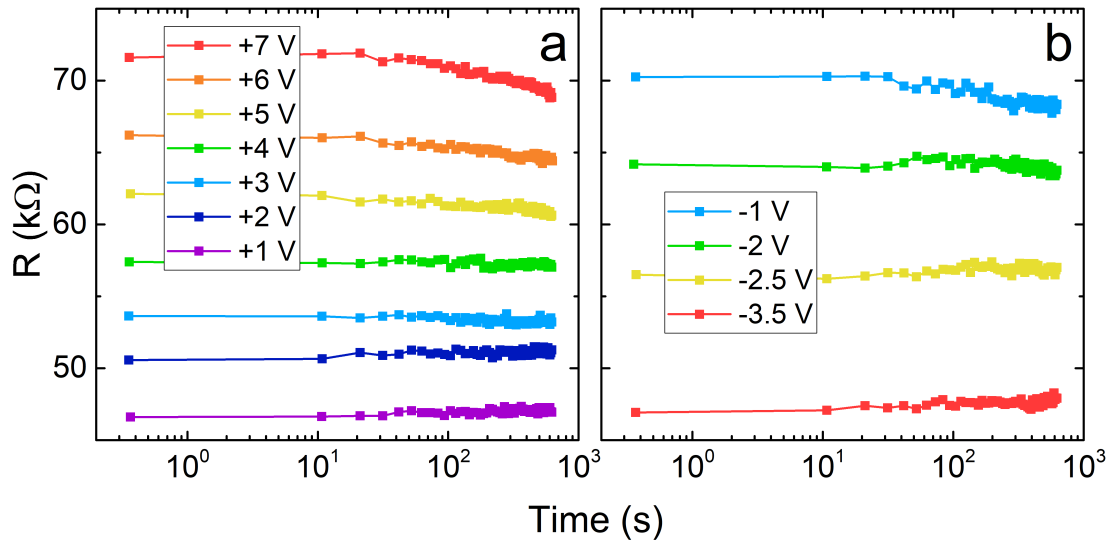

Figure 6.9: Retention, on a 10 min time scale, of resistance states set at different levels by five 1 ms voltage pulses of various positive (a) and negative (b) magnitudes, after one pre-pulse of −3 V (a) and +7 V (b), respectively.

voltage value (−3 V or +7 V), followed by five consecutive writing pulses of various magnitudes: from +1 V to +7 V (fig.6.9a) and from −3.5 V to −1 V (fig.6.9b).

Resistance levels set with mild positive voltage pulses, up to +4 V, and high negative voltages, −2 V and higher by absolute value, are retained adequately throughout the whole 10-min measurement period. However, resistance of the states set with high positive and low negative (by absolute value) voltages begins to decrease after 30 s.

◆ Thus, our devices demonstrate the possibility of continuous, or analog, resistance state tuning with satisfactory reproducibility and stability. This is the primary attribute of memristive behavior. Further, a more detailed analysis of the RS behavior is necessary to determine possible means of neuromorphic operation and their limitations.

6.4 Additional switching features

It has been demonstrated in the previous section (fig.6.7, fig.6.8) that resistance state tuning occurs continuously and non-linearly with the number of applied pulses at a given voltage value. A similar effect is observed, when instead of applying more pulses their duration is increased (**figure 6.10**). To track that, $R(V_{write})$ loops were recorded with the standard write-read procedure using pulses of various duration: from 1 ms to 1 s long. Voltage limits were adjusted to match the corresponding HRS and LRS as much as possible. It is seen that the loops "contract" along the horizontal axis with pulse duration increase, i.e. lower voltage value is necessary in order to set a certain resistance state when longer pulses are used. Equivalently, with a fixed voltage value longer pulses induce larger relative resistance state modification in the absolute values.

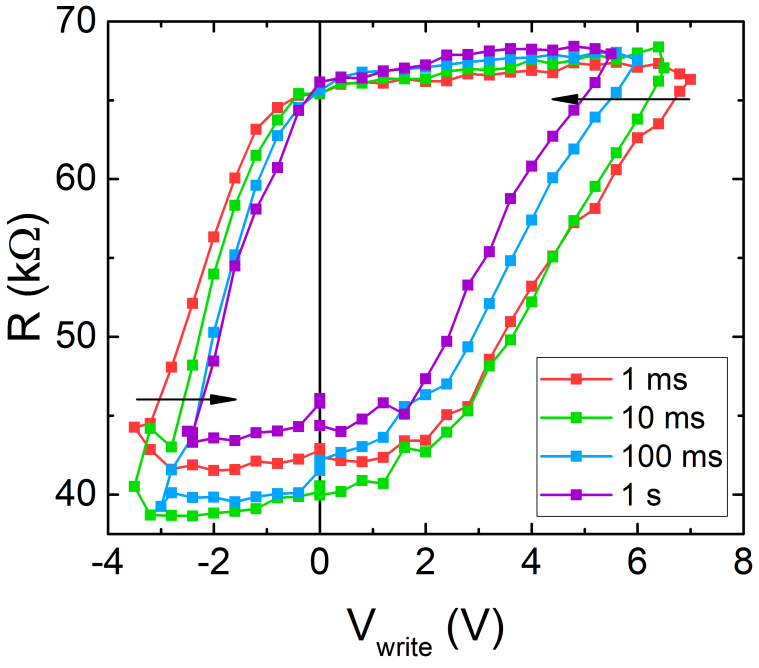

Figure 6.10: $R(V_{write})$ loops measured with different duration of the pulses. Arrows indicate the contraction of the loops along the horizontal axis.

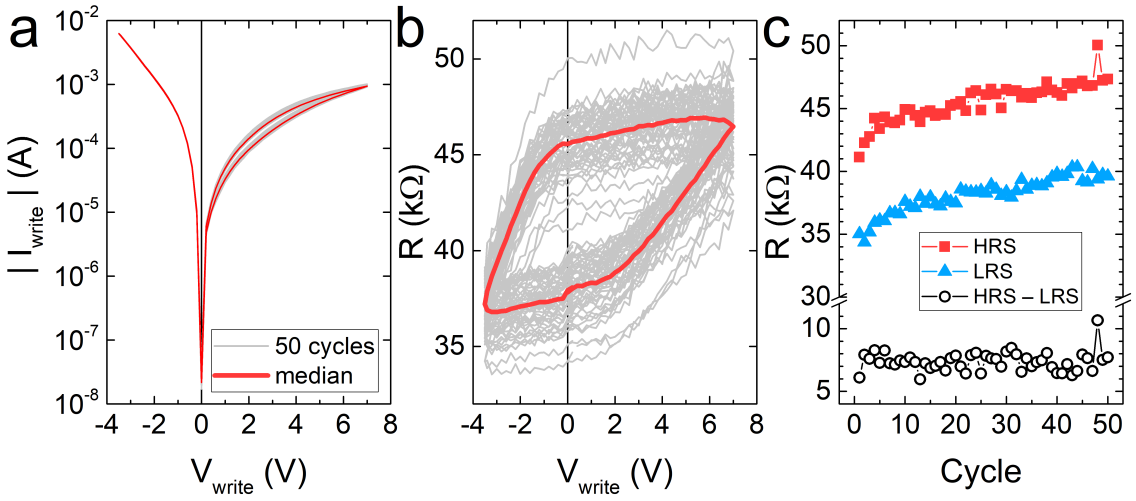

Figure 6.11: 50 cycles between −3.5 V and +7 V (grey) with their median (red). a) $I_{write}(V_{write})$ curves and b) $R(V_{write})$ curves. c) Extracted HRS and LRS values at $V_{write} = 0$ V and their difference with cycling.

◆ Reproducibility of $I_{write}(V_{write})$ and $R(V_{write})$ characteristics with cycling also should be addressed. Measurement of 50 consecutive cycles (**figure 6.11**) shows that, within the chosen voltage limits of −3.5 V and +7 V, the $R(V_{write})$ loops slightly drift to higher resistance values, while preserving the general loop shape and resistance gap between the states $\Delta R = \text{HRS} - \text{LRS}$. This may indicate that the chosen negative limit voltage is insufficient to sustain the constant level of LRS over multiple consecutive cycles, however positive limit voltage results in the consistent resistance modification. $I_{write}(V_{write})$ changes with cycling insignificantly.

◆ After the 50 cycle measurement, endurance of the device was tested with the same write-read pulse pairs, but of only two values (−3.5 V and +7 V), changing in turns consecutively for 10^5 cycles (**figure 6.12**). The trend of resistance state drift to higher values continues here up to almost 2000 cycles, after which both states are

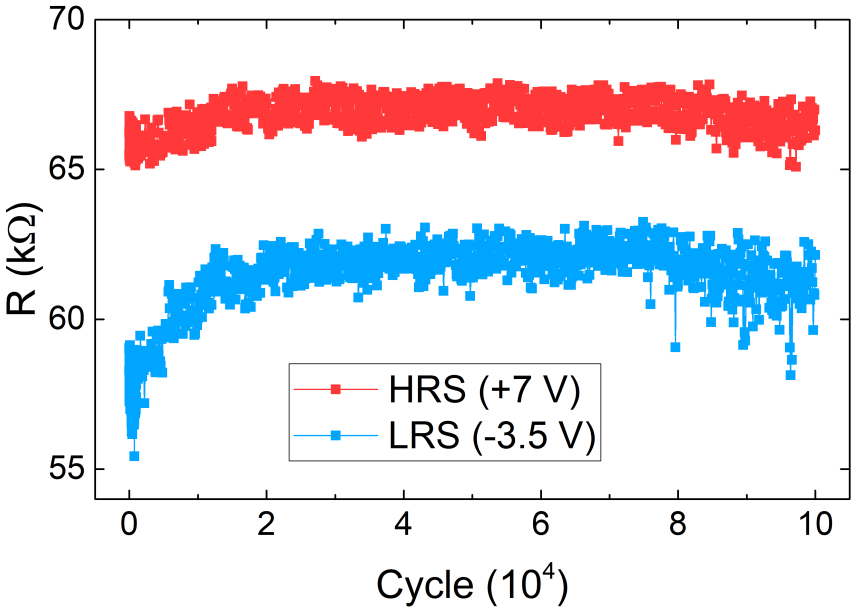

Figure 6.12: Endurance measurement between LRS (−3.5 V) and HRS (+7 V).

stabilized satisfactory. Note that in the initial stabilization region LRS is changing significantly (by ∼8%), while HRS is changing very slightly (by ∼1.5%).

6.5 Conduction and switching mechanism considerations

Some additional details should be addressed to shed light on the possible conduction and RS mechanisms.

◆ $I(V)$ curves were measured in the low voltage range (**figure 6.13**). Here no reading pulses were applied. LRS curve was measured after the half cycle, terminated after -3.5 V application, HRS - after +7 V. The curves were fitted in the region of ±150 mV with the direct tunneling model in the WKB approximation (see section 5.2). The fits yield the parameters of the barrier: ∼4.2 nm thickness, 4.7 eV in LRS and 5.1 eV in HRS potential barrier at the bottom interface, 0.2 eV in LRS and 0.1 eV in HRS potential barrier at the top interface. The higher value found for barrier thickness with respect to the BTO thickness, measured with various methods, is probably resulting from the existence of ion intermixing at the interfaces. Based on the combined TEM+EELS analysis of this particular sample (see section 4.2.5), it was found that at the BTO/bottom LSMO interface there is an intermixed layer, where Mn ions ratio deviates from the nominal in $La_{0.7}Sr_{0.3}MnO_3$ towards more reduced value, and the same was found at the top LSMO/BTO interface, but over the thinner region. As it was shown that intermixed layers demonstrate non-conducting behavior [129], we may conclude that these layers effectively extend the barrier in the junction up to the thickness that matches closely the corresponding fit result: 2.4 nm for pure BTO and 1.6 nm for intermixed layer give the total thickness of 4.2 nm, as measured with TEM.

◆ In order to understand how voltage pulses change resistance values, we investigated the effect of a single voltage pulse application (**figure 6.14a**). Experiment was performed as follows: for some time the device resistance is measured with reading pulses (50 mV, 1 ms) to track the initial state. Then a single pulse, +6 V

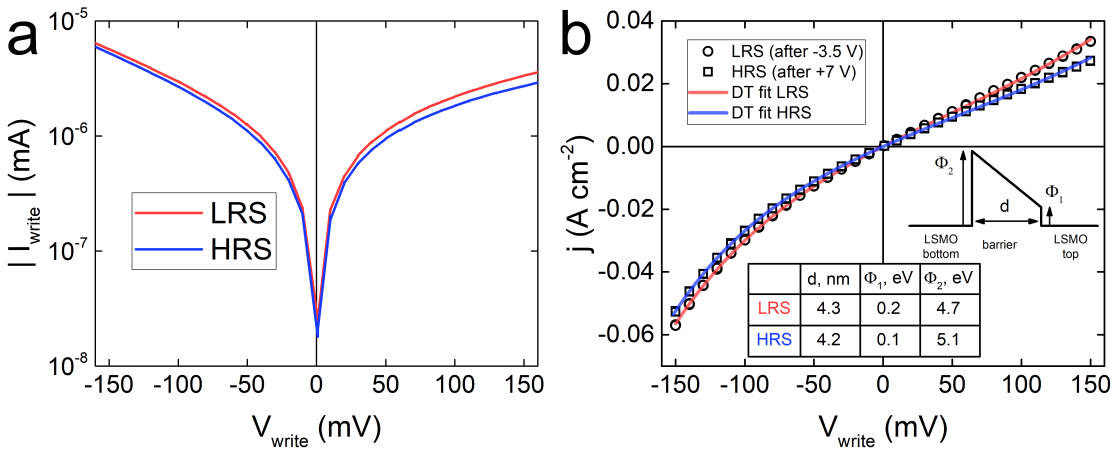

Figure 6.13: $I(V)$ measurements in the tunneling region. a) Corresponding LRS and HRS $I(V)$ curves in the log scale. b) Same curves in linear scale with the direct tunneling fit curves.

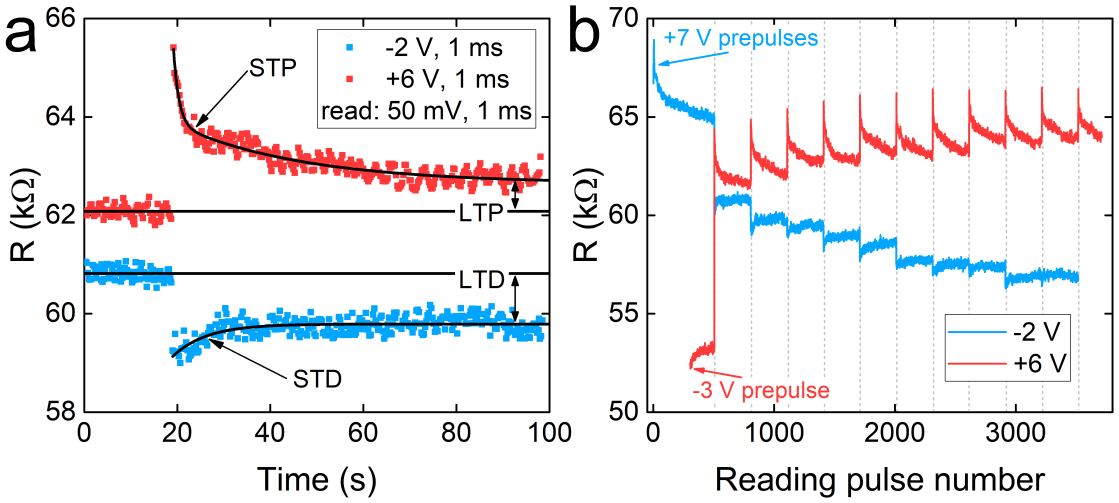

Figure 6.14: Relaxation dynamics from potentiated/depressed states. a) Relaxation of the resistance state, read with 50 mV, after excitation with a single pulse of +6 V (red squares) or −2 V (blue squares). b) Multiple resistance levels are achieved by repeating the same writing pulses, identified by the vertical dotted lines, each followed by reading, tracked with time.

or −2 V (both 1 ms), is applied. Changes after this single writing are tracked with the same reading pulses, as earlier. Pulse application period equals ∼250 ms.

In ∼50 s after the positive voltage pulse application and in ∼10 s after the negative one, a stabilized resistance modification is observed, what was expected, according to fig.6.7. However, right after the writing pulse, the modification is significantly stronger, but is decaying with time. This behavior is analogous to the combination of previously defined LTP/LTD with so called short-term synaptic potentiation/depression effects (STP/STD), which are responsible for, respectively, the long- and short-term memory and learning processes.

The resistance relaxation curves were fitted with decaying exponential function $\exp(-t/\tau)$ to extract the characteristic time constants of the process. It turned out that the time constant of the STD→LTD transition equals ∼7 s, while for the STP→LTP, the sum of two different decaying exponents was necessary for accurate fitting, with the time constants of ∼1 s and ∼27 s. Moreover, the resistance jump in the first moment after writing in the case of +6 V pulse is significantly higher than for the −2 V pulse, while the long-term change is slightly smaller. Therefore, this difference in the first moment jumps occurs not due to absolute pulse voltage value, but rather due to the voltage polarity.

Together these results suggest that there are two transient physical contributions in the resistance behavior after the application of positive voltage pulse and a long-term contribution, possibly different from the first two. After the negative voltage pulse application, there is only one of those transient contribution working (together with the long-term one). Moreover, in this case its conditions are slightly different, what manifests in the modified time constant (7 s) - at this point it is unclear whether it arises from the shorter-term (1 s) or the longer-term one (27 s).

◆ The same stimulation/relaxation procedure was repeated sequentially with the same pulses (**figure 6.14b**). In the beginning of each sequence, the pre-writing was made with one −3 V pulse for the +6 V sequence and five +7 V pulses for

the −2 V sequence - to set the initial state, opposite to the direction of resistance modification. Each next writing pulse was applied after the relaxation had been finished. This lead to a step-like resistance evolution. The values of resistance jumps were extracted from the sequence (**figure 6.15**): ΔR_{long} was calculated as the difference between the stabilized resistance levels after and before the writing pulse, and ΔR_{short} was calculated as the difference between the peak of the resistance jump right after the writing pulse and the stabilized level after the same writing pulse (sketches in the fig.6.15 are given for clarification). It is seen that ΔR_{long} is largest in absolute value after the first applied pulse and approaches 0 with further pulse application - similarly to the switching curves (fig.6.7). This indicates saturation of the resistance state set with a particular voltage and duration of the writing pulses. However, the ΔR_{short} values are nearly constant with pulse application: +3% for the positive and −0.7% for the negative voltage pulses, which is another sign that the long-term (non-volatile) modification of device resistance is physically separable from the short-term (volatile) one. Moreover, although the writing currents in the negative voltage range are significantly higher than in the positive voltage range (see the diode-like $I(V)$ curve in fig.6.6), the intensity of the short-term excitation with positive voltage pulses is four times higher than with negative voltage ones. This supports the implication of the presence of a transient process, triggered only with the positive voltage pulses, together with the second, bipolar, transient process, which is significantly less intense.

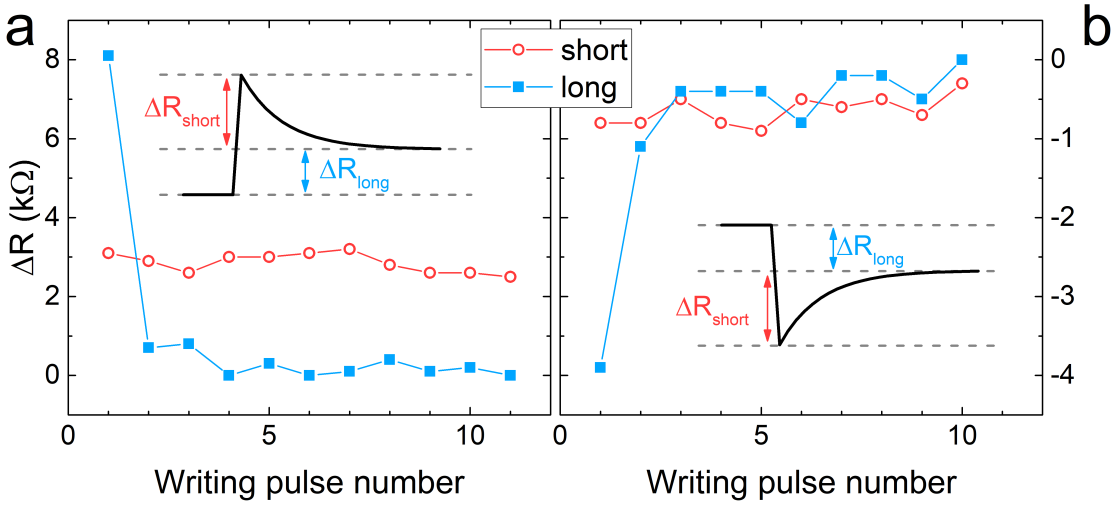

Figure 6.15: Short- and long-term resistance jumps, extracted from fig.6.14 for positive (a) and negative (b) voltage pulse sequences. Inset sketches show the definitions of ΔR_{short} and ΔR_{long}.

◆ Since the ferroelectric nature of BTO may play the role in the switching and conduction of the device, the ferroelectric properties were assessed with PFM measurements, performed on the micro-pillar that was left uncovered with Au pad, directly on the top LSMO surface.

Electric field poling was performed on 10×10 μm^2 area with +7 V, applied to the bottom electrode of the sample (same polarity as in the previous measurements). External area was not poled prior to "reading" scans. The PFM maps (**figure 6.16**) were obtained in the following way: the "writing" scan was performed by moving the line up from the bottom, and the "reading" scan after that was performed by

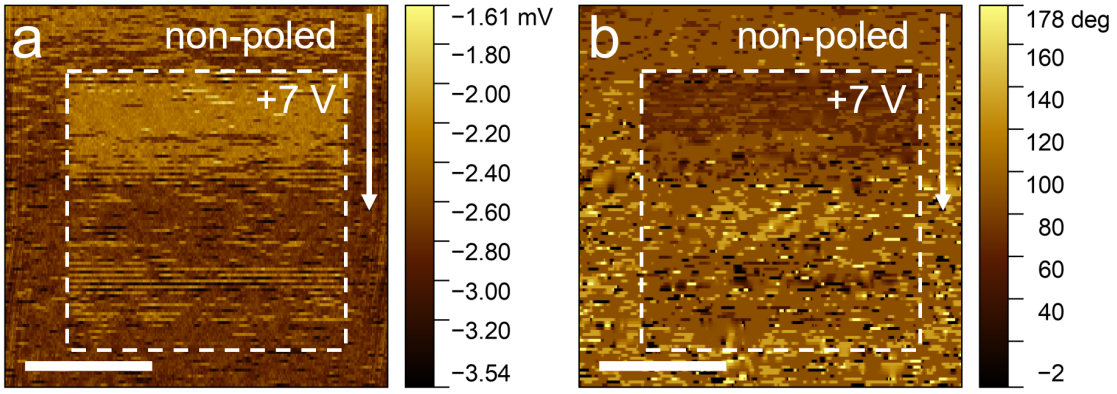

Figure 6.16: PFM amplitude (a) and phase (b) maps. Squares indicate the area, poled with +7 V applied to the sample's bottom electrode, while the external area was not poled. Arrows indicate the scanning direction. Scale bar is 5 μm.

moving down from the top, indicated in the figure with a white arrow. The maps clearly show that the contrast of the poled region is preserved only in the beginning of the "reading" scan, and close to the finish it is almost indistinguishable from the non-poled region both in PFM amplitude and phase. Since the application of +7 V switches the polarization into the "up" state ($\vec{P}$ is pointing from the bottom electrode towards the top electrode), we can conclude that the preferred remnant polarization direction is "down" - both in the non-poled state, and in some time after the positive voltage poling. The effect of the preferred downward polarization of BTO was previously observed and reported in the samples grown in the same PLD set-up [129].

To elaborate the observed effect, the PFM spectra were recorded at various points of the sample surface (**figure 6.17**). The measurements show the conventional amplitude and phase loops, which are shifted towards positive voltage region, which indicates the presence of a built-in electric field. This field does not allow to stabilize

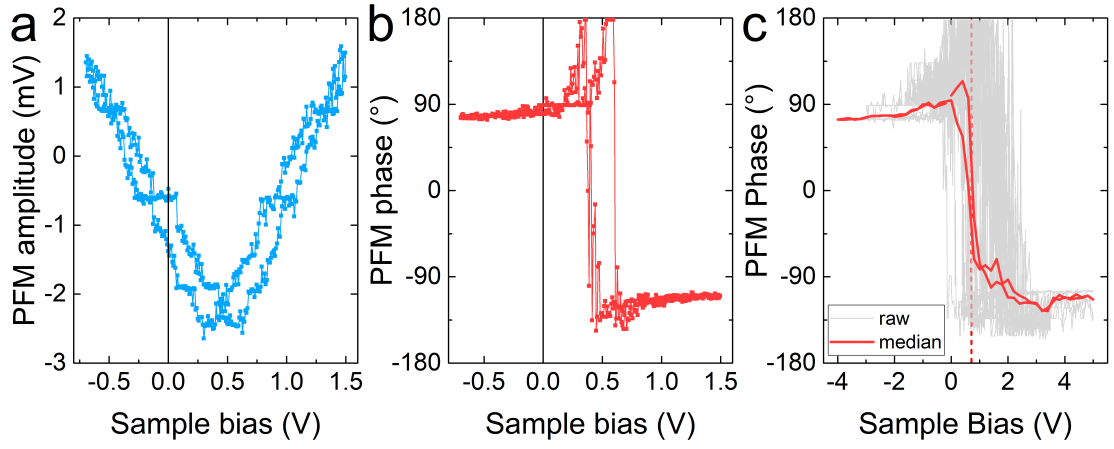

Figure 6.17: PFM amplitude (a) and phase[†](b) spectra. c) 12 PFM phase spectra, measured at 9 different points (grey), and their median (red). Red dashed line indicates the center of the median loop, i.e. average built-in voltage value.

[†]Note, that the PFM phase spectra were not corrected and are presented as measured. The sharp peaks and peculiar shape of the loop in fig.6.17b is likely due to loop flipping, caused by phase overshoot beyond $\pm\pi$ region in the lock-in amplifier.

the "up" polarization direction and leads to a single remnant polarization state - "down". The statistical significance of the effect was verified with multiple measurements of the phase loops at 9 different points over the sample surface (fig.6.17c). In average, the built-in voltage value equals ∼0.7 V. Note, that the voltage values in PFM experiments may be not equivalent to the values in the write-read measurements due to different contacting (local AFM tip contact to top LSMO surface vs wire bonded to a macroscopic Au pad). However, it is clear that the coercive field, extracted from the shifted loop as half of the loop width, is reasonably close to the values, commonly reported for BTO thin films [178].

Such effect of the built-in electric field in LSMO/BTO/LSMO heterostructures with ultrathin BTO layer was previously reported [179]. It occurs likely due to accumulation of oxygen vacancies at the BTO/bottom LSMO interface.

Thus, we believe that the aforementioned transient process, that occurs exclusively after the positive voltage pulse application, corresponds to the switching of BTO polarization. In this case, LSMO/BTO/LSMO heterostructure operates as a conventional FTJ, resistance of which is modulated with polarization direction [180]. The difference from the traditional consideration is that polarization direction in our devices is not stable in time, what makes the resistance also time-dependent during the polarization reversal process.

◆ The remaining bipolar short- and long-term RS processes are related to the chemical properties of our thin-film layers.

It was shown by our group, on the samples grown by the same procedure in the same PLD chamber, that the non-volatile RS may be realized in BTO/LSMO bilayer system via reversible redox reaction at the interface between the layers [129]. Conductive properties of LSMO-based devices are highly sensitive to the ratio between Mn^{3+} and Mn^{4+} ions at the interfaces. It may be affected, for example, by oxygen vacancy accumulation or intermixing with the adjacent layer. Since the presence of short-term resistance overshoots after negative voltage pulse application (fig.6.14) was shown to be independent of the ferroelectricity of BTO, it allows to assume that, with application of the electric field, the drift of positively charged mobile oxygen vacancies is possible along the field direction, with subsequent re-diffusion after the field is removed. Organized in such a way, the vacancy accumulation at the interfaces can temporarily modulate the device resistance. This effect explains the second transient process, that is clearly observed after negative voltage pulse application and, in principle, should have a contribution after positive voltage pulse application, but likely to a lesser extent than ferroelectric polarization relaxation (compare ΔR_{short} in fig.6.15a,b)

Some oxygen vacancies (V_O), accumulated at the interfaces, can take part in the redox reactions[‡] [129]:

$$Mn^{4+} + e^- \rightarrow Mn^{3+}, \tag{6.3}$$

$$Mn^{4+} + \frac{1}{2}O^{2-} \rightarrow Mn^{3+} + \frac{1}{2}V_O. \tag{6.4}$$

According to LSMO phase diagram [181], the maximum conductivity is observed in

[‡]In the chemical consideration, oxygen vacancies are treated just as empty oxygen sites, which are electrically neutral. On the contrary to the quasiparticle description, representing the oxygen ionic movement, where mobile oxygen vacancies are positively charged, similarly to holes in semiconductors.

$La_{0.67}Sr_{0.33}MnO_3$, i.e. with Mn^{3+}/Mn^{4+} cation content ratio approximately equal to 2. Therefore, *both* reduction and oxidation reactions (which modify the Mn cation content ratio) should result in the local conductivity *decrease* of LSMO. If the initial LSMO composition is not optimal (either uniformly over the whole layer, or due to some local non-uniformity), oxidation could lead to increase *or* decrease of conductivity, depending on the initial chemical state, and reduction would necessarily lead to the *opposite* effect. However, slight or local deviations from optimal LSMO composition would be very hard to detect by any method of composition analysis, therefore, not simplifying the consideration significantly. Moreover, in the particular case of the mixed LSMO/BTO interface, some of the Mn cations are substituted by Ti^{4+}, and, while on average this should not change the Mn^{3+}/Mn^{4+} ratio, the details of conductivity behavior in such a complicated system as $La^{3+}_{1-x}Sr^{2+}_{x-y}Ba^{2+}_{y}Mn^{3+}_{1-x+2\delta}Mn^{4+}_{x-y-2\delta}Ti^{4+}_{y}O^{2-}_{3-\delta}$ may differ from $La_{1-x}Sr_xMnO_3$, which, to our knowledge, was never systematically investigated. Therefore, it is quite challenging to predict the exact effect of redox reactions on the conductivity of LSMO/BTO mixed interfaces from general considerations and electrical measurements on LSMO/BTO/LSMO junctions, containing two such interfaces, connected back-to-back.

Thus, in the framework of mobile oxygen vacancies model, when the positive voltage is applied to the bottom electrode (BE) of the junction, oxygen vacancies migrate towards the top electrode (TE), some of those participate in the reduction reaction. In parallel, the oxidation reaction occurs at the BTO/bottom LSMO interface.

Alternative processes could also be considered, such as screening of BTO polarization by free electrons in LSMO. Here with the electric field-induced polarization switching to the upward direction electrons in LSMO have to accumulate at the top interface to screen the positive bound charges. According to the conduction mechanism of LSMO, this may happen only due to hopping between Mn^{3+} and Mn^{4+} cations in the double exchange chains, which in the case of electron accumulation at the top interface would lead to the reduction reaction 6.3. Similarly, the oxidation reaction would occur at the bottom LSMO/BTO interface, the same as in model of mobile oxygen vacancies. High-resolution TEM-EELS analysis of the Mn^{3+}/Mn^{4+} ratio in the upper interface region before and under electric field application could in principle confirm or refute the exact operating mechanism. At the scale of the device, the overall resistance increases, however the effect of the oxidation and reduction on the resistance of each interface cannot be extracted unambiguously (**figure 6.18**).

With pulses of opposite voltage polarity, the same processes are triggered up to the change of signs or reaction direction. However, the asymmetry of top and bottom LSMO/BTO interfaces leads to significant asymmetry of $I(V)$ curves and some differences in set and reset switching, seen from $R(V)$ curves (see fig.6.6). It is possible that the reduction of the top LSMO/BTO interface is reversible to high extent, while the more significant intermixing of the BTO/bottom LSMO interface does not allow for that, which makes the LRS retrievable with low voltages and causes the diode-like $I(V)$ characteristic of the device. Significantly higher barrier at the BTO/bottom LSMO interface than at the top LSMO/BTO interface, extracted from the tunneling experiments (see fig.6.13) is evidence in favor of the suggested model.

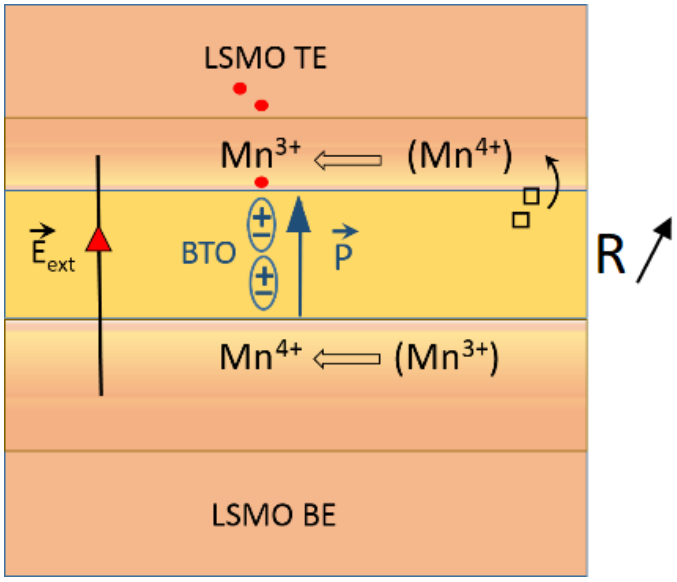

Figure 6.18: Schematic sketch of the RS with a $Mn^{4+} \leftrightarrow Mn^{3+}$ redox reaction occurring at both interfaces under application of a positive voltage to BE. The BTO polarization is switched upwards and the oxygen vacancies (squares) migrate upward, while electrons in LSMO TE accumulate near the interface with BTO for polarization screening. The total device resistance increases.

◆ To summarize, in this chapter the analog RS effect in the thin barrier junctions grown on NSTO substrate was described. Gradual switching was observed in devices of the broad resistance range, and is suggested to occur due to continuous variation of the leakage conditions over the sample area. However, the RS mechanism was found to be the same for all the devices, even of significantly different resistance values. Stable analog switching allows to implement the conventional memristive functionalities, such as LTP/LTD, while STP/STD were realized due to the additional transient features of the RS. The possible RS model was formulated on the basis of the detailed experiments on the device resistance relaxation after single pulse excitation and PFM mapping and spectroscopy. We suggest that the non-volatile RS occurs due to the redox reactions at the BTO/LSMO interfaces, involving oxygen vacancies and/or screening electrons, and thus the long-term resistance level stabilization is realized via variable redistribution of trapped charges at the layer interfaces. On the other hand, mobile oxygen vacancies can accumulate at the interfaces in a non-reactive manner, which allows them to re-diffuse into the BTO layer after external electric field removal. However, this is not the only cause of the time-dependent device behavior. The more significant transient process occurs after the application of the positive voltage (to the BE, while TE is grounded) in the form of BTO polarization reversal to the upward direction (toward TE). Due to large built-in electric field this polarization direction is not stable, resulting in the polarization relaxation to the more stable downward direction (toward BE). The time scales of the suggested transient processes (of the order of 1 s−1 min) are compliant with the literature reports [182, 183].

Chapter 7

Second order memristor for biorealistic emulation of synapses

In this chapter we address more extensively the memristive operation of the semiconducting-like RS devices, described in the previous chapter, in relation to biochemical processes that occur in synapses.

7.1 Justification and prerequisites

In the chapter 6 it was shown that a single voltage pulse excitation with either a positive or negative polarity applied to the BE of our device, with TE grounded, results in a resistance jump, followed by the decay to some level, that is defined by the initial resistance state (see fig.6.14). This transient process is very similar to the short-term plasticity effect in neuroscience [184] (**figure 7.1**). The concept of mimicking the biological properties in neuromorphic electronic devices is well explored in the last decades [20, 22, 185], although in the majority of cases only the long-term plasticity is implemented in memristors as the way of learning emulation. However, the inherent transient behavior in some memristor variants allows to mimic a wider range of important synaptic functions [186–189], which may be used as

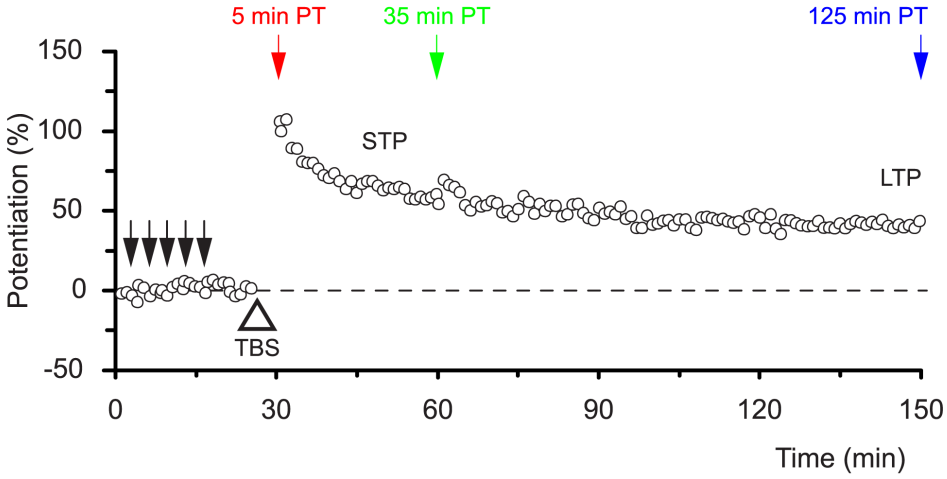

Figure 7.1: Example of the STP effect, recorded in rat hippocampal slices. Potentiation, induced by theta-burst stimulation (TBS, open triangle), consisted of a declining phase (STP) and a sustained phase (LTP). Adapted from ref.184.

the additional functionality for spatio-temporal patterns recognition with hardware spiking neural networks [190–192]. This kind of memristors is referred to as the "second order", due to higher level of biological complexity captured in the electronic device, in comparison with the conventional memristors, that were later dubbed the "first order" ones. At first we will address the biological mechanisms behind such transient behavior in the synapses and compare them to the RS mechanism of our devices to show that, based on the observed resistance relaxation, it should be possible to emulate various synaptic functionalities.

◆ In the biological synapse, the transmission of electric pulses, or "spikes", is carried out by the release of neurotransmitters into the synaptic cleft by a pre-neuron and the recapture of these by the post-neuron, via a complex sequence of events: opening at the level of cell membranes of channels permeable to K^+, Na^+ [14], Ca^{2+} ions [193], fusion of vesicles [194], activation/accumulation of AMPA and NMDA receptors [195], etc. In particular, the sensitivity of the synaptic weight to stimuli is regulated by the concentration of Ca^{2+} ions, which rises under the effect of a spike, then decays exponentially over a range of $10^{-3}-100$ s [196–198]. This effect provides the transient conditions for transmission tuning on a short time scale, with or without long-term effects. Importance of the phenomenon is in the fact that Ca^{2+} content contributes to the ionic conductance of the synapse by itself, and, moreover, increases the modulation effect of the spike if the latter is fired when the Ca^{2+} concentration is still high.

In our LSMO/BTO/LSMO junctions, the transient behavior of BTO polarization and oxygen vacancies is by description very close to Ca^{2+} ionic dynamics, while non-volatile redox effect corresponds to the various processes, responsible for LTP/LTD (**figure 7.2**). Therefore, the memristive functionality of our devices is possible to be extended beyond STP/STD effects, discussed in the previous chapter, to, e.g., paired-pulse facilitation, spike rate-dependent plasticity and spike-timing dependent plasticity (which is also a first order effect, but has the possibility of alternative realization in the second order systems).

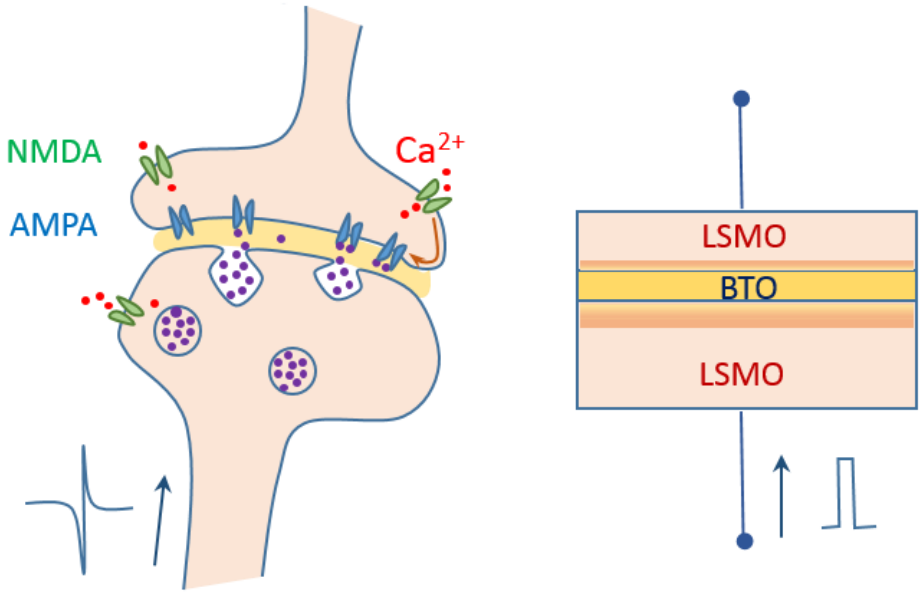

Figure 7.2: Schematic image of a biological synapse and the LSMO/BTO/LSMO memristor.

7.2 Paired-pulse facilitation

Paired-pulse facilitation (PPF) is one of the most explored forms of STP [186,200] (**figure 7.3**). Physical nature of the effect is the following (**figure 7.4a**). A pair of spikes is applied to the synapse with some time delay between them. The first spike induces STP and, possibly, LTP. If the second spike arrives well after the relaxation of STP, its effect is identical to the first one, except the initial synaptic weight level is elevated. Thus, on the long term, the effect of the pair of spikes (LTP in the fig.7.4a) would be just a sum of LTPs of individual spikes, and on the short term, STP of the second spike (STP in the fig.7.4a), considered with respect to the initial moment (before the first spike), would be higher by the amount of LTP of the first spike. On the other hand, if timing of the second spike is such that at the moment of its arrival the content of Ca^{2+} ions in the synaptic cleft has not completely decayed, then its short-term effect would be significantly amplified (PPF short-term in the fig.7.4a), which will result in the enhanced synaptic weight change on the long-term as well, compared to simple sum of two spikes (PPF long-term in the fig.7.4a). Note that the enhanced long-term synaptic change may be induced via spike pairing at low time intervals even when individual spikes are unable to do that (i.e., no potentiation at high interval values), which was demonstrated in the ref.199 on the synapses from different tissues of the hippocampus (fig.7.3). In principle, the lower the interval between the spikes - the higher the paired pulse facilitation effect. Although, with the interval decrease, at some point it may reach the timescale of chemical processes, responsible for synaptic transmission, which technically would make the pair of spikes less and less distinguishable from the single spike, so the PPF effect would decrease rapidly [200].

An important detail of the PPF experiment is the association of one of the electronic device properties with the synaptic weight. Effectively, synaptic weight is a measure of the synapse conductivity, which is usually transposed to the case of memristors as well. However, as was shown in the chapter 6, our device is stabilized

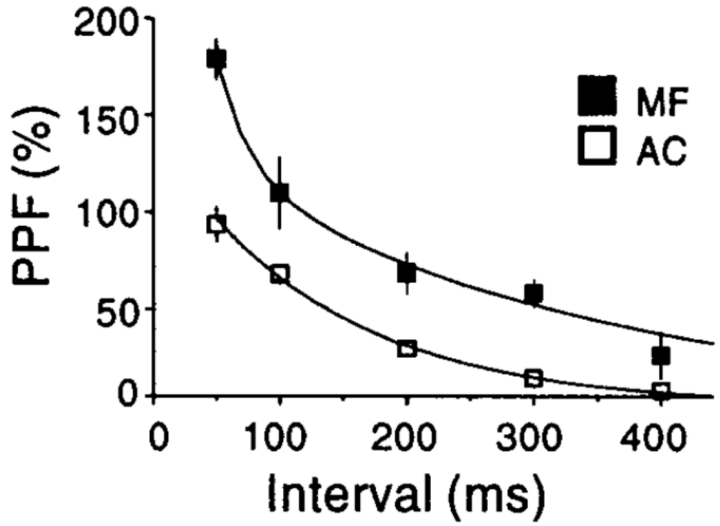

Figure 7.3: PPF measurements in hippocampal slices of guinea pigs, performed in synapses of mossy fibers (MF, filled squares) and associational/commissural fibers (AC, empty squares). PPF was defined as $[(p_2 - p_1)/p_1] \times 100\%$, where p_1 and p_2 are the amplitudes of the excitatory post-synaptic currents, evoked by the first and second applied voltage pulse in the pair, respectively. Taken from ref.199.

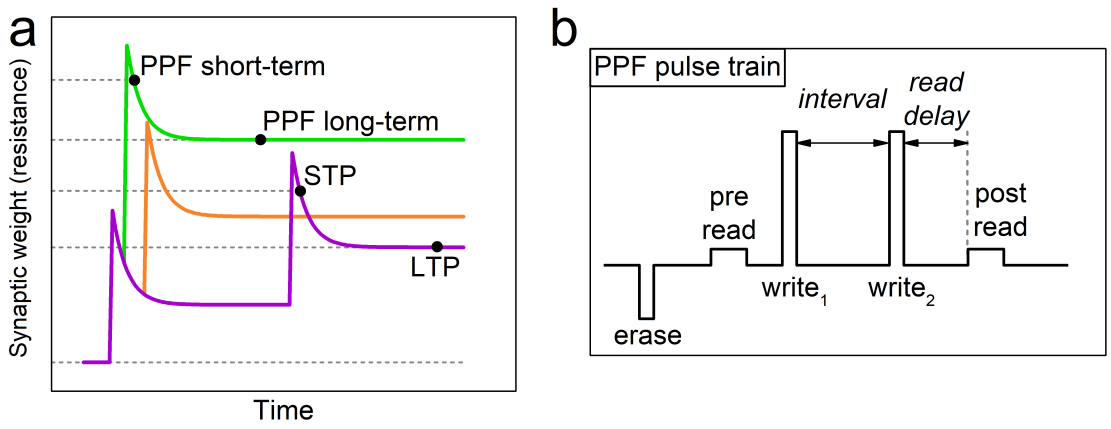

Figure 7.4: Description of the PPF effect in memristors. a) Sketch of the cumulative versus enhanced effects. b) Sketch of the pulse train with an interval between write pulses and a post-read delay that both will be varying.

in the LRS, and the excitation manifests in the resistance increase, i.e., conductance decrease. Therefore, we operate with the device resistance as an analog of the synaptic weight, which will be supported by additional considerations at the end of the section.

◆ PPF experiment is organized in the following way (**figure 7.4b**). A single measurement consists of the application of five consecutive voltage pulses. The first "erase" pulse is aimed at preparing the same consistent initial resistance state R_{pre}, so the resistance modifications could be comparable (which would not be correct otherwise due to non-linear switching curve of the device, see fig.6.7). The erase pulse voltage value is adjusted preliminary for a given writing pair voltage value (usually it is of negative polarity), so the R_{pre} does not change by more than 1% throughout the experiment. The second pulse is used to measure R_{pre}, which is why it is called "pre-read". The pre-read pulse is 50 mV in voltage value and 0.1 ms in duration. Next, a pair of writing pulses is applied at a fixed time interval between them. Finally, the "post-read" pulse is applied to measure the resistance state after the paired excitation, R_{post}. The post-read pulse is the same as pre-read. The time delay between the second pulse in the pair and post-read can be adjusted to differentiate short- and long-term effects.

Two sets of writing voltages (equal for the pulses in a pair) were used for PPF measurements (**figure 7.5**): +5 V and +2 V. The resulting synaptic modification was tracked as the relative resistance change:

$$\frac{\Delta R}{R} = \frac{R_{post} - R_{pre}}{R_{pre}},$$

and was measured at the short (5 ms) and long (2 and 1 s for +5 V and +2 V, respectively) post-read delays. Duration of the writing pulses equaled 70 µs. Value of the time interval between the pulses in the pair was varied from 1.7 to 32 ms. To keep R_{pre} constant, V_{erase} was adjusted to −3 V and −2 V for +5 V and +2 V writing voltages, respectively.

PPF effect is indeed observed in our devices. For the case of +5 V value of the pulse voltage of the writing pair (fig.7.5a), it is seen that $\Delta R/R$ (or PPF index), both for short- and long-term post-read timescale, strongly depends on the time

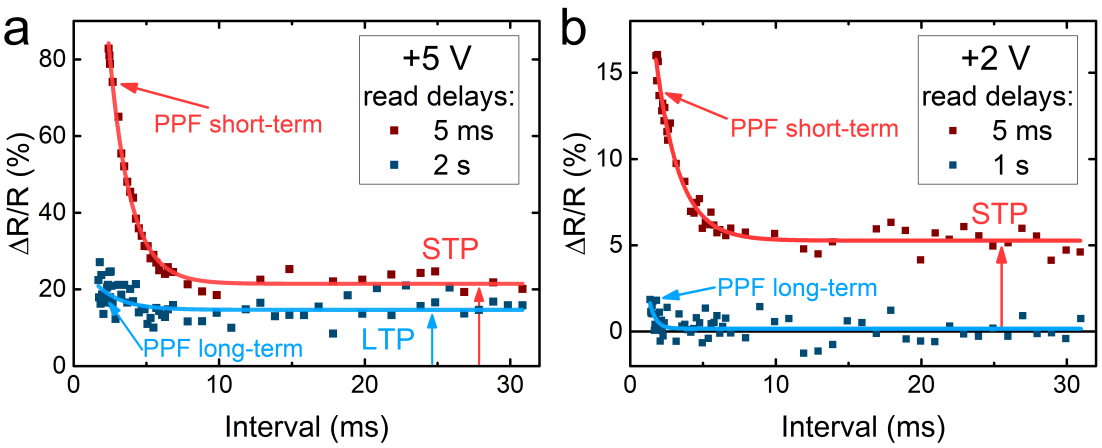

Figure 7.5: Relative change of the junction resistance after the paired-pulse stimulation with respect to the initial resistance value (R_{pre}), as a function of the time interval between two writing pulses of +5 V (a) and +2 V (b). Red (blue) curve corresponds to short (long) post-read delay.

interval between pulses of the pair. The synaptic weight increase is facilitated at short intervals, and with the interval increase the facilitation decreases. The significantly smaller long-term PPF index with respect to the short-term one is another manifestation of the time-dependent second-order dynamics, that was demonstrated earlier with resistance relaxation. The facilitation, induced by pulse pairing, at the smallest pair pulse interval (1.7 ms) decreases from more than 80% at the short term (5 ms post-read delay) to 25% at the long term (2 s post-read delay), while at the largest intervals the facilitation only slightly decreases from 20% to 15% in the same comparison. As for the case of +2 V pair of pulses (fig.7.5b), it is seen that on a long-term post-read time scale, the pair induces no resistance modification: PPF index fluctuates around 0 for the major part of the interval range, except the smallest ones, where $\Delta R/R$ reaches about 2%. However, on the short-term post-read time scale, at the small intervals between paired pulses, the facilitation of up to 15% is still induced, while at 7 ms interval and higher the change is only around 5%, which corresponds to the STP of individual +2 V pulses. This result shows that even when sufficiently low voltage pulses are applied, so that no LTP is induced, the short-term PPF still may be significant. Notably, after approximately 7 ms intervals for the short post-read delay and no more than 5 ms for the long one, the PPF index dependency goes to a plateau, what allows to set the time limit of the transient process activity.

It is also worth noting, that with the use of negative voltage pulse pairs PPF was not observed in our devices. This is another argument to treat resistance as an analog of the synaptic weight, since it is the resistance that demonstrates excitation and relaxation after the application of the voltage of positive polarity. Due to asymmetry of the explored transient processes with respect to voltage polarity, we can assume that ferroelectric polarization relaxation is the key process that allows PPF to occur, while oxygen vacancy diffusion is likely decaying too quickly to be implemented in PPF using the SMU time scale accessible with our apparatus. Although the resulting PPF time scales are qualitatively correlating with the resistance relaxation times, observed after excitation of the devices with single voltage pulses, the accurate time constant values of the considered physical processes may be assessed only with more complicated measurement techniques, for example, impedance spectroscopy.

7.3 Spike rate-dependent plasticity

Spike rate-dependent plasticity (SRDP) is a synaptic effect that involves an absolutely different paradigm, in comparison to LTP/LTD, STP/STD and PPF (**figure 7.6**). First of all, although all these effects were demonstrated in the biological samples, the conditions of their observation are relatively artificial and idealized. In the operational brain, the spikes never arrive at the synapse completely isolated for substantial time periods. Instead, the spikes are being sent rather regularly, with the intensity of the external stimuli coded into the spike sequences via varying the firing timing or the frequency of spike arrival, as possible realistic options. SRDP emerged as a model of such process in the framework of initially phenomenological Bienenstock-Cooper-Munro (BCM) theory of plasticity in visual cortex [201–203], that was subsequently experimentally confirmed and explained on the basis of the microscopic mechanism of Ca^{2+} ionic dynamics [193, 195].

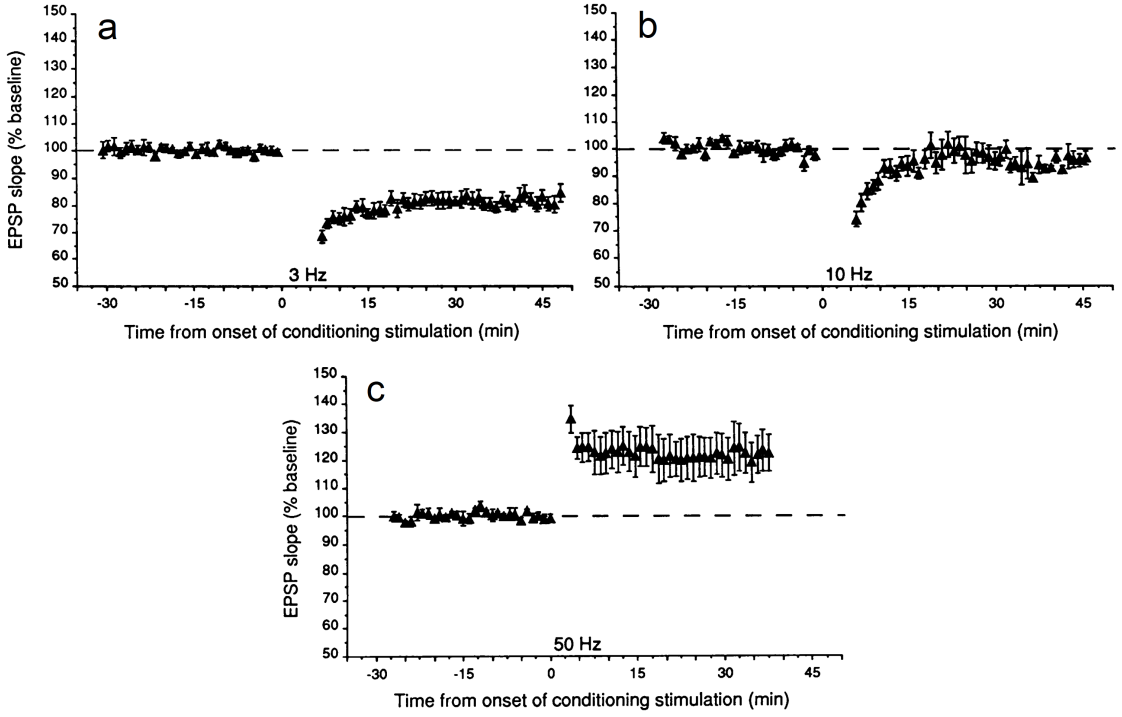

Figure 7.6: Neurological example of SRDP: temporal dynamics of excitatory postsynaptic potential (EPSP), measured in albino rat hippocampus as a response to 900 pulses of various frequencies: 3 Hz results in STD and LTD (a), 10 Hz results only in STD (b) and 50 Hz results in STP and LTP (c). Adapted from [204].

The concept is as follows. An organism is continuously subjected to various stimuli, such as light, what constantly generates sensory signals. After processing in the intermediate layers of the brain, the signals reach the visual cortex neurons. There, in the process of learning and memorizing, when the spikes are transmitted between the neurons, it is the frequency of the spike sequence that defines whether the synaptic weight between those neurons is going to be increased or decreased. High frequencies will induce potentiation, low frequencies - depression, and at some characteristic frequency - the so called "threshold" frequency - no synaptic modification will be made (**figure 7.7**). Moreover, SRDP demonstrates the so called

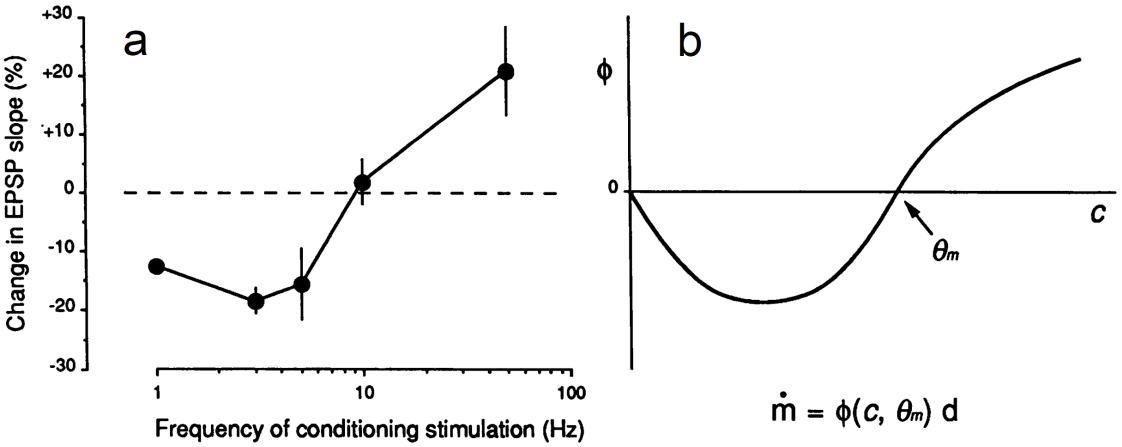

Figure 7.7: Comparison of experimental results (a), extracted from SRDP data (fig.7.6), and the BCM theory [201] calculation (b). Adapted from ref.204.

"experience" dependence [204, 205]: effect of a particular spike sequence frequency depends on the frequency of the previous excitation. On the short time scale, when the previous frequency is lower than the current one, the synaptic weight will increase, and vice versa. This feature is one of the manifestations of a more general effect, which is the "sliding threshold". At any particular moment the outcome of the following spike sequence is defined by the threshold frequency, which can be tuned by the history of external stimulation. In case the organism was subjected to sensory deprivation, activity of the corresponding neurons is inhibited, what results in the depression of the corresponding synaptic weights and the decrease of the threshold frequency. Thus, the spike sequences that were inducing depression due to low frequency in case of normal environment, would instead induce potentiation after a period of sensory deprivation. To summarize, this is a rather sophisticated synaptic functionality that might be quite useful for biorealistic implementation of the so called spatio-temporal pattern recognition tasks (i.e. analysis of the patterns varying both in space and time, such as real-time computer vision), which are in particular demand in the field of artificial neural networks. Therefore, it is advantageous for the particular memristor concept, if SRDP with experience dependence and sliding threshold is demonstrated.

◆ Prior to the main SRDP experiments, certain technical details have to be assessed. In the approach of the fixed frequency spike train application, especially when the frequency needs to be varied sequence after sequence, application of the read pulses, as was done earlier to track the resistance modification, interrupts the desired dynamics, as was seen in the preliminary experiments. Therefore, the synaptic weight should be extracted from the measurements in some other way. It was observed in the write-read experiments (fig.6.7) that the device resistance R during the application of the sequences of identical pulses of positive voltage polarity is correlated with the writing current intensity I_{write}: I_{write} is largest at the first writing pulse of the sequence and exponentially decays down to a certain asymptotic value, similarly to R, which monotonously increases also up to a certain asymptotic value. The dependence between R and I_{write} is close to inversely proportional. So it was decided to use the I_{write} value, measured during application of each pulse of the sequences, as an intermediate measure of synaptic weight. For convenience, a

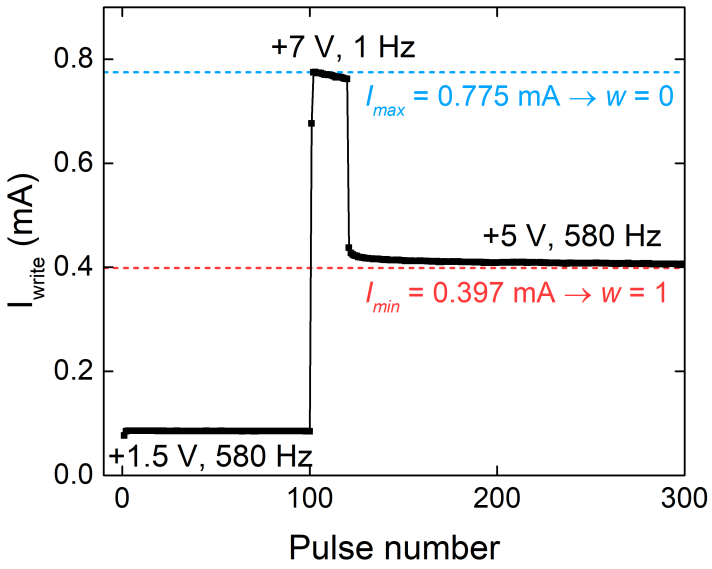

Figure 7.8: Calibration curve for $I_{write} \rightarrow w$ recalculation, where w is the synaptic weight.

calibration procedure was performed to recalculate the current values into weights (**figure 7.8**). +5 V pulses were chosen for SRDP experiments, like for PPF. The I_{write} value of 0.397 mA that is stabilized after the application of 2000 +5 V pulses at 580 Hz (highest accessible frequency for our SMU) was set as synaptic weight w equal to 1. To reach it from the higher current values, the +5 V sequence was preceded by the 100 pulse sequence of +1.5 V at 580 Hz and 20 pulse sequence of +7 V at 1 Hz - during which the peak I_{write} value of 0.775 mA was set as $w = 0$. This I_{write} range covers the whole range of currents that were obtained during SRDP experiments. The recalculation to the weights is done through linear transformation:

$$w(I) = \frac{I_{max} - I}{I_{max} - I_{min}}.$$

While not being exactly equal to the device resistance values, normalized by HRS, the synaptic weight defined with this method allows to correctly track the potentiation/depression phenomena.

◆ The SRDP measurement was performed within the earlier suggested procedure, firstly, with the option of two spike sequence frequencies: 1 Hz and 150 Hz (**figure 7.9**). All the pulses were of voltage value of +5 V, 0.1 ms in duration. 1 Hz sequences consisted of 20 pulses, 150 Hz - of 300. Indeed, we observe the dependence of synaptic weight modification on the spike frequency, with the identical spikes used. The 150 Hz sequence results in monotonous w increase with each spike, or potentiation, and the 1 Hz sequence, in turn, results in monotonous depression. Moreover, the process repetitions yield the same result.

A prominent feature of the experiment is that it is possible to implement synaptic inhibition, or "forgetting", without the necessity of the spikes of opposite polarity. The memristor relaxation occurs naturally during the time when the voltage pulses are not applied, following the mechanism described in the chapter 6. Since the spike sequence frequency is inverse to the spike arrival period, which differs negligibly from the device idle period (pulse duration equals 0.1 ms, while the maximum accessible

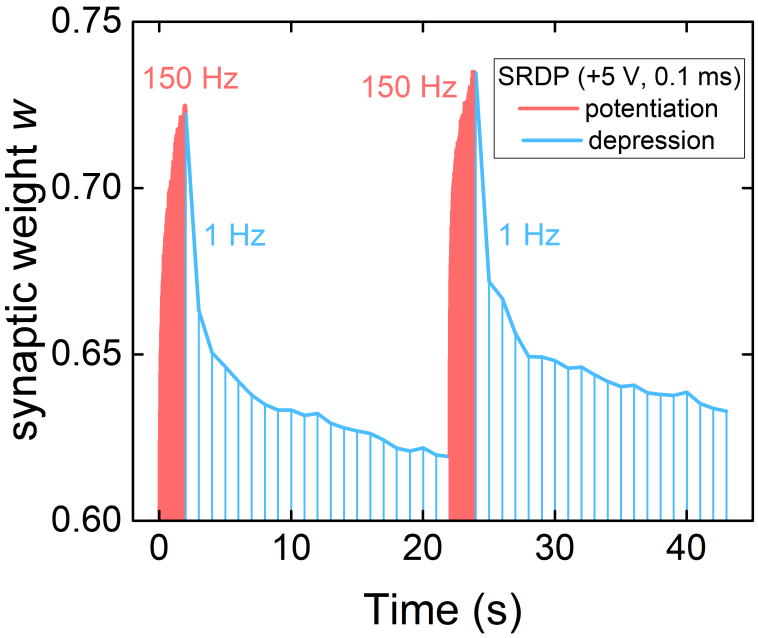

Figure 7.9: SRDP measurement. High frequency (150 Hz) regions correspond to the synaptic potentiation, and low frequency (1 Hz) to the synaptic depression, whereas the same writing voltage value (+5 V) is used at both frequencies.

frequency of 580 Hz yields the period of 1.7 ms), the SRDP potentiation/depression effect is essentially equivalent to paired pulse facilitation/depression (PPF/PPD) for the case of larger number of pulses.

◆ SRDP measurements were extended in order to emulate the experience-dependent plasticity (**figure 7.10**). The same writing pulses were applied at three different frequencies: low, intermediate, and high (5, 50, and 120 Hz, respectively) with different number of pulses in the sequence (10, 50, and 100, respectively). The low frequency sequence always induces synaptic depression, as well as the high frequency always induces potentiation, without any dependence on the order of sequence application. For the intermediate frequency (50 Hz) sequence, the character of the synaptic modification depends on the frequency of the previous sequence: if the previous one is of the low frequency (5 Hz), the weight gradually increases; otherwise (after 120 Hz sequence), the weight decreases.

The weight modification $\Delta w/w$ was extracted for each individual sequence. It was calculated as the relative weight change from the first spike in the sequence to the last: $(w_{last} - w_{first})/w_{first}$. The relative modifications are well reproduced from sequence to sequence, starting from the first 50 Hz sequence (**figure 7.11a**). The weight changes at 50 Hz clearly form two separate groups, that correspond to the different orders of sequence application.

The consistency of relative weight modification with the fixed number of pulses for the sequences of the fixed frequency allows to vary the conditions before the sequence application and compare the results. Experiment was organized as follows. A set of pulse sequences was applied, with the frequencies changing in ascending order from 1 Hz to 580 Hz. Each sequence was preceded by a prepulsing sequence to emulate the various sensory deprivation conditions. Various values of the prepulsing sequence frequencies were tested: 20, 50, 100, 200 and 400 Hz. During each

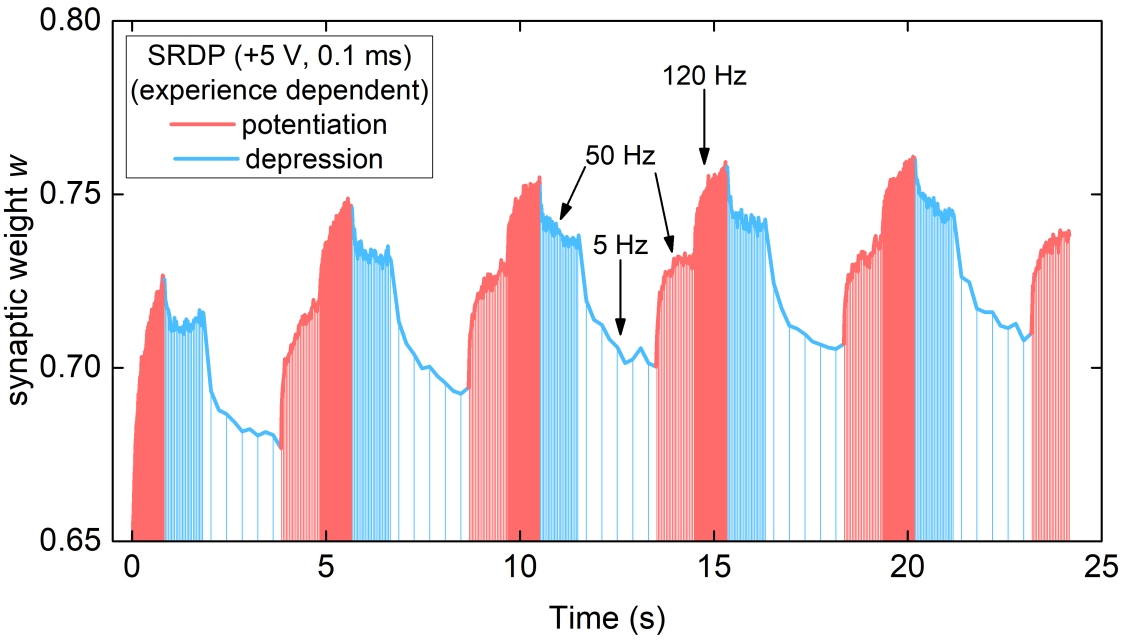

Figure 7.10: SRDP measured with different frequency orders of the successive sequences, attesting of experience-dependent plasticity. Potentiation (depression) regions are indicated with red (blue) lines. Every second drop line was skipped for clearer presentation.

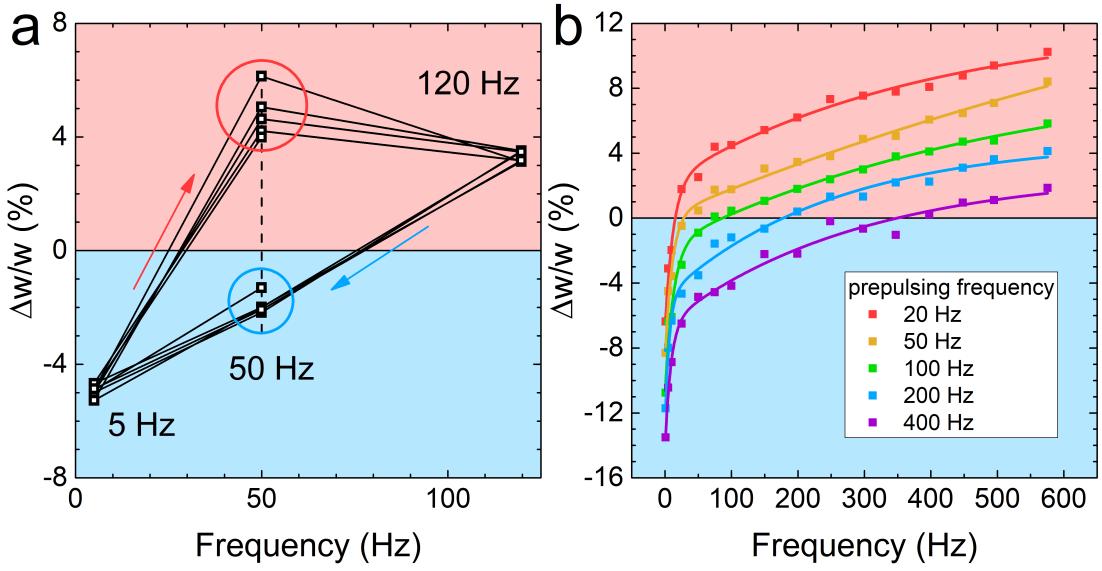

Figure 7.11: Extracted weight modifications with experience dependent SRDP. a) The relative synaptic modification during a spike sequence at a given frequency, extracted from each sequence considered in fig.7.10. b) Frequency dependence of the relative synaptic change during a spike sequence which was preceded by a prepulse sequence with different frequencies, as given in the legend. Same number of pulses (100) was used for all sequences

measurement the prepulsing frequency was fixed, all the sequences consisted of 100 pulses. The relative weight modification values were extracted for each main sequence (i.e., from the ascending frequency list), and presented as five curves, each corresponding to a fixed value of prepulsing frequency (**figure 7.11b**). For each individual curve, the frequency dependence closely reproduces the corresponding one from the biological counterpart [204–207]. The curve intersection of the horizontal axis ($\Delta w/w = 0$) indicates the threshold frequency. The shifts of the curves, corresponding to different prepulsing frequency values, manifest the sliding threshold effect: lower prepulsing frequencies emulate the sensory deprivation, what directly leads to decrease of the threshold frequency, and vice versa.

The threshold frequency values were extracted and compared with the corresponding prepulsing frequency values (**figure 7.12**). The dependence is very close to the straight line of unit slope, i.e. to $f_{threshold} = f_{prepulse}$, but is slightly below this line. In practice, when the main set frequency equals the prepulsing frequency, they act effectively as a single sequence, because the frequency was not changed. Therefore, the weight change at this frequency value depends on the number of pulses and the previous main frequency value from the list: if the number of pulses is large enough to saturate the current, $\Delta w/w$ will equal exactly 0; otherwise, during the main sequence application the w change direction of the prepulsing sequence will be continued - and this direction is defined by the previous applied frequency, as was shown earlier. Thus, the $f_{threshold}(f_{prepulse})$ dependence anyway has to be close to the straight line of the unit slope, but in case the number of pulses in the sequences is not large enough to saturate the current change, each value will slightly deviate from the line in direction, defined by the order of different frequency sequence application.

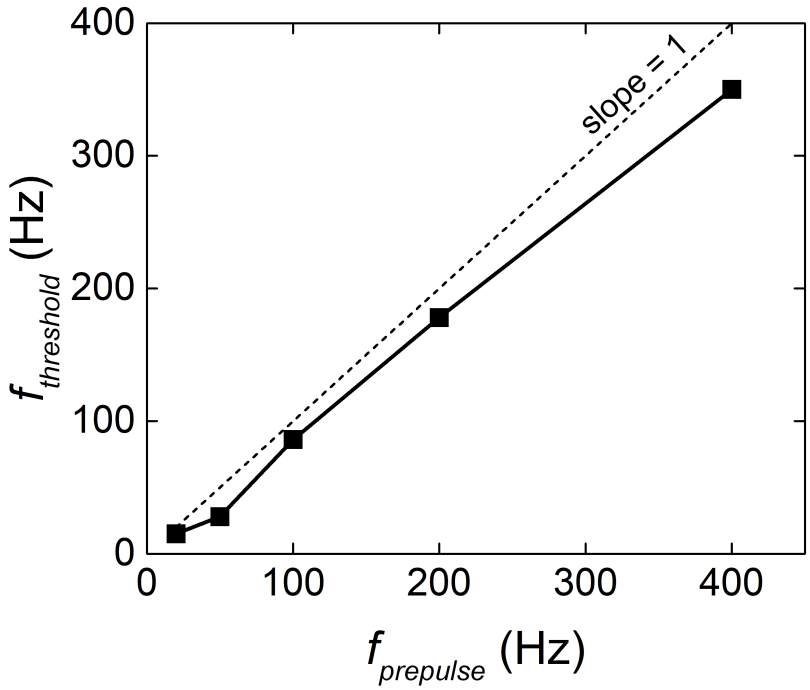

Figure 7.12: Sliding threshold frequency versus prepulse frequency, extracted from experience dependent plasticity measurements (fig.7.11b).

7.4 Spike timing-dependent plasticity

Spike timing-dependent plasticity (STDP) is a relatively more traditional synaptic functionality, implementation of which is usually aimed in memristors as a conventional learning rule (**figure 7.13**). It can be described on the basis of the classical Hebbian theory [208] and any threshold neuronal model (for example, integrate-and-fire) [209]. A synapse is considered between two neurons, one of which is denoted as the "pre-neuron" and the second one - as the "post-neuron". A pre-neuron is considered to be exciting the post-neuron through the given synapse. Any neuron integrates the input spikes, and after a certain voltage threshold is reached, it fires the spikes through its axon for output, which also triggers the so called "echo pulse", propagating in the opposite direction and reaching its input synapses. If the post-neuron firing occurs right after the firing of the pre-neuron, it is considered that this particular pre-neuron caused the firing (the causality is correct) and the corresponding synaptic weight is increased. Otherwise, the pre-neuron was not a primary cause of the post-neuron firing, or the causality is considered to be incorrect, and the synaptic weight is decreased. Moreover, the effect is strongest at small time intervals between the pre- and post-spikes, and decays with its increase. The phenomenon described here is the simplest asymmetric Hebbian STDP learning rule, however in biological systems various combinations of symmetric and asymmetric, Hebbian and anti-Hebbian STDP may be observed.

STDP in the first order memristors is conventionally emulated with the use of specifically programmed spike profiles. This kind of memristors do not require the demonstration of any temporal dynamics. In order to emulate the STDP behavior, approximations of the classical Hodgkin-Huxley neuronal action potential [14] are chosen as a shape for individual spikes. Then the effect of pre-/post-spike arrival to

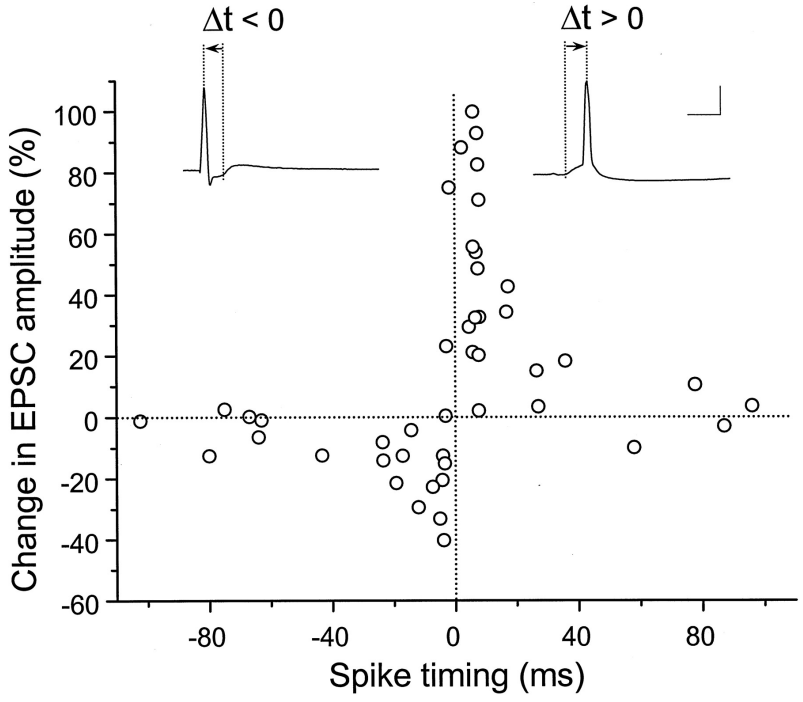

Figure 7.13: STDP measured in cultures of dissociated rat hippocampal neurons. Adapted from ref.21.

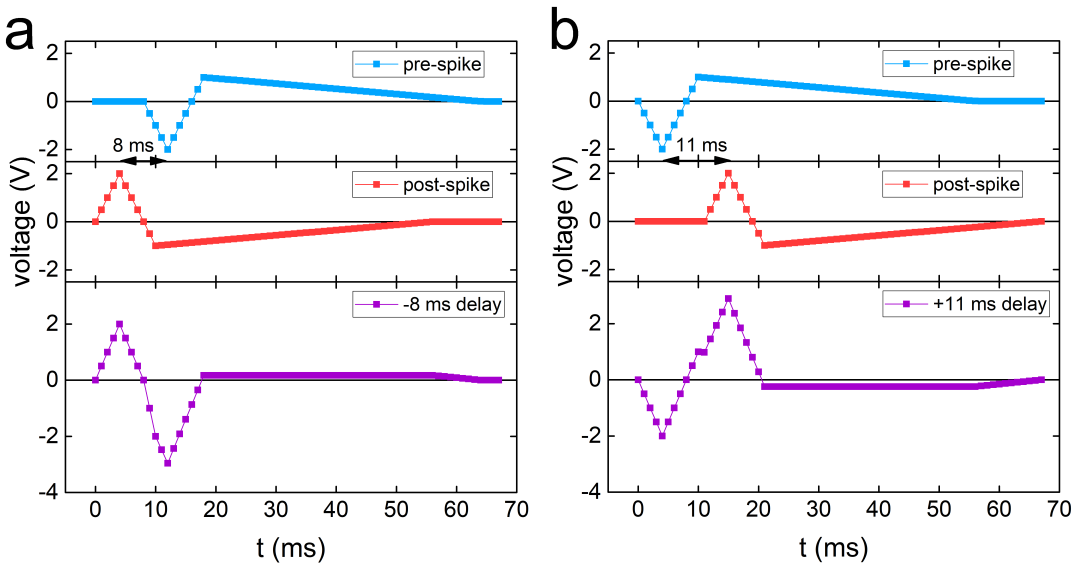

Figure 7.14: Sketches of the pre-spike, post-spike and their sum for cases of -8 ms (a) and +11 ms (b) delays, used for first order STDP measurements.

a single synapse is achieved either with direct application of the spikes to opposite electrodes of a memristor, or with digital mixing of the spikes of opposite polarity and application of the final spike mix to a single electrode.

In our devices the first order STDP measurement was implemented in the following procedure. The single spikes were programmed as three linear voltage ramp pieces, with 0.5 ms step resolution. Spike amplitude was set to 2 V, with 1 V tail of opposite polarity (pulse/tail duration ratio is 1/6). Pre- and post-spikes, instead of independent application with separated SMUs to the opposite electrodes, were emulated with opposite polarities, and their mix was acquired through point-by-point sum for subsequent application to a single electrode (**figure 7.14**). After each spike mix application, the resistance was measured after 1 ms delay with a 20 mV, 10 ms reading pulse (with the initial resistance value measured before the first spike). The resulting STDP curve is presented via the relative resistance change with respect to the resistance level at the horizontal parts of the curve (**figure 7.15**). Peak $\Delta R/R$ values were obtained at -8 ms and +11 ms delays. The first order STDP functionality is shown to be operational in our memristors with the intensity up to 10%.

◆ Since our memristors demonstrate the inherent temporal dynamics, this may allow to implement STDP with simple rectangular voltage pulses as spikes, in the purely second order manner (**figure 7.16**). Pre-spike voltage was set to -3 V, post-spike to $+5$ V, both 100 µs in duration. The spike pair application was repeated for 20 cycles at each time delay value to amplify the effect, with 20 ms time distance kept between the cycles. Before each spike pair cycles series, the device was prepared in the same initial resistance state of 33.5 ± 0.3 kΩ with a -3.5 V, 50 ms erase pulse (that controllably sets global LRS of the device) and $+3$ V, 50 ms preset pulse (that controllably sets an intermediate resistance state after the controllable erase), similar to the procedure in PPF measurement. Before and after the spike pair cycles, the resistance was measured with 100 mV, 100 ms reading pulses, from which the

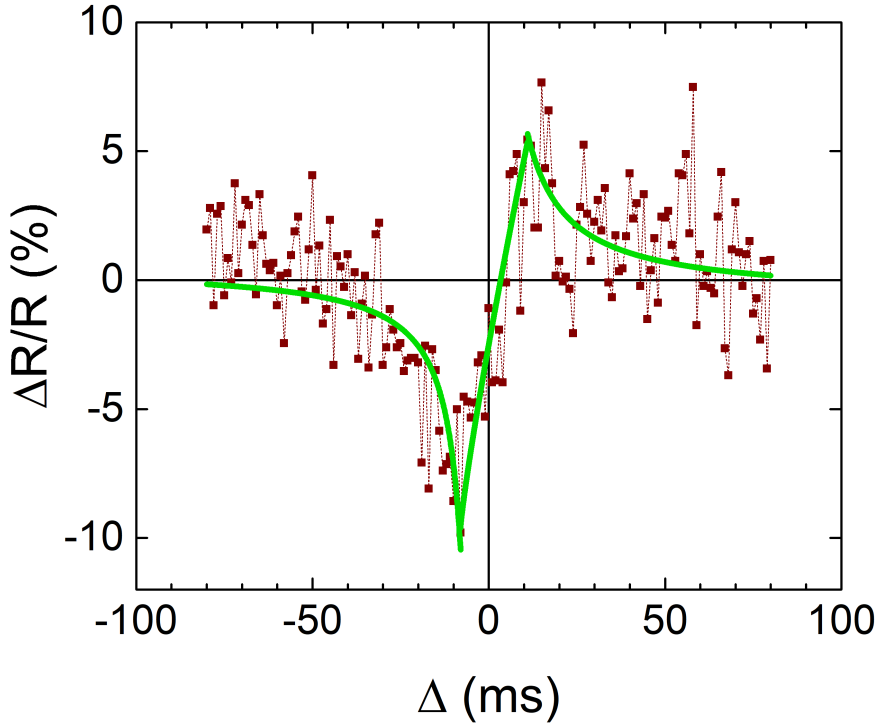

Figure 7.15: First order STDP curve, fitted with hyperbolic functions for clarity

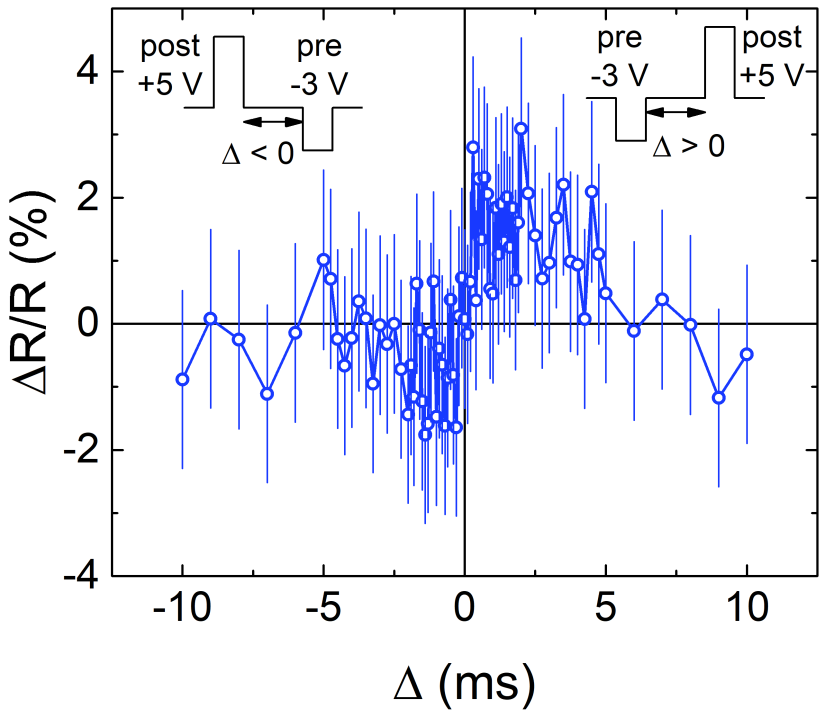

Figure 7.16: Second order STDP measurement. Sketches indicate the order of spike application for the cases of positive and negative intervals.

relative resistance change was calculated. The Gaussian distribution fit of the series of initial resistance values allowed to assign an uncertainty of 1% to the resistance measurement and calculate the error bar values, shown in the figure.

The second order STDP magnitude is significantly smaller in comparison to the conventional first order experiment. One of the possible reasons for that could be the fact that the temporal processes in our second order memristor are essentially bipolar, i.e. a significant part of the post-spike energy has to be spent on the reversal of the transient process polarity, which diminishes the desired STDP-induced synaptic weight modification. In principle, this kind of physical organization promotes the PPF effect and contradicts the STDP effect. According to the literature reports, in case of the ferroelectric second order memristor, based on $Hf_{0.5}Zr_{0.5}O_2$, the transient process is polarity-dependent as well, however the STDP effect was not reported [189]. On the contrary, in the filamentary second order memristors with transient dynamics based on the device heating [186] and oxygen vacancy mobility enhancement [187], both temperature-dependent and, therefore, voltage polarity-independent, STDP induced synaptic weight modification magnitude is comparable to PPF and SRDP.

◆ In conclusion, in this chapter various memristive functionalities in our devices were demonstrated, based on the specific features of RS. PPF effect was demonstrated under various conditions, as one of the strong manifestations of short-term plasticity. SRDP effect was demonstrated in the fullest extent (with experience dependence and sliding threshold effect), in complete accordance with the BCM theory of cortical plasticity. As the main achievement related to SRDP, the "forgetting" mechanism was implemented purely based on the frequency tuning of the sequences of identical pulses, i.e. with no need of resistance state erase with the opposite voltage polarity application. The conventional STDP learning rule was demonstrated as well. Additional data from other devices showing similar memristive features are provided in appendix A.

Chapter 8

Conclusions and perspectives

In this thesis we concentrated on the study of $La_{0.7}Sr_{0.3}MnO_3$ / $BaTiO_3$ / $La_{0.7}Sr_{0.3}MnO_3$ heterostructures: comprehensively characterized their properties, demonstrated the electro- and magnetoresistance effects and established the operation of our devices as the second order memristors.

8.1 Short summary of the main results

◆ It was shown that our tri-layers are grown epitaxially, with some degree of intermixing at both LSMO/BTO interfaces. Top and bottom LSMO layers are clearly identified by their specific coercive fields. Magnetization of the layers is close to or smaller than expected for LSMO films of similar thicknesses, depending on the substrate choice, STO or MgO, respectively. The loss of magnetic ordering in some regions of the films, grown on MgO, seems related to magnetoresistance effects, intrinsic to each LSMO layer individually.

◆ Samples with thick (8 nm) BTO barrier demonstrated stochastic two-level resistive switching, whose properties may significantly vary from device to device. The resistive switching likely occurs in accordance with the filamentary model.

◆ For thin (2−4 nm) barrier samples, resistive switching, on the contrary, was found to be analog, i.e. with the possibility to induce and stabilize any arbitrary resistance state. The device-to-device variability in this case manifested only in the resistance range, independently from the switching mechanism by itself. A phenomenological compact model, based on a diode in series with a resistance, which may be switched from low to high state and back, and in parallel with a leakage resistance, allows to account for resistance changes in all types of devices, from semiconducting-like to metal-like. It is suggested that the resistive switching mechanism involves three phenomena: a non-volatile redox change of Mn valence at LSMO/BTO interfaces, and two transient events: a voltage-induced migration of oxygen vacancies (and/or accumulation of screening electrons in LSMO electrodes) and a reversal of the BTO polarization with relaxation to an imprinted direction towards bottom LSMO electrode.

◆ Based on the observed resistive switching behavior of the thin barrier samples, the operation of the second order memristor was organized. Several synaptic functionalities were demonstrated, such as long- and short-term potentiation/depression,

paired pulse facilitation, spike timing- and rate-dependent plasticity, including experience dependence and sliding threshold effects, based on Bienenstock-Cooper-Munro theory for cortical plasticity. These results are a step towards biorealistic implementation of artificial synapses, which may be of use for hardware-level spatio-temporal pattern processing.

8.2 Some perspectives for future work

◆ Mixing at the LSMO/BTO interfaces plays a crucial role in all phenomena described throughout the thesis. It was convincingly demonstrated that in pristine state the mixing occurs in the most pronounced way at the bottom LSMO/BTO interface, while for the top LSMO/BTO interfaces it is significantly milder. It was observed that the application of an upwards electric field strongly modifies the system both on short- and long-term time scale, whereas the downwards electric field orientation has no effect with respect to pristine state. However, for thick barriers the resistance decreases when the field is applied upwards, whereas it increases for thin barriers. It seems that filamentary switching is involved in the thick barrier case. Differently, the resistance changes can be achieved in analog way in the thin barrier case, supporting the view of reduction/oxidation of Mn ions at the interfaces. It is quite difficult to discriminate between purely electronic mechanisms, consisting of charge trapping/detrapping, and ionic mechanisms, involving oxygen vacancies. Clearly, additional dedicated experiments are necessary to investigate the microscopic changes of the interfacial charge distribution, Mn ions chemical state or accumulation of oxygen vacancies (uniformly at the interfaces or as conductive filaments). Ultrahigh resolution TEM could allow to resolve oxygen vacancy accumulation via local lattice distortions, and the combination with high resolution EELS would allow to assess the Mn chemical modification with higher precision than proposed in the thesis. An important element of such imaging is the possibility to track the changes in observations with the application of electric fields. In the simplest case, it can be organized via *ex situ* switching, which would only allow capture the long-term changes of the limited amount of resistance states and would be quite time consuming. *In operando* imaging, i.e. when microscopy is performed in parallel with the electrical operation of the device, would be perfect for this purpose. Conductive AFM performed on specially prepared cross-section could also contribute to the understanding of the resistive switching in LSMO/BTO/LSMO junctions. Conductivity mapping of the junction cross-section could allow to separate the contributions of the interfaces from bulk regions. While sample preparation for these experiments is exceptionally complicated, the organization of *in situ* voltage application would be significantly easier in comparison to TEM. One however would be in direct contact with air during the experiments, with probable intrusion of air molecules. Some insights could also be obtained from spectroscopic experiments, such as X-ray photoelectron spectroscopy. Indeed, the technique of standing wave hard XPS (SW-HAXPES) allows to probe the chemical state of the samples with depth resolution without etching.

◆ An additional magnetic functionality of the LSMO/BTO/LSMO junctions was explored with magnetoresistance experiments. The conventional tunneling magnetoresistance effect is highly sensitive to the quality of the interfaces of the ferromag-

netic layers and the barrier itself. Therefore, the observed intermixing phenomena prevent the observation of classical TMR. However a weak magnetoresistance effect in the current-perpendicular-to-plane geometry was observed. Moreover, four distinct magnetoresistance regions were seen, instead of two in conventional TMR case. The correlation of the magnetic fields, at which the peak magnetoresistance was observed, with the coercive fields, measured with VSM, hints to the independence of MR behavior on the relative direction of magnetizations of LSMO layers, implying instead that MR could could occur in the LSMO layers separately. Synchrotron-based spectroscopic methods, such as X-ray absorption or XPS, may be implemented with the magnetic dichroism option (X-ray magnetic circular dichroism, XMCD, and magnetic dichroism in the angular distribution, MCDAD, respectively). These allow to track the changes in magnetism of particular atoms of the sample, however the information is usually averaged over the whole sample. Implementation of standing wave technique, allowing to focus the X-ray intensity with depth resolution, would be preferred, however would also significantly complicate the set-up. Alternatively, polarized neutron reflectometry may be used. It allows to reconstruct the magnetization profile of the magnetic multilayers with reflectivity curve fitting. In the case of LSMO/BTO/LSMO junctions it would help not only to contribute to the explanation of complex MR behavior, but also would give insights on the conducting state of the interfaces with BTO, since magnetic and conducting properties of LSMO are correlated.

◆ Neuromorphic operation of our LSMO/BTO/LSMO devices is quite rich, represented by LTP/LTD, STP/STD, PPF, SRDP (including experience dependence) and STDP synaptic functionalities. SRDP behavior is particularly interesting in the context of spiking neural networks or in-memory computing, e.g., for spatio-temporal pattern recognition tasks. Further characterization of SRDP is one of the interesting tasks for future experiments. It was shown in chapter 7 how changing pulse voltage in PPF experiments it was possible to emulate behavior of different kinds of synapses. Similarly, experiments centered on the voltage and pulse duration dependencies of SRDP could unveil all functionalities for reconfigurable device operation.

◆ An important aspect of the work on LSMO/BTO/LSMO junctions is assessment of the device operation beyond proof-of-concept. In the thesis it was demonstrated that device-to-device variability is quite high for all the considered samples. The growth and fabrication procedure should be further examined to find out possible sources of variability and to attempt to eliminate them. On the other hand, since devices of significantly different resistance ranges demonstrate qualitatively the same resistive switching and memristive behavior, the variability feature could be exploited as an emulation of natural variability of synapses in different regions of the brain. Concerning the cycle-to-cycle variability of individual devices, it was tested that endurance of one semiconducting-like thin barrier device is at least 10^5 cycles, with some signs of wake-up and fatigue effects. Testing endurance of a significantly larger number of device would be desirable. The major challenge in the device assessment would be scaling. Currently, square devices of only 25, 50 and 100 μm in lateral size were fabricated. Testing the operation of devices down to 5 μm could be realistic, since the fabrication may be performed with optical UV lithography, while scaling down to nanometric devices would require electron beam lithography,

which is more complicated. Scaling question is a part of the general challenge of CMOS integration of perovskite materials, which to this day remains problematic. As possible steps in this direction, growth of LSMO/BTO/LSMO junctions on Si with interlayers, or use of more CMOS-friendly materials, with attempts to preserve the operation discovered in this thesis, could be considered.

Appendix A

Resistive switching and memristive data from additional devices

The RS behavior, described in the chapter 6, is universal for the devices on LSMO/thin BTO/LSMO//NSTO sample. The quantitative variability is in the device resistance ranges and their temperature evolution, what was addressed with the compact model (see section 6.2). Here we provide results of RS and memristive experiments on additional devices of different resistances to support the statement.

A.1 Additional semiconducting-like device

The additional SC-like device was of the same lateral size as in the chapter 6, 100×100 μm^2. Its multilevel characteristics (**figure A.1**) are highly similar, both $I_{write}(V_{write})$ and $R(V_{write})$ curves with various V_{max} follow one path during the voltage increase. The $I_{write}(V_{write})$ curve hysteresis in the positive voltage region is even more pronounced. The resistance levels set at various V_{max} relax quite significantly as voltage gets to 0 V, what could be due to slightly different measurement pro-

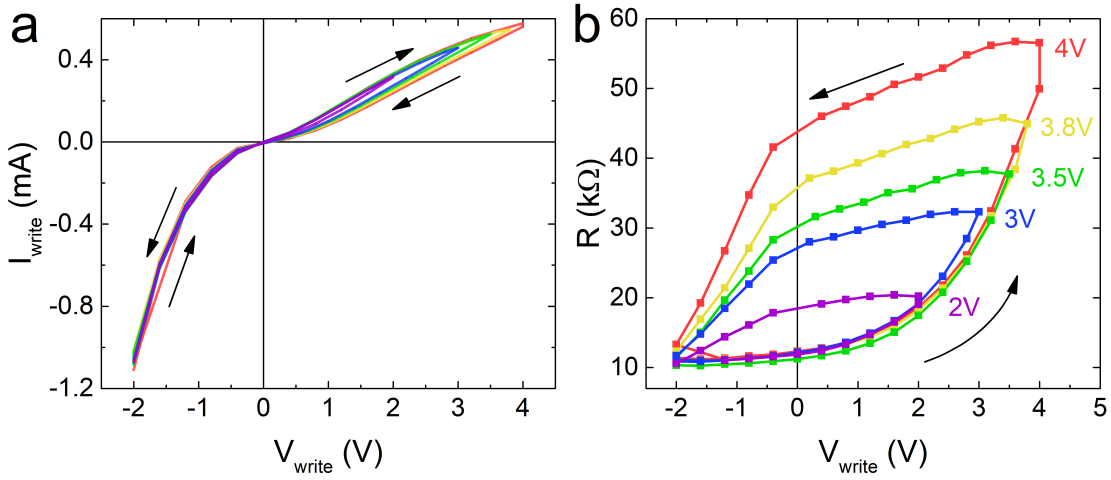

Figure A.1: Multilevel $I_{write}(V_{write})$ (a) and $R(V_{write})$ (b) curves, cycling between -2 V and various V_{max} values, measured on additional 100 μm SC-like device. Arrows indicate the voltage sweeping order.

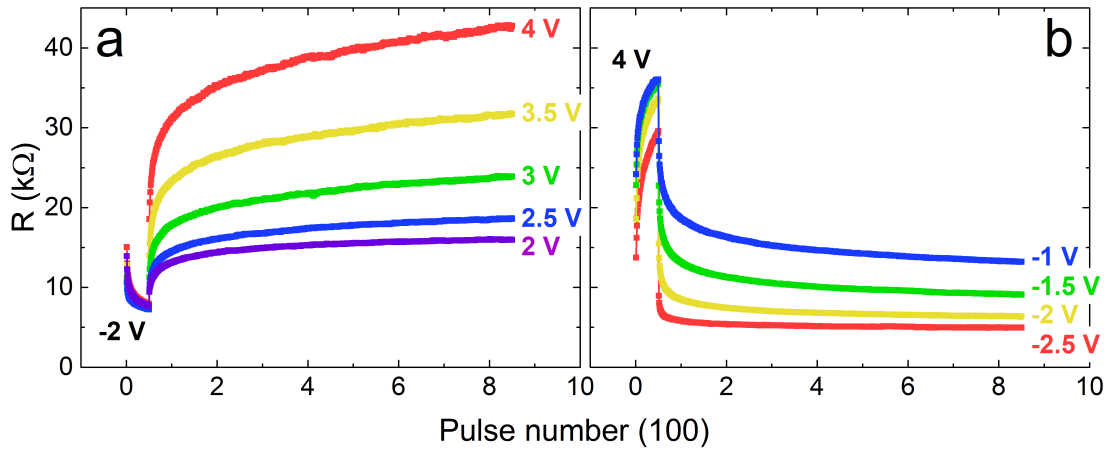

Figure A.2: Multilevel resistance states (from additional SC-like device) set with positive (a) or negative (b) writing pulses, after 50 prepulses of −2 V (a) or +4 V (b). Reading was made with 50 mV.

cedure: here voltage is applied following the same write-read profile (see fig.5.1), but in DC mode instead of pulse mode. Effectively, this works as pulses with high duration - of the order of 100 ms long, what slightly affects the resistance value, as was demonstrated earlier (see fig.6.10).

◆ LTP/LTD behavior in this device is highly similar to the device described in the main text (**figures A.2** and **A.3**), and curve reproducibility here is even higher. Resistance range is slightly less wide here, compared to the $R(V_{write})$ curve in fig.A.1 due to the use of 1 ms pulses, instead of the DC mode, i.e., cumulative voltage application time gets significantly smaller.

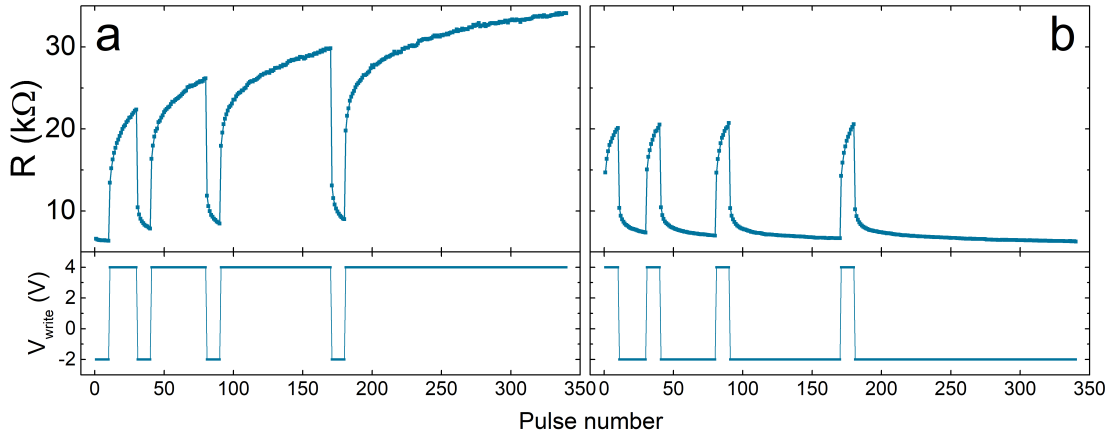

Figure A.3: a) Pulse series (from additional SC-like device) of −2 V writing, followed by +4 V writing, repeated in sequences, in which the number of pulses in the even groups doubles. Reading was made with 50 mV. b) The same with +4 V pulse series, followed by −2 V pulse series.

◆ Resistance relaxation after the single pulses occurs in the same manner as discussed in section 6.5, manifesting STP/STD effects in addition to LTP/LTD (**figure A.4**). The feature of the asymmetric effect of positive and negative voltages is preserved.

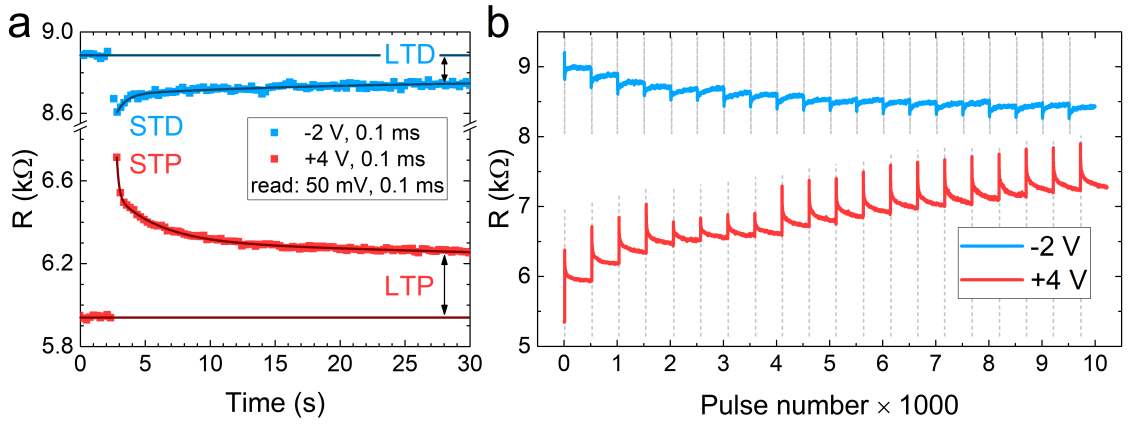

Figure A.4: Relaxation dynamics from potentiated/depressed states, measured on additional SC-like device. a) Relaxation of the resistance state, read with 50 mV, after excitation with a single pulse of +4 V (red squares) or −2 V (blue squares). b) Multiple resistance levels are achieved by repeating the same writing pulses, identified by the vertical dotted lines, each followed by reading, tracked with time.

◆ The second order memristive effects were observed in this additional device as well although these particular measurements were not optimized to yield the most efficient synaptic modification.

Presence of PPF is confirmed (**figure A.5**) with the use of the pairs of +2.5 V writing pulses (70 µs in duration); the same erase procedure was performed to maintain the initial device resistance constant throughout the whole measurement (see fig.7.4b). At the short time scale (50 mV/0.1 ms reading pulse applied in 1.8 ms after the pair of writing pulses) PPF index reaches 12% for the shortest intervals (1.7 ms), and at the large interval values of up to 30 s it stabilizes at the STP of about 6%. The use of moderate writing voltage values allowed to bring the long-term effect (reading after 2 s) effectively to 0 at all accessible interval values.

Experience-dependent SRDP is confirmed as well (**figure A.6**). Here three frequencies were used: 1, 30 and 500 Hz, the $I_{write} \rightarrow w$ calibration was performed analogous to fig.7.8. As demonstrated in the chapter 7, the high frequency (500 Hz) sequences each time result in the large weight (w) increase, while the low frequency (1 Hz) sequences result in the w decrease, independently of the frequency order. Effect of the intermediate frequency (30 Hz) sequences depends entirely on the value of the frequency of the previous sequence applied: following the higher frequency sequence it will result in depression and vice versa.

◆ Thus, the additional SC-like devices reproduces the entire set of results, presented in the chapters 6 and 7.

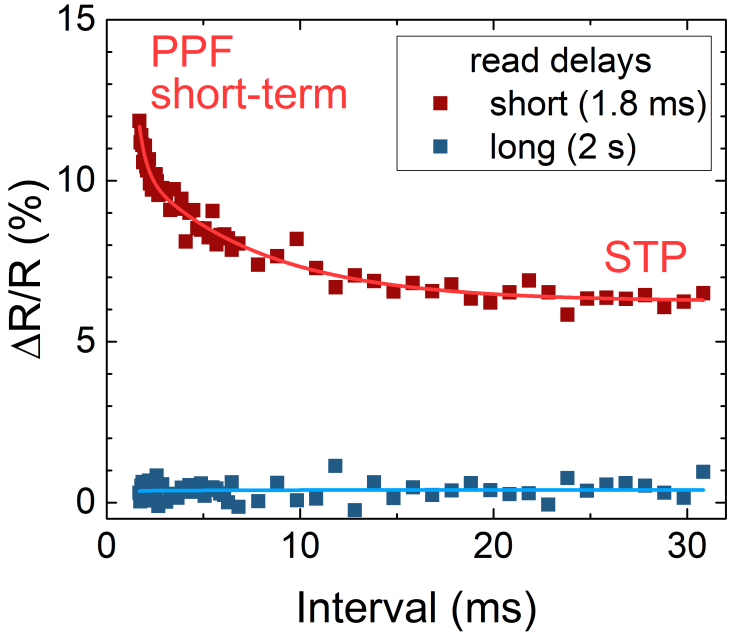

Figure A.5: Relative change of the additional SC-like device resistance after the paired-pulse stimulation with respect to the initial resistance value (R_{pre}), as a function of the time interval between two writing pulses of +2.5 V (with the initial erase pulse of −1 V). Red (blue) curve corresponds to short (long) post-read delay.

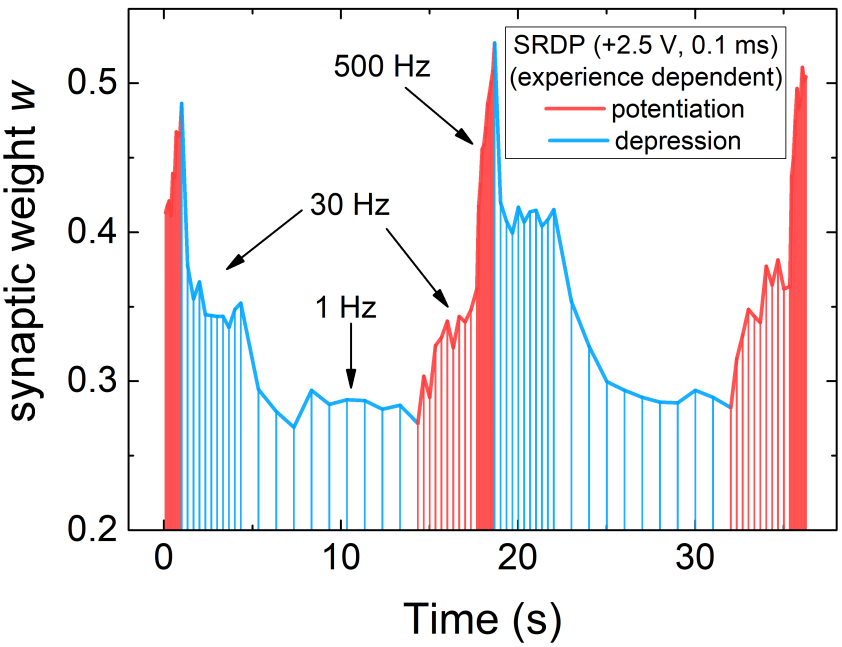

Figure A.6: SRDP from additional SC-like device, measured with different frequency orders of the successive sequences, attesting of experience-dependent plasticity. Potentiation (depression) regions are indicated with red (blue) lines.

A.2 Additional metal-like device

The additional metal-like device is 25 μm in lateral size. It was tested in the wide range of T, from 10 K to 300 K, to demonstrate the peculiar temperature evolution combined with relatively low resistance values (< 1 kΩ).

The $I_{write}(V_{write})$ curves of this device are almost symmetric in the whole T range (**figure A.7a**). I_{write} values increase monotonously with cooling. However, the resistance values evolve non-monotonously with T (**figure A.7b**). While $R(V_{write})$ curves preserve the same shape at all temperatures, with the slightly higher resistance close to 0 V than at maximum positive voltages, both LRS and HRS values increase with cooling down to 100 K and decrease further, what is seen well in the extracted temperature dependencies (**figure A.8**).On the other hand, the ER value increases monotonously with cooling from ∼5% at 300 K up to more than 80% at 10 K.

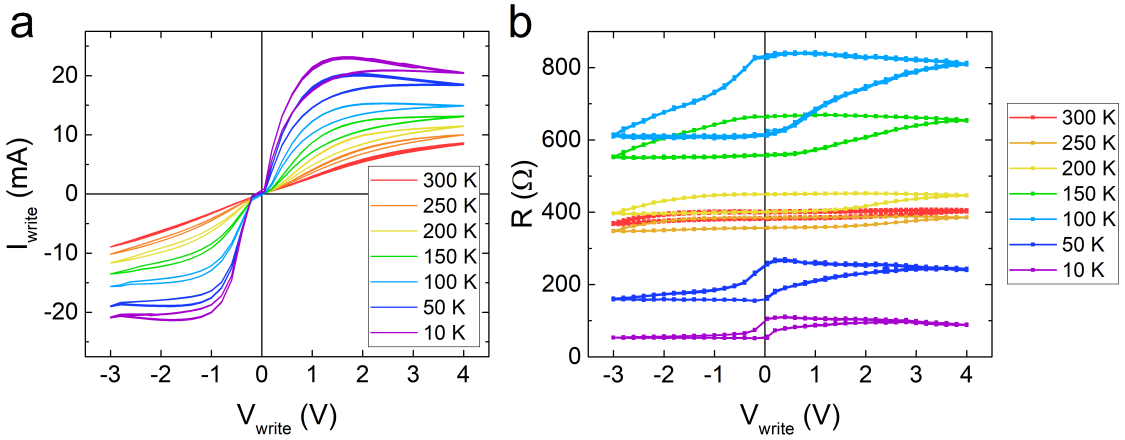

Figure A.7: $I_{write}(V_{write})$ (a) and $R(V_{write})$ (b) curves, cycling between −3 V and +4 V values, measured on additional 25 μm metal-like device at various temperatures.

Additionally, the $R(T)$ dependence was measured continuously with heating (green line in the fig.A.8). At 50 K the LRS was set, and then resistance was measured approximately every 1.4 s during the T sweep up at the rate of 6 K/min. The curve quite closely reproduces the extracted LRS(T) dependence, although the resistance extremum position is slightly higher - at ∼130 K. The discrepancy could be due to quite high temperature sweep rate, which did not allow for thermalization of the sample, while the write-read cycles at fixed T were performed well after the sample T had been stabilized. Alternatively, the peak resistance was simply not captured either at 100 K or 150 K, since there were no measurements at the intermediate T. The presented metal-like device is considered so due to corresponding R value, however the observed T dependence is hybrid with respect to the examples of SC-like and metal-like behavior (see fig.6.3). This kind of temperature evolution is, in fact, quite normal in LSMO films and is usually related to the metal-insulator transition (MIT) [181]. T_{MIT} may shift above 300 K, what makes the $R(T)$ dependence monotonically increasing in the conventionally chosen temperature range in cryogenic experiments. This observation demonstrates the domination of LSMO and weak contribution of the barrier in the overall conduction of this LSMO/BTO/LSMO device.

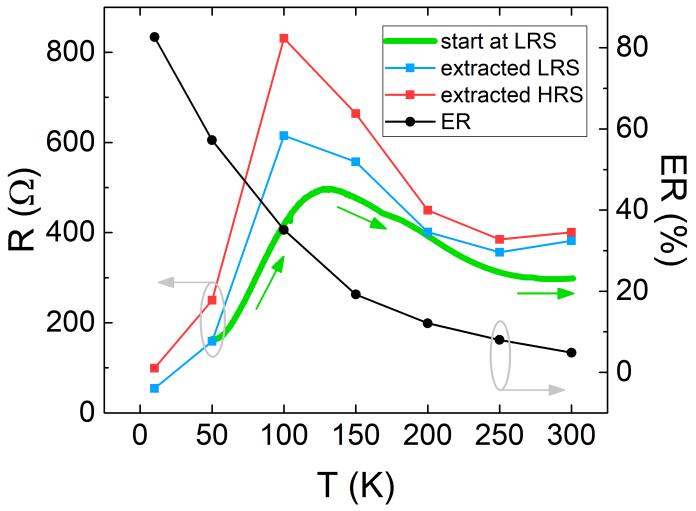

Figure A.8: Temperature dependencies of LRS (blue line and squares, left axis), HRS (red line and squares, left axis) and ER (black line and circles, right axis), extracted from fig.A.7, and continuous $R(T)$ measurement with heating (green line, left axis, arrows indicate T sweeping direction), starting from the LRS set at 50 K.

◆ Write-read measurement of 30 consecutive cycles at 50 K demonstrates excellent reproducibility of both $I_{write}(V_{write})$ and $R(V_{write})$ curves (**figure A.9**).

◆ The multilevel write-read measurements were also performed at 50 K (**figure A.10**). Both $I_{write}(V_{write})$ and $R(V_{write})$ curves follow almost the same path during the voltage increase before reaching the stopping point at various V_{max}. Note, that the LRS is saturated at relatively low negative voltages when previous V_{max} was also low.

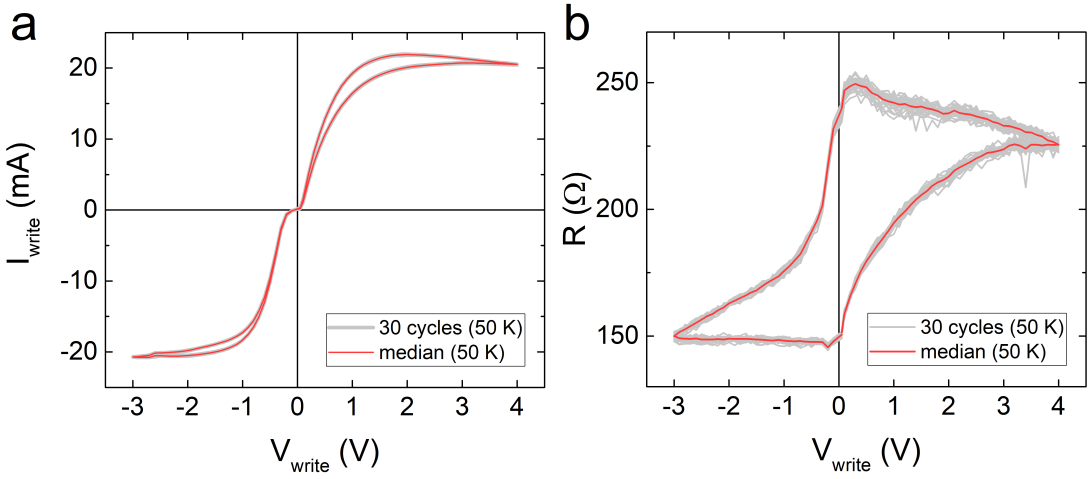

Figure A.9: 30 cycles between −3 V and +4 V (grey) with their median (red), measured on the additional 25 µm metal-like device at 50 K. a) $I_{write}(V_{write})$ curves and b) $R(V_{write})$ curves.

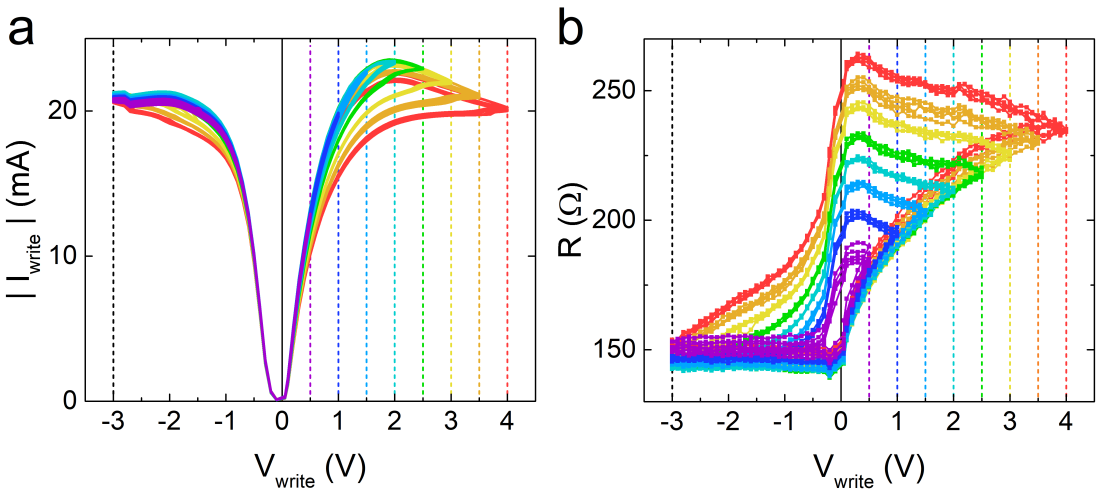

Figure A.10: Multilevel $|I_{write}|(V_{write})$ (a) and $R(V_{write})$ (b) curves, cycling between -3 V and various V_{max} values, measured on additional 25 µm metal-like device at 50 K. Colored dashed lines indicate V_{max}.

◆ Continuous resistance level setting, their reproducibility and stability are also demonstrated here in the same way as for SC-like devices.

Application of various voltage pulses leads to stabilization of different resistance levels that do not mix after equal amounts of pulses (**figure A.11**).

Series of doubling numbers of pulses show good reproducibility of LTP and LTD processes (**figure A.12**).

Long-term retention of the multilevel states is stable even after setting with only

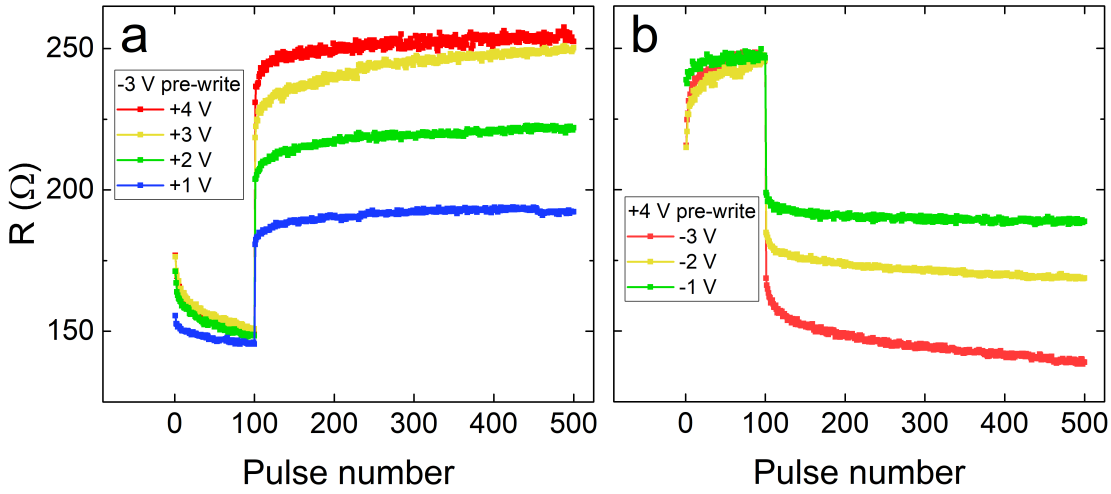

Figure A.11: Multilevel resistance states (from additional metal-like device at 50 K) set with positive (a) or negative (b) writing pulses, after 100 prepulses of -3 V (a) or $+4$ V (b). Reading was made with 50 mV and duration of 100 ms, period of write pulse (duration 1 ms) application equal to ∼650 ms.

one 1 ms writing pulse (**figure A.13**).

◆ Resistance relaxation after excitation with single pulses and the step-like long-term resistance modification are also observed (**figure A.14**). In this device, however, the voltage polarity asymmetry is reversed: excitation with negative voltage

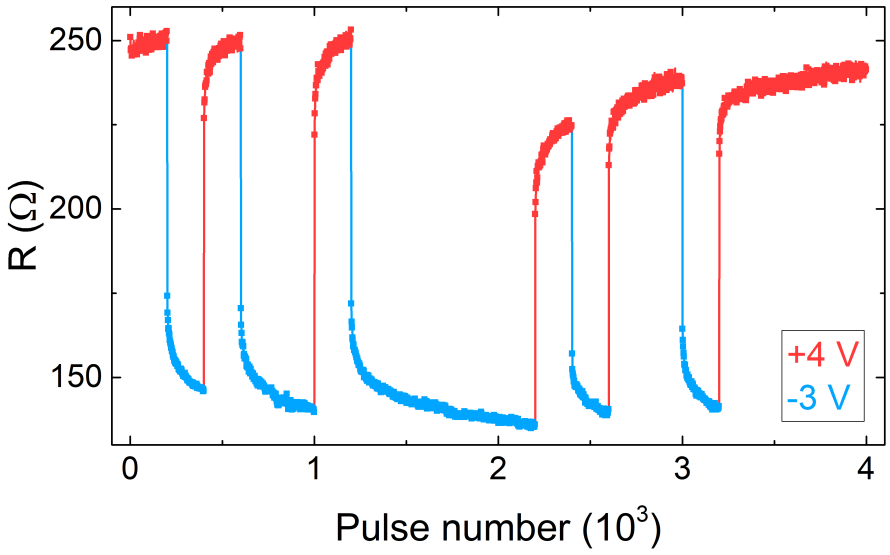

Figure A.12: a) Pulse series (from additional metal-like device at 50 K) of +4 V writing, followed by −2 V writing, repeated in sequences, in which the number of pulses in the even groups doubles, followed by the same sequence with reversed voltage order. Reading was made with 50 mV and duration of 100 ms, period of write pulse (duration 1 ms) application equal to ∼600 ms.

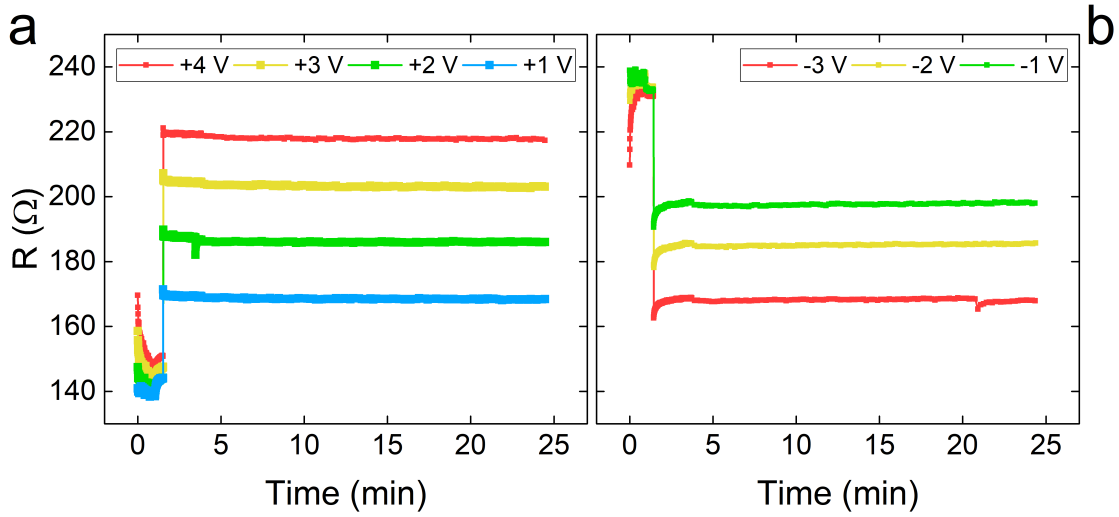

Figure A.13: Retention, on a 25 min time scale, of resistance states set at different levels by one 1 ms voltage pulse of various positive (a) and negative (b) magnitudes, after 100 pre-pulses of −3 V (a) and +4 V (b), respectively. Measured on the additional metal-like device at 50 K.

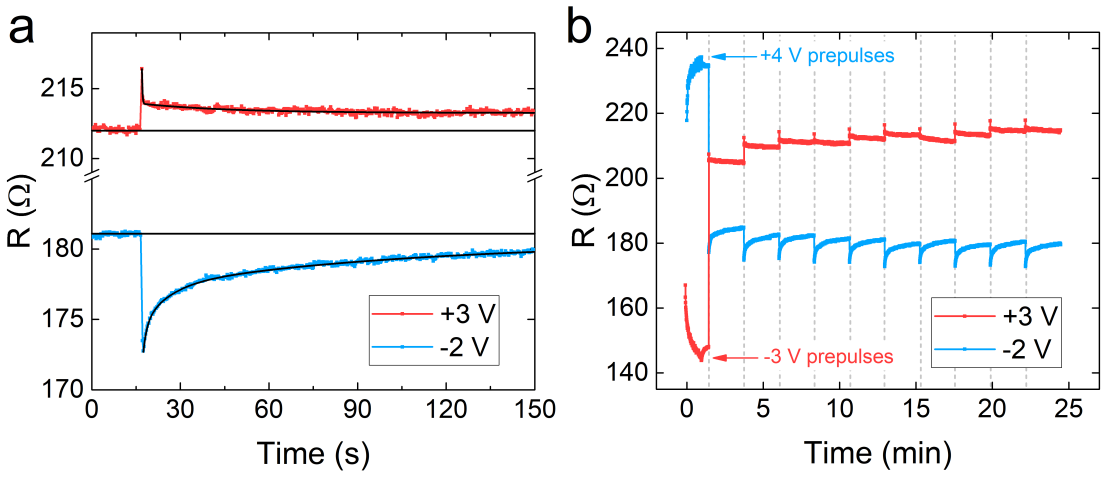

Figure A.14: Relaxation dynamics from potentiated/depressed states, measured on additional metal-like device at 50 K. a) Relaxation of the resistance state, read with 50 mV, after excitation with a single pulse of +3 V (red squares) or −2 V (blue squares). b) Multiple resistance levels are achieved by repeating the same writing pulses, identified by the vertical dotted lines, each followed by reading, tracked with time.

pulse is more intense and decays longer, while effect of the positive voltage pulse relaxes almost instantly. It was suggested in the phenomenological model of the RS that the difference between SC-like and metal-like devices arises from the variation of leakage path resistance (see section 6.2). Taking into account the understanding of three physical processes that contribute the most to the device conductance (see section 6.5), we can attribute this $R_{leakage}$ variation to the non-uniformity of the interface LSMO/BTO intermixing, which, in fact, has an effect on all three processes. Therefore, it may be considered not as surprising that the properties of the resistance relaxation in this particular metal-like device differ from the SC-like devices. A more detailed investigation of the phenomenon is necessary to unambiguously verify the suggested RS mechanism in the metal-like devices, such as TEM+EELS study of this exact device cross-section or various spectroscopic techniques, such as X-ray absorption spectroscopy, possibly with magnetic circular dichroism (XAS/XMCD), X-ray photoelectron spectroscopy, possibly with magnetic circular dichroism in the angular distribution of photoelectrons (XPS/MCDAD), implemented *in operando*.

◆ In summary, we have demonstrated the reproducibility of the RS and memristive measurements, presented in the chapters 6 and 7, on the examples of additional SC-like and metal-like devices. Indeed, it is observed that the RS features are similar: resistance multilevel setting, reproducibility and stability, transient excitation phenomena and second-order memristive effects.

Bibliography

[1] Moore, G. E. Cramming more components onto integrated circuits. *Electronics* **38**, 114 (1965). https://doi.org/10.1109/N-SSC.2006.4785860.

[2] Rupp, K. 42 years of microprocessor trend data (2018). https://www.karlrupp.net/2018/02/42-years-of-microprocessor-trend-data.

[3] Rupp, K. Microprocessor trend data (2022). https://github.com/karlrupp/microprocessor-trend-data.

[4] Moore, G. No exponential is forever: but "Forever" can be delayed! In *2003 IEEE International Solid-State Circuits Conference, 2003. Digest of Technical Papers. ISSCC.*, vol. 1, 20–23 (2003). https://doi.org/10.1109/ISSCC.2003.1234194.

[5] IEEE. International Roadmap for Devices and Systems: Executive Summary (2022). https://irds.ieee.org/editions/2022/executive-summary.

[6] Andrae, A. S. G. & Edler, T. On Global Electricity Usage of Communication Technology: Trends to 2030. *Challenges* **6**, 117–157 (2015). https://www.mdpi.com/2078-1547/6/1/117.

[7] Wulf, W. A. & McKee, S. A. Hitting the memory wall: Implications of the obvious. *SIGARCH Comput. Archit. News* **23**, 20–24 (1995). https://doi.org/10.1145/216585.216588.

[8] Efnusheva, D., Cholakoska, A. & Tentov, A. A Survey of Different Approaches for Overcoming the Processor - Memory Bottleneck. *Computer Science and Information Technology* **9**, 151–163 (2017). https://doi.org/10.5121/ijcsit.2017.9214.

[9] Aspray, W. & Burks, A. W. (eds.) *Papers of John von Neumann on computing and computer theory*, vol. 12 of *Charles Babbage Institute reprint series for the history of computing* (MIT Press; Tomash Publishers, Cambridge, Mass.: Los Angeles, 1987).

[10] Zou, X., Xu, S., Chen, X., Yan, L. & Han, Y. Breaking the von Neumann bottleneck: architecture-level processing-in-memory technology. *Science China Information Sciences* **64**, 160404 (2021). https://link.springer.com/10.1007/s11432-020-3227-1.

[11] Hung, J.-M., Jhang, C.-J., Wu, P.-C., Chiu, Y.-C. & Chang, M.-F. Challenges and Trends of Nonvolatile In-Memory-Computation Circuits for AI Edge Devices. *IEEE Open Journal of the Solid-State Circuits Society* **1**, 171–183 (2021). https://doi.org/10.1109/OJSSCS.2021.3123287.

[12] Goodfellow, I., Bengio, Y. & Courville, A. *Deep Learning* (MIT Press, 2016). http://www.deeplearningbook.org.

[13] Hebb, D. O. *The organization of behavior: A neuropsychological theory* (Wiley, New York, 1949).

[14] Hodgkin, A. L. & Huxley, A. F. A quantitative description of membrane current and its application to conduction and excitation in nerve. *The Journal of Physiology* **117**, 500–544 (1952). https://physoc.onlinelibrary.wiley.com/doi/abs/10.1113/jphysiol.1952.sp004764.

[15] Abiodun, O. I. *et al.* State-of-the-art in artificial neural network applications: A survey. *Heliyon* **4**, e00938 (2018). https://www.sciencedirect.com/science/article/pii/S2405844018332067.

[16] Furber, S. Large-scale neuromorphic computing systems. *Journal of Neural Engineering* **13**, 051001 (2016). https://dx.doi.org/10.1088/1741-2560/13/5/051001.

[17] Davies, M. *et al.* Advancing Neuromorphic Computing With Loihi: A Survey of Results and Outlook. *Proceedings of the IEEE* **109**, 911–934 (2021). https://doi.org/10.1109/JPROC.2021.3067593.

[18] Chua, L. Memristor - The Missing Circuit Element. *IEEE Transactions on Circuit Theory* **18**, 507–519 (1971). https://doi.org/10.1109/TCT.1971.1083337.

[19] Yin, Z., Tian, H., Chen, G. & Chua, L. O. What are memristor, memcapacitor, and meminductor? *IEEE Transactions on Circuits and Systems II: Express Briefs* **62**, 402–406 (2015). https://doi.org/10.1109/TCSII.2014.2387653.

[20] Jo, S. H. *et al.* Nanoscale Memristor Device as Synapse in Neuromorphic Systems. *Nano Letters* **10**, 1297–1301 (2010). https://pubs.acs.org/doi/10.1021/nl904092h.

[21] Bi, G.-q. & Poo, M.-m. Synaptic Modifications in Cultured Hippocampal Neurons: Dependence on Spike Timing, Synaptic Strength, and Postsynaptic Cell Type. *Journal of Neuroscience* **18**, 10464–10472 (1998). https://www.jneurosci.org/content/18/24/10464.

[22] Strukov, D. B., Snider, G. S., Stewart, D. R. & Williams, R. S. The missing memristor found. *Nature* **453**, 80–83 (2008). http://www.nature.com/articles/nature06932.

[23] Chua, L. Resistance switching memories are memristors. *Applied Physics A* **102**, 765–783 (2011). http://link.springer.com/10.1007/s00339-011-6264-9.

[24] Kim, H., Sah, M. P., Yang, C., Roska, T. & Chua, L. O. Memristor Bridge Synapses. *Proceedings of the IEEE* **100**, 2061–2070 (2012). https://doi.org/10.1109/JPROC.2011.2166749.

[25] Chua, L., Sbitnev, V. & Kim, H. Hodgkin–Huxley Axon Is Made Of Memristors. *International Journal of Bifurcation and Chaos* **22**, 1230011 (2012). https://doi.org/10.1142/S021812741230011X.

[26] Tuma, T., Pantazi, A., Le Gallo, M., Sebastian, A. & Eleftheriou, E. Stochastic phase-change neurons. *Nature Nanotechnology* **11**, 693–699 (2016). http://www.nature.com/articles/nnano.2016.70.

[27] Yang, J. J., Strukov, D. B. & Stewart, D. R. Memristive devices for computing. *Nature Nanotechnology* **8**, 13–24 (2013). http://www.nature.com/articles/nnano.2012.240.

[28] Burr, G. W. *et al.* Neuromorphic computing using non-volatile memory. *Advances in Physics: X* **2**, 89–124 (2017). https://doi.org/10.1080/23746149.2016.1259585.

[29] Slesazeck, S. & Mikolajick, T. Nanoscale resistive switching memory devices: a review. *Nanotechnology* **30**, 352003 (2019). https://doi.org/10.1088/1361-6528/ab2084.

[30] Marković, D., Mizrahi, A., Querlioz, D. & Grollier, J. Physics for neuromorphic computing. *Nature Reviews Physics* **2**, 499–510 (2020). http://www.nature.com/articles/s42254-020-0208-2.

[31] Celano, U. *et al.* Non-filamentary (VMCO) memory: A two-and three-dimensional study on switching and failure modes. In *2017 IEEE International Electron Devices Meeting (IEDM)*, 39.1.1–39.1.4 (2017). https://doi.org/10.1109/IEDM.2017.8268519.

[32] Sawa, A. Resistive switching in transition metal oxides. *Materials Today* **11**, 28–36 (2008). https://www.sciencedirect.com/science/article/pii/S1369702108701196.

[33] Gallo, M. L. & Sebastian, A. An overview of phase-change memory device physics. *Journal of Physics D: Applied Physics* **53**, 213002 (2020). https://dx.doi.org/10.1088/1361-6463/ab7794.

[34] Stevens, L. D. The Evolution of Magnetic Storage. *IBM Journal of Research and Development* **25**, 663–676 (1981). https://doi.org/10.1147/rd.255.0663.

[35] Baibich, M. N. *et al.* Giant Magnetoresistance of (001)Fe / (001)Cr Magnetic Superlattices. *Physical Review Letters* **61**, 2472–2475 (1988). https://link.aps.org/doi/10.1103/PhysRevLett.61.2472.

[36] Binasch, G., Grünberg, P., Saurenbach, F. & Zinn, W. Enhanced magnetoresistance in layered magnetic structures with antiferromagnetic interlayer exchange. *Physical Review B* **39**, 4828–4830 (1989). https://link.aps.org/doi/10.1103/PhysRevB.39.4828.

[37] Julliere, M. Tunneling between ferromagnetic films. *Physics Letters A* **54**, 225–226 (1975). https://www.sciencedirect.com/science/article/pii/0375960175901747.

[38] Parkin, S. S. P. *et al.* Giant tunnelling magnetoresistance at room temperature with MgO (100) tunnel barriers. *Nature Materials* **3**, 862–867 (2004). https://www.nature.com/articles/nmat1256.

[39] Yuasa, S., Nagahama, T., Fukushima, A., Suzuki, Y. & Ando, K. Giant room-temperature magnetoresistance in single-crystal Fe / MgO / Fe magnetic tunnel junctions. *Nature Materials* **3**, 868–871 (2004). https://www.nature.com/articles/nmat1257.

[40] Schuhl, A. & Lacour, D. Spin dependent transport: GMR & TMR. *Comptes Rendus Physique* **6**, 945–955 (2005). https://www.sciencedirect.com/science/article/pii/S1631070505001647. Spintronics.

[41] Kyung, H. *et al.* Effect of microstructure on the magnetoresistive properties of NiFe / Co(CoFe) / Al(Ta)–oxide / Co(CoFe) tunnel junctions. *Journal of Applied Physics* **89**, 2752–2755 (2001). https://doi.org/10.1063/1.1343519.

[42] Slonczewski, J. Current-driven excitation of magnetic multilayers. *Journal of Magnetism and Magnetic Materials* **159**, L1–L7 (1996). https://www.sciencedirect.com/science/article/pii/0304885396000625.

[43] Buck, D. A. Ferroelectrics for Digital Information Storage and Switching. Technical Report, MIT Digital Computer Laboratory (1952). http://dome.mit.edu/handle/1721.3/40244.

[44] Fujitsu Semiconductor Memory Solution. What is FeRAM? (2022). https://www.fujitsu.com/jp/group/fsm/en/products/feram/overview/.

[45] Mikolajick, T. *et al.* Next generation ferroelectric materials for semiconductor process integration and their applications. *Journal of Applied Physics* **129**, 100901 (2021). https://doi.org/10.1063/5.0037617.

[46] Zhuravlev, M. Y., Sabirianov, R. F., Jaswal, S. S. & Tsymbal, E. Y. Giant Electroresistance in Ferroelectric Tunnel Junctions. *Physical Review Letters* **94**, 246802 (2005). https://link.aps.org/doi/10.1103/PhysRevLett.94.246802.

[47] Chanthbouala, A. *et al.* A ferroelectric memristor. *Nature Materials* **11**, 860–864 (2012). https://www.nature.com/articles/nmat3415.

[48] Kim, D. J. *et al.* Ferroelectric Tunnel Memristor. *Nano Letters* **12**, 5697–5702 (2012). https://doi.org/10.1021/nl302912t.

[49] Mikheev, V. *et al.* Memristor with a ferroelectric HfO_2 layer: in which case it is a ferroelectric tunnel junction. *Nanotechnology* **31**, 215205 (2020). https://dx.doi.org/10.1088/1361-6528/ab746d.

[50] Halter, M. *et al.* Back-End, CMOS-Compatible Ferroelectric Field-Effect Transistor for Synaptic Weights. *ACS Applied Materials & Interfaces* **12**, 17725–17732 (2020). https://doi.org/10.1021/acsami.0c00877.

[51] Eerenstein, W., Mathur, N. D. & Scott, J. F. Multiferroic and magnetoelectric materials. *Nature* **442**, 759–765 (2006). http://www.nature.com/articles/nature05023.

[52] Spaldin, N. A., Cheong, S.-W. & Ramesh, R. Multiferroics: Past, present, and future. *Physics Today* **63**, 38–43 (2010). https://doi.org/10.1063/1.3502547.

[53] Hill, N. A. Why Are There so Few Magnetic Ferroelectrics? *The Journal of Physical Chemistry B* **104**, 6694–6709 (2000). https://doi.org/10.1021/jp000114x.

[54] Yun, K. Y. *et al.* Structural and multiferroic properties of $BiFeO_3$ thin films at room temperature. *Journal of Applied Physics* **96**, 3399–3403 (2004). https://doi.org/10.1063/1.1775045.

[55] Chu, Y.-H. *et al.* Electric-field control of local ferromagnetism using a magnetoelectric multiferroic. *Nature Materials* **7**, 478–482 (2008). https://www.nature.com/articles/nmat2184.

[56] Prasad, B. *et al.* Ultralow Voltage Manipulation of Ferromagnetism. *Advanced Materials* **32**, 2001943 (2020). https://onlinelibrary.wiley.com/doi/abs/10.1002/adma.202001943.

[57] Manipatruni, S. *et al.* Scalable energy-efficient magnetoelectric spin–orbit logic. *Nature* **565**, 35–42 (2019). http://www.nature.com/articles/s41586-018-0770-2.

[58] Vaz, D. C. *et al.* Functional Demonstration of a Fully Integrated Magneto-Electric Spin-Orbit Device. In *2021 IEEE International Electron Devices Meeting (IEDM)*, 32.4.1–32.4.4 (2021). https://doi.org/10.1109/IEDM19574.2021.9720677.

[59] Thiele, C., Dörr, K., Bilani, O., Rödel, J. & Schultz, L. Influence of strain on the magnetization and magnetoelectric effect in $La_{0.7}A_{0.3}MnO_3$ / PMN−PT(001) (A = Sr, Ca). *Physical Review B* **75**, 054408 (2007). https://link.aps.org/doi/10.1103/PhysRevB.75.054408.

[60] Radaelli, G. *et al.* Electric control of magnetism at the Fe / $BaTiO_3$ interface. *Nature Communications* **5**, 3404 (2014). http://www.nature.com/articles/ncomms4404.

[61] Dmitriyeva, A. *et al.* Magnetoelectric Coupling at the Ni / $Hf_{0.5}Zr_{0.5}O_2$ Interface. *ACS Nano* **15**, 14891–14902 (2021). https://doi.org/10.1021/acsnano.1c05001.

[62] Tsymbal, E., Gruverman, A., Garcia, V., Bibes, M. & Barthélémy, A. Ferroelectric and multiferroic tunnel junctions. *MRS Bulletin* **37**, 138–143 (2012). http://link.springer.com/10.1557/mrs.2011.358.

[63] Valencia, S. *et al.* Interface-induced room-temperature multiferroicity in $BaTiO_3$. *Nature Materials* **10**, 753–758 (2011). https://www.nature.com/articles/nmat3098.

[64] Huang, W. *et al.* Interfacial Ion Intermixing Effect on Four-Resistance States in $La_{0.7}Sr_{0.3}MnO_3$ / $BaTiO_3$ / $La_{0.7}Sr_{0.3}MnO_3$ Multiferroic Tunnel Junctions. *ACS Applied Materials & Interfaces* **8**, 10422–10429 (2016). https://pubs.acs.org/doi/10.1021/acsami.6b02150.

[65] Yin, Y.-W. *et al.* Octonary Resistance States in $La_{0.7}Sr_{0.3}MnO_3$ / $BaTiO_3$ / $La_{0.7}Sr_{0.3}MnO_3$ Multiferroic Tunnel Junctions. *Advanced Electronic Materials* **1**, 1500183 (2015). https://onlinelibrary.wiley.com/doi/abs/10.1002/aelm.201500183.

[66] Huang, W. *et al.* Solid-State Synapse Based on Magnetoelectrically Coupled Memristor. *ACS Applied Materials & Interfaces* **10**, 5649–5656 (2018). https://pubs.acs.org/doi/10.1021/acsami.7b18206.

[67] Jona, F. & Shirane, G. *Ferroelectric crystals* (Dover Publications, New York, 1993).

[68] Kay, H. & Vousden, P. XCV. Symmetry changes in barium titanate at low temperatures and their relation to its ferroelectric properties. *The London, Edinburgh, and Dublin Philosophical Magazine and Journal of Science* **40**, 1019–1040 (1949). https://doi.org/10.1080/14786444908561371.

[69] Jaffe, B., Cook, W. R. & Jaffe, H. Barium titanate. In *Piezoelectric Ceramics*, chap. 5, 53–114 (Academic Press, 1971). https://www.sciencedirect.com/science/article/pii/B978012379550250009.

[70] Vijatovic, M., Bobic, J. & Stojanovic, B. History and challenges of barium titanate: Part I. *Science of Sintering* **40**, 155–165 (2008). http://www.doiserbia.nb.rs/Article.aspx?ID=0350-820X0802155V.

[71] Vijatovic, M., Bobic, J. & Stojanovic, B. History and challenges of barium titanate: Part II. *Science of Sintering* **40**, 235–244 (2008). http://www.doiserbia.nb.rs/Article.aspx?ID=0350-820X0803235V.

[72] Dubourdieu, C. *et al.* Switching of ferroelectric polarization in epitaxial $BaTiO_3$ films on silicon without a conducting bottom electrode. *Nature Nanotechnology* **8**, 748–754 (2013). http://www.nature.com/articles/nnano.2013.192.

[73] Jiang, Y. *et al.* Enabling ultra-low-voltage switching in $BaTiO_3$. *Nature Materials* **21**, 779–785 (2022). https://www.nature.com/articles/s41563-022-01266-6.

[74] Boschker, H. & Mannhart, J. Quantum-Matter Heterostructures. *Annual Review of Condensed Matter Physics* **8**, 145–164 (2017). https://doi.org/10.1146/annurev-conmatphys-031016-025404.

[75] Garcia, V. *et al.* Giant tunnel electroresistance for non-destructive readout of ferroelectric states. *Nature* **460**, 81–84 (2009). http://www.nature.com/articles/nature08128.

[76] Gruverman, A. *et al.* Tunneling Electroresistance Effect in Ferroelectric Tunnel Junctions at the Nanoscale. *Nano Letters* **9**, 3539–3543 (2009). https://doi.org/10.1021/nl901754t.

[77] Zenkevich, A. *et al.* Electronic band alignment and electron transport in Cr / $BaTiO_3$ / Pt ferroelectric tunnel junctions. *Applied Physics Letters* **102**, 062907 (2013). https://doi.org/10.1063/1.4792525.

[78] Wang, X. *et al.* Electroresistance of Pt / $BaTiO_3$ / $LaNiO_3$ ferroelectric tunnel junctions and its dependence on $BaTiO_3$ thickness. *Materials Research Express* **6**, 046307 (2019). https://dx.doi.org/10.1088/2053-1591/aafae0.

[79] Wen, Z., Li, C., Wu, D., Li, A. & Ming, N. Ferroelectric-field-effect-enhanced electroresistance in metal / ferroelectric / semiconductor tunnel junctions. *Nature Materials* **12**, 617–621 (2013). https://www.nature.com/articles/nmat3649.

[80] Wang, X. *et al.* Effect of a semiconductor electrode on the tunneling electroresistance in ferroelectric tunneling junction. *Applied Physics Letters* **109**, 163501 (2016). https://doi.org/10.1063/1.4965708.

[81] Xi, Z. *et al.* Giant tunnelling electroresistance in metal / ferroelectric / semiconductor tunnel junctions by engineering the Schottky barrier. *Nature Communications* **8**, 15217 (2017). http://www.nature.com/articles/ncomms15217.

[82] Ma, C. *et al.* Sub-nanosecond memristor based on ferroelectric tunnel junction. *Nature Communications* **11**, 1439 (2020). http://www.nature.com/articles/s41467-020-15249-1.

[83] Guo, R. *et al.* Control of Synaptic Plasticity Learning of Ferroelectric Tunnel Memristor by Nanoscale Interface Engineering. *ACS Applied Materials & Interfaces* **10**, 12862–12869 (2018). https://doi.org/10.1021/acsami.8b01469.

[84] Li, C. L., Chen, Z. H., Zhou, Y. L. & Cui, D. F. Effect of oxygen content on the dielectric and ferroelectric properties of laser-deposited $BaTiO_3$ thin films. *Journal of Physics: Condensed Matter* **13**, 5261–5268 (2001). https://doi.org/10.1088/0953-8984/13/22/319.

[85] Pintilie, L. & Alexe, M. Metal-ferroelectric-metal heterostructures with Schottky contacts. I. Influence of the ferroelectric properties. *Journal of Applied Physics* **98**, 124103 (2005). https://doi.org/10.1063/1.2148622.

[86] Li, M. *et al.* Controlling Resistance Switching Polarities of Epitaxial $BaTiO_3$ Films by Mediation of Ferroelectricity and Oxygen Vacancies. *Advanced Electronic Materials* **1**, 1500069 (2015). https://onlinelibrary.wiley.com/doi/abs/10.1002/aelm.201500069.

[87] Lü, W. *et al.* Multi-Nonvolatile State Resistive Switching Arising from Ferroelectricity and Oxygen Vacancy Migration. *Advanced Materials* **29**, 1606165 (2017). https://onlinelibrary.wiley.com/doi/abs/10.1002/adma.201606165.

[88] Hernandez-Martin, D. *et al.* Controlled Sign Reversal of Electroresistance in Oxide Tunnel Junctions by Electrochemical-Ferroelectric Coupling. *Physical Review Letters* **125**, 266802 (2020). https://link.aps.org/doi/10.1103/PhysRevLett.125.266802.

[89] Qian, M., Fina, I., Sulzbach, M. C., Sánchez, F. & Fontcuberta, J. Synergetic Electronic and Ionic Contributions to Electroresistance in Ferroelectric Capacitors. *Advanced Electronic Materials* **5**, 1800646 (2019). https://onlinelibrary.wiley.com/doi/abs/10.1002/aelm.201800646.

[90] Soni, R. *et al.* Giant electrode effect on tunnelling electroresistance in ferroelectric tunnel junctions. *Nature Communications* **5**, 5414 (2014). http://www.nature.com/articles/ncomms6414.

[91] Li, J. *et al.* Giant Electroresistance in Ferroionic Tunnel Junctions. *iScience* **16**, 368–377 (2019). https://linkinghub.elsevier.com/retrieve/pii/S2589004219301804.

[92] Kohlstedt, H. *et al.* Method to distinguish ferroelectric from nonferroelectric origin in case of resistive switching in ferroelectric capacitors. *Applied Physics Letters* **92**, 062907 (2008). https://doi.org/10.1063/1.2841917.

[93] Yang, S. M. *et al.* Mixed electrochemical–ferroelectric states in nanoscale ferroelectrics. *Nature Physics* **13**, 812–818 (2017). http://www.nature.com/articles/nphys4103.

[94] Goodenough, J. B. Electronic and ionic transport properties and other physical aspects of perovskites. *Reports on Progress in Physics* **67**, 1915 (2004). https://dx.doi.org/10.1088/0034-4885/67/11/R01.

[95] Cesaria, M., Caricato, A. P., Maruccio, G. & Martino, M. LSMO – growing opportunities by PLD and applications in spintronics. *Journal of Physics: Conference Series* **292**, 012003 (2011). https://dx.doi.org/10.1088/1742-6596/292/1/012003.

[96] Fujishiro, H., Fukase, T. & Ikebe, M. Charge Ordering and Sound Velocity Anomaly in $La_{1-X}Sr_XMnO_3$ (X $\geq$ 0.5). *Journal of the Physical Society of Japan* **67**, 2582–2585 (1998). https://doi.org/10.1143/JPSJ.67.2582.

[97] Bowen, M. *et al.* Nearly total spin polarization in $La_{2/3}Sr_{1/3}MnO_3$ from tunneling experiments. *Applied Physics Letters* **82**, 233–235 (2003). https://doi.org/10.1063/1.1534619.

[98] Imada, M., Fujimori, A. & Tokura, Y. Metal-insulator transitions. *Reviews of Modern Physics* **70**, 1039–1263 (1998). https://link.aps.org/doi/10.1103/RevModPhys.70.1039.

[99] Tokura, Y. & Tomioka, Y. Colossal magnetoresistive manganites. *Journal of Magnetism and Magnetic Materials* **200**, 1–23 (1999). https://www.sciencedirect.com/science/article/pii/S0304885399003522.

[100] Pailloux, F. *et al.* Nanoscale analysis of a $SrTiO_3$ / $La_{2/3}Sr_{1/3}MnO_3$ interface. *Physical Review B* **66**, 014417 (2002). https://link.aps.org/doi/10.1103/PhysRevB.66.014417.

[101] Ott, F. *et al.* Interface magnetism of $La_{0.7}Sr_{0.3}MnO_3$ thin films studied by neutron reflectometry. *Journal of Magnetism and Magnetic Materials* **211**, 200–205 (2000). https://www.sciencedirect.com/science/article/pii/S0304885399007349.

[102] Borges, R. P., Guichard, W., Lunney, J. G., Coey, J. M. D. & Ott, F. Magnetic and electric "dead" layers in $(La_{0.7}Sr_{0.3})MnO_3$ thin films. *Journal of Applied Physics* **89**, 3868–3873 (2001). https://doi.org/10.1063/1.1331658.

[103] Mottaghi, N. *et al.* Insights into the magnetic dead layer in $La_{0.7}Sr_{0.3}MnO_3$ thin films from temperature, magnetic field and thickness dependence of their magnetization. *AIP Advances* **8**, 056319 (2018). http://aip.scitation.org/doi/10.1063/1.5005913.

[104] Porter, S. B. *et al.* Magnetic dead layers in $La_{0.7}Sr_{0.3}MnO_3$ revisited. *IEEE Transactions on Magnetics* **53**, 1–4 (2017). http://ieeexplore.ieee.org/document/8000351.

[105] Tebano, A. *et al.* Evidence of orbital reconstruction at interfaces in ultrathin $La_{0.67}Sr_{0.33}MnO_3$ films. *Physical Review Letters* **100**, 137401 (2008). https://link.aps.org/doi/10.1103/PhysRevLett.100.137401.

[106] Zakharova, A. *et al.* Interplay between magnetism and interface-induced effects in ultrathin manganites. *Physical Review Materials* **5**, 124404 (2021). https://link.aps.org/doi/10.1103/PhysRevMaterials.5.124404.

[107] Liao, Z. *et al.* Thickness Dependent Properties in Oxide Heterostructures Driven by Structurally Induced Metal–Oxygen Hybridization Variations. *Advanced Functional Materials* **27**, 1606717 (2017). https://onlinelibrary.wiley.com/doi/abs/10.1002/adfm.201606717.

[108] Li, X., Lindfors-Vrejoiu, I., Ziese, M., Gloter, A. & van Aken, P. A. Impact of interfacial coupling of oxygen octahedra on ferromagnetic order in $La_{0.7}Sr_{0.3}MnO_3$ / $SrTiO_3$ heterostructures. *Scientific Reports* **7**, 40068 (2017). http://www.nature.com/articles/srep40068.

[109] Lee, J.-S. *et al.* Controlling competing interactions at oxide interfaces: Enhanced anisotropy in $La_{0.7}Sr_{0.3}MnO_3$ films via interface engineering. *Physical Review B* **85**, 235125 (2012). https://link.aps.org/doi/10.1103/PhysRevB.85.235125.

[110] Tebano, A. *et al.* Strain-induced phase separation in $La_{0.7}Sr_{0.3}MnO_3$ thin films. *Physical Review B* **74**, 245116 (2006). https://link.aps.org/doi/10.1103/PhysRevB.74.245116.

[111] Liao, Z. *et al.* Origin of the metal-insulator transition in ultrathin films of $La_{2/3}Sr_{1/3}MnO_3$. *Physical Review B* **92**, 125123 (2015). https://link.aps.org/doi/10.1103/PhysRevB.92.125123.

[112] Matou, T. *et al.* Reduction of the magnetic dead layer and observation of tunneling magnetoresistance in $La_{0.67}Sr_{0.33}MnO_3$-based heterostructures with a $LaMnO_3$ layer. *Applied Physics Letters* **110**, 212406 (2017). https://doi.org/10.1063/1.4984297.

[113] Guo, E.-J. *et al.* Removal of the Magnetic Dead Layer by Geometric Design. *Advanced Functional Materials* **28**, 1800922 (2018). https://onlinelibrary.wiley.com/doi/abs/10.1002/adfm.201800922.

[114] Chen, Y. *et al.* Significant Reduction of the Dead Layers by the Strain Release in $La_{0.7}Sr_{0.3}MnO_3$ Heterostructures. *ACS Applied Materials & Interfaces* **14**, 39673–39678 (2022). https://doi.org/10.1021/acsami.2c12899.

[115] Wan, Q. *et al.* Oxygen vacancies effects on phase diagram of epitaxial $La_{1-x}Sr_xMnO_3$ thin films. *Science China Physics, Mechanics & Astronomy* **60**, 057711 (2017). http://link.springer.com/10.1007/s11433-017-9018-8.

[116] Trappen, R. *et al.* Effect of oxygen stoichiometry on the magnetization profiles and negative magnetization in LSMO thin films. *Journal of Applied Physics* **126**, 105301 (2019). https://aip.scitation.org/doi/abs/10.1063/1.5111858.

[117] Rajak, P. *et al.* Evidence of Mn-Ion Structural Displacements Correlated with Oxygen Vacancies in $La_{0.7}Sr_{0.3}MnO_3$ Interfacial Dead Layers. *ACS Applied Materials & Interfaces* **13**, 55666–55675 (2021). https://doi.org/10.1021/acsami.1c15599.

[118] Yao, L., Inkinen, S. & van Dijken, S. Direct observation of oxygen vacancy-driven structural and resistive phase transitions in $La_{2/3}Sr_{1/3}MnO_3$. *Nature Communications* **8**, 14544 (2017). http://www.nature.com/articles/ncomms14544.

[119] Cao, L. *et al.* Reversible Control of Physical Properties via an Oxygen-Vacancy-Driven Topotactic Transition in Epitaxial $La_{0.7}Sr_{0.3}MnO_{3-\delta}$ Thin Films. *Advanced Materials* **31**, 1806183 (2019). https://onlinelibrary.wiley.com/doi/abs/10.1002/adma.201806183.

[120] Meyer, T. L. *et al.* Enhancing interfacial magnetization with a ferroelectric. *Physical Review B* **94**, 174432 (2016). https://link.aps.org/doi/10.1103/PhysRevB.94.174432.

[121] Wilhelm, M. *et al.* Photoemission electron microscopy of magneto-ionic effects in $La_{0.7}Sr_{0.3}MnO_3$. *APL Materials* **8**, 111102 (2020). https://doi.org/10.1063/5.0022150.

[122] Lu, H. *et al.* Electric modulation of magnetization at the $BaTiO_3$ / $La_{0.67}Sr_{0.33}MnO_3$ interfaces. *Applied Physics Letters* **100**, 232904 (2012). http://aip.scitation.org/doi/10.1063/1.4726427.

[123] Cui, B. *et al.* Magnetoelectric Coupling Induced by Interfacial Orbital Reconstruction. *Advanced Materials* **27**, 6651–6656 (2015). https://onlinelibrary.wiley.com/doi/10.1002/adma.201503115.

[124] Wang, H. *et al.* Atomic-Scale Control of Magnetism at the Titanite-Manganite Interfaces. *Nano Letters* **19**, 3057–3065 (2019). https://pubs.acs.org/doi/10.1021/acs.nanolett.9b00441.

[125] Chi, X. *et al.* Enhanced Tunneling Magnetoresistance Effect via Ferroelectric Control of Interface Electronic/Magnetic Reconstructions. *ACS Applied Materials & Interfaces* **13**, 56638–56644 (2021). https://pubs.acs.org/doi/10.1021/acsami.1c15836.

[126] Guo, R. *et al.* Interface-engineered electron and hole tunneling. *Science Advances* **7**, eabf1033 (2021). https://www.science.org/doi/10.1126/sciadv.abf1033.

[127] Yin, Y. W. *et al.* Enhanced tunnelling electroresistance effect due to a ferroelectrically induced phase transition at a magnetic complex oxide interface. *Nature Materials* **12**, 397–402 (2013). https://www.nature.com/articles/nmat3564.

[128] Tornos, J. *et al.* Ferroelectric Control of Interface Spin Filtering in Multiferroic Tunnel Junctions. *Physical Review Letters* **122**, 037601 (2019). https://link.aps.org/doi/10.1103/PhysRevLett.122.037601.

[129] Jedrecy, N. *et al.* Resistive Switching and Redox Process at the $BaTiO_3$ / (La,Sr)MnO_3 Multiferroic-Type Interface. *Advanced Electronic Materials* **7**, 2000723 (2021). https://onlinelibrary.wiley.com/doi/10.1002/aelm.202000723.

[130] Chen, L. *et al.* Enhancement of tunneling electroresistance by interfacial cation intermixing in ferroelectric tunnel junctions. *Applied Surface Science* **512**, 145707 (2020). https://linkinghub.elsevier.com/retrieve/pii/S0169433220304633.

[131] Qin, Q. H. *et al.* Resistive Switching in All-Oxide Ferroelectric Tunnel Junctions with Ionic Interfaces. *Advanced Materials* **28**, 6852–6859 (2016). https://onlinelibrary.wiley.com/doi/10.1002/adma.201504519.

[132] Zhang, Q., Li, X. & Zhu, J. Direct Observation of Interface-Dependent Multidomain State in the $BaTiO_3$ Tunnel Barrier of a Multiferroic Tunnel Junction Memristor. *ACS Applied Materials & Interfaces* **13**, 43641–43647 (2021). https://pubs.acs.org/doi/10.1021/acsami.1c11661.

[133] Eason, R. (ed.) *Pulsed Laser Deposition of Thin Films: Applications-Led Growth of Functional Materials* (John Wiley & Sons, Inc., Hoboken, NJ, USA, 2006). http://doi.wiley.com/10.1002/0470052120.

[134] Rabe, K. M., Dawber, M., Lichtensteiger, C., Ahn, C. H. & Triscone, J.-M. Modern Physics of Ferroelectrics: Essential Background. In *Physics of Ferroelectrics*, vol. 105, 1–30 (Springer Berlin Heidelberg, Berlin, Heidelberg, 2007). http://link.springer.com/10.1007/978-3-540-34591-6_1. Series Title: Topics in Applied Physics.

[135] Kittel, C. *Introduction to solid state physics* (Wiley, Hoboken, NJ, 2005), 8 edn.

[136] Csiszár, S. *X-ray diffraction and X-ray absorption of strained CoO and MnO thin films*. Ph.D. thesis, University of Groningen (2005). https://research.rug.nl/en/publications/a88750de-cc3b-4ebe-95a2-3ee6c067829b.

[137] Gibaud, A. & Hazra, S. X-ray reflectivity and diffuse scattering. *Current Science* **78**, 1467–1477 (2000). http://www.jstor.org/stable/24104319.

[138] Parratt, L. G. Surface Studies of Solids by Total Reflection of X-Rays. *Physical Review* **95**, 359–369 (1954). https://link.aps.org/doi/10.1103/PhysRev.95.359.

[139] Vineyard, G. H. Grazing-incidence diffraction and the distorted-wave approximation for the study of surfaces. *Physical Review B* **26**, 4146–4159 (1982). https://link.aps.org/doi/10.1103/PhysRevB.26.4146.

[140] Atomic force microscopy. https://en.wikipedia.org/wiki/Atomic_force_microscopy.

[141] Piezoresponse force microscopy. https://en.wikipedia.org/wiki/Piezoresponse_force_microscopy.

[142] Morgan, D. & Bøgh, E. On the application of Rutherford scattering and channelling techniques to study semiconductor surfaces. *Surface Science* **32**, 278–286 (1972). https://www.sciencedirect.com/science/article/pii/0039602872901598.

[143] Geiger, D. H. & Marsden, E. LXI. The laws of deflexion of a particles through large angles. *The London, Edinburgh, and Dublin Philosophical Magazine and Journal of Science* **25**, 604–623 (1913). https://doi.org/10.1080/14786440408634197.

[144] Rutherford, E. LXXIX. The scattering of α and β particles by matter and the structure of the atom. *The London, Edinburgh, and Dublin Philosophical Magazine and Journal of Science* **21**, 669–688 (1911). https://doi.org/10.1080/14786440508637080.

[145] Foner, S. Versatile and sensitive vibrating-sample magnetometer. *Review of Scientific Instruments* **30**, 548–557 (1959). https://doi.org/10.1063/1.1716679.

[146] Kawasaki, M. *et al.* Atomic Control of the $SrTiO_3$ Crystal Surface. *Science* **266**, 1540–1542 (1994). https://www.science.org/doi/abs/10.1126/science.266.5190.1540.

[147] Ohnishi, T. *et al.* Preparation of thermally stable TiO_2-terminated $SrTiO_3$(100) substrate surfaces. *Applied Physics Letters* **85**, 272–274 (2004). https://doi.org/10.1063/1.1771461.

[148] Bachelet, R., Sánchez, F., Palomares, F. J., Ocal, C. & Fontcuberta, J. Atomically flat SrO-terminated $SrTiO_3$(001) substrate. *Applied Physics Letters* **95**, 141915 (2009). https://doi.org/10.1063/1.3240869.

[149] Connell, J. G., Isaac, B. J., Ekanayake, G. B., Strachan, D. R. & Seo, S. S. A. Preparation of atomically flat $SrTiO_3$ surfaces using a deionized-water leaching and thermal annealing procedure. *Applied Physics Letters* **101**, 251607 (2012). https://doi.org/10.1063/1.4773052.

[150] Koster, G., Kropman, B. L., Rijnders, G. J. H. M., Blank, D. H. A. & Rogalla, H. Quasi-ideal strontium titanate crystal surfaces through formation of strontium hydroxide. *Applied Physics Letters* **73**, 2920–2922 (1998). https://doi.org/10.1063/1.122630.

[151] Sirena, M., Steren, L. & Guimpel, J. Thickness dependence of the properties of $La_{0.6}Sr_{0.4}MnO_3$ thin films. *Thin Solid Films* **373**, 102–106 (2000). https://linkinghub.elsevier.com/retrieve/pii/S0040609000011135.

[152] Zhong, W., Zhang, P., Wang, Y. & Ren, T. Size effect on the dielectric properties of $BaTiO_3$. *Ferroelectrics* **160**, 55–59 (1994). https://doi.org/10.1080/00150199408007694.

[153] Zhao, T., Chen, F., Lu, H., Yang, G. & Chen, Z. Thickness and oxygen pressure dependent structural characteristics of $BaTiO_3$ thin films grown by laser molecular beam epitaxy. *Journal of Applied Physics* **87**, 7442–7447 (2000). https://doi.org/10.1063/1.373007.

[154] Kolodiazhnyi, T., Tachibana, M., Kawaji, H., Hwang, J. & Takayama-Muromachi, E. Persistence of Ferroelectricity in $BaTiO_3$ through the Insulator-Metal Transition. *Physical Review Letters* **104**, 147602 (2010). https://link.aps.org/doi/10.1103/PhysRevLett.104.147602.

[155] Cordero, F. *et al.* Probing ferroelectricity in highly conducting materials through their elastic response: Persistence of ferroelectricity in metallic $BaTiO_{3-\delta}$. *Physical Review B* **99**, 064106 (2019). https://link.aps.org/doi/10.1103/PhysRevB.99.064106.

[156] Miller, A. M. *et al.* Extracting information from X-ray diffraction patterns containing Laue oscillations. *Zeitschrift für Naturforschung B* **77**, 313–322 (2022). https://doi.org/10.1515/znb-2022-0020.

[157] Landau, L. & Lifshitz, E. *Quantum Mechanics: Non-Relativistic Theory.* Course of theoretical physics (Elsevier Science, 1991).

[158] Kim, Y., Ryu, S. & Jeen, H. Strain-effected physical properties of ferromagnetic insulating $La_{0.88}Sr_{0.12}MnO_3$ thin films. *RSC Advances* **9**, 2645–2649 (2019). http://dx.doi.org/10.1039/C8RA09851D.

[159] Lu, Y. *et al.* Large magnetotunneling effect at low magnetic fields in micrometer-scale epitaxial $La_{0.67}Sr_{0.33}MnO_3$ tunnel junctions. *Physical Review B* **54**, R8357–R8360 (1996). https://link.aps.org/doi/10.1103/PhysRevB.54.R8357.

[160] Ding, J. F. *et al.* Interfacial spin glass state and exchange bias in manganite bilayers with competing magnetic orders. *Physical Review B* **87**, 054428 (2013). https://link.aps.org/doi/10.1103/PhysRevB.87.054428.

[161] Li, T., Ma, D., Li, K. & Hu, Z. Self-biased magnetoelectric coupling effect in the layered $La_{0.7}Sr_{0.3}MnO_3$ / $BaTiO_3$ / $La_{0.7}Sr_{0.3}MnO_3$ multiferroic heterostructure. *Journal of Alloys and Compounds* **747**, 558–562 (2018). https://linkinghub.elsevier.com/retrieve/pii/S0925838818309046.

[162] Ott, F. Neutron studies of magnetic oxide thin films. *Journal of Physics: Condensed Matter* **20**, 264009 (2008). https://doi.org/10.1088/0953-8984/20/26/264009.

[163] Steren, L. B., Sirena, M. & Guimpel, J. Magnetic ordered phase in $La_{0.6}Sr_{0.4}MnO_3$ ferromagnets. *Physical Review B* **65**, 094431 (2002). https://link.aps.org/doi/10.1103/PhysRevB.65.094431.

[164] Pallecchi, I. *et al.* Probing of micromagnetic configuration in manganite channels by transport measurements. *Physical Review B* **76**, 174401 (2007). https://link.aps.org/doi/10.1103/PhysRevB.76.174401.

[165] Huijben, M. *et al.* Critical thickness and orbital ordering in ultrathin $La_{0.7}Sr_{0.3}MnO_3$ films. *Physical Review B* **78**, 094413 (2008). https://link.aps.org/doi/10.1103/PhysRevB.78.094413.

[166] Pantel, D. & Alexe, M. Electroresistance effects in ferroelectric tunnel barriers. *Physical Review B* **82**, 134105 (2010). https://link.aps.org/doi/10.1103/PhysRevB.82.134105.

[167] Majumdar, S., Huhtinen, H., Paturi, P. & Majumdar, H. S. Effect of strain and grain boundaries on dielectric properties in $La_{0.7}Sr_{0.3}MnO_3$ thin films. *Journal of Materials Science* **48**, 2115–2122 (2013). http://link.springer.com/10.1007/s10853-012-6986-x.

[168] Majumdar, S., Huhtinen, H., Majumdar, H. S., Laiho, R. & Österbacka, R. Effect of $La_{0.67}Sr_{0.33}MnO_3$ electrodes on organic spin valves. *Journal of Applied Physics* **104**, 033910 (2008). https://doi.org/10.1063/1.2963814.

[169] Gong, J., Zheng, D., Li, D., Jin, C. & Bai, H. Lattice distortion modified anisotropic magnetoresistance in epitaxial $La_{0.67}Sr_{0.33}MnO_3$ thin films. *Journal of Alloys and Compounds* **735**, 1152–1157 (2018). https://linkinghub.elsevier.com/retrieve/pii/S0925838817340021.

[170] Hwang, H. Y., Cheong, S.-W., Ong, N. P. & Batlogg, B. Spin-Polarized Intergrain Tunneling in $La_{2/3}Sr_{1/3}MnO_3$. *Physical Review Letters* **77**, 2041–2044 (1996). https://link.aps.org/doi/10.1103/PhysRevLett.77.2041.

[171] Li, X. W., Gupta, A., Xiao, G. & Gong, G. Q. Low-field magnetoresistive properties of polycrystalline and epitaxial perovskite manganite films. *Applied Physics Letters* **71**, 1124–1126 (1997). https://doi.org/10.1063/1.119747.

[172] Bibes, M. *et al.* Laser patterned arrays of interfaces in magnetoresistive $La_{2/3}Sr_{1/3}MnO_3$ thin films. *Applied Physics Letters* **75**, 2120–2122 (1999). https://doi.org/10.1063/1.124936.

[173] Zhang, C. *et al.* Large Low-Field Magnetoresistance (LFMR) Effect in Free-Standing $La_{2/3}Sr_{1/3}MnO_3$ Films. *ACS Applied Materials & Interfaces* **13**, 28442–28450 (2021). https://doi.org/10.1021/acsami.1c03753.

[174] Dallocchio, M. *et al.* Tunable magnetic and magnetotransport properties in locally epitaxial $La_{0.67}Sr_{0.33}MnO_3$ thin films on polycrystalline $SrTiO_3$, by control of grain size. *Journal of Physics D: Applied Physics* **55**, 235303 (2022). https://doi.org/10.1088/1361-6463/ac5a1f.

[175] Jin, S. *et al.* Thousandfold Change in Resistivity in Magnetoresistive La-Ca-Mn-O Films. *Science* **264**, 413–415 (1994). https://www.science.org/doi/abs/10.1126/science.264.5157.413.

[176] Shockley, W. The theory of p-n junctions in semiconductors and p-n junction transistors. *The Bell System Technical Journal* **28**, 435–489 (1949). https://doi.org/10.1002/j.1538-7305.1949.tb03645.x.

[177] Banwell, T. & Jayakumar, A. Exact analytical solution for current flow through diode with series resistance. *Electronics Letters* **36**, 291–292(1) (2000). https://digital-library.theiet.org/content/journals/10.1049/el_20000301.

[178] Jo, J. Y., Kim, Y. S., Noh, T. W., Yoon, J.-G. & Song, T. K. Coercive fields in ultrathin $BaTiO_3$ capacitors. *Applied Physics Letters* **89**, 232909 (2006). https://doi.org/10.1063/1.2402238.

[179] Sanchez-Santolino, G. *et al.* Resonant electron tunnelling assisted by charged domain walls in multiferroic tunnel junctions. *Nature Nanotechnology* **12**, 655–662 (2017). http://www.nature.com/articles/nnano.2017.51.

[180] Tsymbal, E. Y. & Kohlstedt, H. Tunneling across a ferroelectric. *Science* **313**, 181–183 (2006). https://www.science.org/doi/abs/10.1126/science.1126230.

[181] Majumdar, S. & van Dijken, S. Pulsed laser deposition of $La_{1-x}Sr_xMnO_3$: thin-film properties and spintronic applications. *Journal of Physics D: Applied Physics* **47**, 034010 (2013). https://dx.doi.org/10.1088/0022-3727/47/3/034010.

[182] Zafar, S. *et al.* Oxygen vacancy mobility determined from current measurements in thin $Ba_{0.5}Sr_{0.5}TiO_3$ films. *Applied Physics Letters* **73**, 175–177 (1998). https://doi.org/10.1063/1.121746.

[183] Zhao, D. *et al.* Depolarization of multidomain ferroelectric materials. *Nature Communications* **10**, 2547 (2019). http://www.nature.com/articles/s41467-019-10530-4.

[184] Volianskis, A., Collingridge, G. L. & Jensen, M. S. The roles of STP and LTP in synaptic encoding. *PeerJ* **1**, e3 (2013). https://peerj.com/articles/3.

[185] Zhang, Y. *et al.* Brain-inspired computing with memristors: Challenges in devices, circuits, and systems. *Applied Physics Reviews* **7**, 011308 (2020). https://doi.org/10.1063/1.5124027.

[186] Kim, S. *et al.* Experimental Demonstration of a Second-Order Memristor and Its Ability to Biorealistically Implement Synaptic Plasticity. *Nano Letters* **15**, 2203–2211 (2015). https://doi.org/10.1021/acs.nanolett.5b00697.

[187] Du, C., Ma, W., Chang, T., Sheridan, P. & Lu, W. D. Biorealistic Implementation of Synaptic Functions with Oxide Memristors through Internal Ionic Dynamics. *Advanced Functional Materials* **25**, 4290–4299 (2015). https://onlinelibrary.wiley.com/doi/abs/10.1002/adfm.201501427.

[188] Wang, Z. *et al.* Memristors with diffusive dynamics as synaptic emulators for neuromorphic computing. *Nature Materials* **16**, 101–108 (2017). https://www.nature.com/articles/nmat4756.

[189] Mikheev, V. *et al.* Ferroelectric Second-Order Memristor. *ACS Applied Materials & Interfaces* **11**, 32108–32114 (2019). https://pubs.acs.org/doi/10.1021/acsami.9b08189.

[190] Pershin, Y. V. & Di Ventra, M. Neuromorphic, Digital, and Quantum Computation With Memory Circuit Elements. *Proceedings of the IEEE* **100**, 2071–2080 (2012). http://ieeexplore.ieee.org/document/6035950/.

[191] Zidan, M. A., Jeong, Y. & Lu, W. D. Temporal Learning Using Second-Order Memristors. *IEEE Transactions on Nanotechnology* **16**, 721–723 (2017). https://doi.org/10.1109/TNANO.2017.2710158.

[192] Kumar, S., Wang, X., Strachan, J. P., Yang, Y. & Lu, W. D. Dynamical memristors for higher-complexity neuromorphic computing. *Nature Reviews Materials* (2022). https://www.nature.com/articles/s41578-022-00434-z.

[193] Kullmann, D. M., Perkei, D. J., Manabe, T. & Nicoll, R. A. Ca^{2+} Entry via postsynaptic voltage-sensitive Ca^{2+} channels can transiently potentiate excitatory synaptic transmission in the hippocampus. *Neuron* **9**, 1175–1183 (1992). https://linkinghub.elsevier.com/retrieve/pii/089662739290075O.

[194] Rizo, J. & Rosenmund, C. Synaptic vesicle fusion. *Nature Structural & Molecular Biology* **15**, 665–674 (2008). http://www.nature.com/articles/nsmb.1450.

[195] Bear, M. F. & Malenka, R. C. Synaptic plasticity: LTP and LTD. *Current Opinion in Neurobiology* **4**, 389–399 (1994). https://www.sciencedirect.com/science/article/pii/0959438894901015.

[196] Shouval, H. Z., Bear, M. F. & Cooper, L. N. A unified model of nmda receptor-dependent bidirectional synaptic plasticity. *Proceedings of the National Academy of Sciences* **99**, 10831–10836 (2002). https://www.pnas.org/doi/abs/10.1073/pnas.152343099.

[197] Graupner, M. & Brunel, N. Calcium-based plasticity model explains sensitivity of synaptic changes to spike pattern, rate, and dendritic location. *Proceedings of the National Academy of Sciences* **109**, 3991–3996 (2012). https://www.pnas.org/doi/abs/10.1073/pnas.1109359109.

[198] Yang, S.-N., Tang, Y.-G. & Zucker, R. S. Selective Induction of LTP and LTD by Postsynaptic $[Ca^{2+}]_i$ Elevation. *Journal of Neurophysiology* **81**, 781–787 (1999). https://doi.org/10.1152/jn.1999.81.2.781.

[199] Salin, P. A., Scanziani, M., Malenka, R. C. & Nicoll, R. A. Distinct short-term plasticity at two excitatory synapses in the hippocampus. *Proceedings of the National Academy of Sciences* **93**, 13304–13309 (1996). https://www.pnas.org/doi/abs/10.1073/pnas.93.23.13304.

[200] Creager, R., Dunwiddie, T. & Lynch, G. Paired-pulse and frequency facilitation in the CA1 region of the in vitro rat hippocampus. *The Journal of Physiology* **299**, 409–424 (1980). https://physoc.onlinelibrary.wiley.com/doi/abs/10.1113/jphysiol.1980.sp013133.

[201] Bienenstock, E., Cooper, L. & Munro, P. Theory for the development of neuron selectivity: orientation specificity and binocular interaction in visual cortex. *Journal of Neuroscience* **2**, 32–48 (1982). https://www.jneurosci.org/content/2/1/32.

[202] Cooper, L. N., Intrator, N., Blais, B. S. & Shouval, H. Z. *Theory of Cortical Plasticity* (World Scientific, 2004). https://www.worldscientific.com/doi/abs/10.1142/5462.

[203] Cooper, L. N. & Bear, M. F. The BCM theory of synapse modification at 30: interaction of theory with experiment. *Nature Reviews Neuroscience* **13**, 798–810 (2012). http://www.nature.com/articles/nrn3353.

[204] Dudek, S. M. & Bear, M. F. Homosynaptic long-term depression in area CA1 of hippocampus and effects of N-methyl-D-aspartate receptor blockade. *Proceedings of the National Academy of Sciences* **89**, 4363–4367 (1992). https://www.pnas.org/doi/abs/10.1073/pnas.89.10.4363.

[205] Kirkwood, A., Rioult, M. G. & Bear, M. F. Experience-dependent modification of synaptic plasticity in visual cortex. *Nature* **381**, 526–528 (1996). http://www.nature.com/articles/381526a0.

[206] Philpot, B. D., Cho, K. K. & Bear, M. F. Obligatory Role of NR2A for Metaplasticity in Visual Cortex. *Neuron* **53**, 495–502 (2007). https://linkinghub.elsevier.com/retrieve/pii/S0896627307000682.

[207] Feldman, D. E. The Spike-Timing Dependence of Plasticity. *Neuron* **75**, 556–571 (2012). https://linkinghub.elsevier.com/retrieve/pii/S0896627312007039.

[208] Caporale, N. & Dan, Y. Spike Timing–Dependent Plasticity: A Hebbian Learning Rule. *Annual Review of Neuroscience* **31**, 25–46 (2008). https://doi.org/10.1146/annurev.neuro.31.060407.125639.

[209] Andrew, A. M. Spiking Neuron Models: Single Neurons, Populations, Plasticity. *Kybernetes* **32** (2003). https://www.emerald.com/insight/content/doi/10.1108/k.2003.06732gae.003/full/html.

Abbreviations

A

AFM	atomic force microscopy

B

BE	bottom electrode
BTO	barium titanate, $BaTiO_3$

E

EELS	electron energy loss spectroscopy
ER	electroresistance

F

FE	ferroelectric
FM	ferromagnet, ferromagnetic metal
FTJ	ferroelectric tunnel junction

H

HRS	high resistance state

I

IP	in-plane

L

LRS	low resistance state
LSMO	lanthanum-strontium manganite, $La_{1-x}Sr_xMnO_3$
LTD	long-term depression
LTP	long-term potentiation

M

MFM	metal-ferroelectric-metal junction
MFS	metal-ferroelectric-semiconductor junction
MIT	metal-insulator transition
MR	magnetoresistance
MTJ	magnetic tunnel junction

N

NSTO	Nb doped strontium titanate, Nb:$SrTiO_3$

P

PFM	piezoresponse force microscopy
PLD	pulsed laser deposition
PPD	paired-pulse depression
PPF	paired-pulse facilitation
PPMS	physical property measurement system
PZT	lead zirconate-titanate, $Pb(Zr_xTi_{1-x})O_3$

R

RBS	Rutherford backscattering spectrometry
RS	resistive switching
RSM	reciprocal space mapping
RT	room temperature

S

SC	semiconductor
SMU	source-measure unit
SRDP	spike rate-dependent plasticity
STD	short-term depression
STDP	spike timing-dependent plasticity
STO	strontium titanate, $SrTiO_3$
STP	short-term potentiation

T

TE	top electrode
TEM	transmission electron microscopy
TER	tunneling electroresistance
TMR	tunneling magnetoresistance

V

VSM	vibrating sample magnetometer

X

XRD	X-ray diffraction
XRR	X-ray reflectometry

Symbols

2θ	angle between incident and diffracted X-ray beams
a	in-plane lattice parameter
c	out-of-plane lattice parameter
C_i	magnetic moment of the i^{th} component, divided by the total volume of the ferromagnetic film
Δ	time delay between pre-spike and post-spike
H	magnetic field
H_c	coercive field
I	electric current intensity
I_{read}	reading current intensity
I_{write}	writing current intensity
j	electric current density
λ	wavelength
M	magnetization
M_s	saturation magnetization
ω	grazing angle of incident X-ray beam to sample surface
R	device resistance
σ	surface or interface roughness
T	temperature
T_C	Curie temperature
V	voltage
V_{read}	reading voltage
V_{write}	writing voltage
w	synaptic weight

List of Figures

1.1 50 years of microprocessor trend data . . . 3
1.2 Share of communication technology of global electricity usage 2010–2030 4
1.3 Yearly improvement of processor and DRAM memory speeds, for a time period of three decades . . . 5
1.4 Artificial neural network size increase over time . . . 5
1.5 Memristor-synapse analogy . . . 7
1.6 Sketches of the filamentary switching mechanisms . . . 9
1.7 Sketches of the non-filamentary switching mechanisms . . . 10
1.8 Phase-change memory device principle . . . 10
1.9 Schematic pictures of GMR and TMR effects . . . 12
1.10 Tunneling magnetoresistance ratio vs applied magnetic field for SiO_2 / NiFe / Co / Al_2O_3 (13, 43 and 63 Å) / Co structure . . . 13
1.11 Three types of ferroelectric devices together with the corresponding current response curves . . . 14
1.12 Ferroelectric tunnel junction operation principle . . . 15
1.13 Ferroelectric memristor operation . . . 16
1.14 Magnetoelectric La:$BiFeO_3$-based device . . . 17
1.15 A magnetic tunnel junction and a ferroelectric tunnel junction are combined into a multiferroic tunnel junction . . . 17

2.1 Unit cell of $BaTiO_3$ . . . 19
2.2 Temperature dependence of $BaTiO_3$ unit cell parameters . . . 20
2.3 $BaTiO_3$ hysteresis loops . . . 20
2.4 Tunneling electroresistance effect in a ferroelectric tunnel junction at the nanoscale . . . 21
2.5 Resistive switching mechanism of the metal/FE/semiconductor tunnel junctions . . . 22
2.6 Competition between ferroelectric switching and oxygen vacancy migration . . . 23
2.7 Schematic image of double exchange interaction and phase diagram of $La_{1-x}Sr_xMnO_3$ . . . 24
2.8 TMR and CMR effects in $La_{1-x}Sr_xMnO_3$ . . . 25
2.9 Electric field modification of dead layers in $La_{1-x}Sr_xMnO_3$ . . . 26
2.10 Interfacial magnetic couplings across the $BaTiO_3$ / $La_{1-x}Sr_xMnO_3$ interfaces via Mn orbital occupation . . . 27
2.11 Properties of intermixed $BaTiO_3$ / $La_{1-x}Sr_xMnO_3$ interface . . . 28

3.1 Simplified sketch of the pulsed laser deposition method . . . 32
3.2 Sketch of the lithography steps . . . 33

3.3 Sketch of the XRD measurements . . . 35
3.4 XRR measurement: sketch and example of an experimental curve . . 36
3.5 Atomic and piezoresponse force microscopy description . . . 37
3.6 RBS measurement description . . . 38
3.7 RBS spectrum of Ta_2O_5/Si sample with its simulation . . . 39
3.8 Sketch of the device connection for electrical measurements. . . . 40

4.1 Surface topography of the samples . . . 45
4.2 Symmetric θ-2θ diffraction patterns of thick barrier samples (Rigaku) 46
4.3 Symmetric θ-2θ diffraction pattern of thick barrier sample (X'Pert) . 47
4.4 Fits of the diffraction peaks . . . 48
4.5 Diffraction pattern with Laue function simulation . . . 50
4.6 Symmetric θ-2θ diffraction patterns of thin barrier samples . . . 51
4.7 RSM in the region of 103 reflections . . . 52
4.8 XRR curves of the thick barrier samples . . . 53
4.9 RBS spectra of thick barrier samples . . . 54
4.10 TEM of thin barrier $SrTiO_3$ substrate sample cross-section . . . 55
4.11 EELS spectra from a thick barrier sample . . . 56
4.12 $M(H)$ loops of thick barrier samples . . . 57
4.13 Temperature dependency of M_s, extracted from magnetization loops of thick barrier samples . . . 58
4.14 Temperature dependencies of H_c and relative magnetic moment of the magnetization components for thick barrier samples . . . 59
4.15 Magnetization loop and temperature dependence of total saturation magnetization of thick barrier MgO substrate sample (optimized geometry) . . . 61
4.16 Temperature dependencies of H_c and relative magnetic moment of the magnetization components of thick barrier MgO substrate sample (optimized geometry) . . . 61
4.17 Magnetization loop and temperature dependence of total saturation magnetization of thin barrier MgO substrate sample . . . 62
4.18 Temperature dependencies of H_c and relative magnetic moment of the magnetization components of thin barrier MgO substrate sample 63
4.19 Magnetization loop and temperature dependence of total saturation magnetization of thin barrier $SrTiO_3$ substrate sample . . . 64
4.20 Temperature dependencies of H_c and relative magnetic moment of the magnetization components of thin barrier $SrTiO_3$ substrate sample 64

5.1 Sketch of the voltage profile for write-read measurements. . . . 65
5.2 $I_{write}(V_{write})$ and $R(V_{write})$ curves of a 50 µm device on $SrTiO_3$ substrate sample . . . 66
5.3 Switching curves with pulses of various V_{write} of a 50 µm device on $SrTiO_3$ substrate sample . . . 67
5.4 $j(V_{write})$ curves of a 50 µm device on $SrTiO_3$ substrate sample in low V range . . . 69
5.5 $I_{write}(V_{write})$ and $R(V_{write})$ curves at 150 K and temperature dependence of resistance of a 100 µm square device on MgO substrate sample. 70
5.6 MR measurements at various magnetic field angles and various T . . 71
5.7 Extracts from MR data . . . 72

6.1 $I_{write}(V_{write})$ and $R(V_{write})$ curves of a 100 µm semiconducting-like device from Nb:$SrTiO_3$ substrate sample . . . 76
6.2 $I_{write}(V_{write})$ and $R(V_{write})$ curves of a 100 µm metal-like device from Nb:$SrTiO_3$ substrate sample . . . 77
6.3 Extracted temperature dependencies of LRS, HRS and ER of the semiconducting-like and metal-like devices . . . 77
6.4 Circuit diagram of the simplified device model. . . . 78
6.5 Modelled $I(V)$ and $R(V)$ curves of semiconducting-like and metal-like devices . . . 80
6.6 Multilevel $I_{write}(V_{write})$ and $R(V_{write})$ curves . . . 81
6.7 Multilevel resistance states set with positive or negative writing pulses 82
6.8 Writing pulse sequences . . . 83
6.9 Retention of resistance states set at different levels . . . 83
6.10 $R(V_{write})$ loops measured with different duration of the pulses . . . 84
6.11 50 cycles between −3.5 V and +7 V with their median . . . 85
6.12 Endurance measurement between LRS (−3.5 V) and HRS (+7 V). . . 85
6.13 $I(V)$ measurements in the tunneling region . . . 86
6.14 Relaxation dynamics from potentiated/depressed states . . . 87
6.15 Short- and long-term resistance jumps . . . 88
6.16 PFM amplitude and phase maps . . . 89
6.17 PFM amplitude and phase spectra . . . 89
6.18 Schematic sketch of the resistance switching mechanism . . . 92

7.1 Example of the STP effect, recorded in rat hippocampal slices . . . 93
7.2 Schematic image of a biological synapse and the $La_{1-x}Sr_xMnO_3$ / $BaTiO_3$ / $La_{1-x}Sr_xMnO_3$ memristor . . . 94
7.3 PPF measurements in hippocampal slices of guinea pigs . . . 95
7.4 Description of the PPF effect in memristors . . . 96
7.5 PPF measurements . . . 97
7.6 Neurological example of SRDP . . . 98
7.7 Comparison of experimental results, extracted from SRDP data, and the Bienenstock-Cooper-Munro theory calculation . . . 99
7.8 SRDP weight calibration . . . 100
7.9 SRDP measurement . . . 101
7.10 Experience dependence of SRDP . . . 102
7.11 Extracted weight modifications with experience dependent SRDP . . 102
7.12 Sliding threshold frequency, extracted from experience dependent plasticity . . . 103
7.13 STDP measured in cultures of dissociated rat hippocampal neurons . 104
7.14 STDP spike sketches . . . 105
7.15 First order STDP measurement . . . 106
7.16 Second order STDP measurement . . . 106

A.1 Multilevel $I_{write}(V_{write})$ and $R(V_{write})$ curves, measured on additional semiconducting-like device . . . 113
A.2 Multilevel resistance states set with positive or negative writing pulses (from additional semiconducting-like device) . . . 114
A.3 Writing pulse sequences (from additional semiconducting-like device) 114

A.4 Relaxation dynamics from potentiated/depressed states (from additional semiconducting-like device) . . . 115
A.5 PPF measurement (from additional semiconducting-like device) . . . 116
A.6 Experience dependence of SRDP (from additional semiconducting-like device) . . . 116
A.7 $I_{write}(V_{write})$ and $R(V_{write})$ curves from additional metal-like device, measured at various temperatures . . . 117
A.8 Temperature dependencies of extracted LRS, HRS and ER, and continuous $R(T)$ measurement with heating (from additional metal-like device) . . . 118
A.9 30 cycles between -3 V and $+4$ V with their median, measured on the additional 25 µm metal-like device at 50 K . . . 118
A.10 Multilevel $|I_{write}|(V_{write})$ and $R(V_{write})$ curves (from additional metal-like device at 50 K) . . . 119
A.11 Multilevel resistance states set with positive or negative writing pulses (from additional metal-like device at 50 K) . . . 119
A.12 Writing pulse sequences (from additional metal-like device at 50 K) . 120
A.13 Retention of resistance states set at different levels (from additional metal-like device at 50 K) . . . 120
A.14 Relaxation dynamics from potentiated/depressed states (from additional metal-like device at 50 K) . . . 121

List of Tables

4.1 Summary table of all grown samples. 43
4.2 Lattice parameters calculated from the XRD fits 48
4.3 Parameters of the Laue oscillations simulation 50
4.4 Summary table of the film thicknesses, obtained by XRR simulation . 53
4.5 Summary table of the film thicknesses, obtained by RBS simulation . 54

Titre : Nanostructures d'oxydes multiferroïques : états multi-résistances

Résumé : Les nouveaux défis de la microélectronique depuis déjà deux décennies nécessitent le développement de matériaux et dispositifs bien au-delà des exigences de compatibilité avec la technologie silicium. Parmi ces défis figurent la miniaturisation des éléments de circuit intégrés et l'intégration 3D, pour surmonter le goulot d'étranglement de von Neumann, ainsi que l'élaboration de dispositifs neuromorphiques à base de memristors. Les fonctionnalités supplémentaires, offertes par la mise en œuvre de matériaux ferroélectriques et magnétiques, permettraient de réaliser des progrès significatifs dans tous les domaines évoqués.

Dans cette thèse, nous étudions l'hétérostructure tri-couche multiferroïque (c'est-à-dire ferroélectrique et ferromagnétique simultanément) $La_{0.7}Sr_{0.3}MnO_3$ / $BaTiO_3$ / $La_{0.7}Sr_{0.3}MnO_3$. Nous étudions en détail les propriétés structurales, chimiques et magnétiques des couches minces fabriquées ainsi que leurs interfaces pour établir les fondements nécessaires à la compréhension des expériences de transport électronique sur les dispositifs finaux. Dans les échantillons avec une barrière épaisse de $BaTiO_3$, nous observons une commutation de résistance stochastique et une magnétorésistance à champ faible plutôt complexe. Dans les dispositifs à barrière mince, nous démontrons la commutation de résistance quasi-analogique (sur de multiples niveaux de résistance) et mettons en évidence une forte dynamique temporelle, liée à la polarisation et aux lacunes d'oxygène. Le comportement de notre memristor s'avère reproduire idéalement celui des synapses biologiques, en particulier concernant les effets de second ordre intervenant dans la transmission des impulsions neuronales et qui proviennent de la dynamique transitoire d'ions Ca^{2+}.

Via la mise en place d'expériences adaptées, nous mettons en exergue plusieurs réponses synaptiques de second ordre dans notre memristor multiferroïque. Nos résultats suggèrent un nouveau concept physique de memristor de second ordre pour l'émulation bioréaliste des synapses et constituent une première étape dans la mise en œuvre matérielle de réseaux de neurones artificiels.

Mots clés : ferroélectrique, ferromagnétique, oxyde, commutation résistive, memristor

Title: Multiferroic oxide nanostructures: multi-resistance states

Abstract: New challenges in microelectronics already for two decades have been requiring the development of materials and device concepts way beyond conventional Si scaling. Among these challenges are integral circuit elements' miniaturization and 3D integration, overcoming the von Neumann bottleneck and elaboration of memristor-based neuromorphic hardware. Additional functionalities, offered with implementation of ferroelectric and magnetic materials, would allow to achieve significant progress in all the mentioned fields.

In this thesis, we study the tri-layer multiferroic (i.e., ferroelectric and ferromagnetic simultaneously) heterostructures $La_{0.7}Sr_{0.3}MnO_3$ / $BaTiO_3$ / $La_{0.7}Sr_{0.3}MnO_3$. We thoroughly investigate the structural, chemical and magnetic properties of the fabricated thin layers and interfaces between them to establish the foundation for further electronic transport experiments. In thick $BaTiO_3$ barrier samples, we observe stochastic resistance switching and a rather complex low-field magnetoresistance. In thin barrier devices, we demonstrate the multilevel quasi-analog resistance switching that shows a strong temporal dynamic, in relation with polarization and oxygen vacancies. This behavior is found to emulate very accurately that of the biological synapses, with the emphasis on the so called second order effects, which are originating from the transient dynamics of Ca^{2+} ions, mediating the neural pulse transmission.

Via appropriate experiments, we demonstrate the operation of several second order synaptic functions in our multiferroic memristors. Our findings suggest the new physical concept of second order memristor for biorealistic emulation of synapses and make a step toward the hardware implementation of artificial neural networks.

Keywords: ferroelectric, ferromagnetic, oxide, resistive switching, memristor